Joining Lightweight Dissimilar Alloys by Using Electron Beam Welding

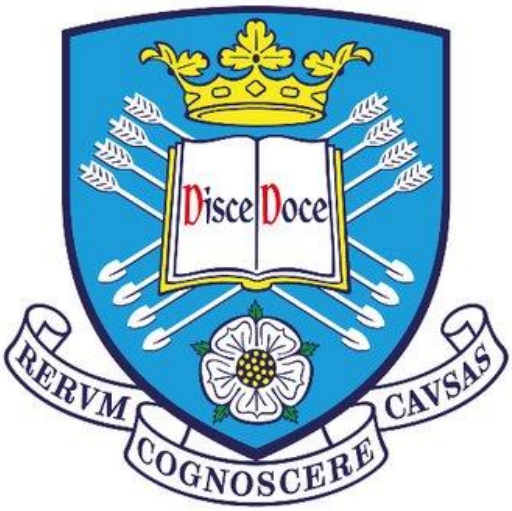

Affaan Uthman Moosa

A thesis submitted for the degree of Doctor of Philosophy

Department of Materials Science and Engineering
The University of Sheffield

2019

To my late father, God rest his soul,

Uthman Moosa

11.07.2018

DECLARATION

I hereby declare that the dissertation entitles “Joining Lightweight Dissimilar Alloys by using Electron Beam Welding” was conducted, completed and written by me. I also declare it did not previously submitted for the award of any qualification or other similar title of this for any other examining body or University. This thesis contains fewer than 62,000 words, and this includes footnotes, equations, tables and bibliography. Also, it has fewer than 80 figures.

Acknowledgements

I would like to express my sincere gratitude to my supervisor Professor Iain Todd for his valuable guidance, endless support, encouragements and patience throughout my PhD study, without his guidance and great patience, this work could not have been accomplished. I benefitted a great deal from his advice and his knowledge during my work on this project. I would like to thank my co-supervisor Professor Brad P. Wynne for the valuable information and support during my study. I also want to thanks Dr Martin Jackson and Dr Richard Thackray for their helpful discussions.

A special thank you must go to Dr Everth Hernández-Nava for the considerable help and support on all the Electron Beam welding work performed during this study. I also would like to thank Dr Meurig Thomas, Dr Phil Mahoney and Dr Guan Dikai for their support.

I would like to thank all the technical staff in the Materials Science and Engineering Department at The University of Sheffield for helping me to carry out my experimental work, their skills and guidance helped me to operate different machines and equipment confidently, and they never hesitate to help me.

I would also like to acknowledge my sponsor, the Iraqi ministry of High Education and Scientific Research and the Iraqi cultural attaché for the generous financial support during my study. I would also like to thank all the staff at the Engineering Technical College, Middle Technical University, Baghdad, Iraq, for their support.

I would like to thank my beloved family, my mother Aidah, my father Uthman (God rest his soul) my brother Ammar, sisters Abeer and Olaa for the love, encouragement, and non-stop prayer for me.

Finally, I would like to thank my father-in-law Dr Abdulnafa Shakir and my mother-in-law Awaz for their support. My lovely wife Shireen and my children Abdullah, Sarah and Adel, thank you all.

Abstract

An investigation was carried out to study the ability to carry out dissimilar welding between Ti-6Al-4Valloy and commercially pure vanadium alloy. Electron beam melting machine (EBM) was adopted for EBW for the dissimilar welding process using an Arcam S12 system. A promising beam setting was generated using the design of experiment (DoE). DoE normalised parameters and discrete parameters were suggested to find the best beam welding setting. Using different normalising approaches helped to establish a full penetration weld with acceptable characteristics: weld root and weld undercut when set II was applied. Powder technology means and Spark Plasma Sintering was employed to design a filler metal to be used in dissimilar welding. Based on the microstructures and mechanical analysis, the designed filler metals Ti/V, Ti/V2 and Ti/V3 were selected as the designated interlayers to be prefixed in the joints between titanium base metal (Ti-BM) and vanadium base metal (V-BM) in the pre-welding process. Dissimilar welding was performed based on the best beam parameters obtained from the beam optimisation methods. A successful full penetration weld was achieved between Ti-6Al-4V and CP-V alloys directly, without filler metals, which offered a tensile strength reaching to 282 MPa. When the 5 mm thin interlayer was added to the welding zone, the welds W1, W2 and W3 achieved strength close to that of the non-filler weld AW0. The hardness measurements for the welding zone (WZ) revealed increments in hardness values when the V content was increased in the WZ, reaching a maximum value of 345 HV_1 for the WZ of weld type W2. The W2 weld sample, also, showed superior strength, reaching to ~270 MPa. The presence of solid-solution phase βTi-V reduced the hardness values from 375±5 HV_1 in the case of the keyhole titanium weldtracks to about 354 HV_1 in the WZ of the Ti-V dissimilar joint. Hardness measurements showed that the highest and lowest hardness values were in the titanium heat affected zone (Ti-HAZ) and vanadium heat affected zone (V-HAZ), respectively. Additionally, tensile tests confirmed that material failure occurred in the base metal with lower mechanical properties, i.e. vanadium, and not in the weld joint. Necking condition was observed in the V-HAZ in all the tensile samples with and without the filler metals, and as the failure took place outside the WZ this suggests that the attempt to carry out dissimilar welding between Ti-6Al-4V alloy and CP-V alloy was successful.

TABLE OF CONTENTS

LIST OF FIGURES

LIST OF TABLES

Nomenclature

BM	Base metal
HAZ	Heat affected zone
WZ	Welding zone
DW	Dissimilar welding
PAW	Plasma arc welding
LBW	Laser beam welding
EBW	Electron beam welding
EBM	Electron beam melting
GMAW	Gas metal arc welding
FW	Friction welding
FSW	Friction stir welding
PWHT	Post welding heat treatment
SPS	Spark plasma sintering
CP-V	Commercially pure vanadium
α	Titanium α phase
α'	Martensitic phase
β	Titanium β phase
ρ	Material density g/cc
ρr	Relative density
Vf	Volume fraction
ρth	Theoretical density
m	Mass (kg)
*q**	Normalised beam power
*v**	Normalised traverse rate
T	Temperature, ˚C
T0	Initial temperature, ˚C
Tm	Melting temperature, ˚C
η	Surface absorptivity
rb	Spot diameter, mm
λ	Thermal conductivity, W/mK
*Lm**	Volumetric latent heat of melting, J/m3
*Lv**	Volumetric latent heat of vaporisation, J/m3
q	Beam power, kW
v	Beam speed, mm/s
α	Thermal diffusivity, m2/s
HV	Vickers hardness number

CHAPTER 1: INTRODUCTION

1.1 Introduction

Welding is a vital manufacturing process that offers the ability to use different types of alloys to fabricate complex structures which cannot be produced by other manufacturing methods. Interest in the fabrication of complex structures by welding methods has increased rapidly, especially in relation to titanium alloys[1]. Titanium alloys have been used widely in different industrial applications. Essential properties of titanium such as strength, toughness and fracture resistance make these alloys favourable for applications such as the aerospace and automotive industries[2].

The weldability of some titanium alloys adds an additional favourable factor that has led to these alloys being investigated in a wide range of applications[3]. Therefore, extensive studies have been conducted to develop the use of titanium in the industry in a way that is cost effective[4]. There has been a recent global trend directed toward studying the joining of titanium alloys with different metals to produce a low-cost method of fabricating a sophisticated structure with superior properties of excellent strength with the lightweight. Different factors that affect dissimilar welding between titanium and other metals include such as the materials' solubility[5], phase transformation upon solidification[3], the weldability of the alloy, and the rate of cooling cycle[6].

Special consideration is required for titanium welding as this alloy is very reactive with oxygen and hydrogen at elevated temperature and there is a high potential for porosity to form in the welding zone (WZ) when conventional welding methods are used. Welding methods have usually used shielding gas to protect the WZ from oxygen and other contaminants during the melting process. Gases such as Argon, Helium, or a mix of Argon and helium have been used with the gas tungsten arc welding process (GTAW) and plasma welding process (PAW) [7], CO_2 with laser beam welding process (LBW)[8]–[10] or in

vacuum condition which is considered the most reliable method when carrying out titanium alloy welding by using electron beam welding method (EBW), since the vacuum atmosphere reduces oxidation and thereby prevents the formation of porosity in the WZ [11], [12].

However, even when optimal conditions have been set for the welding of titanium, weld defects from the welding process will still be present. Squillace et al. [9] reported the effect of heat input on the WZ geometry, as with high heat input a vaporising effect of the molten metal during the fusion process will take place, leaving the molten pool with a shortage amount of melted metal. Upon solidification, a concave shape at the welding face will form, which known as underfill.

Additionally, Cao et al.[8] reported a reduction in ductility when using the LBW process in titanium welding. The effect of welding parameters, such as welding speed on the WZ dimension was directly proportional. Although CO_2 was applied during the welding process to protect the WZ during the melting, pores still formed in the WZ. Another problem is the presence of intermetallic compounds (IMCs) in the WZ which is caused by solute enrichment, as reported by Tsai et al. [13] when post welding heat treatments are applied to increase the hardness.

A few studies have reported the welding of vanadium alloys among these, Chung et al.[14] studied the effect of post-weld heat treatments on the distribution of hardness measurements across the welding zone. A comparison was carried out for the WZ as-received condition with the WZ subjected to a 1000˚C annealing treatment. A reduction was observed in hardness values with an improvement in impact resistance as the PWHT was applied.

Furthermore, dissimilar welding between pure vanadium and 316L stainless steel was carried out by Nogami et al. [15], [16] using the EBW method. The study investigated the effect of beam position and PWHT on the microstructure and mechanical properties. Precipitation hardening was present, and the hardness values incremented as the annealing treatment was applied, a NiV_3 and Ni_2V_3 precipitates were advanced the hardness values.

Studying this type of welding can provide components with a fully soluble WZ and minimum potential for the brittle fracture to take place as no intermetallics can be formed upon solidification. As yet, minimal research has been published regarding welding of vanadium alloys, and the joining between titanium alloys and vanadium alloys was limited in terms of the way in which vanadium was used as an interlayer to improve the microstructure and mechanical properties of the weld metals.

1.2 The aim of the project

The aims of this work are to:

1. Investigate the ability to carry out dissimilar metal welding between Ti-6Al-4V alloy and commercially pure vanadium (CP-V) alloy.
2. Investigate the ability to develop a new method of welding by using an additive manufacturing powder bed Arcam S12 system to achieve the welding operations.
3. Design new alloys to be used as filler metals to weld Ti-6Al-4V alloy and CP-V alloy by powder technology means and spark plasma sintering.
4. Investigate the effect of the designed filler metal type on the microstructure and mechanical properties of the dissimilar welded samples.

CHAPTER 2: LITERATURE REVIEW

2.1 Introduction

The discovery of titanium can be traced back to the British chemist and mineralogist William Gregor in 1791. Gregor called his discovery “mechanite”. An impure alloy was produced by isolating the iron from black sand taken from a local river using a magnet and HCL acid. Then, four years later, Martin Heinrich Klaproth, a chemist from Berlin, managed to produce “rutile”, which is a titanium oxide extracted from a Hungarian mineral. In the year 1932, Wilhelm Justin Kroll was able to produce the titanium alloy for the first time. He demonstrated that by mixing titanium tetrachloride TiCl4 with magnesium, titanium could be commercially produced. By the end of WWII, titanium alloys were becoming an essential material in the aircraft industry. Finally, in 1948, for the first time, titanium was produced commercially by DePont Company using the Kroll process. Aerospace industries are still the prime consumer of titanium and its alloys due to their superior properties such as high strength to weight ratio and elevated corrosion resistance. Therefore vast numbers of parts of airframe and jet engines are made of titanium alloys. Despite the cost of titanium alloys, comparing to other alloys [17] a continuous and growing demand as their compatibility with CFRP (Carbon Fiber Reinforced Plastic) to form composite structures helps to fuel costs saving. During the general meeting of the International Titanium Association (ITA) in 2012, a 34% increase in the consumption of titanium alloys from 2006 to 2010 was reported, and that consumption would keep on rising and double by during the next decade, figure 2.1. Additionally, in other markets, such as architecture, chemical processing, medicine, marine engineering and transportation, there is now increasing acceptance of the use of these alloys in their manufacturing applications [2].

2.2 Metallurgy and Classification of Titanium Alloys

2.2.1 Crystal structure

When the temperature of titanium reaches about 882˚C, an allotropic phase transformation occurs[18], allowing the titanium crystal structure to change from α phase (hcp) to β phase (bcc) see figure 2.2. Above all, alloying elements such as Al, Sn, O, N, C can shift the structure toward the left by stabilising α phase through increasing the α-β-transus temperature. On the other hand, elements such as V, Mo, H, will lower the α-β-transus

temperature in order to stabilise the β-phase. So depending on the alloying elements and the dominant phases at room temperature, titanium alloys can be classed as α-alloys, β alloys, or α/β alloys[17].

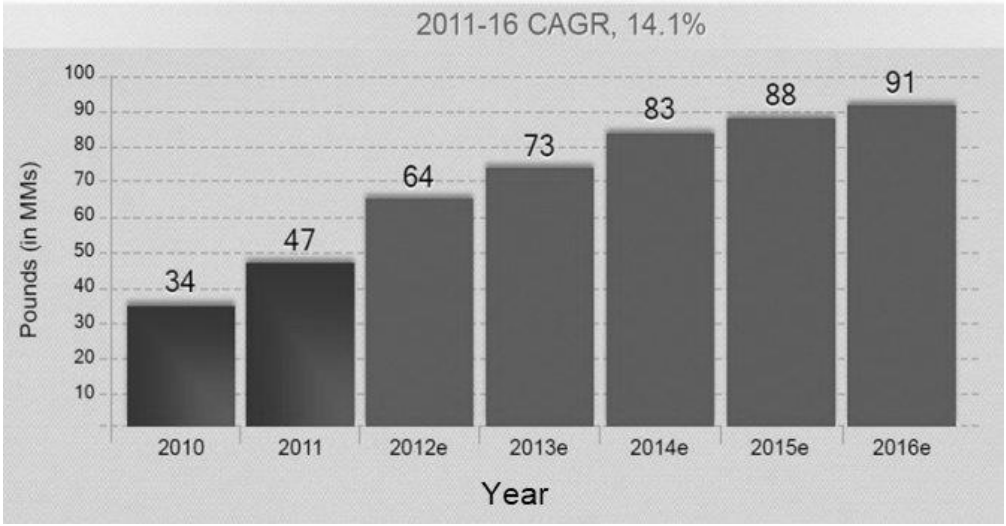

Figure 2.1 Global demand for titanium alloys in aerostructures [2].

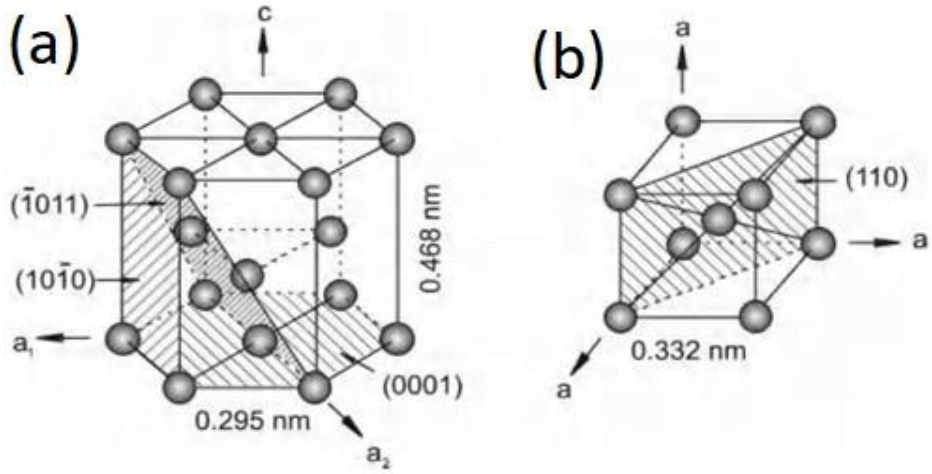

Figure 2.2 Crystal structure of (a) hcp α phase and (b) bcc β phase[1].

In the titanium alloys, the β transus temperature is affected by the type of alloying elements used. Neutral, α- stabilisers, and β stabilisers represent three types of alloying elements that can extend the α-phase that occurs under high temperature. However, in the case of β stabilisers, some other elements perform the role of shifting the β- transus temperature

downwards, figure 2.3[17]. Titanium alloys can be divided into α- alloys, near α- alloys, α/β alloys, and β-Ti alloys depending on the phases present.

The α-Ti alloys and near α-Ti alloys consists mainly of the α-phase. However, α/β alloys, contain α phase at room temperature, but they are mainly β phase at the high-temperature allotrope. However, β-Ti alloys when they are heat-treated and quenched, a full structure of β-phase can retain upon rapid cooling from β- transus temperature [19].

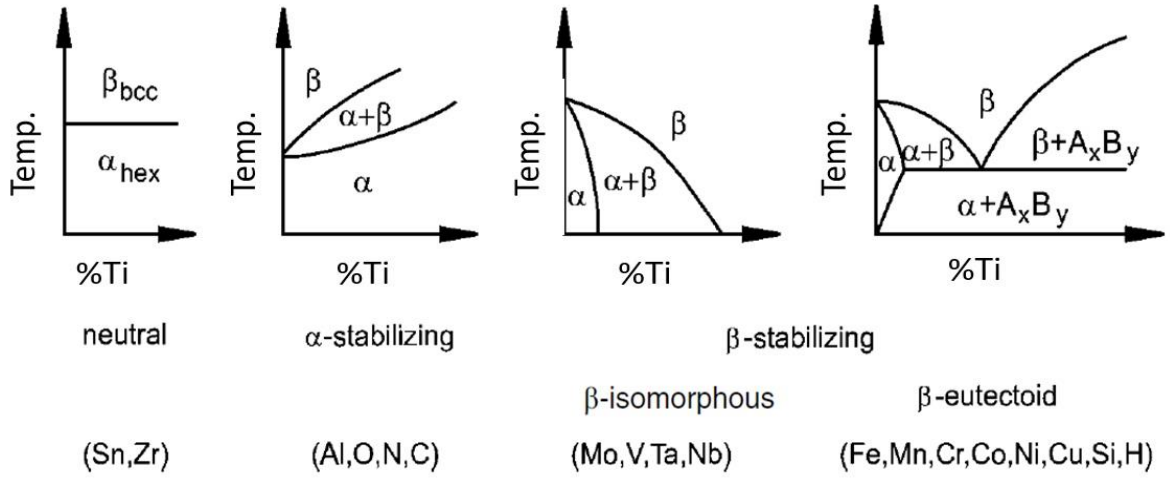

Figure 2.3 Effects of alloying elements on the phases of the titanium alloys [1]

2.2.1.1 α- alloys

The primary structure of α- alloys is hcp α phase. Alloying elements such as Al, N, C and O are the primary chemical composition, and they stabilise α-phase in the structure. Commercially pure titanium (CP-Ti), Ti-2.5Cu, Ti-5Al-2.5Sn are some of the most common types of α- Ti alloys. Aluminium in this type of alloy is the primary α stabilisers and important alloying element to produce those α alloys. The higher α stabiliser amounts extend the α phase higher temperatures. Excellent corrosion resistance and excellent deformability α-Ti alloys become favourable candidates for the chemical and power plant industries. Although CP titanium is non-heat treatable, it shows excellent weldability, reasonably high ductility and high strength [18] when compared to the strength of 300 series stainless steel, but with about 40% less density[17], [20].

2.2.1.2 Near α-alloys

The primary structure is hcp α phase. However, the grain morphologies can span from equiaxed to acicular (martensitic) as a factor affected by the process conditions[21]. They referred as near α-alloys as they contain small amounts of Mo and V which they are a β stabiliser and a minimal β phase retained at room temperature upon cooling. Near α-alloys such as Ti-3Al-2.5V, Ti-8Al-1Mo-1V and Ti-6Al-2Sn-4Zr-2Mo retain good ductility, and they show good weldability.

Furthermore, the strength of the HAZ in the annealed alloys is less affected by the welding process, although the heating effect due to the welding process causes a drop in the HAZ strength in the case of cold work alloys. Hence, it is recommended that all welding of this type of titanium alloy should be performed in the annealed condition. Moreover, it has been reported that creep resistance is increased by adding a small amount of Si alloy, up to 0.5% of Si [17]. Therefore, the near α-alloys are preferred for elevated temperature applications because of the retention of their mechanical properties such as high creep resistance and oxidation resistance at elevated temperatures [18][22].

2.2.1.3 α/β alloys

The combination of excellent properties, corrosion resistance and strength, which is higher than the near α-alloys properties [21] makes them applicable to many different processes. At a working temperature of about 315˚C to 400°C, Ti6A14V, Ti6AI6V2Sn and Ti6AI2Sn4Zr6Mo preferable alloys for this task. Solution treatment below the *β*- transus temperature applicable to establish age-hardenability. Figure 2.4 shows three different types of titanium alloys phases [20]. The type of microstructure and phases controls the alloy strength. The Ti6AI4V alloys are widely used in creating welding components with different alloy. Stanley Abkowitz, in the early of 1950, proves the improvement in titanium ductility and alloy strength with the addition of vanadium alloy [18]. However, the reduction in weldability increased as *β* stabiliser increased, and an increment in hardness was observed. Weight savings in an aeroplane was achieved with using titanium alloy comparing to the steels and aluminium frames [23]. As compared to α-Ti alloys and near *α*-Ti alloys, the annealed condition of *α/β* alloys, however, welding thermal cycle reduce the WZ and HAZ ductility [20].

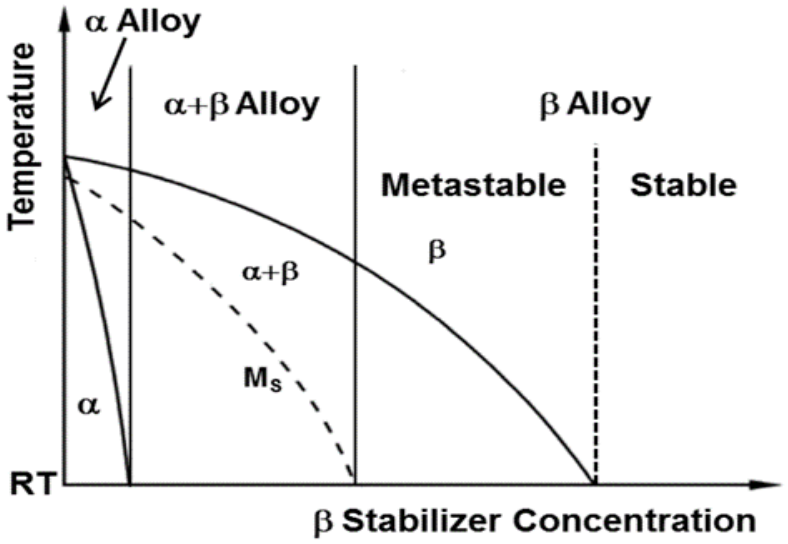

Figure 2.4 Schematic to show the Pseudo-binary section of three types of titanium alloys through the α/β phase diagram [5].

2.2.1.4 β- alloys

These alloys are of a single-phase *β* structure, and rich with *β* stabiliser elements such as vanadium, molybdenum, niobium and tantalum. The full metastable *β* phase is produced upon rapid cooling from *β-transus* temperature. *β* stabiliser alloys avoid the formation of martensitic structure and ultimately retain the *β* phase during cooling. The phases of *β* alloys are classified into stable - non-heat treatable - or metastable - heat treatable - phases. This cubic structure lattice, figure 2.2 [17], of the metastable phase, provides *β* titanium alloys with excellent forgability.

Moreover, they have a high tendency to transform to *α/β* phase, so the application of a solution heat treatment (450 to 650˚C) works to disperse the fine *α* particles in the retained *β* structure[20]. The ageing treatments provide the *β* alloys with high fracture toughness and high yield strength, and they can be coldly deformed easily, especially in the large cross-section parts. Figure 2.5 illustrates how the phases' structural properties behave according to the presence of alloying elements and how the characteristics of the final titanium alloys are influenced by these alloying elements. *β* alloys weldments exhibit good ductility, but lower strength in the annealed or solution treated conditions. However, *β* alloys weldments can become more brittle if they are exposed to highly elevated temperatures during service. Therefore, the process of joining these types of alloys must be implemented carefully by achieving welds in the annealed condition, followed by cold work applied to the weldments,

and then applying a post-welding heat treatment (PWHT) in order to obtain weld parts with full joint strength and good ductility[17][18], [23].

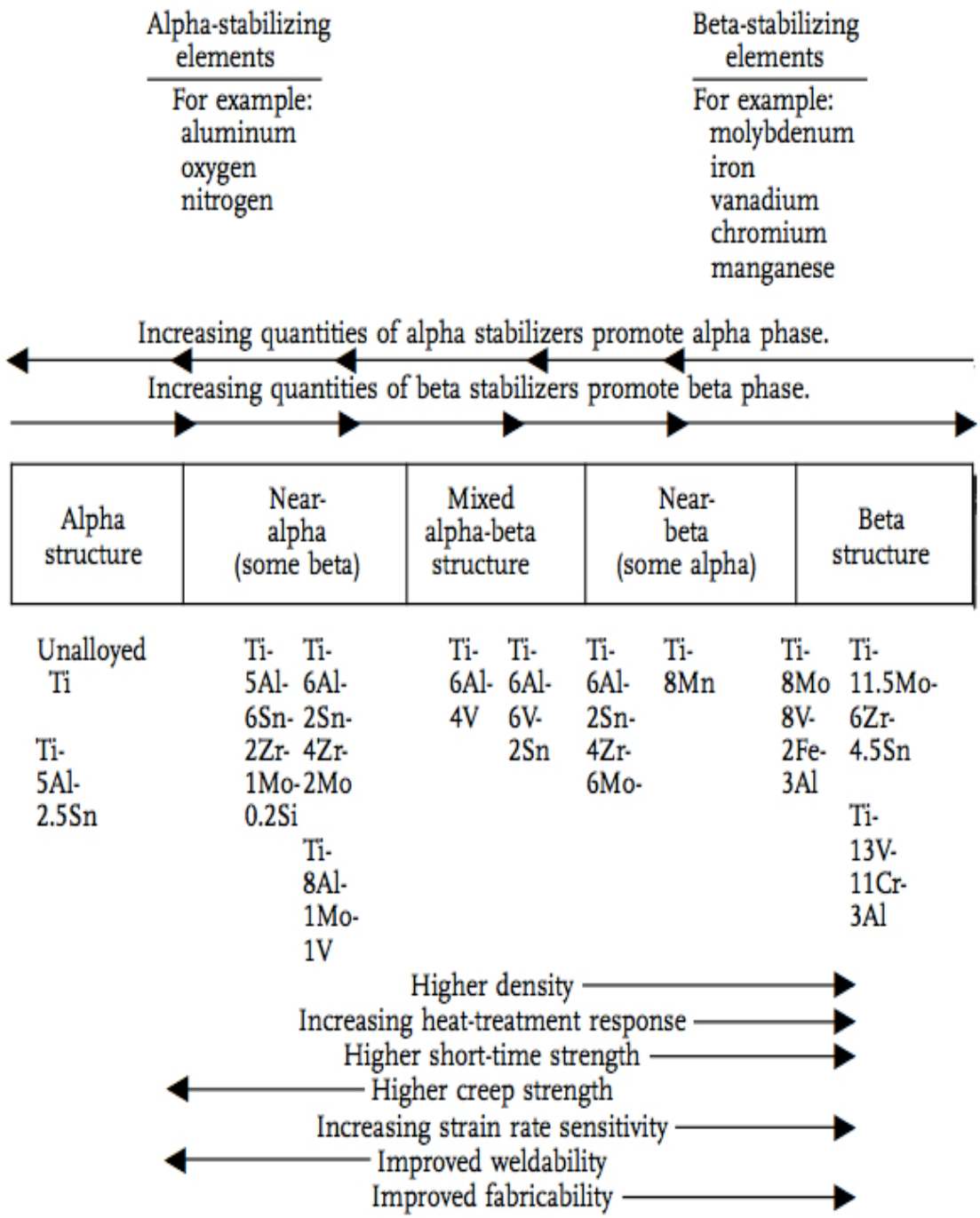

Figure 2.5Effects of alloying elements on the mechanical properties and phase structure[5].

2.2.2 Phase Transformation

The β-transus temperature is the borderline where α phase or α/β phase changes to become all β phase upon heating. From figure 2.4, the β-transus temperature is important as it is considered the reference temperature where most of the thermal processing is achieved, with few incremental temperatures occurring above the transus line. When the titanium contains a small percentage of α stabiliser only, below the β-transus, the structure will be α- phase. However, with any presence of β stabilisers with α stabiliser, upon cooling the alloy structure will be α/β phase. In terms of factor effects, alloys such as aluminium, carbon, oxygen, tend to increase the β-transus temperature and maintain the α phase steady to a high temperature. On the other hand, the transformation temperature, or β-transus temperature, can be lower with element alloys such as molybdenum, vanadium tantalum, and niobium, and form a homogeneous β structure as a result. An additional advantage is that hardenability is extended by the presence of β stabiliser alloys [20]. During the cooling process, with the aid of the alloying elements, the bcc β phase transforms to hcp α phase. However, a slight distortion in the atomic structure occurs upon the transformation, due to the large distance between the basal planes in α-phase as compared to the planes in the β phase. The two-orientation relationship given below explains the transformation direction of the bcc slip planes into hcp basal planes:

$$\{110\}_{\beta} // \{0001\}_{\alpha}$$

$$[111]_{\beta} // [1120]_{\alpha}$$

2.2.2.1 Martensitic transformation

Below the β-transus temperature, during the cooling stage, the β phase starts to transform into a hexagonal "basketweave" structure with a plate-like appearance. This process is called martensitic transformation. Depending on the cooling rate[17], [20], this structure divides into one of two types, α' or α''. However, although no embrittlement takes place during this transformation, there is a slight enhancement in the strength as a result of this phase change. Under a rapid cooling rate [24], a hexagonal structure with a very fine needle-like character is formed, called α' martensitic phase or Widmanstätten structure or α prime [25].

On the other hand, as shown in figure 2.5b, when the cooling rate becomes slower, a coarse martensitic formation trend takes place. Also, the symmetrical hexagonal structure become distorted as the α stabiliser increased, forming what known as orthorhombic α" phase[26]. Figure 2.6a shows the martensitic structures α′ formed under rapid cooling rates and the formed basketweave in figure 2.6b in case of slower cooling rate.

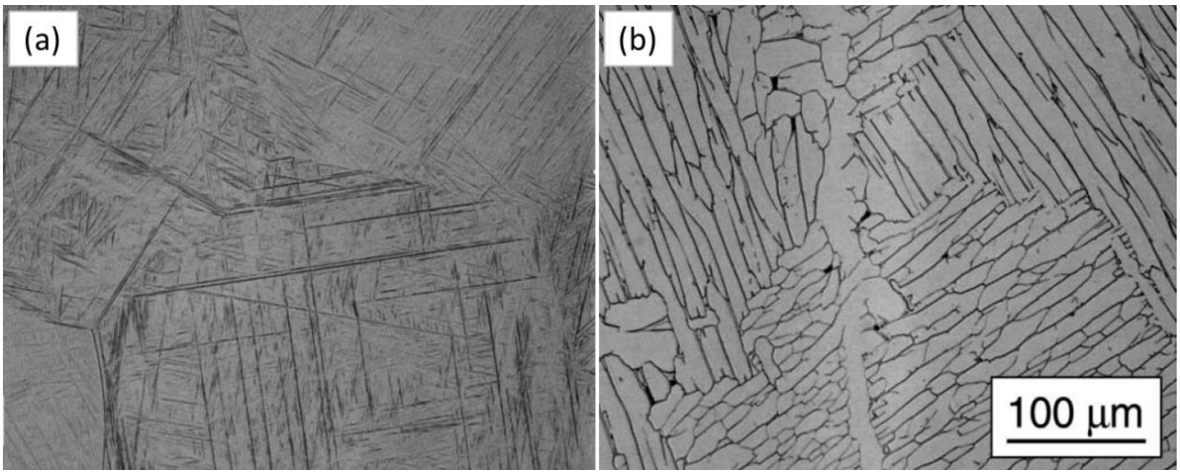

Figure 2.6 Titanium structures formed upon cooling from 1040˚C: a) fine needle-like α′ with water quenched to room temperature, and b) the basketweave structure from furnace cooling[12].

2.2.2.2 Nucleation and Diffusional Growth

In general, the cooling rate has a significant effect on the nucleation process. As the titanium alloy's temperature drops below the β-transus, an allotropic phase transformation takes place and, dependent on the cooling rate, a wide range of different structures can be formed[27]. At a slow rate, first, nucleation starts at the β-grain boundaries toward the inside of the β grain, forming a plate-like structure known as the α phase. Upon continuous cooling, the α phase also starts to nucleate from the interfaces of the new α-plates. These new α plates, figure 2.6b, are named α-lamellar.

Furthermore, as the new α plates continue to grow from the β grain boundaries, they eventually come into contact with other new α plate-like structures that have already grown from the other side of the β grain boundaries, forming what looks like a basket-weave structure and is known as α colony[25], figure 2.7a. The α plate in the new structure is usually separated by a β plate retained after the cooling stage is complete. The slower cooling process, figure 2.7b, tends to result in thicker α-plates.

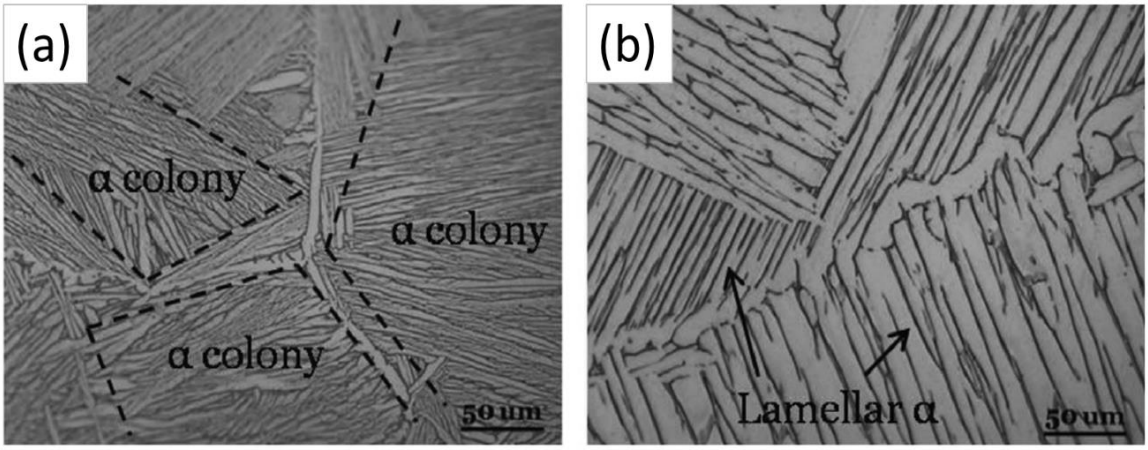

Figure 2.7 α-colonies formed from β grain boundaries upon slow cooling [14].

2.3 Titanium alloy Ti-6Al-4V

Presently, Ti-6Al-4V is one of the most widely used titanium alloys[28]. Accounting for more than half of all the world's titanium tonnage, Ti-6Al-4V has a dominant position in the industrial sectors which no other alloys can currently threaten. This *α/β* alloy attracts interest from a wide range of industries, such as marine, petrochemical, automotive and medical applications[11]. Its attraction is that the microstructure of this alloy offers excellent physical and mechanical properties that can be obtained easily when this alloy is subjected to thermomechanical processing.

Furthermore, because this alloy offers excellent qualities of high specific strength, low density and corrosion resistance, more than 80% of its usage is in the aerospace industry[29]. Ti-6Al-4V is a dual-phase alloy referred to as *α/β* alloy. The hexagonal close-packed (hcp) structure is the *α* phase, and the inclusion of 6% aluminium helps to stabilise this phase and increase the alloy strength.

Additionally, the inclusion of 4% vanadium, upon cooling to room temperature, helps to stabilise the body-centred cubic (bcc) system which structures the *β* phase that distributed along the boundary of the α-structure and improves the workability at elevated temperatures [30], [31]. Furthermore, the strength of the alloy increases when the content of interstitial elements such as 0.2wt%. Oxygen and 0.05% nitrogen increases. Table 2.1 shows the chemical composition of Ti-6Al-4V in both cast and wrought condition.

Table 2.1 Ti-6Al-4V chemical composition at: a) cast, and b) wrought condition [20].

Ti	Al	V	Fe	C	N	O	H
[a]Bal.	5.5-6.75	3.5-4.5	<0.3	<0.1	<0.05	<0.2	<0.015
[b]Bal.	5.5-5.75	3.5-4.5	<0.3	<0.08	<0.05	<0.2	<0.015

2.4 Phases and structures in Ti-6Al-4V

The post-heat treatment has a significant effect on the final structure of the Ti-6Al-4V as *α/β* dual phase alloy. The combination of cooling rates and solution heat treatments, when applied to this type of alloy, allows different microstructural configurations to be achieved. By applying different thermal treatments, the following three significant morphologies of *α/β* titanium alloys can be produced: lamellar, equiaxed, and bimodal structures[21], [32].

2.4.1 Lamellar structure

When Ti-6Al-4V is subjected to a controlled slow cooling rate by annealing heat treatment from *β* temperature region, *α* plate-like grains start to nucleate from the *β* grains' boundaries. Keeping the cooling process very slow allows *α*- laths to become thicker. Moreover, the *α* grains, upon slow cooling, become coarser and form what is known as α- colony. However, short and fine *α′*- plate-like grains, figure 2.6, are formed when the cooling rate becomes more rapid, such as by air cooling or water cooling.

Furthermore, a basket-weave microstructure, representing the *α*- colonies, is obtained through the formation of new fine α plate-like grains generated not only from the *β* grains' boundaries but also from the grain boundaries of the newly formed *α* laths. The formation of lamellar structure provides a ductile phase with high fracture toughness and excellent creep resistance. However, the fine *α* colonies formed by rapid cooling rate have reduced ductility and strength but provide excellent fatigue properties[17][18][23][33].

2.4.2 Equiaxed structure

An equiaxed structure can be obtained when the cooling rate during the annealing process is sufficiently low. Large-sized *α* grains are formed as the primary α grains keep growing during the cooling process without any *α* lamellar being allowed to form [26]. A fully equiaxed structure is generated by means of a combination of extensive plastic deformation in the *α* phase field and thermal treatment, figure 2.8a. The process involves breaking up the long α lamellar grains by rolling or forging, then applying a recrystallisation annealing temperature of (800-850˚C) to the alloy, followed by a prolonged cooling rate, during which

the lamellar structure will change to an utterly equiaxed α structure. However, whilst this structure has high ductility and excellent tensile strength, it has been shown to have reduced fracture toughness[18], [34], [35].

2.4.3 Bimodal structure

The bimodal structure is also known as a Duplex microstructure[17]. It consists of a primary globular α phase surrounded by a transformed β region (Widmanstätten structure), figure 2.8b. Several thermomechanical stages are required to form the bimodal structure. The cooling rate plays a significant role in determining the formation of the bimodal structure. To summarise the formation process, the lamellar structure derived from rapid cooling is subjected to extensive deformation [36], usually carried out below the upper end of the α/β field[18]. During this stage, the β phase recrystallises and diffuses, causing separation between the primary α grains. After a specific time, a coarse equiaxed structure is formed. Meanwhile, the volume fraction of the primary α grains is determined by controlling the temperature of the solution heat treatment[37]. The obtained bimodal morphology offers a combination of the properties of the lamellar and equiaxed structures. The bimodal morphologies exhibit superior ductility that delays crack initiation, thereby enhancing the fracture toughness and providing excellent tensile strength and high creep resistance[26].

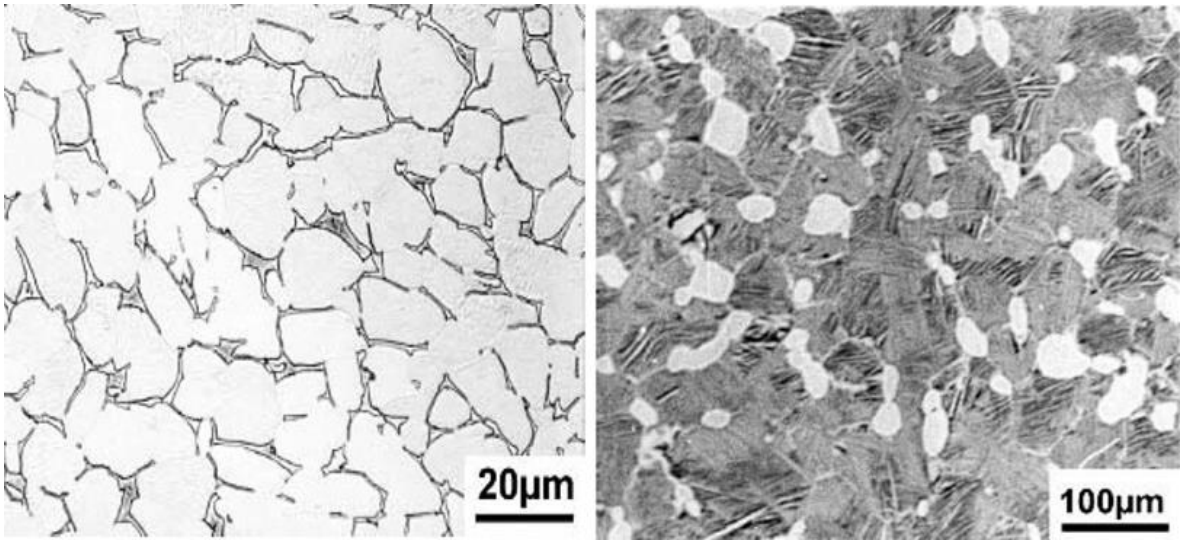

Figure 2.8 Different morphologies of α/β alloy phases: (a) Equiaxed consist mainly of primary α and (b) Bimodal structure consist of primary α and lamellar α/β structures [11].

2.5 Mechanical properties

Primarily, the phases' morphologies and the volume fraction determine the mechanical properties of titanium alloys. A high tensile strength can be achieved of up to1100MPa when Ti-6Al-4V is subjected to thermal treatment[18]. This results in a combination of good ductility and high fracture toughness. As the cooling rate increases, the α plate becomes thinner, and with the production of this fine grain size, both ductility and tensile strength are increased [26]. Moreover, a directly proportional relationship between the cooling rate and the weldment strength has been reported in [10], [11]. The *α/β* titanium alloys show high weldability due to the rapid solidification rate achieved by applying a fast cooling rate; thereby, the weldments of Ti-6Al-4V exhibit high tensile strength [38]. Furthermore, the mechanical properties are also affected by interstitial elements such as oxygen. Several studies were conducted to investigate the effect of oxygen percentage on the characteristics of the titanium alloys. They reported that the increase of oxygen constraint leads to increase of the hardness value and the tensile strength due to the effect of interstitial elements on the lattices parameters (c/a ratio) for the Ti alloys which lead to change in latices strain by increasing the solid-solution as a function of oxygen. However, a reduction in the elongation percentage takes place when the oxygen percentage is inversed [39]. Since the microstructure is strongly influenced by interstitial oxygen, the hardness and tensile strength will be affected as well [40]. The tensile strength can be improved by up to 200MPa by subjecting the Ti-6Al-4V alloy to thermal treatment, upon the microstructure changing, although, only (70- 100) MPa of yield strength can be achieved by modifying the chemical composition with oxygen [35].

2.6 Weldability of Titanium Ti-6Al-4V alloys

The welding process has a significant effect on the mechanical properties of the α-β titanium alloys. As the thermal cycle of the welding process is applied, the metal reaches the melting condition, changing from the duplex phase hcp - α/β phase - to a single phase of bcc structure. This same phase transformation happens in the adjacent area or what is known as the Heat Affected Zone (HAZ) upon heating during the welding cycle. When the fusion process stops, the solidification starts again, and a new acicular and Widmanstatten structure is formed on completion of the process, leading to the produce a weld joint with ductility, strength and toughness differing from that of the base alloy. Both commercially pure titanium alloys and α titanium alloys show excellent weldments with good ductility in the WZ as they are less sensitive to heat treatment. On the one hand, Ti-6Al-4V, as an *α/β* titanium alloy, shows

good weldability in the annealed or the solution-treated conditions. The weldments of this type of alloys show good ductility when compared to other β titanium alloys as they contain a large volume fraction of α phase[17] and a small amount of the brittle β stabiliser alloys. Moreover, the WZ and the HAZ both suffer a slight reduction in ductility due to the phase transformation by the thermal welding cycle upon rapid cooling from the solution treatment temperature or cooling down from the high welding temperature. Nevertheless, the Ti-6Al-4V shows low hardenability, another reason Ti-6Al-4V excellent welded joint properties, cause even with the rapid cooling process a high amount of the desirable Widmanstätten structure is formed, figure 2.9, which is characterised as less hard and less brittle when compared to other α-β titanium alloys containing a high amount of β-stabilisers such as Sn. On the other hand, when β titanium alloys are subjected to the thermal welding cycle, the elevated temperature can lead to the production of a brittle weld zone and HAZ. So as a precautionary process, a plastic deformation followed by post-welding heat treatment is applied to enhance the weldment strength and increase ductility [20][41]. In general, when welding titanium alloys using fusion welding processes, considerable attention is needed.

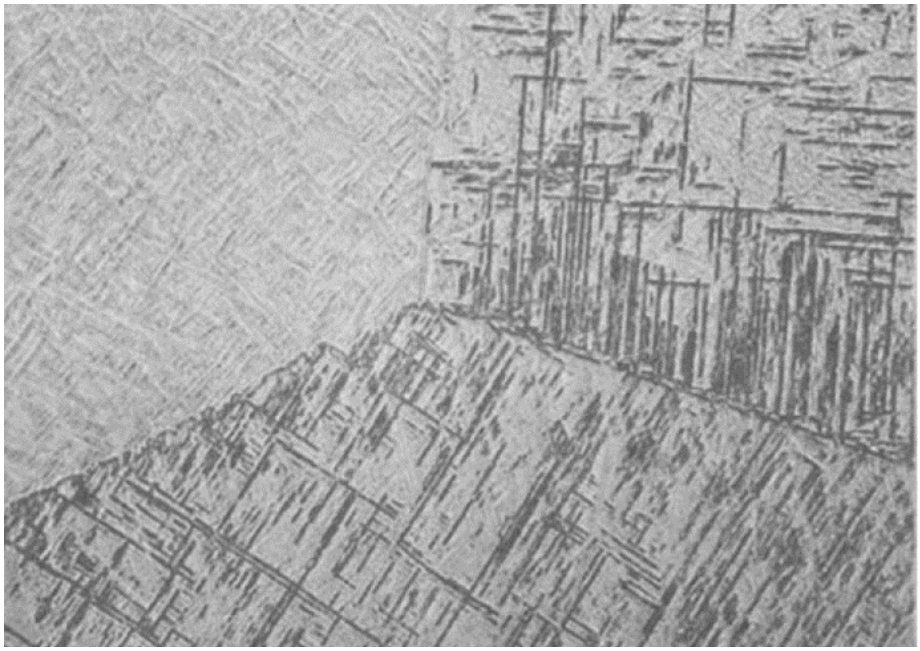

Figure 2.9 Microstructure of the Ti-6Al-4V showing the widmanstätten structure of the welding zone, 250X[28].

Problems and defects such as joint embrittlement and loss of strength occur in the welded zone are associated with parent materials and the welding process. Also, a constant problem with titanium welds is porosity, figure 2.10a [36], which is formed during the solidification of the molten metal and may be caused by hydrogen in solution, moisture in the filler metal, or moisture in the shielding gas that is used to protect the molten welding pool from environmental contamination. Cracks in welds can occur, driven by the effect of residual stress, which is associated with the presence of contaminants and porosity as it considers as a stress concentration where cracks initiate within.

Furthermore, morphology defects can occur, such as; undercut, figure 2.10b [42], which are related to the beam focus offset. Lack of penetration or incomplete penetration, figure 2.11a [43], can be caused by insufficient power intensity since there needs to be a level of power intensity sufficient to penetrate the full thickness of the weld plate. In addition to the problems described above, the droplet condition is a defect that occurs due to overheating of the alloy. It is caused by either excessive heat input or slower travel speed, making the surface tension of the molten metal very weak and unable to hold the melted metal in the WZ, which causes the metal to escape from the welding root by gravity effect and upon solidification appears as droplets below the root. Other defects include concavity in the weld root or the weld face, figure 2.11b [43]. When low heat is applied, and with fast travel speed along the weld line, a concavity profile appears on the weld face, leaving an underfilled metal profile along the weld line. Meanwhile, if the weld root is too wide when the molten metal has cooled, the metal will shrink and be drawn up into the root.

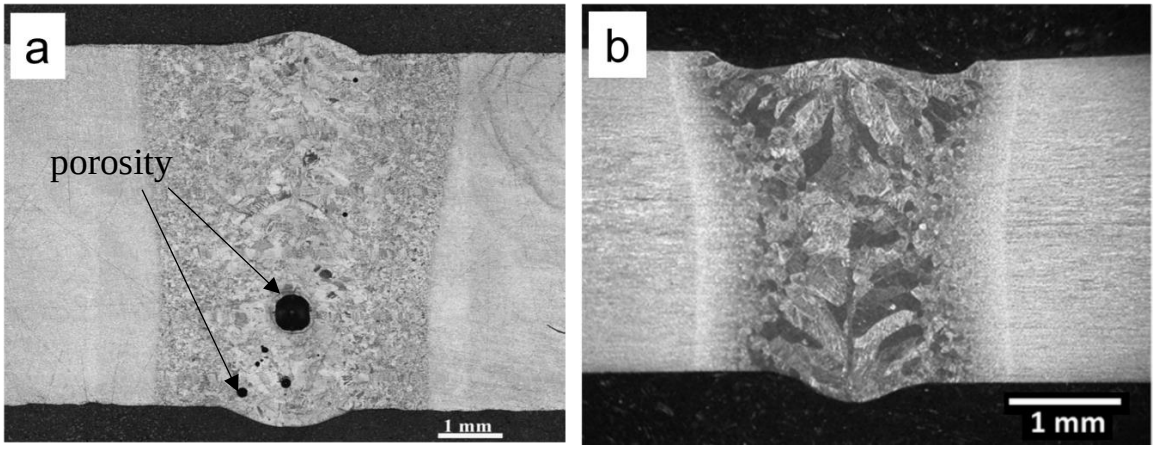

Figure 2.10 Defects in Titanium weld zones: a) porosity in cp-Ti welds [23], and b) undercut profile for a Ti-6Al-4V EBW weld [29].

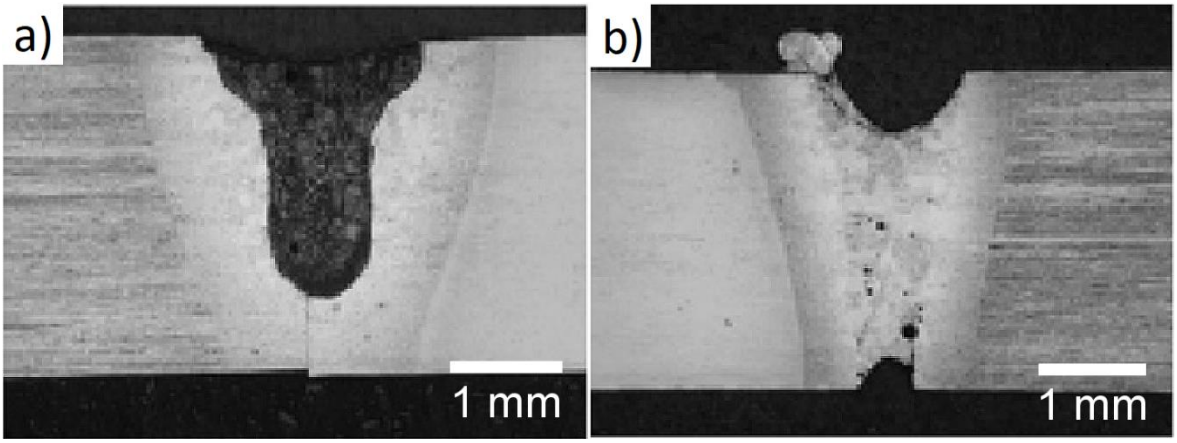

Figure 2.11 Morphology defects in the welding zone: a) lack of penetration caused by low heat input or fast beam speed b) face and root concavity caused by high heat input resulting in metals vaporising[43].

2.7 Fusion welding of similar titanium alloys

Primarily, when welding is carried out, the alloy is heated to an elevated temperature, which changes the alloy's condition from solid to high temperature liquid molten metal. Both the WZ and the HAZ undergo dramatic morphological changes during the welding thermal cycle. Then, once the source of heat is removed, the solidification process takes over. Moreover, upon cooling, complex changes take place, and the final structure of the solidified alloy is determined by different variables such as the welding process type, the chemical composition, and the cooling rate, type of joint, filler metal, shielding gas, etc. [18]. In general, most of the Ti alloys contain less than 20% β- stabiliser alloys show excellent weldability. Titanium alloys such as CP-Ti, α- Ti and near α Ti alloys are always welded in the annealed condition, and because these alloys have very low sensitivity to heat, they provide weld joints with better ductility.

Meanwhile, the thermal welding cycle has a different impact on α/β alloys such as Ti-6Al-4V. However, these alloys can be welded in the annealed or solution treated condition. A series of physical changes is experienced when these alloys reach the fusion stage, leading to form or modified structure, with characteristics differing from those of the base alloy, and possibly the presence of residual stress as a result of the solidification process. Therefore, joining Ti-6Al-4V alloys requires considerable attention, as mechanical properties such as ductility and strength are affected directly by the welding process. In addition, post-weld heating processes such as ageing treatments are applied after welding in order to recover the strength and remove residual stress. Whereas, with Ti alloys containing high β-stabiliser alloys additions, a great potential for embrittlement to be present in the WZ and much higher

as it compared with other Ti alloys with a lower wt.% of β stabiliser elements. So in order to enhance the welding joint of this type of titanium alloy, a particular procedure is required. A two-stage post-weld treatment is carried out which involves subjecting the weld part to plastic deformation and then applying a heat treatment solution to reduce the welding embrittlement and increase the strength of the welding joint [20].

Different welding methods can be used to join titanium alloys. These fusion methods can be divided into conventional welding methods such as Gas Tungsten Arc Welding (GTAW) or Metal Inert Gas (MIG), or Plasma Arc Welding (PAW), and nonconventional welding methods or advanced welding methods such as Electron Beam Welding (EBW), Laser Beam Welding (LBW), and Friction Stir Welding (FSW). The welding method is selected based on the type of application. For applications that require fabrication of structures such as pressure vessels and heat-exchanger fabrication[44], or petrochemical applications that require joining of thin sections, GTAW, MIG [4], [7], [45], or PAW [46], [47] are ideal fusion welding methods. Each of the above processes uses a filler metal that matches the chemical composition of the base metal. And because titanium has the ability to react with the atmosphere when heated above 300 ˚C, an inert gas of (99.99% purity) such as helium or argon is used to provide a gas shield during the welding process to protect the welding pool from contamination by the atmosphere and humidity caused by elements such as oxygen and hydrogen[17], [26].

Meanwhile, when weldments with high quality are required for sensitive applications such as the aerospace and jet engines industries, the conventional joining methods become unfavourable. So to obtain weldments with high integration, different welding methods are required, such as EBW [30], [48]–[50], LBW [43], [51]–[53], Friction welding (FW) [54] and Friction Stir Welding (FSW) [6], [31], [55]. These methods have been used extensively to join and fabricate high-quality structures, and they have been shown to offer an easy way to join a wide range of alloys that are difficult to weld using the conventional methods. Electron beam welding, offering a high depth-to-width ratio, is one of the common joining methods for welding titanium alloys. As a fast-speed welding process, it mainly involves generating an electron beam with a high density and is very focused, allowing achievement of weldments with high thickness and very narrow WZ and heat-affected zone. In most cases, no filler is required when this process is used to join titanium alloys. Also, as the welding process is done under vacuum condition, it offers excellent protection of the welding pool from exposure to any contamination and also prevents the titanium from reacting with hydrogen. Meanwhile, LBW shares the same principles with the EBW process and likewise

offers weldments with a high depth-to-width ratio. The focused high energy beam allows weldments of titanium alloys with high thickness and without the risk of the beam being distorted. Furthermore, in both EBW and LBW the beam can be easily controlled and deflected, offering the possibility to make welds with very complex structure and to weld high thicknesses of up to 100mm with one welding pass and without applying filler [26], [41]. Another joining process is Friction welding (FW), which offers a reliable solid-state joining method. In this process the weld area is subjected to high extensive plastic deformation that heats the contact zone to a high temperature without any melting to the joint area; then, with the aid of applied pressure, a weld joint is generated at the contact zone. Friction stir welding (FSW) uses the same principle, but instead of having one moving part, the two sheet plates are placed in a butt joint position. A hard tool is stirred at high speed and forced into the joint line. The high-speed rotation causes heating of the alloys to a high temperature to enable the required deformation to create the bonding condition without any fusion in the joint area[3]. One of the challenges in the FSW of Ti alloys is the welding tools. Ongoing studies were attempts to study and develops ideas to overcome such problem [11]. In general, Ti-6Al-4V alloy is the most widely used titanium alloy in industry, accounting for at least 50% of the industrial tonnage of titanium alloys [20][56]. This alloy provides desirable mechanical properties such as high tensile strength to weight ratio, an excellent corrosion resistance, low thermal conductivity and the ability to maintain excellent mechanical properties under elevated [43]working conditions[57], [58]. Based on these properties, the demand for these alloys for use in applications in industries such as aviation, automotive, medical and nuclear power has increased rapidly[2], [13]. Furthermore, with the development of new applications, there is an essential requirement for new technological solutions to keep pace with industrial growth and help with cost reduction. Also, applications in industries such as the aerospace present many challenges in terms of joining titanium alloys, since they require fabrication weldments with high efficiency and low distortions [57].

Joining titanium alloys has been studied extensively in various aspects by several researchers. Wang et al. [59] studied the joint efficiency of Ti-6Al-4Vwelds under different heating temperatures, using welding by LBW. The study reported an increase in the ultimate tensile stress for the welded part as compared with the as-received base metal, due to the harder WZthat is mainly of a needle-like martensitic α′ structure. However, there was a reduction in the yield strength in the welded parts, and the elongation was reduced to about 5% as compared to the base metal when the tensile test temperature reached 450˚C.

Additionally, in an attempt to improve the weldment toughness, Mohandas et al. [58] examined the relationship between the fracture toughness and microstructure of the welding zone. The study reported that a crack path deviation takes place at the grain boundary and the toughness is improved if the thickness of the α grains is increased. Moreover, Prasad Rao et al. [60] claimed that Ti-6Al-4V welds with a basketweave structure showed better fracture toughness when compared to the base metal equiaxed structure.

2.7.1 Friction welding

In 1991, the Welding Institute introduced a new solid-state welding method called friction stir welding. FSW which involves placing a rotation tool in the joint part and using high-speed rotation to provide a suitable plastic deformation in the joint zone. As the rotating pin moves forward, a bond is achieved between the two alloys in the butt welding position. This method soon gained much attention from researchers, and the process started to be widely applied to join a wide range of different alloys [61]. Researchers then started to employ this joining method as an alternative welding process instead of using conventional welding methods. As explained previously, when Ti alloys are welded by fusion methods, problems such as porosity, segregation and welding distortion arise. Therefore, FSW of titanium joints has been used to reduce these kind of problems as there is no melting in the WZ and the bonding take place due to the plastic deformation caused by the rotation tools[62], figure 2.12, illustrate a schematic diagram for a friction stir welding method. Sanders et al.[63] conducted a challenging task to fabricate a four-meter engine inlet lip skin from Ti-6Al-4V alloy and achieved by FSW. This research was follow-up work to a project conducted by the Boeing company; they succeeded in producing Ti-6Al-4V welds with mechanical properties approximate to those of the base alloy by employing FSW. This process adds another advantage of narrowing the HAZ and reducing the thermal-mechanical affected zone (TMAZ) in Ti alloys as compared with a prototype of Al alloy. Another study by Sanders et al.[55] addressed the effect of post welding heat treatments on the mechanical properties of the fabricated joints of Ti-6Al-4V alloy produced by FSW. The investigation employed three types of Ti-6Al-4V: as-welded, stress relieved, and stress relieved and machined. The researchers identified a reduction in the yield stress and the ultimate tensile from the as-welded to stress-relieved weldment, but there was an increment of the hardness for the same order. Moreover, most of the failure in the tensile specimens happened outside the WZ at the weld interfaces. In terms of the fracture toughness results, the as-welded samples showed less fracture toughness as compared with the other two conditions, due to the high-stress

concentrations and residual stresses. In another approach, the effect of FSW variables on phase transformation of the Ti-6Al-4V was studied by Gianluca et al.[64], suggested a model predict the phase transformation and mechanical properties. Then, the researchers applied the outcome results from their model in order to validate and compare the model results with real results. They demonstrated that the rotation speed has a significant effect on the final structure in the WZ and by increasing the rotation speed the general trend was that at low rotation the general phases in the WZ would be of fine α' structure, but as the speed increased beyond 300rpm the typical structure would be an α/β phase.

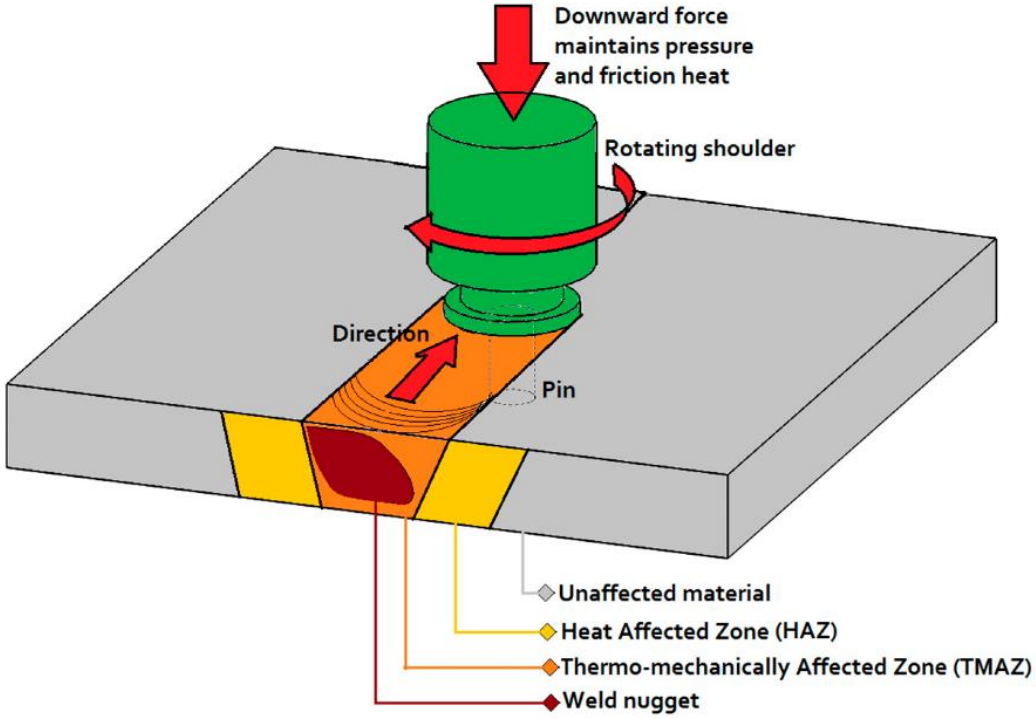

Figure 2.12 Schematics image of the FSW process showing the principle of the welding method and the different zones developed due to the welding thermal cycle of the welding process.

This finding was associated with the heat that is generated during the rotation process since, at high speed, there is a greater chance of the β phase being present after the cooldown of the WZ. Also, the low-speed rotation recorded the lowest UTS as compared with the high-speed rotation condition. The hardness results indicated that as the rotation increases the hardness value becomes ~12% higher than the lower rotation speed. The model established a correlation between the rotation speed and the volume fraction distributions of the developed phases in the WZ. Furthermore, several review papers have been published involving studies of FSW from different aspects. Kapil et al.[65] and Mirono et al.[66]

conducted a review on the relations between the FSW process variables: such as the type of tool materials, the impact of the tool design, thermal impact and the generation of the residual stress on the structure, and the mechanical properties of the welded joint.

2.7.2 Laser beam welding

Laser Beam Welding is one of the reliable welding methods in terms of providing a precision weld with minimum distortion for titanium alloy weldments. Research on welding of titanium alloys using Nd: YAG laser welding was conducted by Akman et al.[43]. Their efforts were focused on studying the factors affecting the formation of keyhole welding in Ti alloys welds. They showed that the formation of a keyhole with full penetration is controlled by two major factors: the pulse energy and the pulse duration. The pulse energy provides the necessary power to melt the alloy surface, but the pulse duration is more important as it allows the keyhole to form when the period is increased to the required extent. However, exposure to high heat input over an extended period during the welding process leads to evaporation of the molten alloy, and both the WZ and the HAZ become much broader. This causes a gradual increase in the hardness with the distance from the base metal and toward the welding centre line as it contains mainly hard martensite. Also, they examined the tensile behaviour in relation to the direct effects of both the microstructure and the porosity on the joint strength. Any presence of voids due to the gases from the welding process will reduce the joint strength. Also, if a PWHT is applied to the WZ, the joint strength will decline due to grain growth. Another observation was regarding the relationship between the power applied and the volume fraction of the grains size. Upon increasing the heat input, the grain size increased due to the slower cooling rate of the FZ, figure 2.13. Leijun et al.[67] examined the relationship between the formation of the martensitic phase and the cooling rate. Used a mathematical model they determined as the cooling process falls to between 1000 ˚C and 600 ˚C, the cooling rate of 115 ˚C per second is the average cooling rate in the WZ at the start of martensitic structure formation. Squillace et al.[9] and Cao et al.[68] analysed the impact of welding parameters such as travel speed in laser method on the microstructures and mechanical properties of a thin plate of the Ti-6Al-4V alloy. With the reduction of the welding travel speed, the width of the WZ increased. However, at a fast speed, there was a reduction not only in the WZ but in the width of the HAZ as well. The main phase in the WZ is acicular α martensite due to the rapid solidification in this area, while the structure of the HAZ is usually primary α mixed with α martensite. In terms of the welding morphology, the welding depth correlates inversely with the welding travel speed.

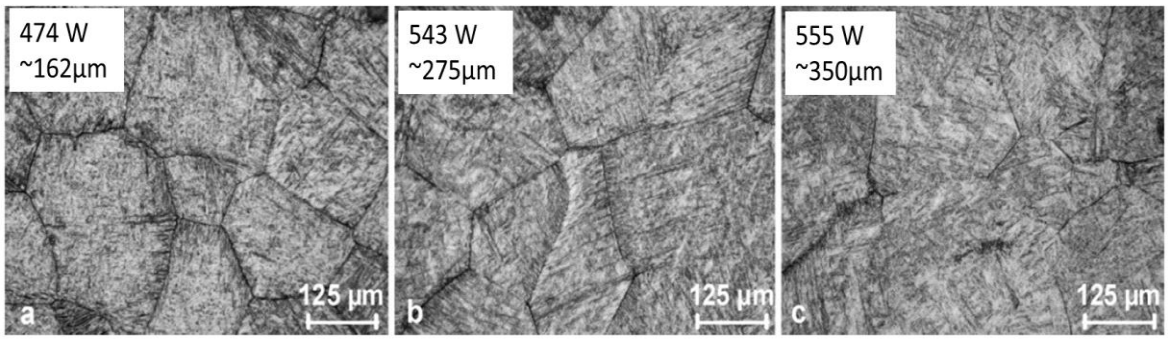

Figure 2.13 Effect of laser power on the Ti-6Al-4V grain size in the WZ, showing an increase in the grain size of the FZ as the heat input increased[43].

This leads to the conclusion that the formation of the keyhole is affected directly by the beam travel speed; hence, at high welding speed the depth of the keyhole becomes very low, whilst a high speed produces a narrow keyhole and enhancement in the joint strength, but the lack of penetration is considered a significant defect. Other defects were observed after the joint cooled down, such as the presence of porosities, inclusions such as Al_2O_3 from CO_2 gas, and cracks in some joints in the HAZ area. Most of the hardness results of this process and other welding methods share the same trend; in other words, the maximum hardness value occurs in the weld centre, and this value decreases with the movement toward the base metal — another report, published by Kabir et al.[68], studied Laser beam travel speed and various focal distances of the welding beam. In this work, the underfill condition was found to be a common weld defect, present with both slow or fast beam travel, due to the evaporation of the molten metal during the fusion process. Figure 2.14 shows that beam focusing has a slit effect on the WZ width, whereas the high defocusing condition makes a wider WZ. Gao et al.[69] compared the effect of different welding methods on the properties of the welded parts produced by TIG and Nd: YAG laser welding methods. This was a wide-ranging study starting from the general morphology, covering the shape of the keyhole, the microstructure, then the mechanical properties and the impact of the process on the residual stresses.

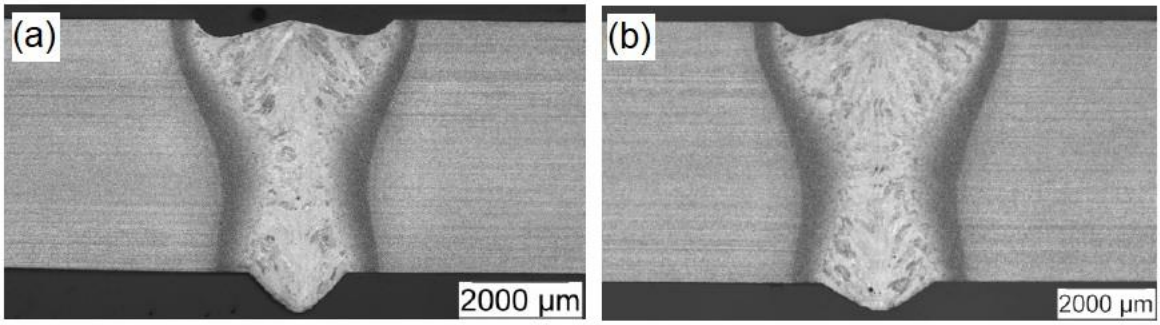

Figure 2.14 Cross-section of Ti-6Al-4V LBW at a travel speed of 1.5m/min and defocusing beam of (a) -1mm, and (b) -2mm, A wider FZ produced with high defocusing value[61].

Their final recommendation was to consider using the LBW process in preference to the GMAW welding method, as both the microstructural and mechanical properties of the Laser beam weldment show better characteristics, such as excellent ductility and high joint strength equal to or better than that of the base metal. A less microporosity is formed with LBW, and it is possible to produce a titanium plate joint with a narrow WZ and narrower width of HAZ, figure 2.15, than with the GM|AW process.

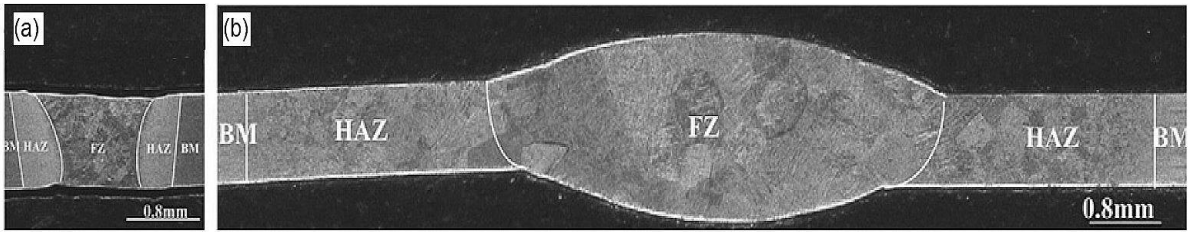

Figure 2.15 Comparison between the cross-section area produced by (a) LBW process and (b) TIG process[62].

As explained before, the formation of microporosity in the WZor in the interface of the WZ and the HAZ has a significant effect on the joint strength as it is considered to create weak points and stress consternation spots. Therefore, further researchers such as Hanchen et al.[70], Xiao-Long et al.[71], and Jiajun et al. [72] studied the factors affecting the formation of microporosity in the WZ. Travel speed, alongside the gas providing a shield from the welding process, is the primary element that can affect the size and number of the formed pores. The findings depended on the observations of the fusion process during the welding cycle, and high-speed thermal imaging indicated that using a relatively fast weld speed and a laser beam of 3kW with 1m/min speed form small pores size as compared when using the speed of 1.6m/min.

2.7.3 Electron beam welding

Reportedly, the first electron beam was produced in France in 1956. The CEA (Atomic Energy Commission) used an electron beam to weld Zirconium, an alloy susceptible to oxidation. Then, in 1960, the first Electron Beam Welding machine was produced for industrial purposes[73]. The Electron Beam welding process was barely known in the aerospace industries as a method for joining Ti alloys until approval was given for production of the F-22. Before that time, there was significant competition between welding methods such as FSW and LBW over, which would be the most dominant joining method in civil aeroplane and aerospace applications[74]. Key features make electron beam welding method more desirable and more applicable than its competitors. One of the increasingly essential requirements is to be able to join alloys with high thickness and to make the join area as narrow as possible. Electron beam welding provides the highest depth to width ratio. As a fast welding process, this method involves using a high-intensity electron beam to $10^{10}W/m^2$ and focusing this beam to a spot size in the 0.3-.08 mm range[75]. When this very high-intensity beam hits the surface of the alloy, it will melt and even vaporise the alloy at the impact zone, pushing down the molten metal to form a void in the alloy known as a keyhole. However, although the beam is concentrated and highly focused, it is quickly scattered if it hits the air particles, so the whole joining process is carried out under high vacuum condition. This method makes it easier to perform welds on alloys with high thickness of up to 300mm [12] with one single pass without the need to carry out multi weld passes, as used to be the case with the conventional welding methods. When the heat source is more concentrated, and of high intensity, the generated keyhole becomes smaller, and even the HAZ becomes much narrower. The reason is that the melting and the joining take place very fast, without allowing the heat to disperse by being conducted into the rest of the workpiece. Also, since the joining happens very fast, this process provides weldments with minimal to zero distortions. Figure 2.16, shows a cross-section of two thick welded joints, one produced with an electron beam and the other by Gas Tungsten Arc welding. Over the last few years, this process has attracted a variety of published research papers, many of which have studied the joining process. Most of these publications have investigated the microstructure, the mechanical and the fracture properties of the welded joints[11]. Chih et al.[13] studied the effect of post-welding heat treatment on the joint efficiency of Ti-6Al-4V weldments. Firstly, they studied the as-weld samples, and typically the base metal microstructure was found to consist of equiaxed α structure and retained β phase. Moving

toward the WZ, the structure starts to take on another form. Due to the high cooling rate during the solidification, the general structure is needle-like or acicular α martensitic within the former β grain boundaries, figure 2.17a. The highest hardness value was recorded in the WZ and the HAZ area, and it reduced gradually with the movement toward the base metal.

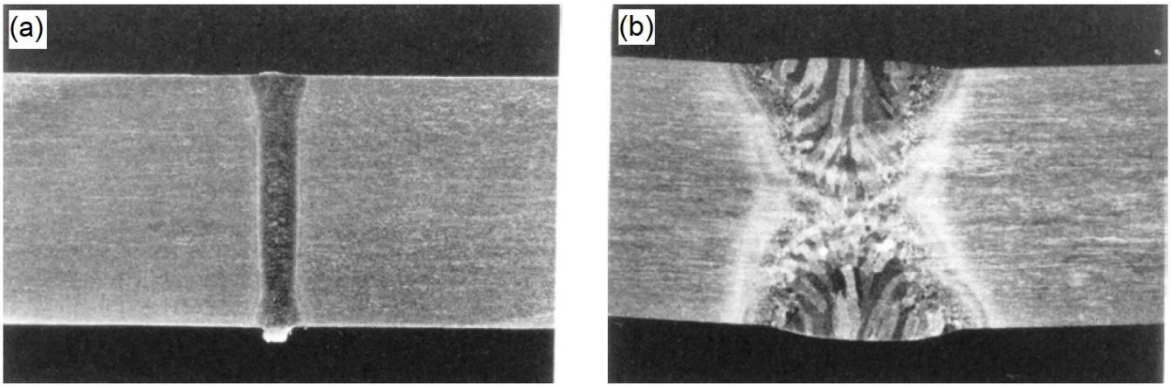

Figure 2.16 Differences in the cross-section area of two weld zones produced by (a) A narrow WZ by electron beam welding (EBW) While (b) shows a wide FZ achieved by GMAW process (GTAW)[67].

Several reports indicated an improvement in the joint strength over the ductility as a result of Ti weldment, figure 2.17b. Then, the researchers applied a post welding heat treatment, involving annealing of the welded parts under different cooling rates using furnace cooling method and air cooling method. The researchers observed an increase in α laths thickness in the structure of the alloys cooled inside the furnace as compared with the samples that cooled in air. However, the elongation properties of the joints cooled in the air were better than those of joints subjected to furnace cooling method; meanwhile, the air-cooled samples had better ductility than the furnace cooled samples. This work led the researchers to highlight the reasons behind the improvement in the hardness and joint strength. It was stated that the fast cooling rate associated with EBW process leads to the formation of solute segregation in the welding zone.

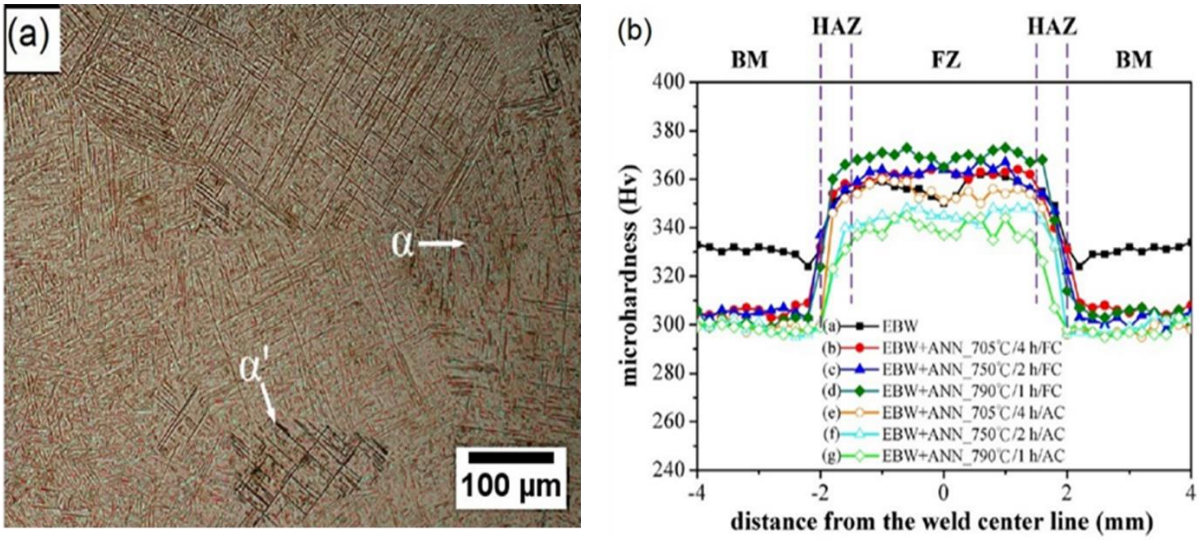

Figure 2.17 (a) Columnar dendritic microstructure of the Ti-6Al-4V weld zone, consisting of martensitic α′ phase and Widmanstätten α phase; (b) general distribution of hardness over the welded joint in EB titanium welds[49].

This newly formed structure enhances the weld joint due to the presence of $\alpha_2+\gamma$ phases in the air-cooled samples, figure 2.18, which are generated in the weld zone during the EBW process. This phase appears because the concentration of α stabilisers reaches a high level of 48% in the WZ during the welding process. Pengfei et al. [76] studied the effect of beam oscillation condition on the microstructures and mechanical properties of 50mm Ti-6Al-4V weldments. They selected three different oscillation beam conditions: circle, triangle and rectangle, and compared the results with those for welds done by a beam without oscillation. They demonstrated that when the beam is subjected to 200 Hz frequency, a stirrer function is generated. The first impression on this process was that the weld line profile is solid and much smoother with no intermittent regions along the weld line as compared to weld lines with zero oscillation beam. This technique can improve the fluidity of the molten metal in the WZ, enhance the solidification process, and provide the ability to achieve full penetration, especially in thick sections. As the beam travels to form the keyhole, the stirrer condition allows sufficient time for the generated gases to move and travel efficiently in the molten metal without being trapped by the solidified metal toward the top surface of the WZ. This leads to the production of welds that are free from defects and pores. However, the oscillation of the beam offers only a slightly wider weld zone, but the homogenisation of the solidification is much better than that produced without oscillation. So, welds with oscillated condition offer high fatigue resistance, and most of the failures occur in the base metal area next to the HAZ compared to welds with no oscillations.

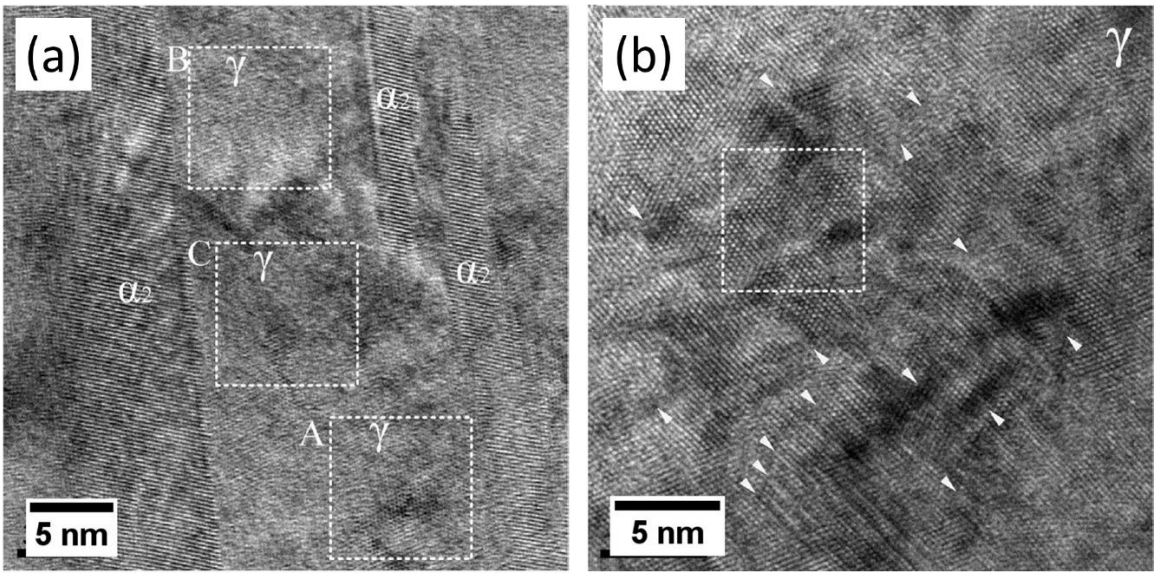

Figure 2.18 TEM image showing the morphology for the Ti-6Al-4V WZ by EBW process: (a) represents the structure resulting from annealing process and air cooling; (b) shows the weld structure following post welding heat treatment by an annealing process.

Hingzhi et al.[77] conducted a study of the impact of heterogeneity on the fatigue properties of T6Al4V weldment by EBW. They tested the fatigue crack growth rate for both the WZ and the HAZ in different depth zones: top, middle and root. Their results showed that the effect of heterogeneity on the fatigue crack growth rate for the HAZ at different depths was the same as for the base metal. However, this rate increased in the case of the welding zone. The rate of fatigue crack growth was very high at the root of the weld area. This rate increased gradually with the movement toward the root zone; this is due to the high level of heterogeneity and the high residual stress in the root zone as compared to the top weld area. The researchers presumed that the length of the α′ martensite has a significant effect on the fracture toughness. The top area of the weld zone showed the lowest fracture growth rate due to the long α martensite grains. The fracture rate was high in the root zone, which occurred because the short α martensite increases microcrack growth. Fatigue properties, for similar weldments of the Ti-6Al-4V alloy, were studied by Xiaoguang et al.[50]. The paper discusses the fatigue life of titanium weldments under high cycle and low cycle fatigue tests and compares the results with fatigue results for the base metal under the same test conditions. Unlike the base metal samples, all the fatigue samples extracted from the weld zone showed excellent resistance to crack propagation, due to the presence of the martensitic structure that enhances the alloy properties and joint efficiency. The presence of pores in the weld zone produces stress concentration and microcrack initiation sites, which causes a

rupture during the test. Balasubramanian et al. [4], [78] investigated the effect of the Electron welding process among other welding methods in relation to the join characteristics. Similar Ti-6Al-4V alloy weldments were fabricated by three different welding methods: GTAW, LBW and EBW. The microstructures, mechanical and fracture properties were studied in both these papers. Welds fabricated by EBW recorded the highest joint tensile strength as compared with the two other processes. Meanwhile, the GTAW weldment showed the highest impact resistance among the other weldments. Due to the high heat input during the process, the structure predominantly consists of coarse grains of acicular α and Widmanstätten structure, which increase the ductility of the weld zone.

2.8 Fusion welding of dissimilar titanium alloys

In recent years, the attract to fabricate complex structures has increased dramatically. Applications for such as aerospace, petrochemicals, nuclear industries, and thermal power stations require the use of fabricated parts with many reliable properties. To achieve this goal, the joining of dissimilar alloys has become the central concern for many researchers, who have directed their efforts toward studying how to fabricate welds that combine different alloys and their different mechanical properties. Automotive companies, for many years, were attracted to aluminium as a lightweight alloy that offers high quality and efficient structures. Meanwhile, steel's excellent strength and reasonable cost have led to steel alloys being in high demand for a wide range of industries that need to fabricate structures of excellent strength using costly efficient joining method. So, increasing importance has been attached to joining alloys such as aluminium and steels to fabricate a structure that combines excellent strength with lightweight and low cost. Titanium alloys have been used extensively in the industry such as aerospace and chemical applications due to their high specific strength to weight ratio, high elevated corrosion resistance[79]. A paper published by Yefei et al.[79] reviewed the efforts made over the last ten years to join Titanium alloys to steel alloys.

The paper tried to cover the most convenient welding methods in terms of achieving successful dissimilar joining results. The dissimilar joining methods were divided into solid-state bonding methods and high energy beam methods. The fusion or conventional welding method was not covered as it is considered an unfavourable process for joining titanium to steel alloy, due to the formation of intermetallic structures in the weld zone which increase the embrittlement in the joining area. Also, the possibility of the presence of pores in the weld zone, due to the high reactivity of titanium with oxygen, and hydrogen during the fusion process.

2.8.1 Diffusion bonding (DB)process

A research study was conducted by Ghosh et al. [80], [81] to examine the reactions at the joint interface of solid-state bonding conducted by diffusion process between stainless steel and CP titanium. For a 950˚C diffusion temperature inside a vacuumed chamber, a set of four holding times: 30, 60, 90, and 120 min, were selected. Figure 2.19 shows the microstructure of diffusion bond joints between CP-Ti and 316 stainless steel alloy at the selected holding times. Each joint was subjected to a uniaxial load of 3MPa. The diffusion bonding reaction was higher at the titanium side than the 304 stainless steel side. The formation of IMCs was observed for all the joints and the size of these increased with the holding time. A successful joint, which was achieved at a holding time of 30 min, had a fine intermetallic structure and provided 71% joint strength. However, the UTS decreased with increasing the holding time. Along with the growth of the intermetallic structure, voids and pores were generated when the holding time increased. Kundu et al. [82] attempted to evaluate the diffusion process between titanium alloy type Ti-6Al-4V and duplex stainless steel. They investigated the microstructure and mechanical properties of the joint interface area. The diffusion process was conducted under vacuum condition, and 4MPa load was applied under the selected joint and diffusion conditions of 850 ˚C for 90 min and 800 ˚C for 120 min. From the SEM images, a limited diffusion-reaction was observed, which led to less intermetallic formation at 800 ˚C diffusion temperature and holding time of 90 min. However, in the case of the longer diffusion time, a σ phase was formed in the bond area next to the stainless steel side, which mainly consisted of FeTi+λ phases, while at the area very near to the bonding zone the phase was β-Ti. Both temperature and time have a direct effect on this layer's width. Also, the formation of pores was observed, and it was noticed that this formation increased as well with increasing time and diffusion temperature, according to Aleman et al.[83], these pores are generated due to the imbalance in the mass flow as the diffusion of titanium is faster that of stainless steel, which leads to turbulence in the diffused zone that then leads to pore formation.

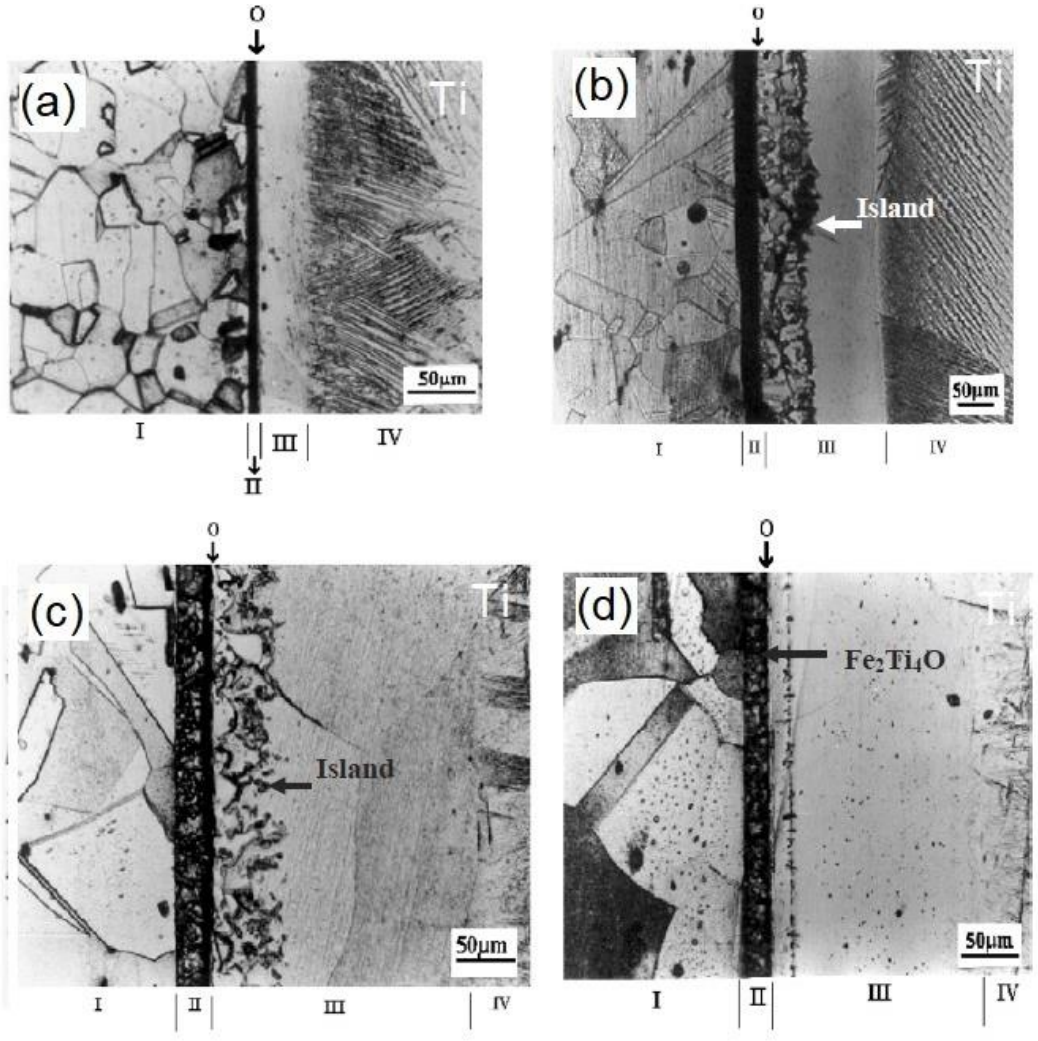

Figure 2.19 Optical images to show the effect of diffusion bonding time: (a) 30min, (b) 60min, (c) 90min and, (d) 120min, on the interface thickness of CP-Ti to 304 Stainless steel joints joined by diffusion bonding at 950˚C [74].

Regarding the mechanical properties, the interface area recorded the highest value in terms of the hardness results. The formation of the intermetallic compound increased the hardness to 1260 VH in the bond area, whilst 510 MPa was the maximum tensile strength recorded for the joint at that bond area, at 850 C for 90 min. It was found, however, that most of the failures took place in the bond area, and that increasing the time or increasing the diffusion temperature decreased the tensile strength significantly. This was due to the increase in the width of the intermetallic compound wall alongside the increases in time and temperature.

Another study of dissimilar diffusion bonding between Ti-6Al-4V and austenitic stainless steel 316L was conducted by Soltani et al. [84]. The study involved using a thin layer of silver-based alloy placed in the joint area. They suggested applying a wetting test for the joint before performing the diffusion process to examine the wetting reaction on the surfaces

of both the Ti-6Al-4V and 316L stainless steel. Improvement was noticed in the wetting process when both brazing time and temperature were increased. However, the wettability on the titanium side was higher than that on the 316L alloy side due to the presence of a thin film of chrome oxide that impeded the wetting process. The wetting test involved heating the joint to 700˚C -850˚C over the time period of 5-60min. The Braizing temperature was carried out by selecting and applying three different temperature levels under a vacuum condition of 5 X 10^{-6}mbar. Three joints were produced using a brazing temperature of 800 ˚C but under three different brazing times: 5, 15, and 30 min. Then for the brazing time of 30 min, it was decided, first, to braze two joints at 830˚C and the third one at 860˚C. It was found that the presence of Ag in the filler metal composition is essential since it prevents the generation of cracks in the welding area by producing a soft phase in the diffused surfaces. However, whilst increasing the time and temperature helped to increase the wettability in the bonding zone, there were two disadvantageous outcomes from these conditions. A reduction in the shear strength was noticed for high diffusion temperature and long diffusion time due to the increase in the formation of IMCs associated with these joining conditions. Further work on diffusion bonded joints between Ti-6Al-4V and 316L was conducted by Zakipour et al. [85]. Their work was focused on the effect of different thicknesses of a pure copper thin layer on the characterisation of the diffused joints. Keeping the discussion temperature fixed at 1100 ˚C and selecting a holding time of 60 min, three thicknesses of pure copper were selected for the study: 50 μm, 100 μm, and 150 μm. It was noticed that the thickness of the interlayer had a direct effect on the joint width, figure 2.20; however, it was also observed that increasing the interlayer thickness tended to reduce the joint strength. While the joints made using a 50 μm interlayer achieved 245 MPa shear strength, a reduction of about 145 MPa in the shear strength was recorded for the joint with 150 μm thickness. The highest HV was recorded in the bond area, where the maximum hardness obtained was a 380VH, due to the formation of hard, brittle intermetallic components, such as FeTi and $FeTi_2$. A different approach of dissimilar joining of titanium alloy to stainless steel by diffusion method was adopted by Peng et al. [86], using multi interlayers placed in the joint area. They used three alloys of Nb+Cu+Ni, with a thickness of 10 μm each and these were combined and placed in the joint as filler alloys. Regarding the diffusion process parameters, six temperature levels were selected: 825˚C, 850˚C, 875˚C, 900˚C, 925˚C, and 950˚C, while the holding times or bonding times were 15, 30, 45, and 60 min. Based on these parameters, they found the best strength was achieved at about 300 MPa, for the joints that were diffused at 850˚C, and over a bonding time range of 30-45 min.

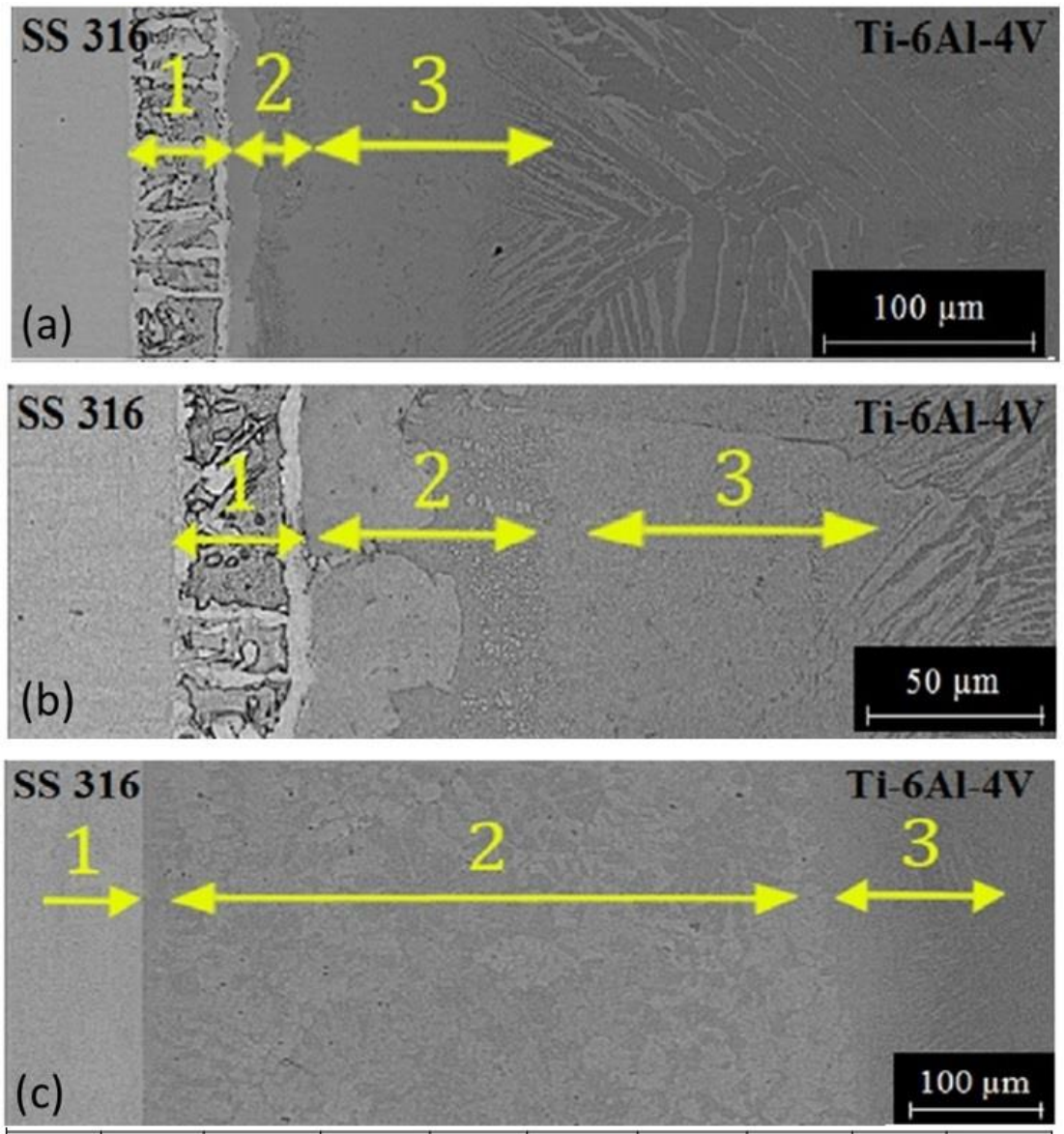

Area	Fe	Ti	Cu	Mn	Cr	Ni	Mo	Al	V
1	62.64 -65	1.98- 9.20	0.01- 4.42	0- 1.98	19.67- 18.41	5.40- 5.75	0.94- 3.59	0- 0.03	0.32- 0.66
2	9.77- 26.55	54.38- 75.34	2.06- 10.82	0- 0.51	3.47- 4.54	1.51- 2.76	0.12- 0.45	1.86- 3.96	0.04- 1.86
3	21.47	60.63	9.41	0	2.05	2.30	0.01	3.27	0.86

Figure 2.20 Diffusion bonds between Ti-6Al-4V and 316L stainless steel using three different thicknesses of Cu foil: a) 50 µm, b)100 µm, and c) 150 µm of pure Cu as an interlayer, three distinct areas were formed, and the table attached shows the EDS analysis wt.% for each area[85].

2.8.2 Friction welding (FW)and friction stir welding (FSW) processes

Another solid-state joining process that is used to perform dissimilar joining between titanium alloys and another alloy is friction welding. Researchers such as [87]–[89] have studied the applicability of using the friction welding process to join titanium alloys to steel alloys. This process involves using two rods, one of titanium alloy and one of stainless steel alloy, of specific length and specific diameter. One of the rods is mounted in a fixed clamp, and the other on the rotary head side. The fixed head is pushed gradually toward the rotary head. A high temperature generates due to the applied force on the fixed head, friction at the contact surfaces causing plastic deformation at the contact joint. Then when a sudden stop applied from the rotation stage, a solid-state bond forms the bonding between the metals. In their work, they studied the effect of different applied forces (100 MPa and 200 MPa) [87] and different rotation speeds (400 rpm, 600 rpm, 1200 rpm, 1500 rpm and 1800 rpm) [89] on the microstructure and the mechanical properties of the welded parts.

Reviews were conducted by Mironov et al. [66] and Tomashchuk et al. [90] to understand the developments in the joining of titanium alloys using friction stir welding. These reviews focused on determining the main problems that usually face the joining process and how they affect the final product. The effect of welding variables[91][92], such as welding tool materials[93][94], the tool design and geometry[62][95], the rotation speed and the welding travel speed[96][97], have a direct impact on the welding joint. Even if all the previous issues are addressed, there is still a significant possibility of another issue, namely the formation of brittle phases of intermetallic compound precipitates in the weld zone, which can especially affect dissimilar joining between titanium and other alloys. So in order to prevent this situation, a thin interlayer of a ductile alloy is placed in the joint area. This technique is performed in order to avoid the formation of brittle phases and reduce the embrittlement of the weld joints. Muralimohan et al.[98] and Kumar et al.[99] studied the effect of a thin layer on the joint properties in friction welding between titanium alloys and steel alloys. They found that adding a thin layer of copper to the joint softened the WZ and minimised the migration of iron toward the titanium, lowering the formation of brittle phases. However, when a thin layer of nickel was used, an IMCs was formed at the joining interfaces which are of TiNi and $TiNi_3$, especially in the zone near to the titanium side. The diffusion depth of the nickel alloy into the titanium side was very high as compared to the stainless steel side, where no reaction was apparent between the steel and the nickel. As shown in figure 2.21, three layers of structures were formed that were distributed between the nickel

interlayer and titanium interface. The intermetallic layer closest to Ti is (I), comprising mainly Ti_2Ni that consists of about ~55.2 – 59.4 % Ti and Ni (bal.). Meanwhile, the zone (II) closest to the Ni interlayer is enriched with nickel alloy and consists mainly of the intermetallic phase $TiNi_3$ (Ni ~75 - 77% and Ti (bal.). The final layer, which is situated between the two previous layers, is composed of ~48 - 53.6% Ti and Ni of 51.79 - 46.3 %, represented by the phase TiNi. As a β stabiliser alloy, Ni diffuses very deep into the Ti side, and the reaction is higher than at the stainless steel side, whereas the Ni layer works as a barrier that avoids any formation of IMCs at the stainless steel side, with no further interaction occurring between Fe, Cr and Ti.

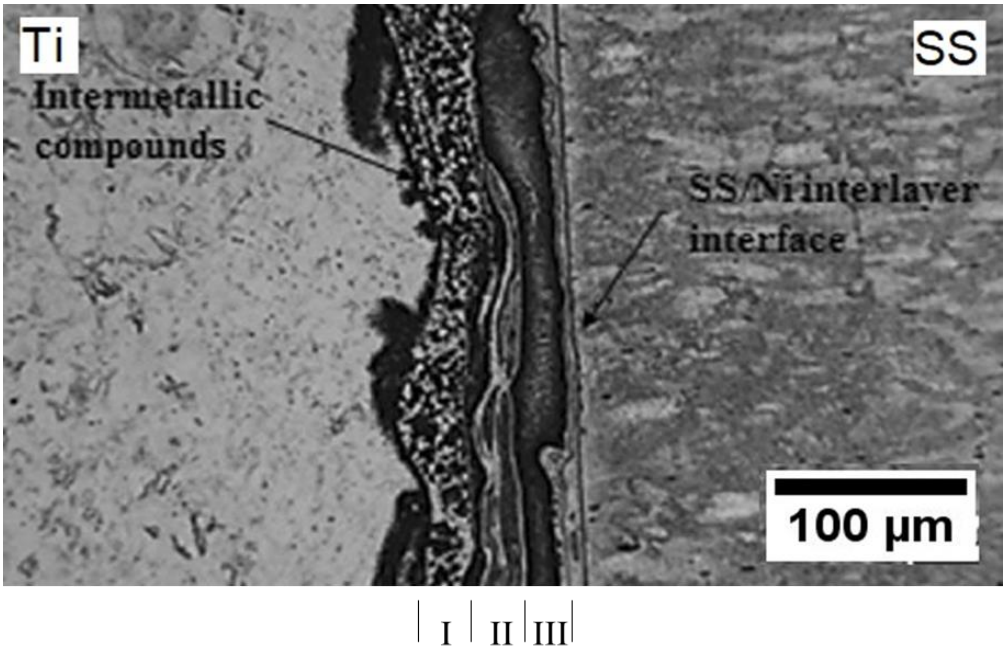

Figure 2.21 The three different layers of IMCs formed alongside the Ti interface: (I) Ti_2Ni, (II) TiNi, and (III) $TiNi_3$ [92].

Regarding the mechanical properties outcome of this join, the maximum hardness was found in the joint zone, with a hardness value of 670 HV, while the hardness values in the base metal for Ti and SS were 342 HV and 325 HV, respectively. Adding the nickel interlayer enhanced the joint strength. It was reported that increasing the upset pressure would lead to increase in the tensile strength but with adding Ni interlayer to the joint, due to the increase in the plasticity of the joint area as a result of the presence of the IMCs [98].

Furthermore, as a solid-state joining process, friction stir welding has been employed in successful attempts to join titanium and stainless steel alloys [100]. Figure 2.22, shows that

two welding positions, butt joint [55] [92], [101],[102] or lap joint [100], [103], [104] ,were selected to perform the joining process. It is an alternative joining process that helps to reduce and minimise the problems that would occur in the weld joint if a conventional welding process were performed. This technique is also used widely to join titanium alloys to aluminium alloys.

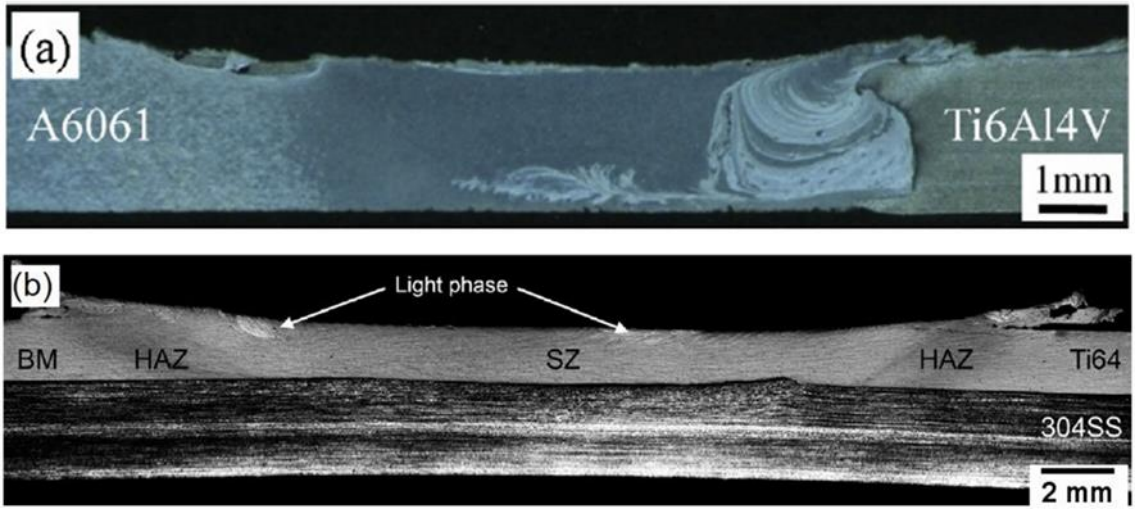

Figure 2.22 Show different welding position depending on the physical properties of the selected alloys to be joined. a) the Butt welding position to join the Ti alloy to the ductile Al alloy [97] while in b) The lap position was more favourable in the case of joining Ti alloy to 304 stainless steel [94].

several studies have been conducted to examine the microstructure and mechanical properties of joints produced by friction stir welding between titanium and aluminium alloys — for example, Yuhua et al.[104] studied two different welding positions: butt and lap. From this work, the researchers found that when FSW was used in the butt joint position, it was challenging to create bonding between the titanium and aluminium alloys and initiation of cracks took place in the weld joint, especially at high-speed tool rotation of 1180rpm and travel speed in the range 90-190rpm. It was found that the more heat generated during the fast rotation speed, the higher the amount of IMCs formed in the weld zone, leaving a brittle structure when the joint cooled down and causing a post-weld crack in the weld line, figure 2.23a. While at the low-speed rotation, insufficient heat was generated to allow for plastic deformation to take place at the weld zone, so that no bonding could be achieved in slow rate rotation, with only an uneven groove occurring behind the rotating tool, figure 2.23b. However, it was found that a combination of parameters of travel speed range of 118 - 150mm/min and a tool rotation speed range of 750 rpm-950 rpm would provide appropriate

joining conditions, figure 2.23c, which would produce a suitable surface finish with less risk of cracks appearing after cooling of the weld temperatures. Meanwhile, in the case of the lap joint, figure 2.24, a 2 mm aluminium layer was placed over a 2 mm of titanium alloy, with the joint shoulder 20mm from the weld centre line.

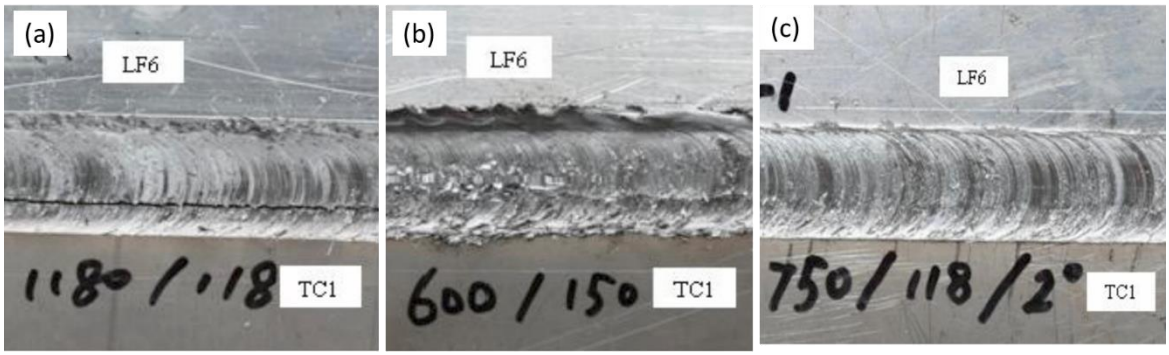

Figure 2.23 Friction stir welding effect of tool rotation speed and welding travel speed on the joint morphology of titanium/ aluminium weldments [98].

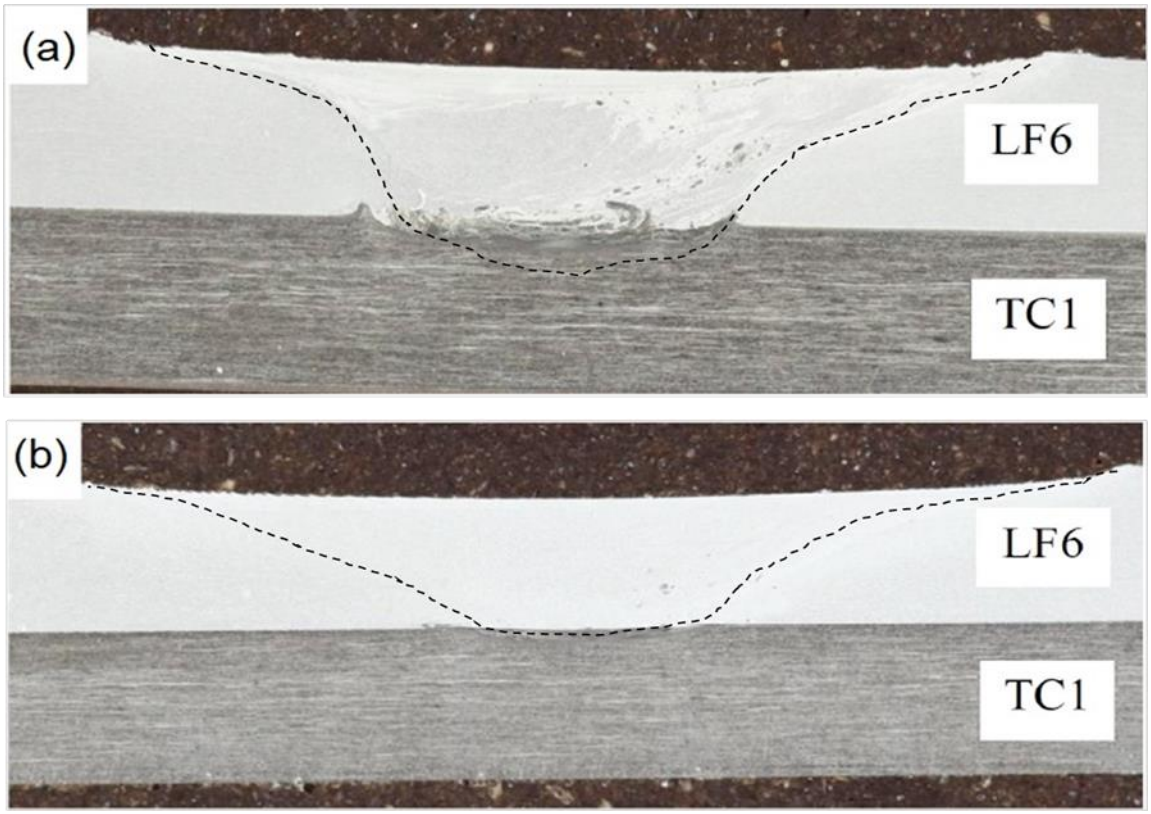

Figure 2.24 A bonding in a lap joint with high depth was achieved between Ti and Al alloys by FSW when rotation speed of the tool was a) 1500rpm, while in b) the speed was 950rpm and no bonding was acompleshed due to insuffeciante heat produced to create plastic deformation [98]

However, the lap joint was affected by the welding speed at a given tool rotation speed of 1500 rpm showing a reduction in joint efficiency upon increasing the welding speed. The maximum joint strength identified for the dissimilar butt weldment was about 131 MPa for Ti-6Al-4V and Al alloy weldments at a travel speed of 150mm/min and tool rotation speed of 950 rpm. However, the maximum joint strength was only 48MPa when the tool rotation speed 1500 rpm and welding speed was 60 mm/min. While fast failer at lap weldment was observed as the rotation speed of the tool was 1500 rpm and 150mm/min welding speed.

2.8.3 Laser Beam Welding (LBW)

In order to increase the possibility of joining titanium alloys to other different ferrous and non-ferrous alloys, a welding process was developed that uses a high energy beam to achieve precision welds and high-speed welding. Methods such as LBW and EBW increased the ability to undertake fusion welding of dissimilar alloys. A few alloys can be considered to be easily weldable to titanium alloys, such as niobium, molybdenum, tantalum, vanadium, and zirconium, but with other alloys, such as steel [29], [90], [105] or aluminium [106]–[108], there is a chance of brittle intermetallic phases forming in the WZ. Copper alloy is one of the alloys most commonly used for placement as an interlayer in the joint between titanium alloy and steel alloys [34], [109], [110]. A study was conducted by Lei et al.[10] to join different titanium alloys, using the laser welding process to join Ti-6Al-4V to Ti-22Al-27Nb titanium alloys. The precision joint was free from cracks and porosity, and the chemical composition of the weld zone was Ti-17Al-11Nb-9V. Three phases were found in the HAZ area next to Ti-6Al-4V alloy, primarily consisting of α, acicular α and martensitic α, while the primary phase in the HAZ area adjacent to Ti–22Al–27Nb alloy was B2 phase with small amounts of α2 phase.

On the other hand, while the WZmorphology is in general semi-circular in shape, the texture in the upper weld structure differs from that in the weld root area. This change in the structure's morphology is related to the amount of heat to which it is subjected during the fusion process and the difference in the thermal expansion coefficient. The main phases in the WZ are martensitic α structure and B2, which form due to the presence of niobium and the high cooling rate. The weld joint achieved 1043 MPa, with 92% of the tensile strength but 40% less elongation when compared to the Ti-6Al-4V base metal. According to the hardness results, the WZ recorded the lowest hardness value,~315HV, while the HAZ exhibited the highest hardness value, ~410HV.

It is well known that there is a high possibility of IMCs forming in the welding joint, especially between titanium and steel alloys. So in order to overcome these problems, it was suggested that the chemical composition of the WZ should be enhanced. The addition of alloys that are more compatible in some ways with the two base metals will prevent or reduce the formation of the brittle phase. This was addressed by using a thin foil of a ductile alloy in the joint area, with other researchers studying the joining of titanium alloy type Ti-6Al-4V to stainless steel using LBW but with the addition of a thin layer inserted in the joint area.

Mitelea et al. [111] used a thin foil of copper to join Ti-6Al-4V to austenitic stainless steel type X5CrNi18-10 using LBW method. They studied the effect of laser welding parameters such as the welding power, beam travel speed, the diameter of the beam spot and the location of the beam spot on the joint area on the joint efficiency and how the placing of the Cu alloy can improve the properties of the joint between these two different alloys. By using the Cu foil, they were able to minimise the interaction between the titanium alloy and stainless steel alloy, thereby reducing the amount of IMCs formed in the welding zone. Also, it was noticed that the laser beam power has a significant effect on the welding keyhole profile. With a high power beam, the keyhole width was narrower and also the formation of voids in the weld line was reduced. Meanwhile, there was much more reaction to the melting process at the stainless steel alloy side than at the Ti alloy side. The beam travel speed was found to affect the joint's efficiency; hence, it was recorded that at a constant power beam increasing the welding speed would reduce the joint strength, whereas using a high power beam of 4000w with fast beam travel of 50mm/sec would achieve the best joining condition between these two alloys. However, with low travel speed, there is a risk of the keyhole being too shallow, and a serious risk of void formation and over melting of the root. The highest UTS was found to be about 400MPa for the welded joint, double the 198MPa recorded for the Cu alloy. Similarly, Ming et al.[112] used a Cu foil to join Ti-6Al-4V to 316L alloy by LBW method. The microstructure for the joint area revealed no interaction between the Cu alloy and the 316L alloy at the steel alloy interface, figure 2.25a, while at the Ti interface side, figure 2.25c, phases such as CuTi and $CuTi_2$ were formed. By adding Si to the filler metal (Cu), a quadrable system of Cu-Fe-Si-Ti was created in the welding zone, figure 2.24b, during the fusion process. The high heat input and the slow cooling rate allow the titanium and iron content to rise in the molten metal, leading to the formation of two main phases in the welding zone, figure 2.25b, Fe_{67}-Si_x-Ti_{33} (the dark-arms), with bright areas represented by α-Cu. Moreover, it was recorded that the volume fraction of this phase is directly

proportional to the heat input, and a change from particles shape to a dendritic structure occurs at high heat input. Also, the homogeneity of the joint structure has a significant effect on joint strength. It was noticed that the homogeneity of the joint increases with increasing the heat input, which leads to improvement of the joint strength.

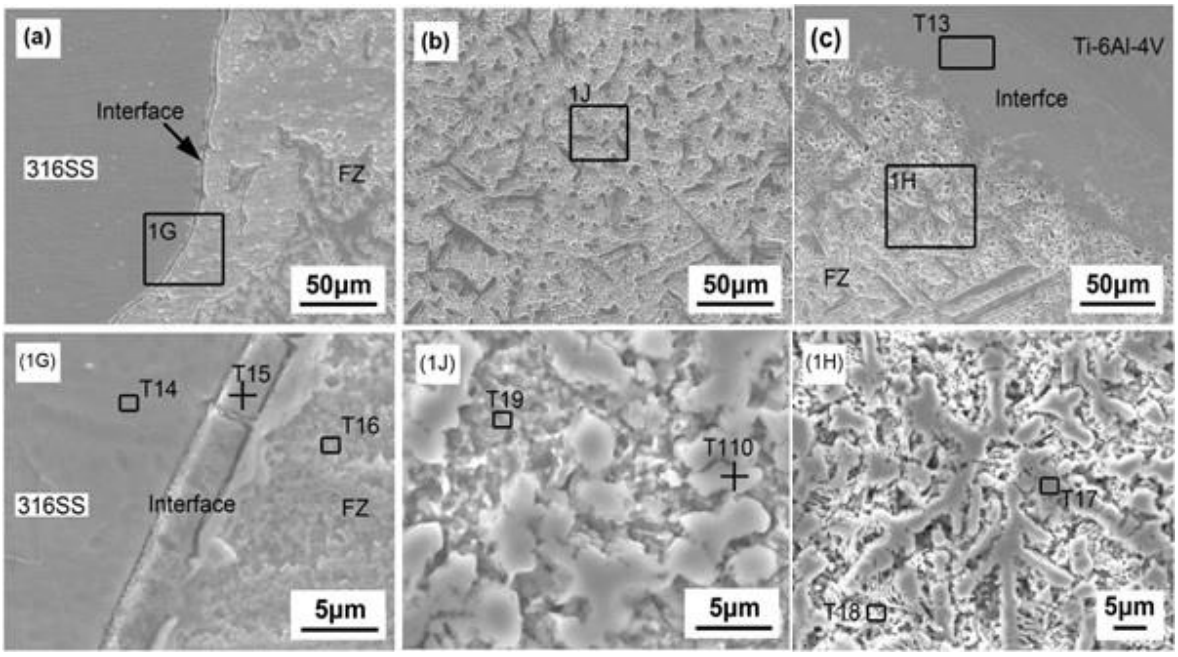

Figure 2.25 Shows three different regions at the joint area of Ti-6Al-4V alloy / 316L stainless steel joined by Laser beam welding: (a) stainless steel interface side, (b) welding zone, and (c) Ti-6Al-4V interface side [107].

Other alloys have been used as an interlayer to achieve welding between titanium and steel alloys, such as vanadium alloys. According to Tomashchuk et al. [113], the excellent solubility of vanadium alloy offers a strong joint between Ti-6Al-4V and 316 stainless steel. Additionally, Li et al. [114] suggested using cobalt alloy as a filler metal to join titanium alloy to stainless steel using laser beam welding. The addition of thin cobalt foil to the welding area improves the microstructure and the mechanical properties. Enhancement of the joint strength was demonstrated by its tensile strength of 347MPa and maximum elongation of 4.2%, while the joint ductility was increased through reduction of the formation of brittle intermetallic structures such as $TiFe_2$, $TiCr_2$. However, when the %Co increased, a reduction in the properties of the welding joint occurs, due to the formation of a brittle Co-Ti phase.

Joining titanium alloys to aluminium alloys requires particular consideration because there is a high potential for the brittle phase to form in the welding area. Phases such as Ti_3Al, TiAl, and $TiAl_2$ can cause the instant failure of Ti/Al weldments. It was reported that the

thickness of the intermetallic layer that forms at the interfaces should be less than 10μm in order to achieve a suitable joint strength with good toughness [115]. As a method to control the thickness of the intermetallic layer, Shuhai et al. [116] succeeded in reducing the formation of the brittle phases by added silicon to the filler metal during the LBW process. Another successful attempt was made by Peyre et al. [117] who managed to reduce the intermetallic layer $TiAl_3$ to 2μm, with the joint strength of the Ti/Al reaching 300N/mm.

2.8.4 Electron Beam Welding (EBW)

This high energy beam fusion welding method is considered one of the reliable and efficient welding processes. Its particular characteristics, in comparison to other joining methods, table 2.2 [118], have led to this method becoming widely used in the aero engineering and automotive industries. Its advantageous properties include high power density beam reaching 10^{13} w/cm^3, high-speed welding that produces very narrow and deep keyhole welds, especially in thick sections [30], and narrow HAZ, with the weld parts less likely to be distorted after cooling. Moreover, the ability to control and manipulate the beam makes it easy to weld complex structures. The welding process is carried out under vacuum condition, so refractory and reactive alloys can be welded easily, as there is no risk of the molten pool being exposed to contamination, and in the case of Ti alloys, there is less chance of the formation of hydrogen porosity which occurs when using other welding processes [12]. The research interest in the dissimilar joining of Ti alloys has been driven by the need to produce a composite structure by combining two different alloys while at the same time retaining the advantages offered by these two alloys' properties [119]. Moreover, producing composite structures intended for use in critical parts of a jet engine requires a precision joining method that will provide joints of high quality. The most intense research efforts have been focused on dissimilar joining between titanium alloys using EBW. These studies aim to characterise the microstructure and mechanical properties of the welded joints [6], [120]–[122],. For instance, Esfahani et al. [120] conducted a study to join two different titanium alloys, Ti55 and TA15, using EBW. They investigated the effect of the EBW parameters on the microstructure and mechanical properties of the welded alloys. They noticed that the hardness of the WZ became higher when the beam offset position shifted toward the Ti55; this was due to the formation of intermetallic phases. When the beam was set away from the centreline and shifted to the Ti55 side, the content of Zr and Si in the HAZ increased, leading to the formation of a hard $(Ti, Zr)_5Si_3$ phase. The hardness value of Ti55 at the HAZ was 358HV, whereas at the TA15 HAZ area the hardness was 319HV.

Table 2.2 Comparison of different high-energy welding methods [113].

Feature	Plasma keyhole	Laser	Electron beam
Energy density (W m^{-2})	3×10^{10}	3×10^{11}	10^{13}
Thickness range (mm)	Up to 12	Up to 20	Up to 200
Travel speed	Higher than GTAW	High	Very high
Materials weldable	All, but aluminium needs DCEP or AC	Most, but difficult on reflective surface (e.g. Cu, Ag)	Most, but not low vapour pressure, e.g. Cd, Zn and coated metal
System requirements	Simple; as for automated GTAW	Highly automated plus screening safety interlocks	Usually vacuum system, x-ray screens and high level of automation
Capital cost	Slightly more than GTAW	10 to 50 times GTAW	10 to 50 times GTAW
Running cost	Low	High	Very high
Cost of weld	Depends on application		

In order to examine the microstructure of the welding zone, the cross-section area was divided into three parts: WZ, high heat affected zone (Hi-HAZ), which is adjacent to the WZ, and the low heat-affected zone (low-HAZ), which is next to the base metal (BM). The WZ structure consisted of martensitic α′ and acicular α phases. Similarly, the main phases at the area adjacent to the WZ or the Hi-HAZ were martensitic α′ and acicular α phases. However, when they examined the Low-HAZ, the phases were primary α, secondary α and prior β phase. Also, as shown in figure 2.26, they noticed the distribution of these phases was the same on both sides of Ti55 HAZ and TA15 HAZ.

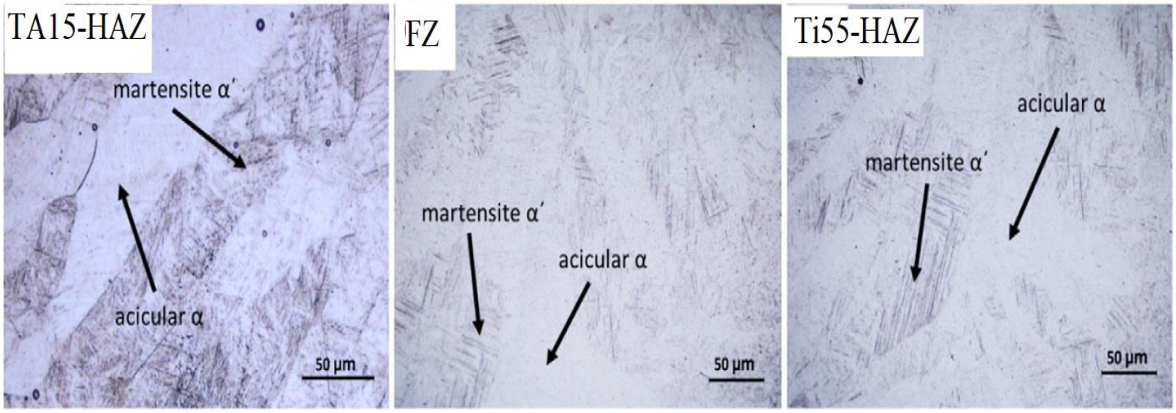

Figure 2.26 The microstructure of the FZ in TA15/Ti55 weldment, showing the formation of martensitic α′ and α acicular upon rapid cooling [120].

The effect of heat input on the mechanical properties of the dissimilar weldments of Ti-6Al-4V/Ti_3Al was investigated by Zhang et al. [121]. A full penetration autogenous weldments were obtained using electron beam welding, and the highest tensile strength of this dissimilar joint reached to 831MPa, which was about 92% of the that of the Ti_3Al-based metal. The study reveals an inverse relationship between the weldments strength and the amounts of the welding heat inputs. A reduction in the joint strength was observed with increasing the welding current, implying a deterioration in the joint ductility. The amount of welding current has a significant influence on the microstructure of the welding zone, causing a variation in the grain size with different heat inputs. The higher the heat inputs, the more dwelling time at a liquid temperature which leads to advance the growth of the grain size and deteriorate the tensile strength of the weldment. The highest hardness value recorded was 380HV for the Ti-HAZ, due to the presence of hard phases such as α2 and acicular α′ martensite while the WZ showed the lowest hardness value of ~308HV, due to the presence of β stabiliser alloys such as vanadium and niobium which improved the ductility of the WZ. Another study by Zhang et al. [122] using the same parameters in [121] to investigate the fracture surface of Ti-6Al-4V/ Ti_3Al alloy weldments joined by EBW process. They found that in most of the samples subjected to the tensile test, the cracks were firstly initiated at the Ti_3Al side at the top of the weld line, and then spread toward the HAZ. When the high heat input was increased, grain growth of the α′ escalated in the welding zone.

Furthermore, several researchers conducted projects to join dissimilar titanium alloys such as Ti-6Al-4V to Ti6Al2Sn4Zr6Mo [6], Ti-6Al-4V to BT9 titanium alloy [123], Ti-6Al-4V to IMI834 titanium alloy [124], Ti-6Al-4V to Ti17 alloy [125].

Other researchers have used the EBW method to study the ability to join Ti alloys to steel alloy. This type of hybrid structure is essential in order to produce the lightweight alloys needed in the automotive industries and also to replace some of the expensive Ti with inexpensive alloys such as stainless steel alloys. However, forming a joint between Ti alloys and steel alloys considered a challenge, due to the high tendency for brittle IMCs to form in the interfaces of the WZ. Moreover, phases such as TiFe, $TiFe_2$ have a severe impact on the joint strength due to the high tendency for post-weld cracks to form. So in order to overcome these problems, a thin foil was placed in the weld joint to reduce the formation of the brittle phase, enhance the joint strength, and reduce the joint embrittlement. For instance, Wang et al. [126] used a 1 mm Cu sheet as an interlayer to join Ti-15-3 alloy to 304L alloy by EBW. In this way, they created a transition layer in the Ti/SS joint, which improved the ductility and offered a joint strength of up to 234MPa. Also, the Cu foil blocks the formation of the intermetallic phase through trapping the formed IMCs in the solid-solution regions.

2.9 Effect of filler metals type on titanium alloy weldments

Over the last decade, the demand for joining dissimilar alloys has increased rapidly. By fabricating a composite structure, there is a high chance of combining different efficient properties in one place. However, in most applications that require structures made from titanium alloys, welding and joining will be the primary methods used to achieve such a structure. Welding and joining Ti alloys to different alloys is quite challenging due to the high possibility of the presence of undesirable brittle intermetallic components in the WZ. The presence of these undesirable phases will lead to premature failure in the WZ or the HAZ. Therefore, it is essential to overcome this problem. An intermediate alloy was prefixed in the weld joint before conducting the welding operation. Improvement was observed in the welding joint as a result of the change in the WZ microstructures, and in the mechanical properties [28]. Several studies were conducted to explore the use of different types of interlayers to join Ti alloys to other alloys. Despite the reduction in embrittlement and the residual stresses at the WZ, as the solid-solution phases formed in the structure, the risk of formation of IMCs is still present; even with optimisation of the welding parameters [107] the joint area is still considered the weakest part in the WZ and few methods have been developed to overcome this problem [115].

Different types of alloys were employed to use as filler metal prefixed in the welding joint, including vanadium, molybdenum, magnesium, tantalum, zirconium and niobium; however, while they reduce the formation of the brittle phases, they are very costly to use. A study

was conducted by Majumdar et al. [106] to join titanium alloy to Al alloy using Nb filler metal. The Nb alloy works as a barrier in the welding zone, as confirmed by Oliveira et al. [127], and also offers a good solid solution phase with titanium alloy and improves the toughness of the IMCs that form in the WZ, such as TiAl and Ti_3Al. Nevertheless, it was noted that although the joint strength is improved from 57MPa without Nb to 127MPa with Nb filler, there is a high chance of cracks forming at the Al side. As Al has high thermal conductivity, a high heat sink takes place in the joint zone that makes the solidification process very fast and leads to cracks formation. Amlan et al. [128] used Nb filler in friction welding to join Ti alloy to Al alloy. It was found that the formation of the NbTi particles suppresses the formation of the hard-brittle IMCs in the welding zone. However, adding the Nb to the joint area increases the ductility, and defects were observed surrounding the Nb particles which led to premature failure of the microstructure, while the welding joint recorded low UTS as compared with the Al base metal.

Furthermore, Zhang et al. [129] applied pure aluminium alloy as an interlayer to join titanium Ti-6Al-4V alloy to 6061 Aluminum alloy using an ultrasound welding method. The presence of the pure aluminium particles was found to improve the joining by increasing the plastic deformation during the welding process; moreover, adding fresh Al particles enhanced the ductility of the welding zone, with no brittle phases formed between the Ti and the pure Al alloy, and the maximum shear strength was 106MPa. Because ultrasound welding uses low welding energy and takes only 1.4 sec to create the bonding, no intermetallic layer will be formed as this requires high temperature and takes a long time. However, despite a joint being formed between the Ti alloy and Al alloy there was a lack of fusion and gaps at the contact area; therefore, it was necessary to increase the welding energy to create a proper dense joint, free from gaps and voids, but this also increased the chance of brittle phases forming at the welding zone.

Hongmei et al. [114] studied the potential of the cobalt (Co) alloy for use as a filler metal to join TiNi to 304 stainless steel alloy. Different thicknesses of Co were used to investigate the percentage effect of cobalt on the joint properties. Adding a 0.2mm foil of Co to the WZ enhanced the joint strength to 347MPa by increasing the ductility by 4.2%. However, whereas the cobalt alloy restrained the formation of brittle phases (IMCs) such as TiFe2 and TiCr2, other brittle phases of Co-Ti formed that decreased the joint strength as the %Co increased. A thin foil of Ni-alloy was used as well as filler metal to allow accessible joining of dissimilar titanium alloys and stainless steel alloys [130], [131]. Kundu et al. [131] studied the interfacial reaction of adding 150μm of nickel alloy to the titanium / stainless steel

welding joint. A reaction takes place at the joint, forming a layer of Ni-rich γFeTi that works as a barrier to prevent the Ti atom from moving toward the Fe atoms. The maximum ultimate tensile strength achieved was 639.9MPa at an optimal brazing temperature of 950˚C and dwelled time of 45min. However, increasing the brazing temperature above 950˚C or increasing the brazing time above 45min would dissolve the NiFe layer and increase the formation of intermetallic compounds (IMCs) of NiTi, $NiTi_2$ and Ni_3Ti, where most fractures originate. Since some of the previous alloys used as intermediate filler metals are costly, researchers began to study other alloys that were considered cheaper and more widely available, such as Cu alloy[126] and Ag[132][133]. Copper alloy is one of the most frequently used as an intermediate alloy to achieve a successful joint between titanium and dissimilar alloys. In their work, Wang et al. [126] used a 1 mm thin foil of Cu alloy to join Ti-15-3 alloy to 304 stainless steel using electron beam welding. The Cu foil creates a thin layer of Cu-Ti and Fe-Cu that is formed at the welding interface. The joint achieved a maximum tensile strength of 234MPa. However, a hard, brittle intermetallic compound (IMCs) of $TiFe_2$ formed in the weld zone, surrounded by a solid-solution of Cu and Fe, figure 2.27a, where N and P represent the solid-solution of Fe and Cu respectively, while O is the IMCs of $TiFe_2$. Less brittle IMCs such as Ti-Cu and Ti-Fe-Cu were formed along the Ti side and exhibited low hardness compared to the Ti-Fe phases. The WZ near the Ti side was divided into three areas according to the phases located in these areas. From figure 2.27b, area (I) consisted of Cu solid-solution and IMCs such as TiFe, $Fe_{0.5}Cu_{0.5}Ti$ and CuTi; area (II) consisted of IMCs such as $Fe_{0.5}Cu_{0.5}Ti$, CuTi and Cu_2Ti. Meanwhile, area (III) consisted of a copper solid-solution and CuTi. Table 2.3 summarises the various phases and IMCs in the WZ.

Despite the satisfactory joint properties, upon applying the tensile load, cleavage fracture started at the weld line near the Ti side due to the high concentration of brittle IMCs located at this area and consequent reduction in the plasticity of the joint making it much more susceptible to fracture. A successful joint by Nd: YAG laser welding was achieved between Ti-6Al-4V and steel alloy type X5CrNi18-10 using 0.6mm Cu foil as a filler metal. Mitelea et al.[111] reported that during the solidification process, the copper alloy formed solid solution phases encircling the brittle phases that formed during the fusion operation. The copper layer increased the joint's ductility while increasing the welding power to 4000W and using 3m/min welding speed was found not only to provide a joint with the maximum tensile strength of 400MPa but also a reduction in the formation of brittle intermetallic phases.

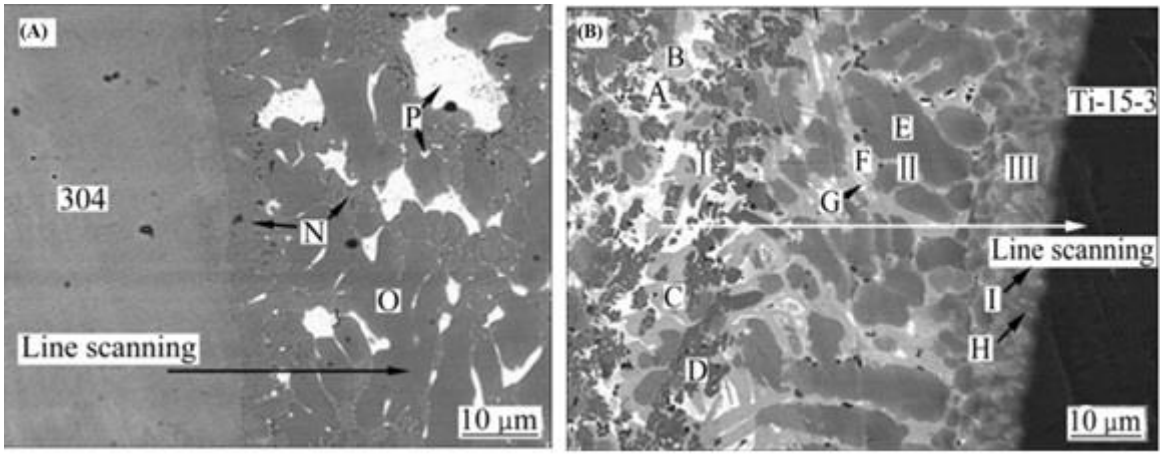

Figure 2.27 Microstructure of the WZ at the interface of (A) near the 304 Stainless Steel side and (B) near the Ti alloy side [120].

Table 2.3 Summarises the phases and IMCs distributed at the welding joint between the Ti-15-3 alloy and 304 stainless steel [120].

Weld near titanium alloy									Weld near steel		
I				II			III				
A	B	C	D	E	F	G	H	I	N	O	P
Cu(ss)	Cu_4Ti_3 or CuTi	$Fe_{0.5}Cu_{0.5}Ti$	TiFe	$Fe_{0.5}Cu_{0.5}Ti$	Cu_4Ti_3 or CuTi	Cu_2Ti	Ti(ss)+ Ti_2Cu	Cu_4Ti_3 or CuTi	Fe(ss)	$TiFe_2$	Cu(ss)

ss—Solid solution.

Furthermore, Tomashchuk et al. [110] studied the effect of welding process type on dissimilar welding joints using copper as an interlayer in the joint area. EBW and LBW were used to join Ti-6Al-4V to low alloy steel type 304L. The presence of the copper did not restrain the formation of the brittle phases, but a reduction was noticed in the amount of the IMCs formed. Due to the high-speed electron beam welding process and the rapid cooling, the joint morphology exhibited two regions: Cu-rich Ti at the titanium side and Cu-rich Fe at the 304L alloy side. Meanwhile, in the case of LBW, a turbulent mix occurred during the fusion process, and the cooling rate was a bit slower than with EBW, allowing for the atoms to be at high temperature for sufficient time for multi-phases to form in the WZ during the solidification process, with resultant formation of different brittle phases.

Another study conducted by Tomashchuk et al. [113] used pure vanadium alloy (CP-V) as a filler metal to join titanium alloy type Ti-6Al04V and alloy steel type 304L using LBW method. A Ti/V/304L joint was successfully welded, and maximum joint strength of 367MPa was recorded. Single-pass and double pass welding were carried out to study the

effect of fusion power application on the microstructure of the WZ. The single-pass joint shows a keyhole with 90% of the V foil melted down and only a small part of the V alloy staying in a solid condition, see Figure 2.28a. The WZ shows a hardness of 400HV, although 100HV was recorded at the unmelted V foil, and the achieved tensile strength was the only 130MPa due to the effect of elements such as Fe, Cr and Ti in increasing the embrittlement of the WZ. Despite the presence of V alloy at the joint area enhancing the ductility, when the iron content reached above 30% at the interface area the joint became highly sensitive to cracking. However, when a double pass of the laser beam was applied at the joint, the WZ of the Ti/304L joint exhibited three regions. The middle part was unmelted V foil, whereas there was a thin layer on the V foil side that was melted and welded to the Ti alloy. The same scenario was repeated at the 304L alloy interface side, with the melting taking place only at the interface of the TI-V foil and 304L-V foil, see Figure 2.28b. It was recommended that in order to accomplish a good joint using the pure V filler to join Ti to stainless steel alloy, the melting layer next to the 304L side should contain a lower amount of V to maintain the ductility and to force the fracture to take place at the unmelted V foil. Another study was conducted by Wang et al. [133] using EBW to join a titanium alloy to a stainless steel alloy. The focus of the work was to study the effects of using different types of filler metal, such as Ag, Cu Ni and pure vanadium, to carry out the joining process. The best result in term of joint strength was obtained with the silver alloy, which achieved a joint strength of 310MPa. Both the pure vanadium alloy and nickel alloy exhibited incomplete melting in the welding zone. The TiFe phase showed the highest hardness value of 1005HV.

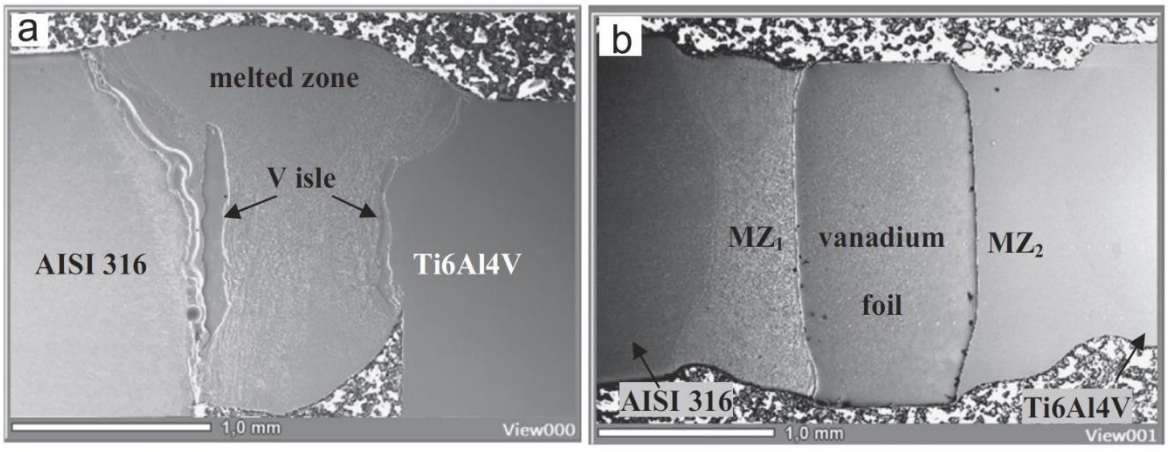

Figure 2.28 Shows the morphology of a Ti-6Al-4V / 304L stainless steel joint produced by LBW using pure vanadium alloy as a filler metal and (a) a joint made with single-pass beam and (b) a joint made with double pass laser beam[108].

Wang et al. [134] offered a different approach to using vanadium as a filler metal. Their method involved using a filler metal of V and Cu, (V-Cu), to achieve a dissimilar joining between titanium and stainless steel. The idea was to have the vanadium facing the titanium and the copper facing the stainless steel alloy, in order to restrain the formation of IMCs between the titanium and the steel. Based on the previous method, the joint achieved a strength of 288MPa when it was subjected to a tension test.

2.10 Vanadium alloys

Vanadium, V, is a BCC alloy. The most common use of vanadium is as an alloying element, added to enhance the mechanical properties of steel alloys. It was reported that ductility of steel could be improved by adding 0.01 to 0.1% of V alloy. Under a low brittle-ductile transition temperature, the V alloy shows good plasticity[135]. Vanadium alloys have become essential candidates for use in the blanket structure of the fusion reactor breeding system, figure 2.29, due to significant properties, such as high irradiation resistance, elevated corrosion resistance, while the single-phase alloy with high melting temperature offers high tensile strength under elevated working temperature and owing to its excellent ductility the alloy has the advantage of easy fabrication [136]. An extensive study on V alloy was conducted in a collaboration between the US, Japan and Russia, with the focus on developing the blanket structure using V alloy as an alternative to ceramics [137].

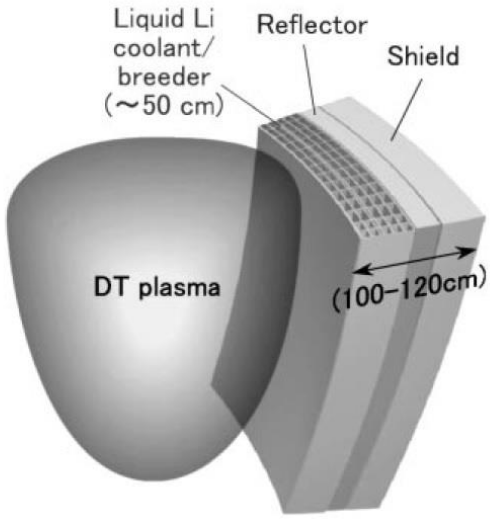

Figure 2.29Cross-section of a self-cooled blanket system using vanadium alloy type V-15Cr-4Ti [130].

2.10.1 Fusion welding of Vanadium alloys

In order to employ vanadium alloys to create the required structures, certain factors must be considered in the joining process. During the welding operation, the joint area between the two alloys is subjected to severe changes, leading to changes in the microstructures and mechanical properties of the welded parts. One of the most essential considerations in the welding of V alloys is to maintain the alloys' properties so that the ductile-brittle transition temperature stays close to the base metal value [138]. The review by Chan et al. [139] highlights the importance of keeping the level of impurities as low as possible so that the ductile-brittle transition temperature stays the same as that of the parent metal.

Chung et al. [14] conducted an investigation into the impact of the welding process on the ductile-brittle transition temperature (DBTT). EBW and LBW were used to create welds beads on the plate using a V-4Cr-4Ti. Then the weld bead samples were subjected to post-welding heat treatment to determine the metallurgical and mechanical behaviour of the weld parts and how they reacted to the heat treatment condition. The welded samples in the as weld condition showed the highest hardness value; however, when the samples were subjected to an annealing process, a reduction in the hardness resulted due to increase in the ductility of the welding zone. A reduction was recorded in the impact results for the as weld samples, while an improvement in the impact resistance value was observed in the samples that were annealed for 1hr under heating treatment of 1000˚C. The general microstructure of the WZ for both EBW and LBW was a long grain with large size. However, when the heat treatment was applied to the WZ samples, the long grains broke down into smaller sized grains, see Figure 2.30.

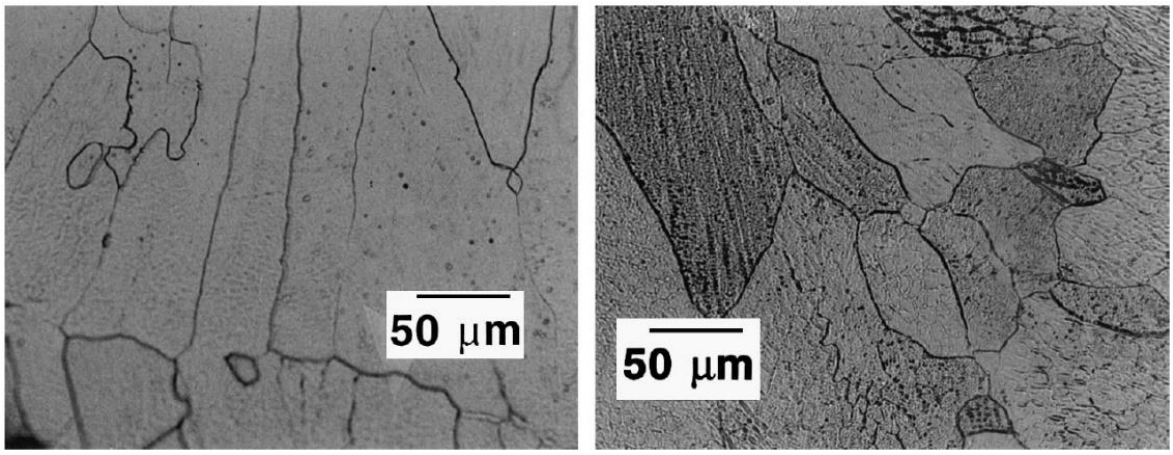

Figure 2.30Showing the FZ microstructure of V-4Cr-4V (left) in as weld condition, and (right) after annealing at 1000˚C for 1hr[134].

Heo et al.[140] reported the direct impact of welding parameters on the morphology of the WZ for the bead on plate weld tracks made by LBW. Both the parent metal of the V-4Cr-4Ti and the WZ showed similar values for the Charpy impact test, contrary to the finding of Chung et al. [14]. Despite the improvement in impact resistance of the welded samples achieved by the annealing process, the hardness value was increased due to the presence of hard-phases. An interesting work of dissimilar joining conducted by Nogami et al. [15] using the EBW method. A pure vanadium alloy and alloy steel type 304L were joint without filler metal. The study was a focus on investigating the effect of beam location and heat treatment on the microstructure and mechanical properties of the dissimilar joint. The study reveal as the beam shifted away from the welding centre line by 0.2 and 0.4 mm the reduction in the hardness value was observed due to the reduction of the σ phase in the WZ as the beam shifted away from the vanadium side. However, the heat-treated samples of the base metal of the (V-BM) and (304L-BM) showed a hardness result almost equal to the as-welded samples except for the HAZ and the WZ; the hardness value was increased twice as compared to as-welded samples. This increment in the hardness was due to the precipitates hard NiV_3 and Ni_2V_3 structures by the annealing process at 600˚C for 1hr. Also, an interlayer between the vanadium base metal and the WZ was formed, and an increase in the thickness of this layer in the range of 20-30 μm was observed. Another attempt by Nogami et al. [139] to join pure vanadium alloy to 304L alloy by EBW was carried out. The study was a follow-up of previous work [15] of dissimilar joining between pure vanadium and stainless steel. The work involved studying the effect of EBW process parameters on the joint properties and long periods of post-welding heat treatments of 1, 10, 500 and 1000hr were used in this study. During the work, the beam location was shifted away by 0.2 and 0.4mm from the welding centre line to inside the V alloy. The cross-section of the welded samples, shows four regions, V-BM, 304L–BM, WZ and the interlayer between the vanadium and the WZ. The maximum hardness was recorded for the WZ and the interlayer (HAZ) while the BM show less hardness in the case of the as-welded samples. Regardless of the beam position, the heat-treated alloys for 600˚C showed a hardness value equal twice to the hardness value of the as-welded samples. The WZ sample that annealed for 1hr at 1000˚C showed a hardness about 900 HV, while the interlayer that heat-treated at 600 ˚C for 1hr showed a hardness value of 1000 HV. The theory behind this increment in hardness was due to the presence of brittle phase such as σ-phase, V_3Ni as a result of the post-welding heat treatment.

2.11 Spark Plasma Sintering (SPS) process

2.11.1 Principles and mechanism of the SPS process

Spark Plasma Sintering (SPS) or Field Assisted Sintering Technology (FAST) is a fabrication method that provides the ability to consolidate different types of powder alloys, over a short period of time, into a fully dense material. A pulsed DC current is employed to heat the conductive powder particles by Joule heating [141]. The process involves creating an atomic diffusion in the contact surfaces of the powder particles by applying high heat temperature and pressure to promotes particle bonding. The diffusion process between the powder particles involves creating a primary contact at the surfaces of the particles. This contact zone is referred to as the "Neck"[142] as shown in figure 2.31. With the progress of the sintering process this zone – the Neck – keeps growing, and with enough time and applied force the two particles become one large particle as the centres of the two particles keep moving toward each other and unite eventually to form a metallurgical bond between the compacted particles, leading to their merging into a single particle. As densification takes place for all the powder particles and in different multi-directions, this will lead to the formation of fully dense material. During the sintering process, rearrangements of the atoms take place in order to fill the voids and pores between the powder particles; this process is driven by an atomic diffusion which promotes the densification process [143]. The heating process is usually carried out below the melting point [144] or in the range of 50% to 75% [145] of the melting temperature of the selected alloy powder. The sintering process involves three main stages: heating, holding and cooling, under vacuum/argon/nitrogen atmosphere. SPS is a rapid unique sintering process as compared with other conventional sintering methods that require long hours to achieve the desired consolidation. With the sintering temperature reaching to 2200 ˚C, the rapid heating rate reaching to 800 ˚C/min, and with the presence of compressive stress, sintering can be completed within 5 min [143].

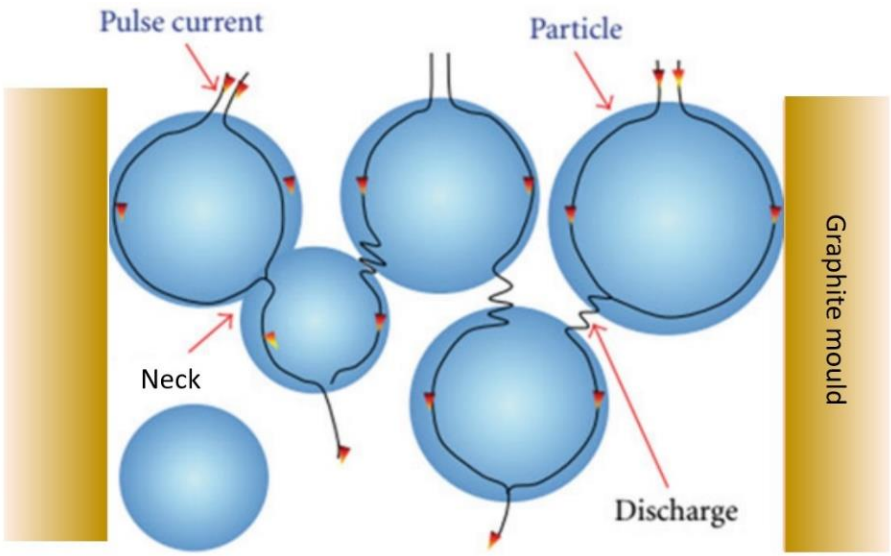

Figure 2.31 Show the atomic diffusion between the powder particles caused by the Joule effect of the DC electric discharges on the powder particles surface[142].

2.11.2 Spark Plasma Sintering of Ti-6Al-4V alloy

SPS can be considered as a well-established technology for processing 'hard-to-sinter' materials. However, in the case of Ti alloys, when it comes to powder technology, precautions are essential when handling and processing these alloys, especially for sensitive applications such as aeronautics and biomedical. It is quite challenging during the processing of Ti and Ti alloys to produce reliable parts, due to the massive effect of interstitials on the mechanical properties of the Ti alloys, i.e. ductility. Several researchers have studied the processing of Ti alloy powder by SPS method, for instance, Zadra et al. [146].

Additionally, a thorough review was presented by Orru et al. [147], showing a wide range of materials processed successfully by SPS. The SPS process shows a great potential to lower the cost of processing for titanium alloys and to save energy. A comparison study conducted by Musa et al. [148] between SPS and conventional hot pressing using Ti-Al_2O_3-TiC powder demonstrated the potential for energy saving of about 90-95% with SPS by lowering the time and temperature of the sintering process. Also, researchers studying the processing of titanium powder alloys by SPS have focused on using Ti processed by SPS for biomedical applications and the production of fully dense ultrafine-grained (UFG) titanium alloys [149]. In this regard, a closer match to bone properties was produced by Nicula et al. [150] by processing Ti powder alloys using SPS to obtain porous titanium to be used as an implant. Further researchers such as Kon et al. [151] and Zhang et al. [152] used SPS to produce porous alloys. High purity of Ti foams for biomedical applications was produced by SPS

using a 700 ˚C sintering temperature, an 8 min holding time and axial pressure of 50 Mpa. The macroporous Ti foam alloy shows a great potential to mimic the human bone structure with a plateau stress of around 27.2-94.2 MPa and Young's modulus of 6.2-36.1 GPa.

Other work included using the SPS process to produce a fully dense titanium alloy with UFG and minimal porosity. In their work, Munoz et al. [153] show that the thermal conductivity of the alloy has a significant impact on the temperature distribution inside the sintered sample during the sintering operation. The higher the thermal conductivity, the higher the distribution, resulting in highly homogeneous structures and a sufficiently dense alloy. Other research, by Garbiec et al. [154], investigated the effect of compacting pressure and heating rate on the microstructure and mechanical properties of Ti-6Al-4V sintered alloy. The study showed an increase in the hardness value when the heating rate increased from 100˚C/min to 400˚C/min. Also, as the compacting pressure increased from 5 MPa to 50 MPa, the same trend in hardness was observed, with the hardness increasing from 293 $HV_{0.05}$ to 373 $HV_{0.05}$. This increment in hardness values was related to the grain size and the presence of porosity. The high heat rate and high compacting pressure prevent the grain from growing.

As a result of the maintenance of fine grains, the diffusion between powder particles is enhanced, and the porosity is minimised. Another study, by Bolzoni et al. [155], showed that the relative density is a function of sintering temperature, and the residual porosity is reduced as the sintering temperature increases. An investigation by Robertson et al. [156] studied the effect of added elements on the relative density of titanium alloy. The conducted work was able to design a titanium alloy that would be readily sintered to near full density, using simple sintering conditions. The SPS process was used to produce a fully dense alloy of Ti-xNi-5Sn – where x is (Ni, Co, Fe and Mo) – by sintering for 2 hr at a temperature of 1100˚C. The addition of some elements helped to advance the sintered density; however, a reduction in the density was observed in the case of Mo additions. A comparison study between one step sintering method and a proposed three steps sintering approach was conducted by Chaudhari et al. [157] to produce a fully dense alloy using commercially pure titanium powder alloy. The single-step sintering involved heating the compacted Ti powder at a sintering temperature of 1300 ˚C using a heating rate of 100 ˚C/min for 10 min holding time and 6 Pa applied force over the sintering mould.

Meanwhile, the three steps sintering approach involves heating the sample to 600˚C at a rate of 100 ˚C/min of continuous heating but with a rate of 25 ˚C/min until reaching the 1100 ˚C temperature, when the sample is subjected to a holding time of 5 min. Then second heating

step proceeds from 1100 ˚C to 1200 ˚C, with the same heating rate of 25 ˚C/min and a 5 min holding time applied again. In the third step, the heating is continued from 1200˚C to 1300 ˚C, and a holding time of 10 min is applied. Once the holding time is finished the samples are subjected to a cooling stage which is conducted inside a vacuumed chamber. The microstructure and mechanical examinations showed that the three steps produced better results than the single-step sintering method, offering a 100% densification. The microstructure varied from a Widmanstätten structure at the periphery of the sample where the cooling rate is rapid, to a flattened bar shape of α colonies toward the centre of the sample. The three-step sintered samples showed a high hardness value of 326 HV, while the single-step sintered sample recorded only 306 HV. The lower hardness of the single-step sintered samples was due to the presence of the ductile phase of βTi in the structure, while no residual βTi formed in the case of samples obtained by the three-step sintering approach.

In general, all the previous studies emphasise the challenges of attaining a full density when sintering titanium alloys below 1000 ˚C as this requires a high compacting pressure and prolonged period of holding time, which may cause undesirable grain growth [158]; therefore, high sintering temperature, high heating rate and uniaxial press are favourable conditions for accelerating the diffusion process between powder particles and reducing the porosity in the sintered bodies.

2.12 The design of experiments (DoE) and keyhole modelling

Design of experiments is an efficient method to obtain sufficient data using a minimum number of experiments. Different methods employed in DoE to design the experimental runs include factorial design, Taguchi design, and response surface methodology (RSM) [159]. The geometry of the welding zone is a function of several variables, such as the type of welding process, the welding process parameters, the physical properties of the alloy and the joint boundary conditions. During the welding process, each of these variables impacts differently on the formation of the keyhole gap when they interact with each other. A trial and error approach using beads on plate method and the skill of the engineer or the machine operator are usually used to set acceptable welding parameters and, based on the outcome of the trials, a determination is made as to whether or not they meet the joint requirements. However, conducting these trials is costly and time-consuming. Therefore, the design of experiments has been adapted by several researchers using different optimisation methods

to reduce the complexity of the input data. By employing physical and mathematical laws, a set of criteria was developed to identify the qualitative inputs using simple measurements.
A genetic algorithm, GA, was used by Dey et al. [160] to determine appropriate electron beam welding parameters to generate a keyhole gap in 12 mm aluminium plate with optimal geometry. In order to find a relationship between the inputs-outputs of the welding process, a regression analysis was carried out. They were able to formulise a problem to produce a full penetration weld bead with a minimum welding zone. An attempt was made by Anawa et al. [161] to use the design of experiments to predict an optimal combination of LBW parameters that would provide the highest joint strength of Ti-Al dissimilar welding. DoE using Taguchi approach was adopted to minimise the welding inputs parameters needed to provide an acceptable welding profile, and ANOVA analysis was carried out to identify the most significant variables that directly affect the tensile strength of the dissimilar welded part. Based on ANOVA outcome results using the tensile test as a response for the welding inputs, welding power and the beam focus position were both shown to have a significant effect on the value of the joint strength. Taguchi method was also employed by Bayazid et al. [162] to predict the effect of FSW parameters on the mechanical properties of dissimilar welds between aluminium alloy types 6063 and 7075. They predicted that with welding parameters of rotation speed and travel speed of 1500rpm and 120 mm/min, respectively, maximum tensile strength of 143.59 MPa could be obtained which would be close to the predicted value of 154 MPa.The responses surface methodology (RSM) was used by Liao et al. [163] to design a statistical model to analyse the influence of GMA welding parameters and welding position on welding zone geometry. The established model was able to predict mathematically the weld bead dimensions based on optimal welding parameters proposed by RSM. A non-linear regression method known as the central composite design was employed by Gunaraj et al. [164] to develop a mathematical model, using five levels four factors, to estimate the geometry of the welding bead upon using submerged arc welding. Using RSM technique, they were able to forecast the weld bead width, penetration, reinforcement and even welding dilution, depending on the suggested inputs of welding variables.

In 1946, a modelling approach developed by Rosenthal suggested that the distributed temperature around a moving heat source, in the quasi-stationary state, in the x-axis direction, can be calculated, assuming the heat source is of constant strength and speed and with the absence of convective and radiative heat flow. With knowing the physical properties of the selected materials, the suggested three-dimension equation by Rosenthal for the moving heat source is:

$$T - T_0 = \frac{Aq}{2\pi\lambda R} exp\left(\frac{-v(x+R)}{2\alpha}\right) \quad \ldots\ldots\ldots\ldots\ldots\ldots (2.1)$$

Where T_0 is the initial temperature, and T is the (treatment temperature for such as hardening, surface melting and keyhole welding); while q and v are the amounts of the heat input and the travel rate, respectively, which are constant values as assumed by Rosenthal. λ, is the thermal conductivity, W/m.K, α is the thermal diffusivity m^2/s, and R represents the treatment volume which is $\sqrt{(x^2 + xy^2 + z^2)}$.

A normalising approach was designed by Ion et al. [165] to quantify the depth of the treatment. Based on previous literature works, a mathematical model was established to predict a set of dimensionless parameters for the CO_2 laser process. The obtained theoretical results, then, were introduced as a graphical diagram to show the effect of both the dimensionless beam power and the dimensionless traverse speed on the bead geometry. A successful validation was achieved, showing the experimental bead depth was close to the predicted theoretical depth, and, also, the method was successfully extended to quantify different treatment depths such as hardening, surface melting, and keyhole welding. The Ion et al. [165] model was built to provide an accurate working condition to minimise the trial and error runs of the laser beam welding method and employ the outcome of this process for different types of materials. When a high heat is introduced to the surface of the metal, the melting process is controlled and affected by: the heat input (*q*), the melting traverse rate (*v*), the size of the melting spot (*rb*); also, the physical properties of the selected alloy, such as the surface absorptivity (*A*), thermal conductivity (λ) W/m.K, and thermal diffusivity (α) m^2/s, have a major effect on the melting process. Equation (1) and (2) show two dimensionless equations suggested by Ion et al. [26]for the laser process:

$q^* = Aq / [rb\,\lambda\,(Tm - T0)]$ (dimensionless beam power)..... (2.2)

$v^* = vr_b/\alpha$ (dimensionless beam traverse rate)..... (2.3)

Where T_m and T_0 represent the melting and initial temperatures, respectively, q^* is the dimensionless beam power, and v^* is the traverse rate of the beam. (A) is the surface absorptivity which has a value in the range of (0.3 for surface melting or 0.8 for keyhole welding). The Ion et al. [165] model was extended to cover three laser processes, namely surface hardening, surface melting and keyhole welding. Regarding the keyhole welding, when the surface alloy reaches high melting temperature, the vaporising level, by combining with the surface absorptivity, a deep vapour cavity is formed in the alloy. Therefore, under a steady heat source, the heat observed in the alloy maintains the formation of the keyhole. Assuming the melted area is cylindrical in shape with a length of the treatment l, which represents the depth of the keyhole and bead width of rb, the typical aspect ratio (depth/width) being about 4 for molten bead, the depth of the welding bead can be predicted and calculated. Therefore, the required heat, q^*, to keep the balance of the absorbed heat and the heat required to maintain melting and vaporising of the metal in the keyhole cavity can be translated into a dimensionless equation as:

$$q^* = l^* v^* L_v^* + \frac{l^{*2} v^* L_m^*}{4} + \frac{2\pi l^*}{\ln(8)} \quad \text{.....(2.4)}$$

Where l^* is the normalised depth of the welding bead, L_v^* and L_m^*, represent latent volumetric heats of vaporisation and melting for metals and alloys.

A design was developed by Thomas et al. [166] as an extension to the approach of Ion et al. [165]to predict the bead depth of a melting process carried out by powder bead additive layer melting system ALM, offering the chance to predict and down-select melting process parameters for different type of alloys. Based on several studies to investigate the effect of heat source type, melting travel speed, and the physical properties of the selected alloy on the melting process of laser beam methods [8]–[10]and electron beam methods [11], [13], Thomas et al. [166] were able to build a useful platform to predict the required power and speed rate to melt an alloy by different melting methods.

The primary data used in the modelling were selected from previous work carried out by Al-bermani [167]. The work involved studying the effect of speed function in EBM on the depth of the melted layer. During the work, two beam speeds, 4mm/s and 188mm/s, were used with 30mA to compare the effect of beam speed on the microstructure of the melted zone. The used parameters showed a macro-scale structure with a low-speed rate of 4mm/sec while using the faster travel rate provided a micro-scale structure in the melted zone. The experiment was conducted using a 10mm Ti-6Al-4V plate, and when the low travel rate, 4mm/s, was used with 30mA, this parameters combination was sufficient to generate a keyhole with full penetration. In this work, the efforts are directed toward employing the Thomas et al. [166] model to design processing parameters for an electron beam melting system, to establish a keyhole weld gap in 6 mm Ti-6Al-4V alloys, following previous attempts in the keyhole regime for 10 mm thick plates by Al-bermani.

2.13 Literature Review Conclusions

This literature review covers some of the vast amounts of processing research conducted on Ti-6Al-4V alloy. Due to its excellent combination of properties such as high specific strength, low density and superior corrosion resistance, Ti-6Al-4V alloy has been considered as one of the preferred engineering alloys and a favourable candidate in many application fields such as aerospace, biomedical and petrochemical industries. Titanium alloys have been replacing different types of metallic alloys, and such as aluminium and steel alloys are commonly used in aerospace industries. However, titanium alloys are considered expensive materials due to the complexity of their production and the machining required. The joining technology became an interesting method in titanium structures fabrications as an effective technique to achieve cost reductions and a method for enhancing the production output. Despite the welding and joining technologies providing a successful method to replace traditional manufacturing technologies such as forming and machining, the fabricated parts produced by welding must provide mechanical properties that meet the standard requirements. Different welding methods were considered for titanium alloys, and the successful outcome from a welding method was based on the capability to deliver high-quality titanium weldments in various setups. The welding technology provides flexibility to fabricate a complex structure combined of different alloys. However, there is great concern in terms of dealing with dissimilar welding of titanium alloys with other metallic alloys. Two major challenges are commonly raised over the dissimilar welding of Ti alloy

to different materials: the formation of brittle intermetallic compounds (IMCs) in the welding zone and the cracks and presence of residual stress which result from the differences in the physical properties of the welded alloys. As a solution, an interlayer of a ductile alloy is prefixed in the joint gap, so that upon welding the formation of solid-state phases will retain the formation of the brittle phases and improve the WZ ductility.

However, much more understanding is still required about developing new methods to improve the dissimilar welding of titanium alloys to other metallic materials and provide high-quality weldments in terms of their mechanical properties. The efforts in this work were directed to studying the ability of dissimilar metal welding of Ti-6Al-4V alloy to produce commercially pure vanadium alloy through employing DoE and powder technology means, i.e. spark plasma sintering, to design an alloy to be used as an interlayer in the welding gap as an approach to control and engineer the chemical composition, the microstructure and consequently the mechanical properties of the welding zone and using the electron beam melting machine process to carry out the welding.

CHAPTER 3: METHODOLOGY

3.1 Introduction

This chapter will cover all the experimental works and procedures used in this project. All the techniques will be explained in detail, including a selection of materials, mixing process, spark plasma sintering, electron beam welding methods, sample preparation and characterisations and testing methods.

3.2 Materials and Alloy Design

3.2.1 Materials selection

In this work, two powder alloys were selected to design the filler alloys. The first one is a Ti-6Al-4V pre-alloyed powder from LPW Technology, prepared by gas atomization process, a high-quality powder production process used for highly reactive alloys such as Titanium[168]. The grade 5 Titanium powder type Ti-6Al-4V has spherical particles sized approximately between 44 μm and 106 μm. The second powder is a pure vanadium powder alloy, produced by TLS Technik GmbH & Co., having an average spherical particle size about 24 μm to 45 μm and physical and mechanical properties of the selected alloys can be seen in table 3.2.

Table 3.1 The chemical composition of the selected alloys (wt.%).

Elements	Ti	Al	Fe	C	V	N	O
Ti6Al-4V (powder)	Balance	6.88	0.18	0.007	4.27	0.026	0.329
Ti6Al-4V (plate)	Balance	6.29	0.19	0.012	4.04	-	0.214
Vanadium (V) powder	-	-	-	-	99.99	-	-
Vanadium (V) plate	<0.001	0.0065	0.0019	0.02	99.9	0.0085	0.025

Table 3.2 Shows the physical and mechanical properties of the selected alloys,Ti and V [11], [21], [138].

Alloy	Melting point/ ˚C	Thermal conductivity (W/mK)	Thermal expansion (µm/mK)	Tensile strength, min, MPa	Hardness (HV)
Ti6Al-4V	1649	6.7	9	900-1200	300-400
Vanadium (V)	1910	35	8.3	800	170

3.2.2 Powder alloys mixing stage

The selected powder alloys were mixed in a specific volume percentage. Following Hofmann's work [169], four mixed powders were prepared, Table 3.3. The mixing rule equation 3.1 was applied to mix the two powders to the exact percentage. The mixing was performed by adding 20% of vanadium powder to Ti-6Al-4V powder. For the second mixture, the V wt.% was increased to 40 and mixed with 60 wt.% of Ti. The third mixture comprised 60 wt.% of vanadium powder mixed with 40 wt.% of Ti powder. The fourth and final mixture comprised 80 wt.% of V with 20 wt.% of Ti powder alloy. Blending was carried out using the ball milling process. This involved putting the mixed powder in a plastic cylinder container containing hard ceramic balls as a milling media and milling the powder at a low rotation speed of 200 rpm for 24 hours. This ball milling method is a Dry Milling technique, with the mixing process based on the principle that as the container rotates, the powder is crushed by the impact of the balls as they tumble from the top of the pile to the bottom, generating impacts along with the rotation. Figure 3.1 shows a mixed powder of Ti-6Al-4V with 20% of pure vanadium subjected to a mixing period of 24 hrs. The milling process has a significant effect on the refinement of the grains and helping to obtain a uniform mix [168], [170], [171].

$$\rho th = Vf\ Ti\ (Ti\rho) + Vf\ V\ (V\rho) \ldots\ldots\ldots\ldots\ldots\ldots\ldots\ldots (3.1)$$

Where: ρ = The density g/cc

V_f = The volume fraction

ρth = Theoretical density.

Table 3.3 Represents the selected mixed percentages of Ti-6Al-4V powder and CP-V powder.

Sample type	Ti-6Al-4V powder wt.%	CP-V powder wt.%
Ti/V1 (80/20)	80	20
Ti/V2 (60/40)	60	40
Ti/V3 (40/60)	40	60
Ti/V4 (20/80)	20	80

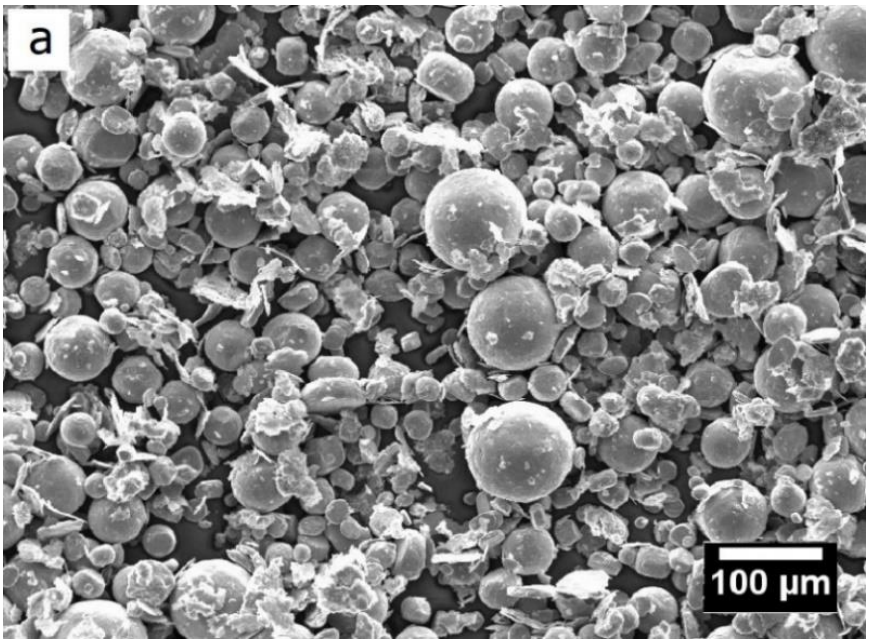

Figure 3.1 Show a mixed powder for the sample type TiV(80/20) mixed for 24hr. The large spherical shapes are the titanium powder while the crushed particles are the vanadium powder.

3.2.3 Spark Plasma Sintering

Spark plasma sintering method was used to consolidate the mixed powders. An FCT Systeme GmbH SPS furnace type HP D25, Figure 3.2, was used to carry out the sintering process. This process involved two stages: preparing the sintering mould and then performing the sintering.

Figure 3.2 The FCT Systeme GmbH Spark Plasma Sintering furnace type HP D25 at the University of Sheffield.

The first stage involves calculating the required amount of powders to achieve the desired thickness for the sintered part. In order to achieve a full dense sintered sample with a thickness of 5 mm the Eq: 3.2 was used to calculate the required mass, (*m)*, where (*ρ)* represents the density of the mixed powder which was calculated from Eq: 3.1 and (*V*) represents the volume of the sintered sample. Eq: 3.3 was used to calculate the required volume, where (*t)* is the required thickness of the sintered sample multiplied by (π) and by the radius squared (r) of the mould.

$$m = \rho V \ldots\ldots\ldots\ldots\ldots\ldots\ldots\ldots\ldots\ldots\ldots\ldots\ldots\ldots\ldots\ldots (3.2)$$

$$V = t * \pi r^2 \ldots\ldots\ldots\ldots\ldots\ldots\ldots\ldots\ldots\ldots\ldots\ldots\ldots\ldots\ldots\ldots (3.3)$$

Where:

m = the mass of the mixed powder in g

ρ= the density of the mixed powder g/cc

V= volume of the graphite mould in mm^3

t = the thickness in mm of the sintered sample

r = radius of the graphite mould in mm

Once the powder amounts had been calculated, a Ø60 mm graphite mould was selected for the sintering process. This mould is made entirely of graphite and consists of a graphite ring with an inner diameter of Ø60 mm and two graphite pistons of Ø60 mm diameter. Before adding the powder to the mould, a thin layer of graphite foil was placed inside the graphite ring. Two graphite disks were cut to Ø60 mm diameter to cover the graphite pistons. Once the thin foil was in place in the graphite ring, one of the pistons or the graphite adapter was inserted into the graphite ring, and graphite foil cut down to disk size was placed over the inserted piston. These graphite foils would prevent the powder from adhering to the mould and also make it easier to remove the sintered sample from the mould. After this, the calculated weight of mixed powder was added to the mould, then a thin layer of graphite foil cut to the shape of the disk was placed over the powder. The second graphite piston or adapter was inserted from the top to close the mould. The assembled mould, shown in Figure 3.3 [172], was then transferred to a manual hydraulic press and a load of 5770 kgf was applied to ensure no powder would leak from the mould. Next, two graphite supports were added to the assembled mould, one on the top of the mould and the second at the bottom,

and then the whole mould was placed between two hydraulic rams and a 5kN load was applied to the mould ready for the next stage of the sintering process.

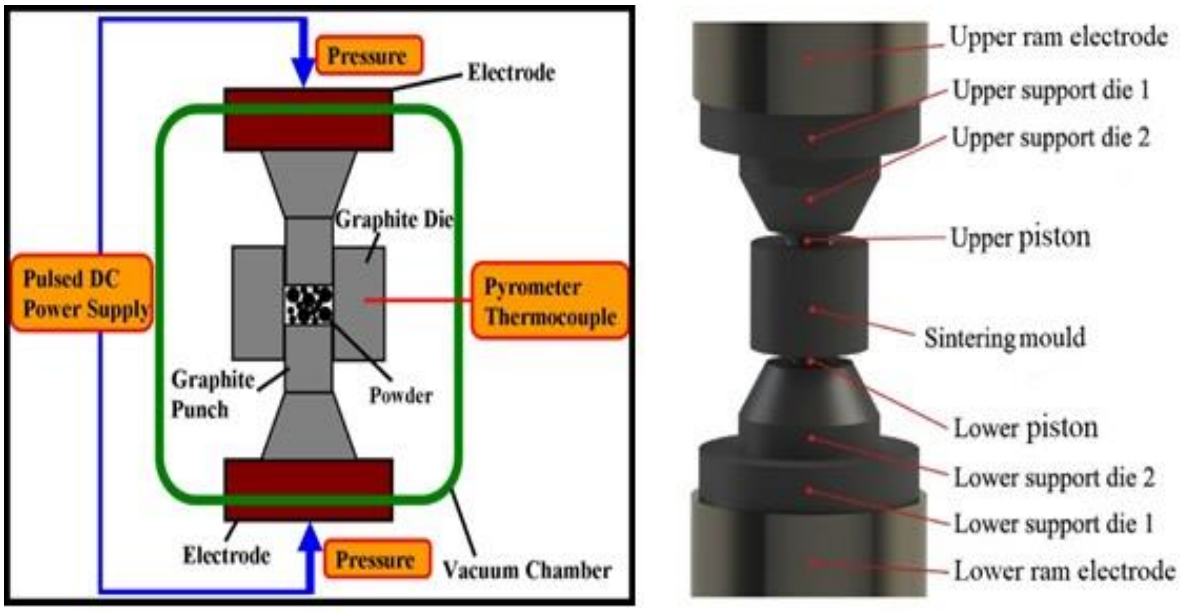

Figure 3.3 Show the schematic of the SPS method (right) and the cross-section schematic on the (left) [142].

The second stage involves setting the sintering parameters. Variables including heating rate, dwell temperature, dwell pressure, dwell time and cooling rate need to be set to the exact value to ensure the sintering process proceeds correctly, as each variable has a direct impact on the final product. The SPS furnace is equipped with software that is used to program the sintering recipe, which represents the sintering thermal cycle. Figure 3.4 shows a schematic of the sintering thermal cycle used in this project. The sintering cycle starts with removing the air from the chamber, as the sintering in this project needed to be done under vacuumed condition. Then the heat was applied and increased gradually at a rate of 100˚C/ min [157], [173] while the assembled mould was subjected to a load of 5kN. Until the temperature reached 600˚C, the load was maintained at 5kN, but once the temperature increased past 600˚C, the applied load was also increased, to reach 44kN when the temperature reached 900˚C. As the temperature kept rising towards its final value of 1200˚C, the load also continued to rise to the maximum value of 99kN. At this point, the heating stage was concluded and was followed by the dwelling stage. In the dwelling stage, both the heating and the applied load remained fixed at 1200˚C and 99kN, respectively. In this project, some sintering variables were kept constant, such as heating rate (100˚C/min)[154], dwell

temperature (1200˚C) [149], [158], [173]–[175] and dwell load (99kN); however, the following four different dwell times (holding time) were selected: 5min, 10min, 15min and 20min, to study the effect of dwell time on the microstructure and mechanical properties of the sintered samples. Once the dwelling stage was completed, the cooling stage was initiated. The load applied to the assembled mould was kept at 99kN for the first 5 min of the cooldown and then was decreased gradually to 5kN. When the sintered sample reached the room temperature, the applied load was removed, and the chamber vented with air. Then the sintered samples were removed from the graphite mould and cleaned using grit blasting process to remove any graphite attached to the sample. Next, the sintered sample would be subjected to standard micrographic preparation procedures which involve sectioning, mounting, grinding, polishing and etching.

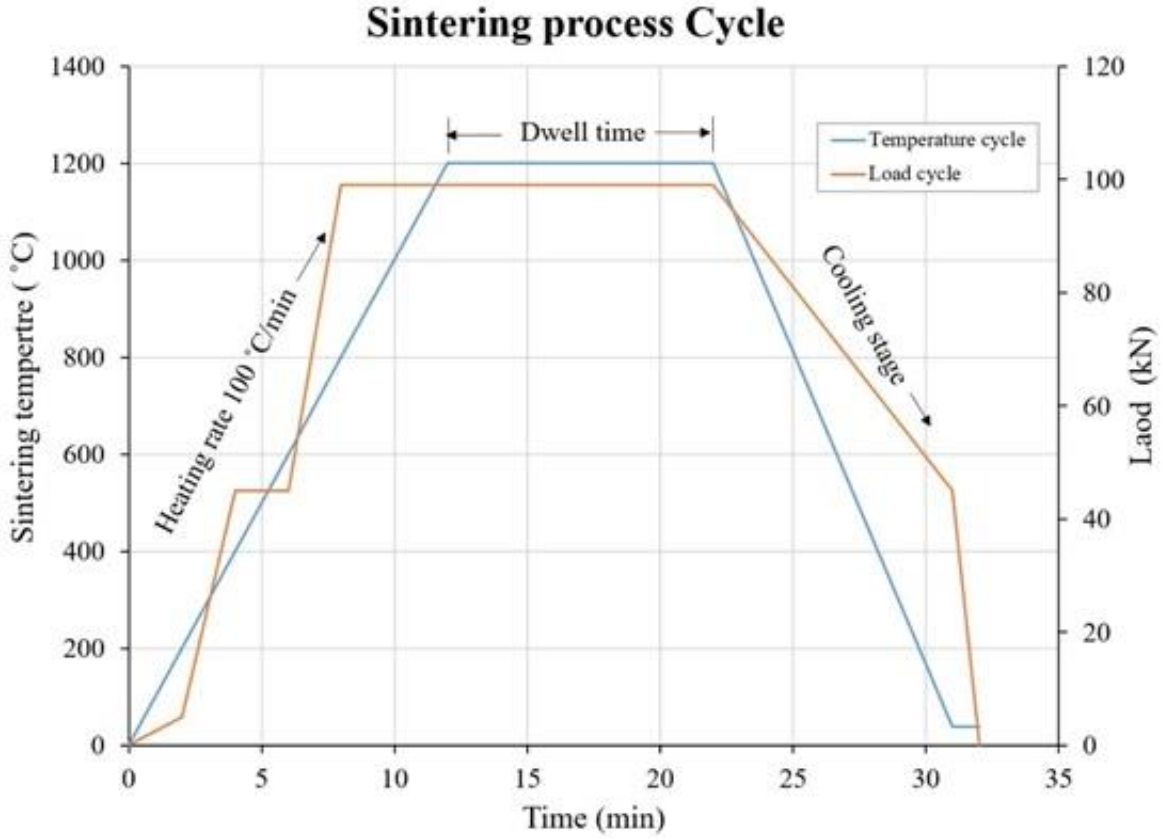

Figure 3.4 Schematic of the Spark Plasma Sintering SPS process cycle, which illustrates the three stages of the process: the heating stage, dwell(holding) stage and cooling stage. It also shows the applied load cycle during the sintering process

3.2.4 Electron Beam Melting (EBM) Process

An Electron Beam Melting machine type Arcam S12 was used to carry out the welding processes. The melting process is based on the principle of converting kinetic energy into thermal energy. An electron beam is generated by heating a thin filament of tungsten with a low current (mA). This beam is rectified and accelerated under vacuumed condition by magnetic lenses which enable the beam to be directed easily at a specific spot. As the beam accelerates, it reaches a speed of about 0.1 to 0.4 of the speed of light [176]. So, when this beam of high-intensity energy is focused on the localised spot, the metal will start to meltdown and even vaporise, forming a deep cavity in the shape of a keyhole in the metal.

The Arcam S12 is a 3D printing machine that uses a high-intensity electron beam to build a three-dimensional model layer by layer. A 0.1 mm amount of powder alloy is spread over a horizontal surface, so when the high-intensity beam hits the powder particles, they will meltdown and the powder particles will weld with other particles. Then another layer of powder alloy is spread over the surface, and the same process takes place of the beam hitting the powder and the thin layer melting and welding with the previous layer. This process is repeated until the building is finished. Regarding the molting pool, the electron beam hits the surface in a certain way according to the specific design, or Theme, set up previously by the Auto CAD software. The welding process using the Arcam S12 machine involved two stages. Firstly, the dimensions of the assembled weld joint were measured. All the dimensions of the assembled weld joint and the fixtures used to hold the joint were measured and recorded. Then the assembled weld joint with fixtures was placed inside the machine work chamber. It was necessary also to measure the position of the assembled weld joint inside the chamber. Then, a levelling procedure was carried out to ensure all the surfaces of the joint were in zero horizontal position. Secondly, once the necessary measurements had been recorded, all the data were transferred to the CAD program to build the Theme of the welding line. On completion of the Theme, the new data from the CAD program were downloaded into the Arcam S12 computer. At this stage, the machine was ready to perform the welding operations, but first, a manual adjustment had to be carried out by using a low energy beam to position the step-in and step-out of the welding beam in the exact weld line. This involves running a low energy beam to ensure it runs over the weld line. Once this confirmation is achieved, the welding operation is carried out by applying a full weld energy beam to the assembled weld joint. At a specific beam current and a specific travel speed,

melting takes place to create a keyhole gap in the molten metal at the weld joint. As the beam travels forward, solidification takes over to perform welding of the joint.

Figure 3.5 Photograph of the Arcam S12 EBM machine; the left side contains the work chamber while the right side contains the machine control unit

3.3 Sample preparation

3.3.1 Sectioning

Both the sintered samples and the weld samples were sectioned using a precision sectioning machine in order to reveal the required surface for study purposes. The sectioning was carried out using a Struers Secotom-50 instrument and non-ferrous cutting blades from Buehler. The sectioning conditions were cutting speed of under 3000rpm and feeding rate of 40mm/sec. Then a conductive Bakelite resin was used to mount the sectioned samples to prepare them for the next stage, grinding and polishing.

3.3.2 Grinding and Polishing

In order to prepare the samples for the microstructure examination, a standard metallographic preparation was used for the sintered samples, weld-bead samples and titanium/ vanadium welds samples. Table 3.4 illustrates the different stages of the grinding and polishing process. All the grinding and polishing was carried out using a Struers Tegrmin-20 instrument. The grinding stage consisted of three grinding levels. Firstly, for 3 minutes, a Struers MD-Piano 500 diamond abrasive disc was used to produce a planar surface. Secondly, a Struers MD-Piano 1200 diamond abrasive was used to grind the samples for 5 minutes to achieve a high fine-grained surface. Then, this was followed by ten minutes polishing using a Struers MD-Largo disc for initial polishing with 9μm water-based diamond suspension as a lubricant during the polishing step. The final step involved chemical polishing using a Struers MD-Chem polishing mat with a polishing solution consisting of a mixture of 90% Colloidal Silica (silicon) and 10% distillate water (H_2O).

3.3.3 Etching

Next, the polished samples need to be etched. According to the previous literature [149], the most widely used solution for etching titanium is Kroll's reagent. However, most of the current study samples contained low to high amounts of vanadium alloy, and Kroll's reagent is unable to reveal particular phases or features of CP vanadium alloys. Therefore an etching solution was prepared according to Nogami et al.[16], consisting of 12.5 ml HNO_3, 2.5 ml HF, 25ml H_2O, and using an etching period of 3 minutes. Vanadium alloy was etched by 3ml HNO_3, 2ml HCl, and 35ml H_2O at a heating temperature of 60˚C at least and 5 min minimum etching time with contentious agitation.

3.4 Characterisation techniques

3.4.1 X-ray diffraction (XRD)

X-ray diffraction analysis was carried out using a Bruker D2 Phaser XRD instrument. The phases were examined in both the sintered samples and weld samples. The scanning was carried out using a scanning angle of (2Theta) with a scanning range of 30-80° and 2 sec scanning time. Then, the ICDD+ database and Diffrac. EVA V3.1 software was used to analyse the peaks from the XRD instrument.

3.4.2 Relative density analysis

Density testing was carried out using the Micromerities AccuPycII 1340 Gas Pycnometer. The procedure involves preparing small-sized test samples cut from the sintered samples, with a maximum size of 2 mm^3, and then loading these into the instrument chamber. The second step is to set the analysis conditions, using helium as the analysis gas. The helium purges the chamber at a pressure of 19.5psi and the test for each sample is run ten times to increase the measuring accuracy. Once the test cycles have finished, the instrument will determine the sample density.

3.5 Microscopy examinations

3.5.1 Optical light microscopy (OLM)

The micro examination was performed using cross-polarised light (PL) technique. A Nikon Microscope type Eclipse LV150 was equipped with a camera, and Buehler Omni Met 9.5 Enterprise edition computer software from Buehler Company. This method allows for the light waves to hit the sample surface at different degrees and reflections, allowing the grain boundaries to be easily distinguished. Also, in the case of the keyhole weld samples, mosaic imaging was carried out using Olympus Microscopy to obtain full-scale images.

3.5.2 Scanning electron microscopy (SEM/EDS) analysis

Scanning electron microscopy was carried out using FEI inspect F equipment. High-resolution imaging was performed under the working distance of ~ 10mm using accelerating voltage of 20kV, according to the image clarity and a beam spot size of 3µm. Both secondary electrons mode (SE) and backscattered electrons mode (BSE) were used to examine the microstructure features. A qualitative and quantitative X-ray micro-analytical technique was

carried out using a Philips XL30s system employed using Energy Dispersive X-ray spectrometry (EDS) mode. The method provides information on the chemical composition of a sample for elements with atomic number (Z) >3. The quantitative EDX microanalysis in SEM calculates the mass fractions or wt. % of the elements present in the sample. Regarding the sample preparation for qualitative analysis, no special preparation is required other than that for SEM imaging; however, for the quantitative analysis, the sample must be in bulk, flat and polished form. The calculated data is then translated into a spectrum, showing the X-ray intensity, which represents the concentration of the elements in the sample versus the X-ray energies, which represent the elements that make up the sample. The elements identified by a standardless quantitative analysis are the spectra obtained from a sample compared with a dataset stored in the EDX system software and calculated previously from different tests.

Alternatively, a fully standardised quantitative analysis, which offers more accurate data, is used by collecting the spectra of the alloy standards on the same instrument for comparison with the spectra of the sample being analysed. In this work, a cobalt alloy is used as a standard reference material to perform the quantitative analysis. The collected spectra of the sample are then compared with cobalt spectra to identify the concentrations in wt. % of the major and the minor elements that make up the sample. Also, in standardless EDS analysis, a ZAF correction method is used for quantifying the sample's elements by converting the Characterisation X-ray into wt % [177]. The use of ZAF correction is highly dependent on the sample geometrically and usually applied in cases of irregular objects as the incident electron angle and take-off angle change from one spot to another [178]. The acronym 'ZAF' describes a procedure for corrections of atomic number effects (Z) which involves using the sum of the two corrections: (1) the backscattered correction and (2) the stopping power. A sample with a high atomic number will generate high backscattered electrons, and these electrons cannot generate X-rays; therefore, a difference in the intensity of the measured X-rays will occur, deviating from the standard value and needing to be corrected. The stopping power represents the loss of energy per unit mass upon electrons penetrating the samples. (A) is the absorption correction which is governed by the equation ($z^* \operatorname{cosec}\psi$), where z is the depth in the sample from which the X-ray is generated, and ψ is the takeoff angle of the detector. (F) is the fluorescence X-rays, which are usually generated as second generation X-rays when the Characteristic X-rays produced from an element have an energy greater than the critical ionisation energy [179].

However, the EDS quantitative analysis has certain limitations including the following:

1. Light elements with Z less than 11, such as (H, He), are difficult to analyse by EDS as they do not have Characteristic X-rays, and their Z is 1 and 2, respectively. The X-ray energy obtained from Li is too low to be detected by EDS as the Z=3. Meanwhile, although the X-rays of elements with Z ranging from 4 to 10 can be detected, they require spatial consideration. The samples and the standards must be closely matched for best results, due to low energy X-rays being highly observed in the samples; also, the shapes and positions of the peaks may change in different compounds as the generated Characteristic X-rays produce valence electrons involved in the chemical bonding of the element.
2. For non-conductive material samples, carbon coating is commonly used for SEM imaging; however, if EDS analysis is required, a different coating material must be used, especially if analysing for carbon.
3. In the case of minerals with oxygen content, it is more accurate to measure the % of the cations and oxygen by stoichiometry than to analyse for oxygen, and this information is not available from EDS analysis.
4. Therefore, a complete analysis of some samples cannot be derived by EDS analysis, especially if they contain structurally bound water or carbonate.

3.6 Mechanical Testing

3.6.1 Microhardness tests

Hardness testing was carried out using a Struers Durascan 70 automated system. The hardness test was performed using a Vickers indentation method. A 1kg load was applied as an indentation load for a dwell time of 20 sec. The hardness value is the resistance of the metal to the indenter when applied under a specified load. As the force is removed from the indenter, a square based pyramidal shape is formed on the sample surface. The Hardness value, which is kgf/mm^2 or HV1, is obtained from equation 3.4:

$$HV = \frac{1.854F}{d^2} \quad \text{..... 3.4}$$

Where (F) in kgf represents the applied force in kilograms and (d) is the average diagonal length of the indent in mm. A set of 20 indentations were applied to obtain accurate hardness values and to prevent individual indentations from interfering with each other; they were separated by a distance of >2.5d [180].

3.6.2 Tensile Tests

Tensile testing was performed at room temperature using a Tinius Olsen testing machine. To study the yield and fracture strength, sub-sized tensile test specimens, see figure 3.6, was prepared according to E8/E8M-13a ASTM standard. Three tensile samples were extracted from each sintered disk sample by the electrical discharge machining, which took place in Electrotech EDM services Ltd. The tests were performed under a crosshead speed of 1mm/min. From the disks, the tensile specimens were machined by electrical discharge machining in dimensions for flat specimens with 12.5 gauge length and 3.2mm in thickness, and a crosshead speed of 0.5mm/min for the sintered samples and 1mm/min for the welded specimens[181].

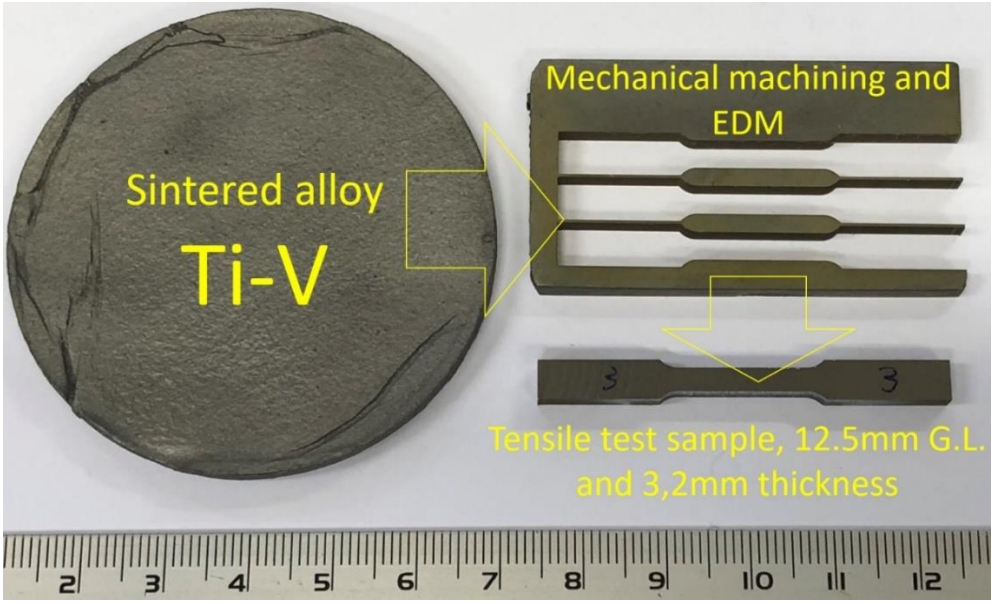

Figure 3.6 showing the sub-sized tensile test specimens obtained from the sintered samples were prepared according to E8/E8M-13a ASTM standard

CHAPTER 4: Microstructure and mechanical properties of Ti-V alloys produced by Spark Plasma Sintering

Abstract

This chapter emphasises the procedure used to design a new alloy using powder technology means. In this work, two powder were selected, tested, mixed in specific percentages, then consolidate using the Spark Plasma Sintering method.

4.1 Introduction

It was reported that titanium composite structures are becoming favourable in aircraft industries, especially in landing gears [182]. Titanium alloys offer a wide combination of strength, density and high thermal corrosion resistance [183] with an improvement in ductility[184]. Spark Plasma Sintering (SPS) was adopted in this work. The thermal sintering cycle, provided by the SPS method, which involves, heating, holding and cooling, can sinter different types of powder alloys in a short matter of time. The main advantage of the SPS process is avoiding grain coarsening during the densification process [93]. Schmidt et al. [185] investigate the properties of fabricating of Ti-6Al-4V/15SiC using SPS. The fabricated structure showed a homogeneous structure, and the sintering process was successful in fabricating a composite structure with fine grains as the mixed powder rapidly densify, which helps to avoid any grain growth may take place in the final structure. However, SPS can also produce a structure with a full density. Microstructure and mechanical properties can be affected by the SPS parameters. Several researches have conducted work to investigate the impact of sintering temperature [154], [183], [186], holding time [172], [187]–[189], heating rates [154], [157], applied pressure [149], [154], [157] on the mechanical properties.

Xin et al. [174] studied the ability of sintering Ti-6Al-4V and Mo alloy to produce a composite structure that can be used in the dental application. Despite adding Mo to the mixed powders which raised the sintering temperature required to achieve fully dense material, this β stabiliser alloys improved hardness and strength of the sintered sample. Heo et al. [175] reported that densification at a lower temperature of 700˚C - 900˚C, can reduce the relative density of Ti-6Al-4V; however, the final structure was homogenised with large porosity. However, at 1300˚C, the Ti-6Al-4V powder showed a 97% relative density with a fine homogenised microstructure and a hardness of up to ~350 HV. Shoa et al. [190] reported

an improvement in corrosion resistance when the sintering temperature increased from 650˚C to 750˚C. Also, an improvement observed in each of density, yield strength and compressive resistance. The best yield strength was 1238 MPa at 750˚C compared to 600 MPa at 650˚C. Zadra et al. [146] claim a large grain with distorted shape will be observed when sintering CP-Ti alloy over 900˚C. Dariusz et al. [5] studied the effect of the heating rates and applied forces on the properties of Ti-6Al-4V sintered at 1000˚C for 5 min holding (dwell) time.

A full densified parts were obtained under all the selected heating rates, showing that the effect of heating rate is a minor on the sintering process. Also, under rapid heating rate, the ability to obtain full densification is equal to the conditions under slow heating rates. However, the amount of the applied force has a contrast effect when it comes to the percentage of the achieved density and density proportion directly with applied force. The effect of the applied load is related to the fundamentals of SPS. Under low pressure, the diffusion process will be dependent upon the electric discharge taking place at the surface of the powder, with low pressure, it will require longer holding time to achieve the required density.

However, increasing the applied load will increase the diffusion process between powder particles and materials with full density can be obtained in a short time. Related to that increasing the pressure will reduce the percentages of porosities and decreases the grain size, and according to Hall-Petch relation, hardness will increase as well. From the above, Dariusz confirmed if a Ti-6Al-4V powder heated in the rate of 300˚C/min and sintered for 5 min at 1000˚C under an applied load of 25 MPa, will be appropriate variables to achieve sintered parts with 138 GPa elastic module, 1414 MPa compression resistance and microhardness reaches to 373 HV0.5.

In general, most of the studies of the SPS process involves studying the sintering of Ti alloys mixed with other elements to produce composite metals. It is known that pre-alloyed powders are expensive, and they used explicitly in additive manufacturing. So the trend was directed to use the SPS method to fabricate and produce composite structure less expensive and can be applied in different applications.

Vanadium, mainly used as alloying elements [191], [192], and even if it used in the powder technology, it is only used in small percentages. In the consolidation process, as a less diffusible, vanadium powder makes it hard to be sintered by the convention sintering method. To the best of knowledge, few studies reported the sintering of V powder by SPS. Yang et al. [193] investigate the sintering of a V- powder alloy 66.7V-13.3Fe-20Al mixed

with CP-Ti alloy. Under vacuum condition, the sintering was performed, and 1100˚C was the sintering temperature. Three holding times were set; 5 min, 15 min, 30 min and two isothermal loads applied 15 MPa and 30 MPa. The resulted sintered alloy was Ti-10V-2Fe-3Al. As the holding time increases from 5 min to 30 min, the V powder diffuse rate increased as well. The V-rich region became undetectable. The homogenised structure was readily obtained even at 5 min holding time when using the SPS method. The SPS process was very effective to accelerate the diffusion rate of V within the Ti powder even when V wt.% increased from 10% to 17%. The new composite metal has a tensile strength of 1250MPa and elongation reached 10%, which is values close to the values in the wrought condition.

Qian et al. [194] were able to produce a composite structure by mixing HDH Ti and 40V/60Al powder. Two sintering temperatures were selected 900˚C and 1100˚C at 5 min dwell time. At 900˚C, the microstructure consisted of two reigns, the 40V/60Al particles and the α/β colonies. Also, there was a thin border between the 40V/60Al and the α/β colonies, which mainly formed from the diffusion of V and Al into Ti region. However, as the sintering temperature set to 1100˚C and 5 min sintering time, the α/β colonies size increased and the particles size of the remaining 40V/60Al stated to become less distinguished with a reduction in its particles size. However, the main structures still appear homogenised. So increasing the sintering time from 5 min to 15 min was sufficient to refine the grains size, boost the homogenization in the microstructure and reduce the porosity. It offers an ultimate tensile strength of ~1037 MPa with a maximum elongation of 21.8%. The resulting mechanical properties were higher than the obtained from sintering the PA Ti-6Al-4V by SPS using the same sintering conditions.

Therefore, the attention was directed to produce a composite homogenised structure which has full density and minimal porosity. The selected powder alloys were mixed into specific amounts, milled, the best sintering parameters depending on the previous literature [146], [154], [156], [183], [190], [195], [196] were selected.

4.2 Materials and methods of the sintering samples

Two powder alloys were selected for this work, titanium powder G5 type Ti-6Al-4V and commercially pure vanadium alloy. Table 3.1 shows the chemical composition of both Ti-6Al-4V alloy and CP-V alloy powder carried out by AMG analytical Ltd. Titanium powder Ti-6Al-4V has a spherical particle size approximately between 44 μm and 106 μm, while the CP-V powder produced by TLS Technik GmbH & Co with an average size of 24 μm and 45

μm. The selected four mixed powders, shown in table 3.3, were mixed in a low energy mixer. An attrition ball milling for 24hrs at 200 rpm was used to perform the mixing operation[197], [198]. Figure 4.1 shows the images of the selected powder before and after the mixing process. The morphology and distribution of the mixed powder particles are showing both large spheroidals, which Ti particles, and small crashed irregular shapes with a thin plate-like structure are the pure V particles, see figure 4.1c for example.

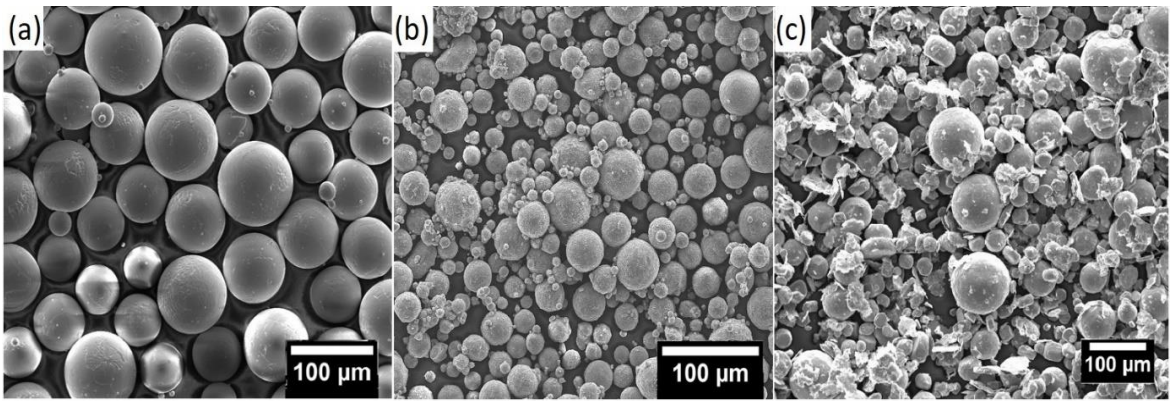

Figure 4.1 Show the selected powders before milling (a) titanium alloy type Ti-6Al-4V, (b) commercially pure vanadium, and (c) the mixture of the two previous powders after 24hrs mixing at 200 RPM (c).

The consolidation process was carried out using FCT system GmbH Spark Plasma Sintering furnace type HP-D25 located at the University of Sheffield –MAPP centre. The sintering process was applied to each mixed powders, and the sintering variables were, the heating rate of 100˚C/min, the sintering temperature of 1200˚C and cooling rate 50˚C, applied force was 99kN for mould diameter of 60 mm. The dwell time was 5, 10, 15 and 20 min. The final sintering product was a solid disk with a thickness of ~5 mm and Ø40 mm and Ø60 mm diameter, see figure 4.2.

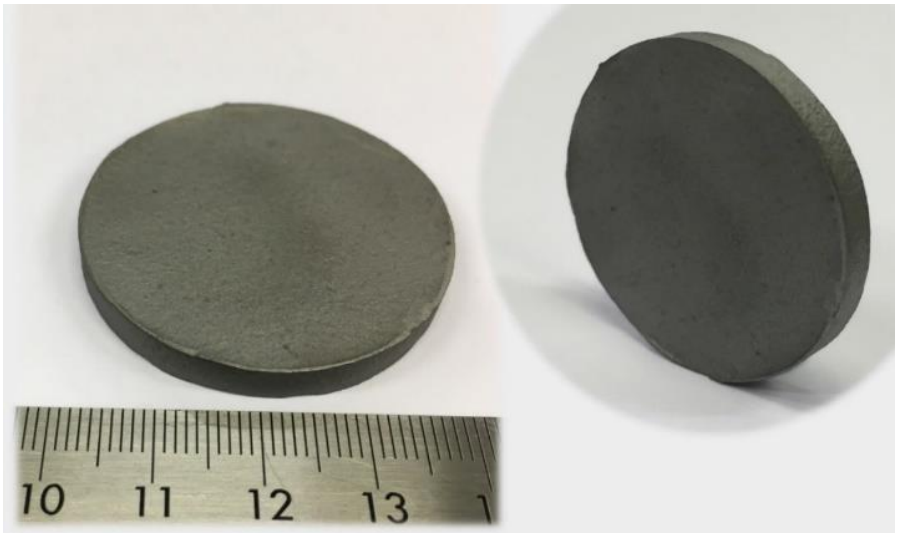

Figure 4.2 Show a typical example of Ti/V disc produced via Spark Plasma Sintering (SPS) method. An output of a sintered part with dimensions of Φ 40mm x 5.5mm thickness.

The material analysis was carried out, as explained previously in chapter three, by micro preparation of sintered samples sections cutting, grinding, polishing and etching surfaces with HF acid following the Nogami et al.[16] procedure. A solution was prepared to etch the sintered samples for 3 min, which consists of 12.5ml HNO_3, 2.5ml HF and H_2O. The microstructure examination by Optical microscopy (OM) was carried out using a Nikon eclipse LV150 with crossed-polarised light imaging. Additionally, a FEG Philips XL 30S system equipped with energy dispersive spectroscopy EDS analysis using 20kV of beam voltage, 3µm spot size and 10 mm of working distance was used for SEM imaging. The mechanical characterisations were involved; (1) microhardness measurements were obtained in the line of 10 indents using a Struers Durascan 70 automated indenter system applying 1kg of load and 20 seconds of dwell time. (2) For the Tensile tests, three specimens were extracted from a sintered sample prepared with dimensions of 5 mm thickness and Ø60 mm diameters. The sintered samples were machined to a thickness of 3.2 mm, and the machining carried out by Special testing Ltd Sheffield. The wire, cutting in dimensions for flat specimens with 12.5 gauge length according to the E8/E8M-13a ASTM standard. The wire cutting took place in Electrotech EDM services Ltd; tensile testing was carried using a Tinius Olsen testing machine. Figure 3.6 shows the tensile specimens obtained from the sintered samples.

4.3 Results and Discussion

4.3.1 Effect of sintering time on the relative density of Ti/V sintered samples

Figure 4.3 shows the relative density of the sintered samples under different sintering (dwell) time. A directly proportional correlation between dwell (sintering) time and relative density was observed [190]. An average density of 94% - 98% was obtained for the alloys Ti/V (80/20), (60/40) and (40/60). The highest relative density at a sintering time of 20 min, was close to values reported previously [146], [175]. While Ti/V4 (20/80) shows a density value of 88% which is less than the other alloys and this was due to the presence of porosity and also the diffusion process between powder particles which requires longer time as the V alloys consider a low diffuse elements when it is compared with the titanium alloy [193].

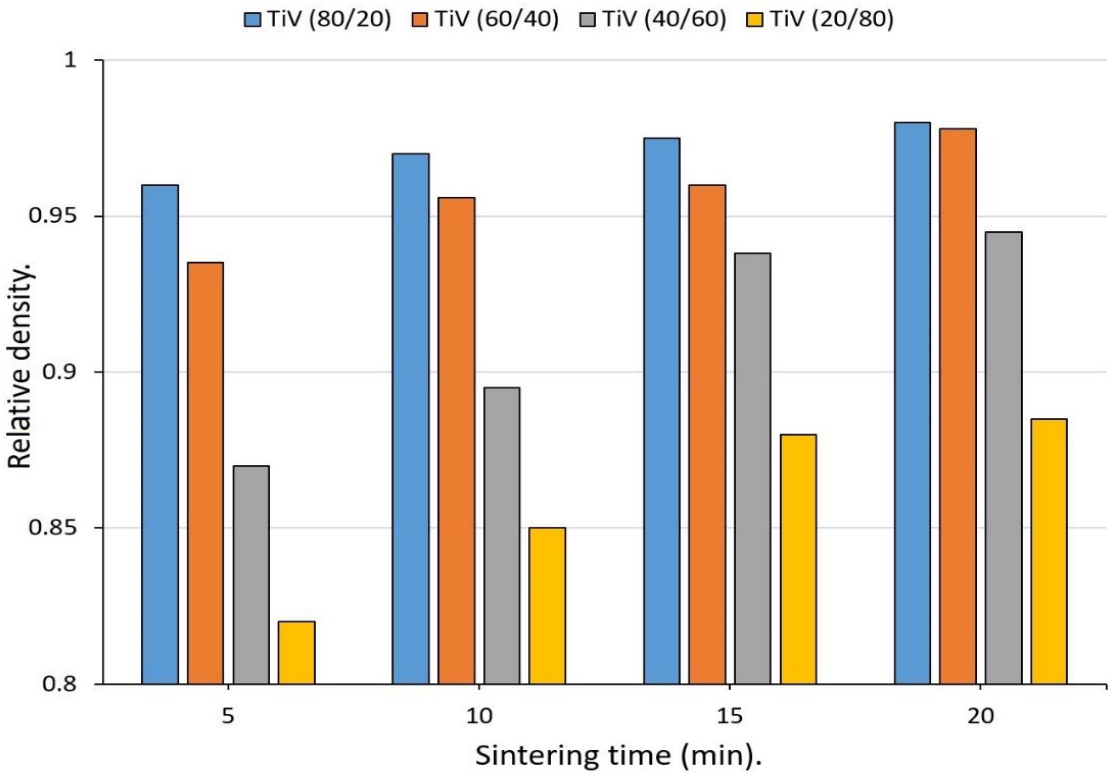

Figure 4.3 Show the effect of spark plasma sintering time on the sintering density of different mixed powders, which shows how increasing the sintering time helps to increase the density of the sintered samples. Also, a reduction in the density was observed as V wt.% increases, due to the presence of pores between V powder particles as the V alloys are less diffusible as compared to Ti alloys.

4.3.2 XRD analysis of Ti/V sintered samples

Fig 4.4 shows the XRD patterns of sintered alloys; it shows that with increasing the dwell time, their peak intensity decreased. Adding the V powder will make the peaks of the binary Ti-V for Ti/V1, Ti/V2, Ti/V3 and Ti/V4 alloys will match the peaks intensity of the α-Ti phase. Also, a reduction in the peaks intensity takes place upon expanding the sintering time from 5 to 20 min. Meanwhile, IMCs and carbides start to formed, such as Ti-V-C. In the case of Ti/V2 (60/40) alloy, the α-Ti phase showed low intensity, while the peak intensity of β-Ti phase starts to rise gradually. These XRD patterns shows a traced of C, which may promotes the hardness values especially for sintered alloys type Ti/V2.

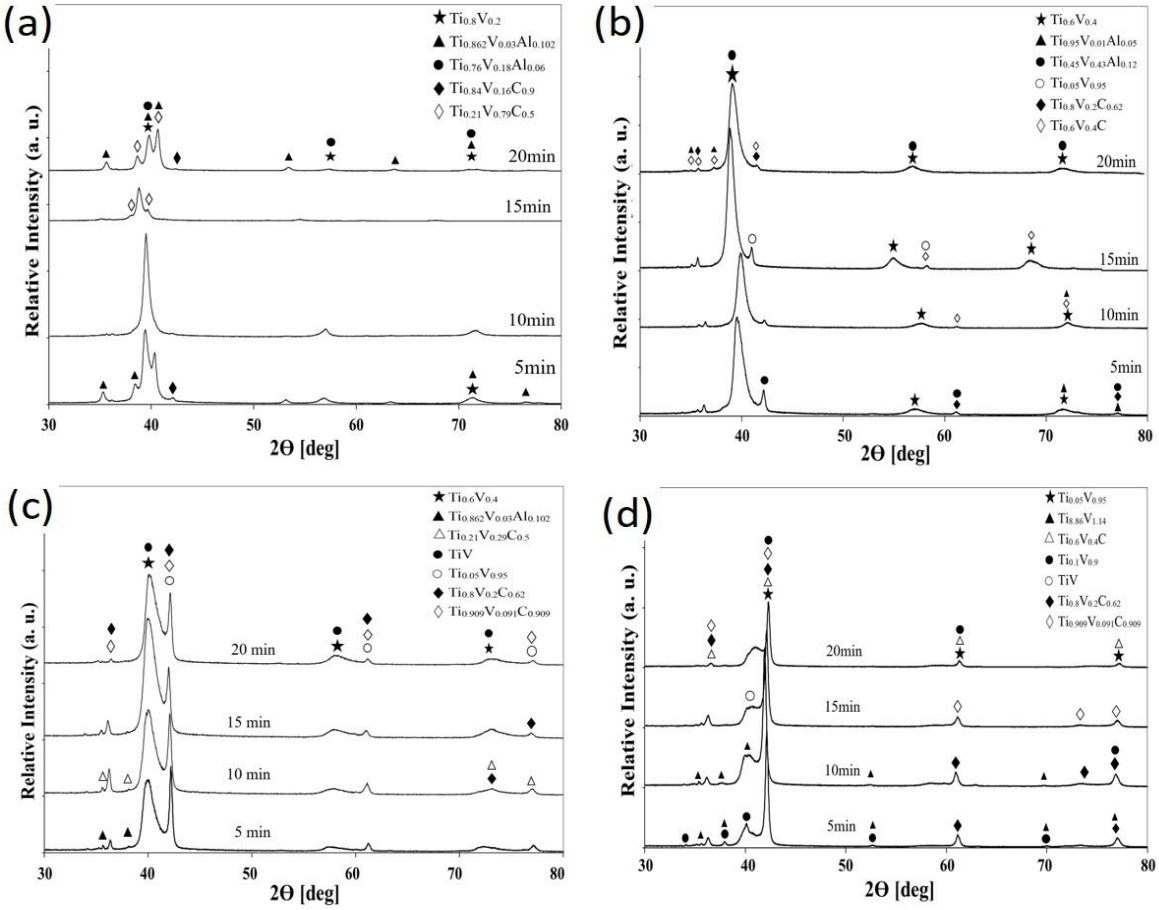

Figure 4.4 Show the XRD patterns for the sintered samples (a) Ti/V1, (b) Ti/V2, (c) Ti/V3 and (d) Ti/V4. As the sintering time and V wt.% increases the peaks intensity decreased of the Ti-V and the βTi phases.

With high wt.% of V alloy, the intensity of the βTi-V and the solid-state phase of Ti-V become higher. XRD patterns of the Ti/V4 (20/80), shows weak shoulder peaks with higher amount of vanadium and no significant difference for the alloys when it sintered under different dwell time.

4.3.3 Microstructure analysis of the sintered samples (Ti/V)

Figure 4.5 shows the sintered microstructure of the Ti-6Al-4V alloy, which represents the final structure when Ti sintered at 5 min, 10 min, 15 min and 20 min, respectively. In all of the obtained sintered samples, the microstructure consists mainly of lamellar α/β phase. However, it seems that the α′ laths become thicker as the sintering time increased from 5 min to 20 min. Using ImageJ software, the average laths thickness measurements were 0.345µm, 0.522µm, 0.710µm and 0.811 µm for the Ti sintered samples at a holding time of 5 min, 10 min, 15 min and 20 min, respectively.

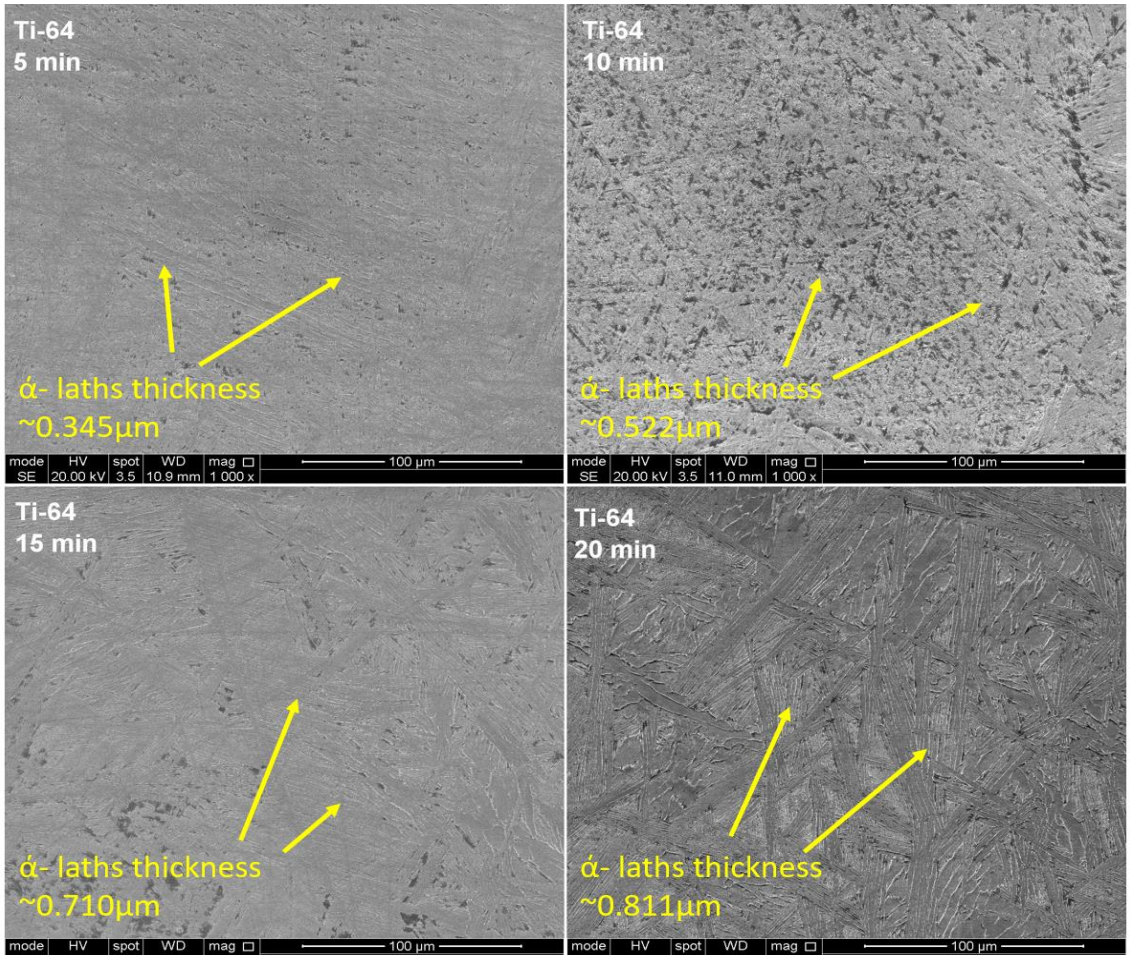

Figure 4.5 SEM images showing the structure of Ti-6Al-4V sintered samples at 1200 ˚C for 5 min,10 min, 15 min and 20 min. The increase in the sintering time allows the α lathes to become thicker.

The effect of holding time on the lath thickness was also confirmed in a previous study[157]. The homogenised structure is attributed to the sintering above the β-transus temperature, which all the α-phase transformed into β phase, then due to the rapid cooling rate take place when removing the heat source, then an α/β structure formed. Figure 4.6 shows the microstructure for the sintered sample type Ti/V1 with the addition of 20 wt.% of CP-V to

80 wt.% Ti-6Al-4V powder at different sintering time. The microstructure exhibits the same structure of the sintered Ti alloy of the fine acicular structure of α/β phase and reveals light colour zones in a shape of rings surrounding darker areas[184]. These light regions are βT-V, and the dark areas are α/β structures. The small wt.% of V in this mixed powder upon sintering, diffused completely. A thin layer of solid-solution βT-V was recognised easily for the sintered sample at 5 min and 10 min. However, this phase became hard to distinguish in the structure of the Ti/V1 sintered samples, as the holding time set to 15 min and 20 min, due to the diffusivity of the V particles in the Ti matrix as a function of time as seen in figure 4.6. The uniformity in the structure was desirable as a UTS of 854 MPa was achieved when sintered for 20 min. Also, density and hardness were improved with this holding time.

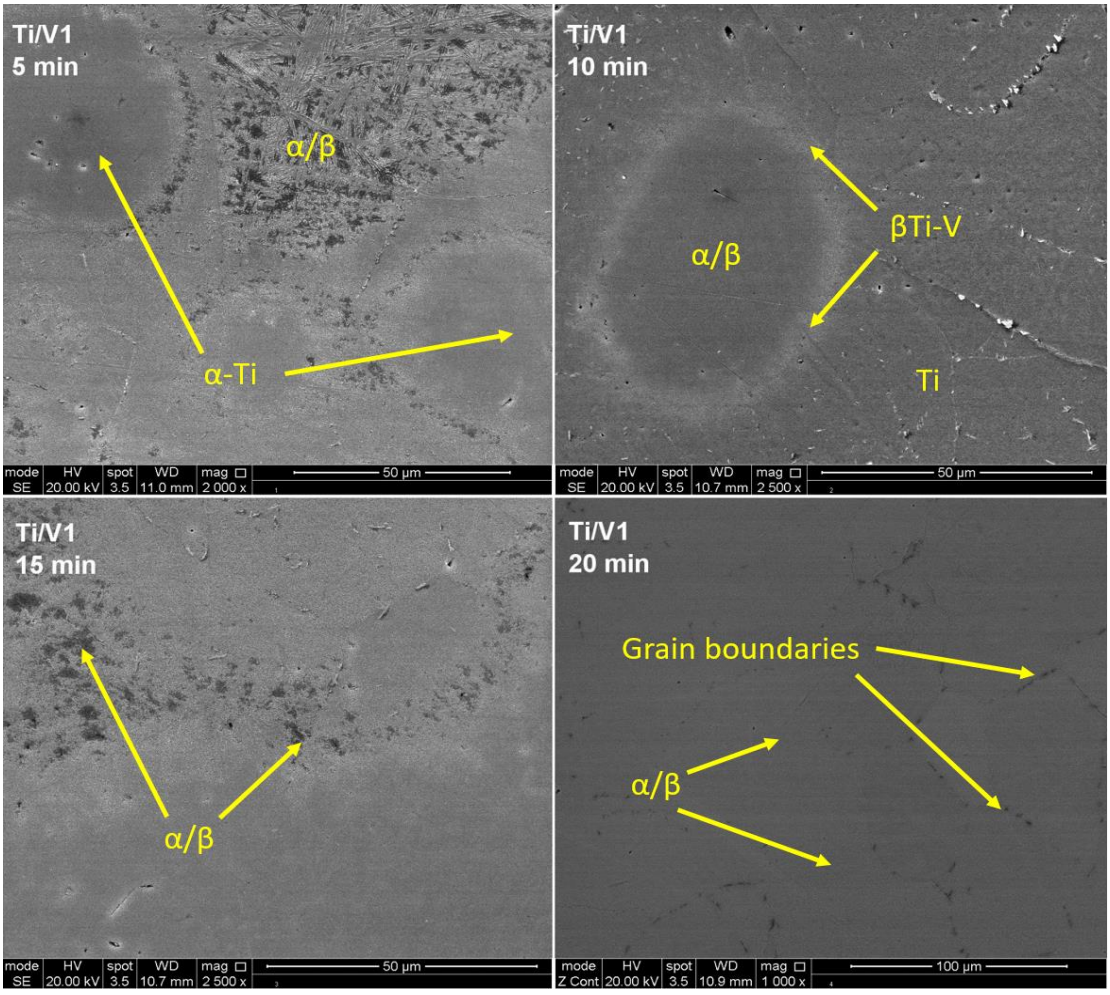

Figure 4.6 SEM images showing the microstructure of Ti-6Al-4V/CP-V sintered samples type Ti/V1 at 1200 ˚C for 5 min, 10 min, 15 min and 20 min. The V powder becomes hard to detect as the sintering holding time increased.

A three regions were identified in the microstructure of the sintered sample type Ti/V2, see figure 4.7, for example. Despite the near fully dense condition, the microstructure examination revealed large regions of undiffused V powder particles at all the selected periods of sintering holding time. The dark colores regions consist mainly of ~76 wt.% of Ti and ~19 wt.% of CP-V. The diffusion regions, which are βTi-V phases, were located at the vicinity of α/β regions and surrounded by undiffused V particles. The presence of porosity within the V-rich regions were recognised. Increasing the sintering time from 5 min to 10 min to 15 min, and the 20 min promotes the diffusion process between the powder particles, the image was used to measure the thickness of the βTi-V regions. An increment for the diffusion regions was recorded of 19.4μm, 21.8 μm, 40.8 μm and 44.3 μm for the sintered samples at 5 min, 10 min, 15 min and 20 min sintering time, respectively.

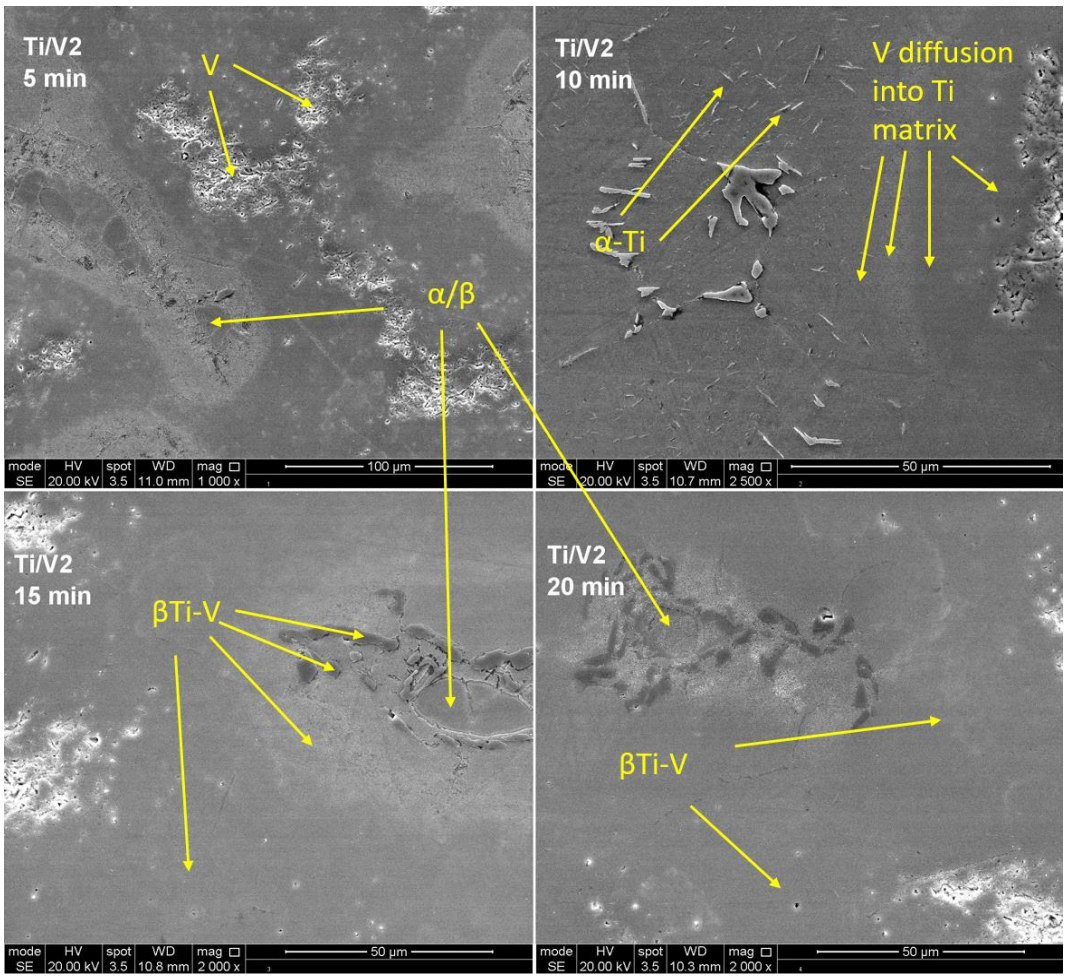

Figure 4.7 SEM images for the Ti/V2 samples sintered at 1200 ˚C for 5 min, 10 min, 15 min and 20 min. An increment in the diffusion layer βTi-V region which located between Ti-rich regions and V-rich regions were identified as the sintering time increased from 5min to 20min

Even with longer sintering holding time, 20 min, porosity was identified within the V particles, due to the lower diffusivity of V particles. Despite that, the porosity remained after sintering and both relative density and hardness were increased, and maximum hardness of 465 HV was obtained for Ti/V2 alloy. The sintering temperature at 1200˚C with extended dwell time allowed upon rapid cooling to precipitate fine α´ platelets [174] from the β phase and formed next to the grey zones, see figures 4.6, 4.7 and 4.12, which increments the hardness value. From figure 4.8, the same three regions were also observed in Ti/V3 structures. However, as the V content increased to 60 wt.% and Ti content reduced to 40 wt.%, hardness declined, and the presence of pores at V-region was recognised. Figure 4.8a-b shows the gradual diffusion of V powder within the Ti matrix as the holding goes up from 5 min to 20 min. The thickness of the diffusion layer between Ti-rich regions and V-rich regions were ~20.2 μm, 25.4 μm, 28 μm and 26.2 μm for the Ti/V3 samples sintered at 5 min, 10 min, 15 min and 20 min sintering time, respectively. The lower hardness of this sintered sample reflect in a superior tensile strength reaches about ~797 MPa, which is higher than the obtained strength from Ti/V2 as it only recorded 544 MPa.

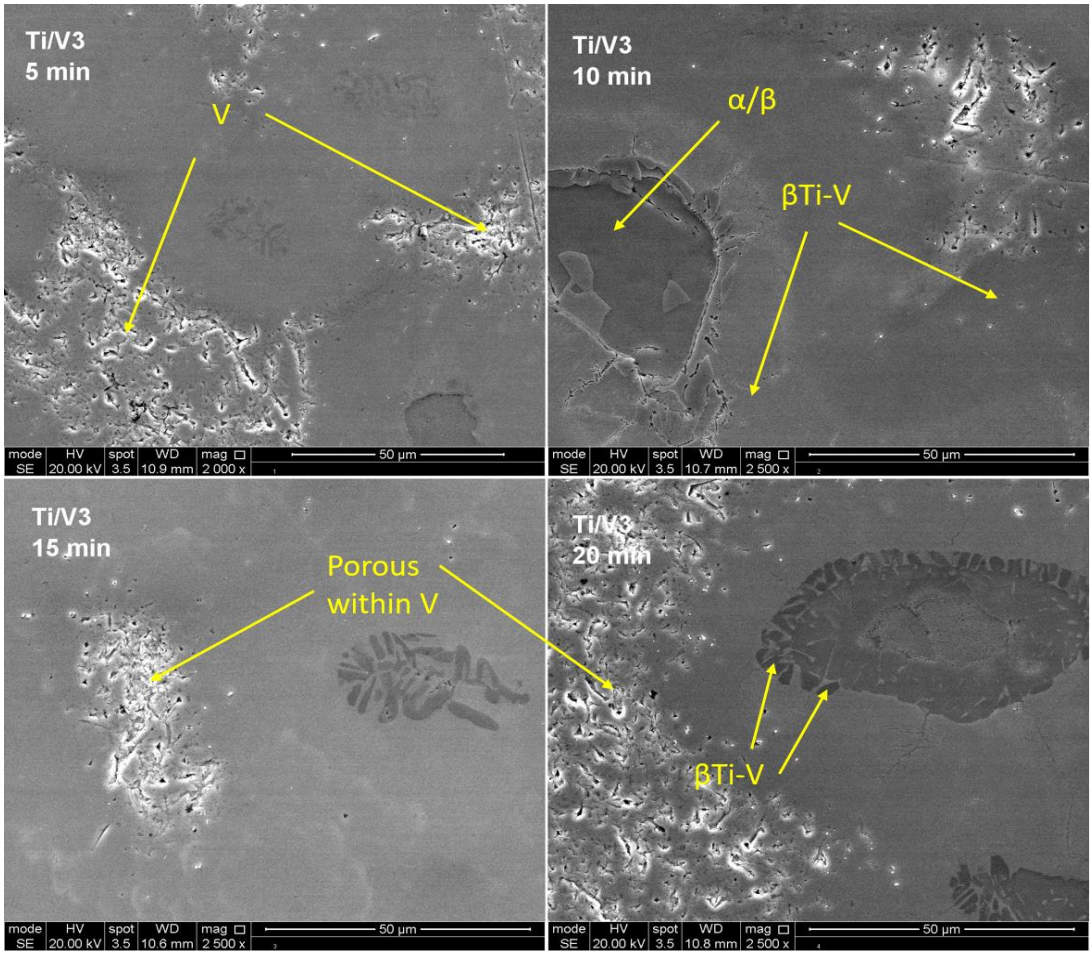

Figure 4.8 SEM images for the Ti/V3 samples at 1200˚C for 5min, 10min, 15min and 20 min. An increase in the diffused regions (βTi-V) as a function of sintering holding time. Also, two different types of βTi-V phases with different colours depending on the Ti wt.% and V wt.% in the βTi-V phase.

As the V wt.% set to 80 and Ti wt.% set to 20 for the sintered sample Ti/V4, a large amount of porosity observed at the vicinity of the V-rich regions, which indicate that, the sintering temperature of 1200˚C and even at longer holding time of 20 min was insufficient to obtain diffusion between V particles. Also, a defect of microcracks was observed in this type of sintered alloy. As a result, the maximum tensile test achieved for the Ti/V4 alloy for 20 min holding time was only 450 MPa. Figure 4.9 shows the microstructure of the Ti/V4 sintered sample vs sintering time. The calculated βTi-V regions show an increase in the diffusion layer thickness, which encircled by V-rich regions, as the holding time increased from 5 min to 20 min. The measurements of the diffused layers were 15.9 µm, 17.8 µm, 20.3 µm and 32.6 µm for the Ti/V4 alloy samples sintered for 5 min, 10 min, 15 min and 20 min, respectively.

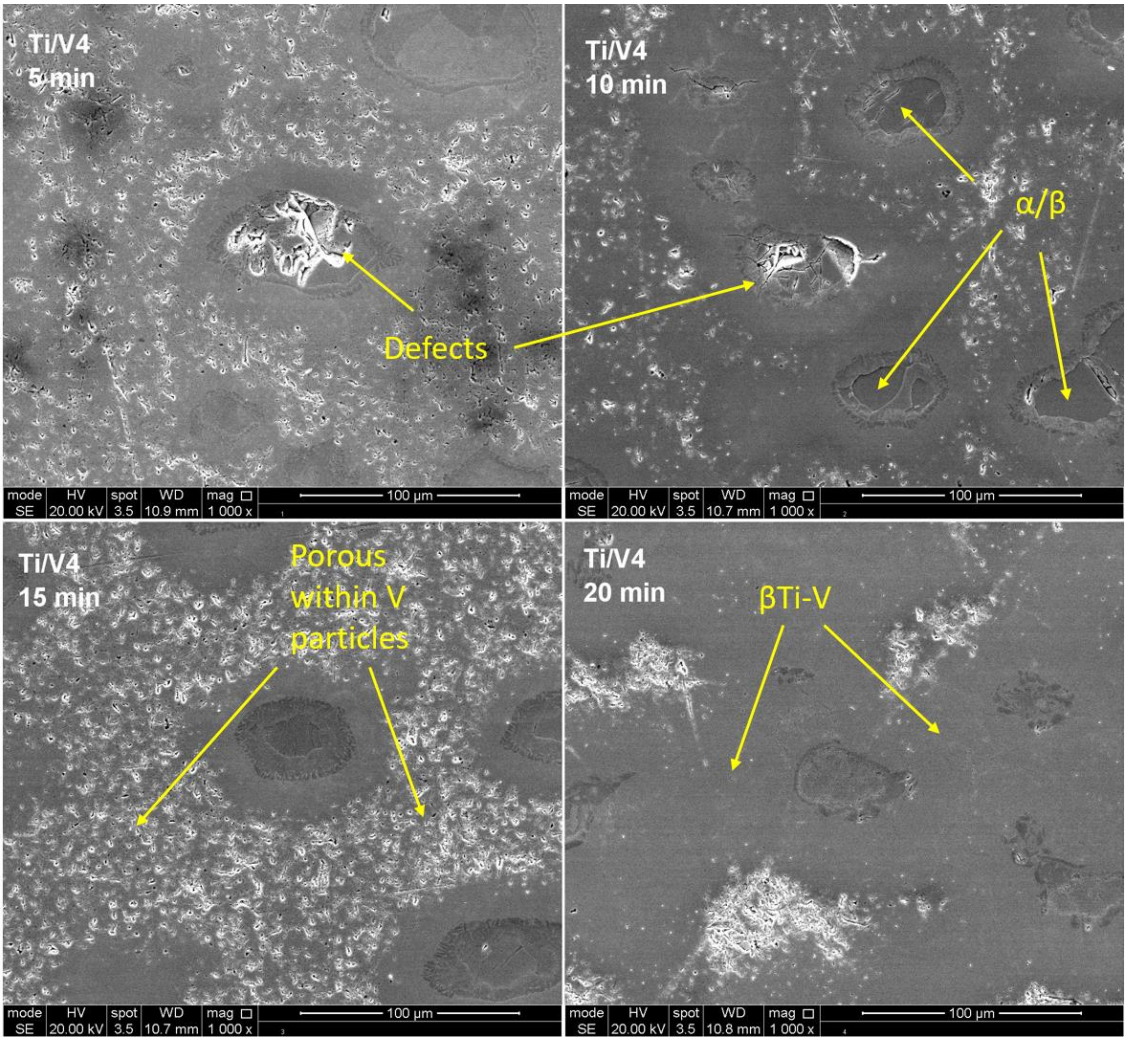

Figure 4.9 SEM images for the Ti/V4 alloy sintered at 1200˚C, showing an increase in the diffusion regions located between Ti-rich regions and V-rich regions as a function of sintering holding time.

The SEM imaging for all the sintered samples, as mentioned before, shows three main regions. Each one of these regions has been allocated a distinct colour, which is a result of the chemical reaction between the sintered particles during the consolidation process, see figure 4.11, for example. EDS analyser was applied to examine the amounts of Ti, V and Al in these three regions and how they are distributed across the sintered samples. Figure 4.12a-b can provide an indication of how the distribution is taking place and how the percentages of Ti and V are fluctuated according to this line scans approach. Ti-rich regions represented by α/β phases has a dark colour. The V-rich regions have distinguished features of bright colour with pores. The final regions represent the chemical reaction between V alloy and Ti alloy forming grey areas surrounding the dark regions[199]. This chemical reaction is the diffusion of vanadium into the Ti matrix, and it was observed as the dwell time increased the area surrounding the Ti increased as well, see figures 4.6, 4.7, 4.8 and 4.9. These grey

areas, according to the phase diagram[200], consist of the solid solution phase of Ti-V. The mapping in figure 4.10 is showing the distribution of Al particles all over the sintered area but with a low amount. In all, the sintering process, according to EDS measurements, Al was in the range between (0-6) wt.%, as there is no Al addition to the mixed powder. However, adding the vanadium powder to the mixture affect the microstructures and mechanical properties of the sintered samples[193].

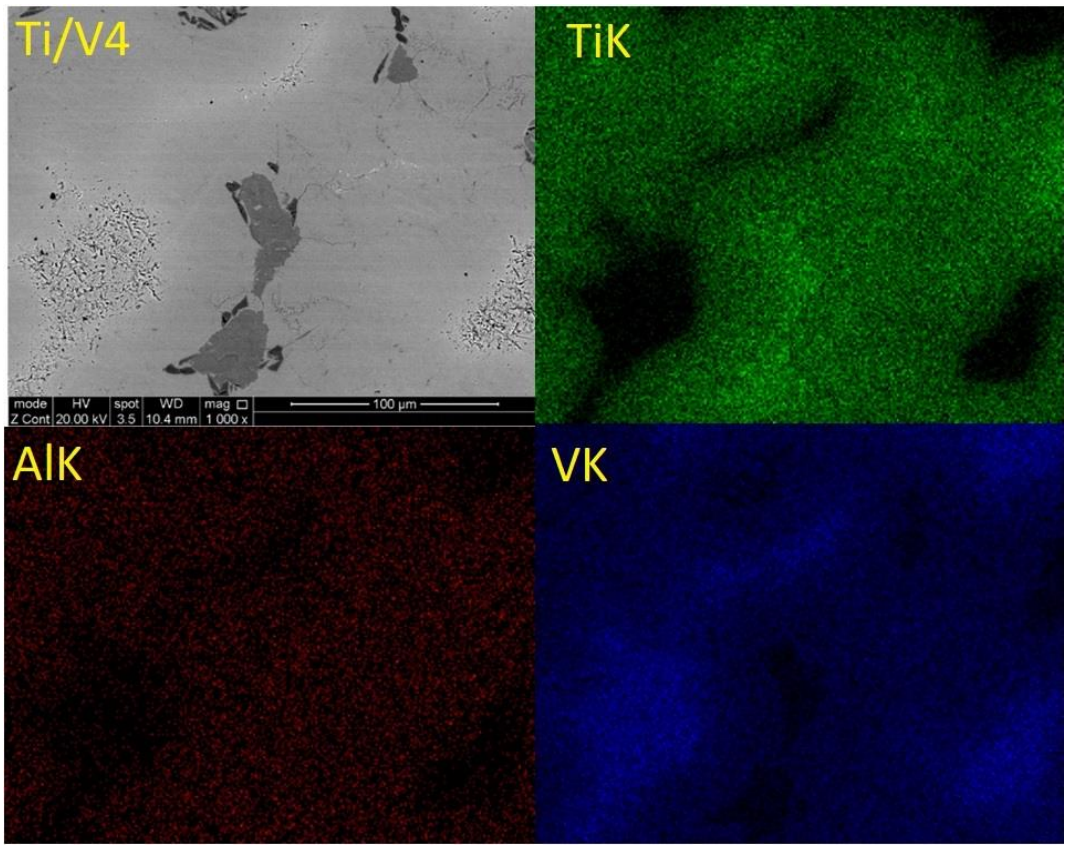

Figure 4.10 SEM images showing the region of sintered sample Ti/V4. The Mapping scan method is showing the distribution of titanium, vanadium and aluminium, across the sintered sample, respectively.

Due to the high melting point, the V alloy was indeed for higher sintering temperature, and longer sintering time to diffuse completely in the Ti matrix, however, the incomplete diffusion was located in the samples with higher V amounts. The diffusion effect has been achieved in case of the mixed powder type Ti/V1, as the 20% of vanadium was undetectable at different sintering times, see figure 4.6, for example.

Figures 4.12, 4.13, 4.14, 4.15 and 4.16 shows the use of point and ID approach in order to analysis the region in a more specific way. The tables below each image show the specific chemical composition of the tested points. From the conducted EDS measurements, the

regions of Ti and V have a typical composition, however, the composite grey areas show different composition percentages of Ti and V. It was noticed as the scan carried out from the V regions toward Ti-rich zone, the Ti-V solid-state phase show a reduction in vanadium and an increase in Ti content and vice versa. The addition of the V to the Ti matrix effect on the Al content, therefore it was observed a low amount of Al in the βTi-V. Besides, C was also detected in the sintered samples. The presence of C was due to the sintering process, which involves wrapping the powder with carbon felt to prevent heat loss by radiation and also for ease removing from the mould. A-line scan by EDS was carried out across the sintered samples, and the images show the percentages of the composite elements become higher when the scanner reaches a single elements region see figure 4.11, for example.

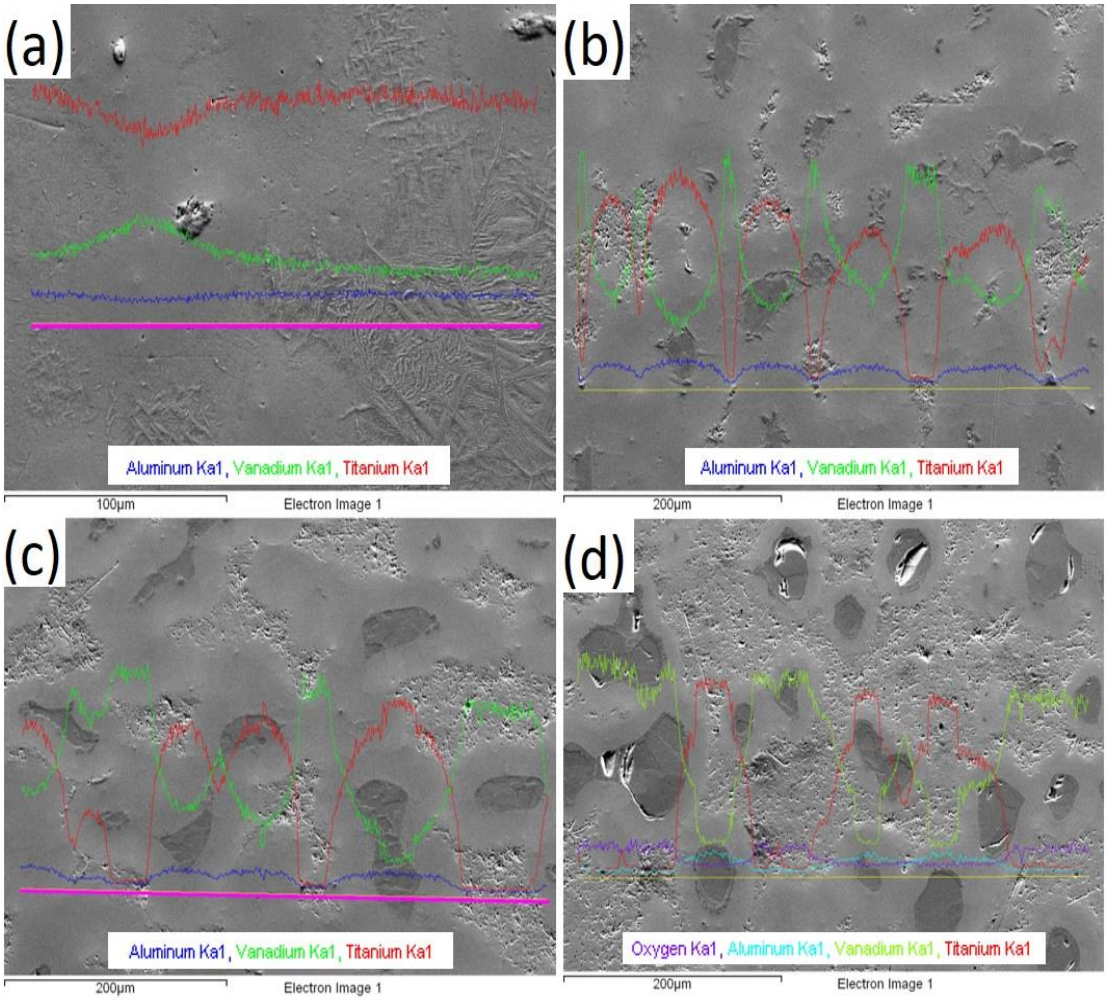

Figure 4.11 EDS line scan analysis across the sintered samples (a) Ti/V1, (b) Ti/V2, (c) Ti/V3 and (d) Ti/V4. A fluctuation in the line mapping with high intensity observed when the scanning reaches a Ti region or V region, see, images b,c, and d, While Ti/V1 shows a study map line indicating a complete diffusivity of the 20 wt% of the V in this sample compared with the other sintered samples.

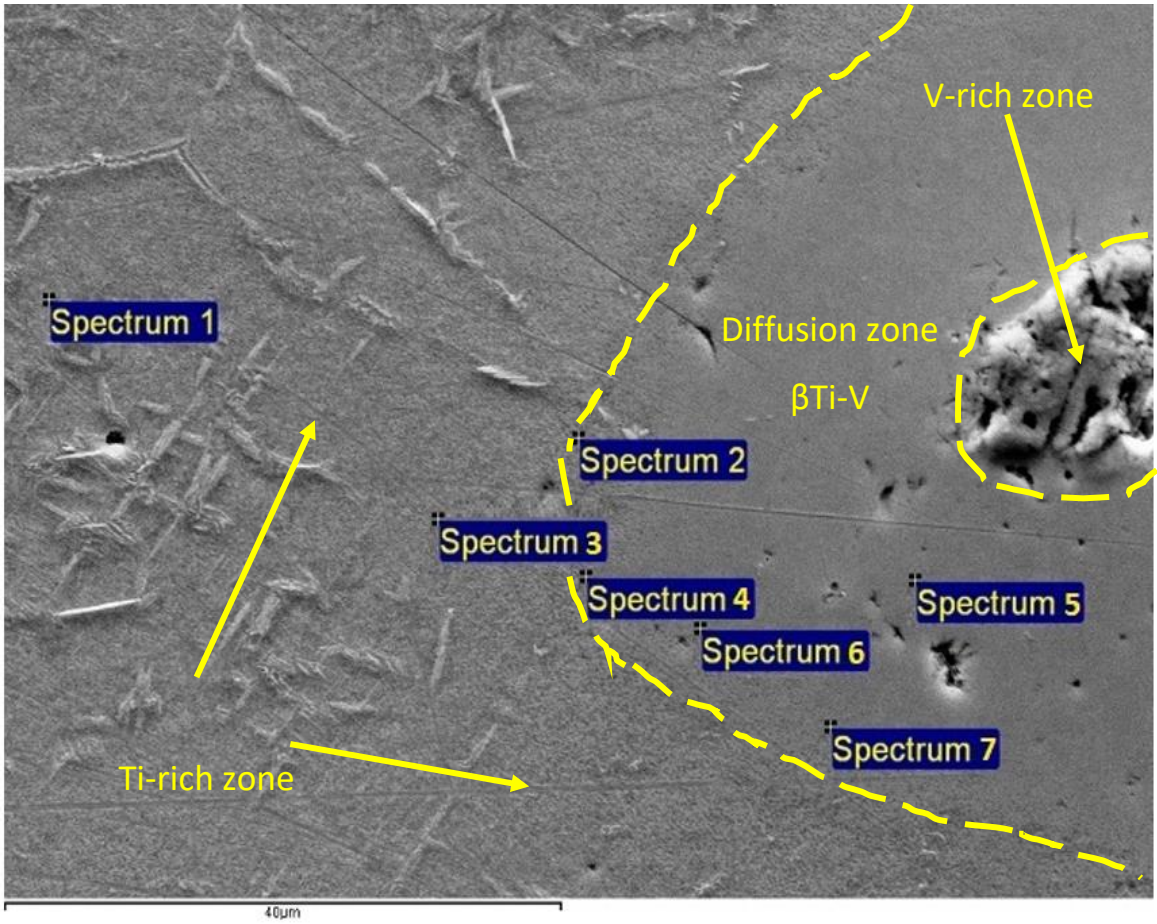

Spectrum	In stats.	Al	Ti	V	Total
Spectrum 1	Yes	0.66	-0.41	99.74	100.00
Spectrum 2	Yes	0.01	-0.38	100.37	100.00
Spectrum 3	Yes	6.00	78.27	15.73	100.00
Spectrum 4	Yes	5.57	75.35	19.08	100.00
Spectrum 5	Yes	3.42	54.58	42.01	100.00
Spectrum 6	Yes	5.08	69.40	25.52	100.00
Spectrum 7	Yes	0.02	-0.51	100.50	100.00

Figure 4.12 Show the EDS analysis of the sintered sample type Ti/V1 and the approximate wt.% of Ti, V and Al across the diffusion zone.

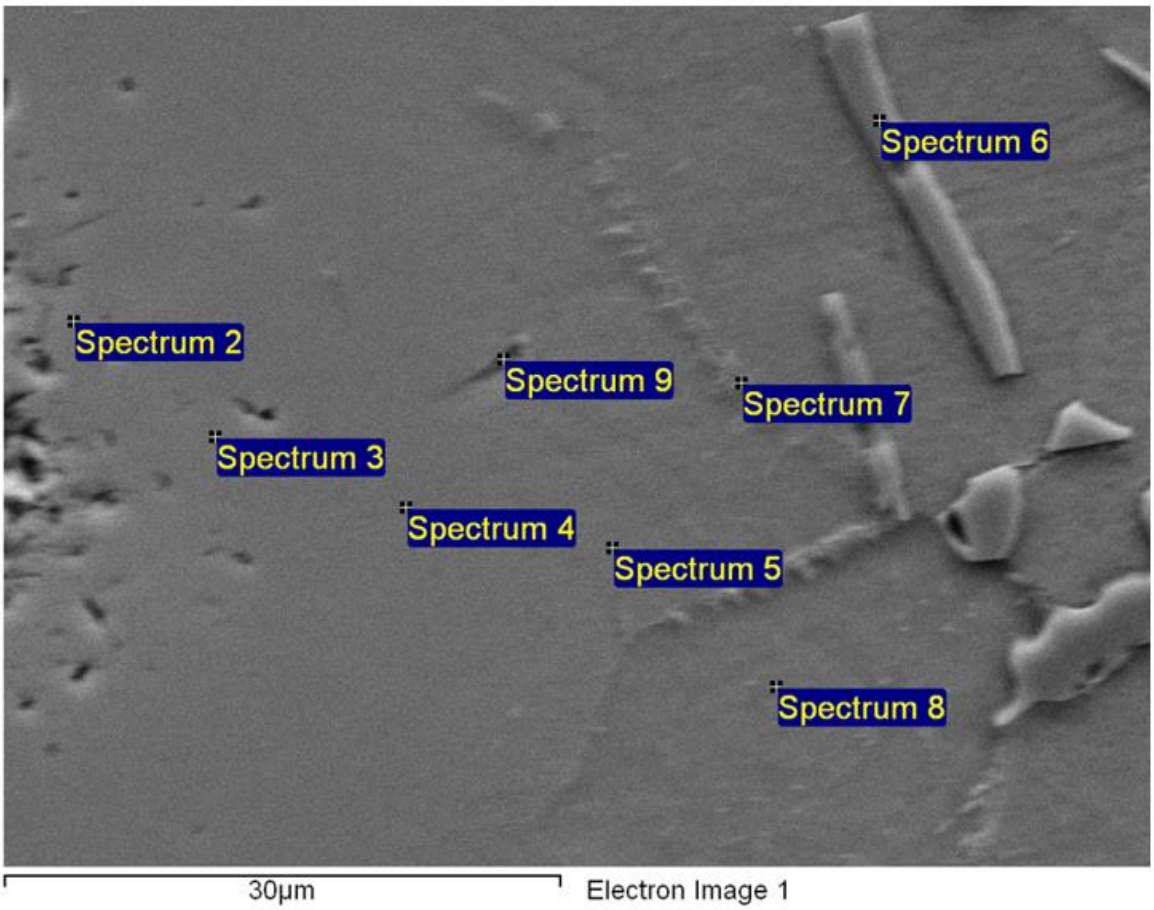

Spectrum	In stats.	Al	Ti	V	Total
Spectrum 2	Yes	1.18	19.26	79.56	100.00
Spectrum 3	Yes	2.78	38.82	58.41	100.00
Spectrum 4	Yes	4.09	55.26	40.66	100.00
Spectrum 5	Yes	4.90	64.03	31.07	100.00
Spectrum 6	Yes	1.22	94.27	4.51	100.00
Spectrum 7	Yes	5.18	69.02	25.80	100.00
Spectrum 8	Yes	4.94	68.13	26.93	100.00
Spectrum 9	Yes	4.27	61.73	34.00	100.00

Figure 4.13 The EDS analysis of the sintered sample type Ti/V1at different location showing the approximate wt.% of Ti and V in the diffusion region between the Ti-rich side and V-rich side.

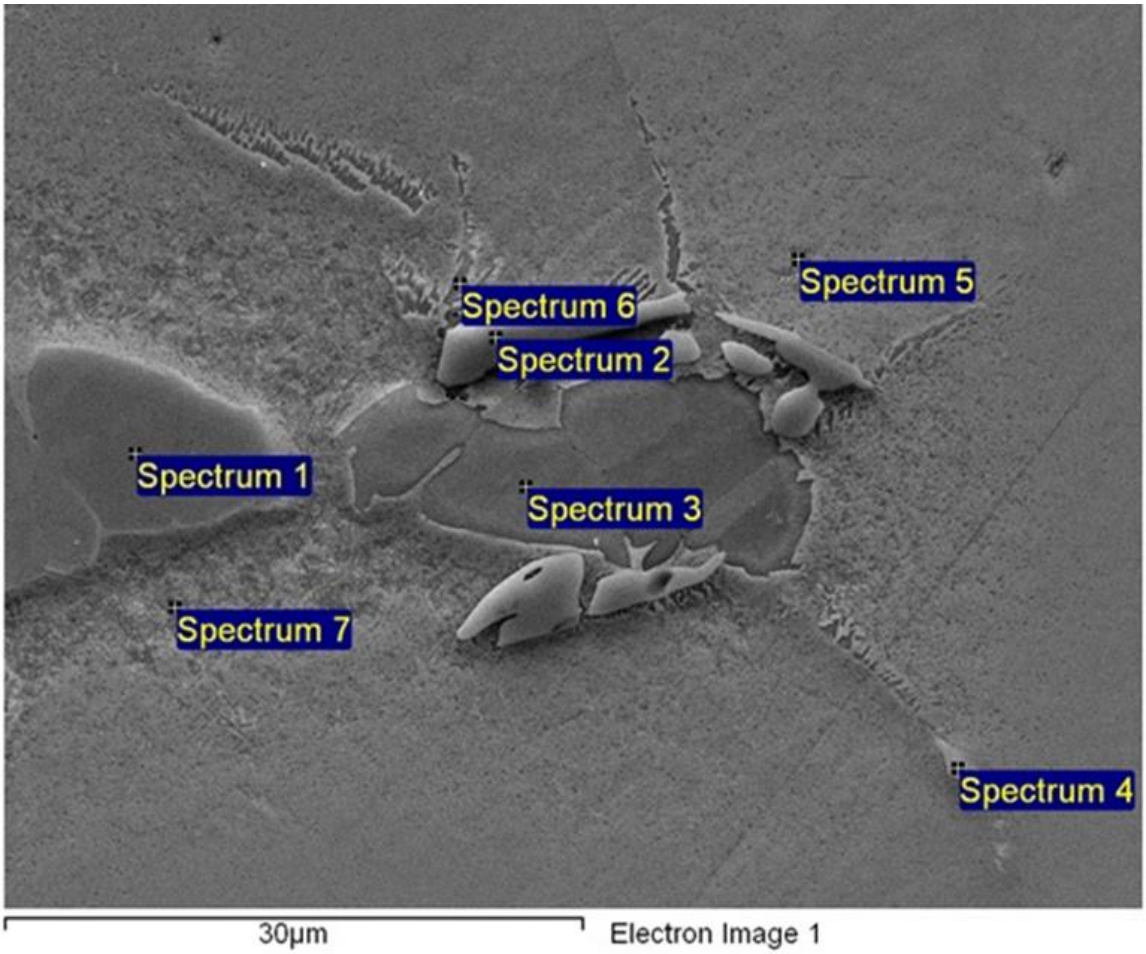

Spectrum	In stats.	Al	Ti	V	Total
Spectrum 1	Yes	5.82	89.40	4.78	100.00
Spectrum 2	Yes	0.89	95.66	3.44	100.00
Spectrum 3	Yes	6.03	89.23	4.74	100.00
Spectrum 4	Yes	4.67	75.28	20.04	100.00
Spectrum 5	Yes	5.85	74.19	19.95	100.00
Spectrum 6	Yes	6.57	73.85	19.58	100.00
Spectrum 7	Yes	6.30	76.49	17.21	100.00

Figure 4.14 The EDS analysis of the sintered sample type Ti/V2 showing an approximate wt.% for Ti, V and Al at a different locations.

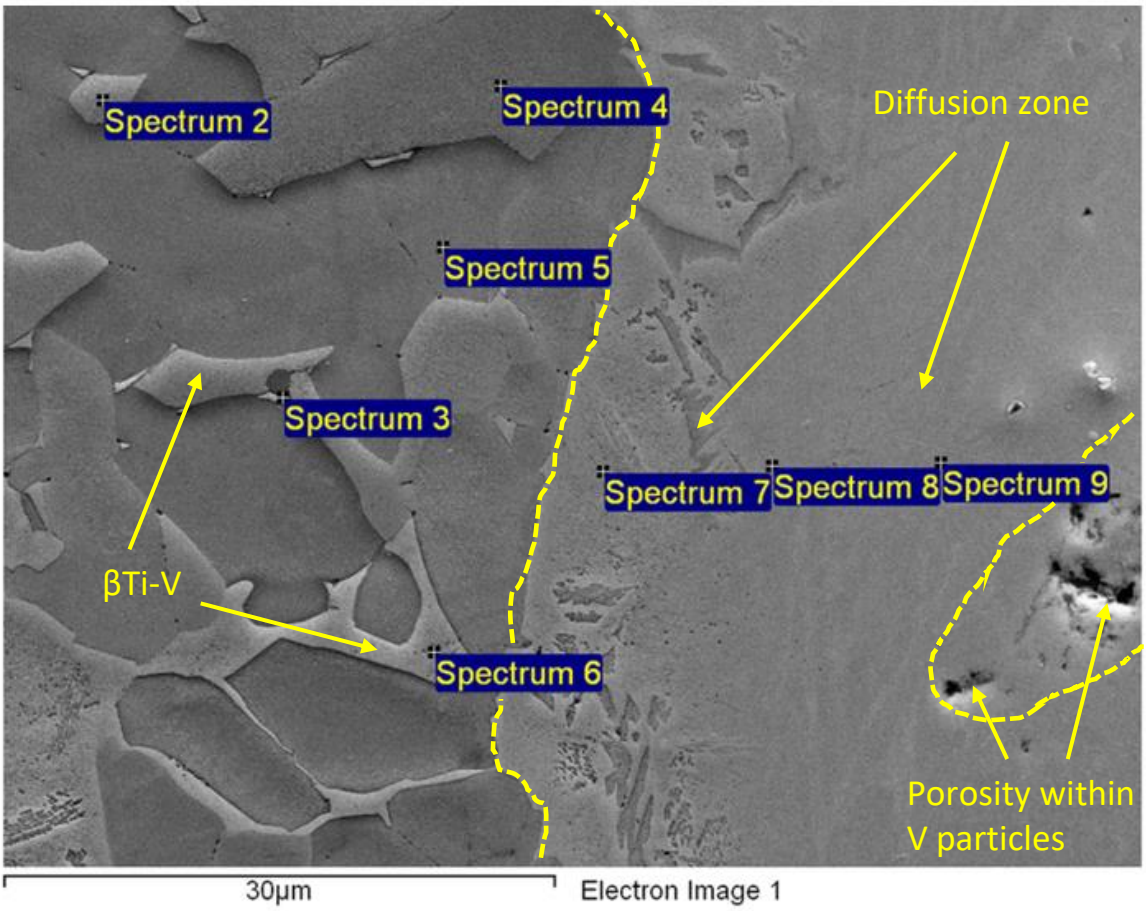

Spectrum	In stats.	Al	Ti	V	Total
Spectrum 2	Yes	6.19	89.39	4.42	100.00
Spectrum 3	Yes	7.93	81.63	10.44	100.00
Spectrum 4	Yes	6.29	89.66	4.05	100.00
Spectrum 5	Yes	6.19	89.48	4.34	100.00
Spectrum 6	Yes	7.35	69.03	23.62	100.00
Spectrum 7	Yes	6.03	72.32	21.65	100.00
Spectrum 8	Yes	5.38	68.79	25.83	100.00
Spectrum 9	Yes	4.38	56.35	39.28	100.00

Figure 4.15 The EDS analysis is showing the variation of approximate wt.% for Ti, V and Al concentrations at different locations across the Ti/V3 sintered sample.

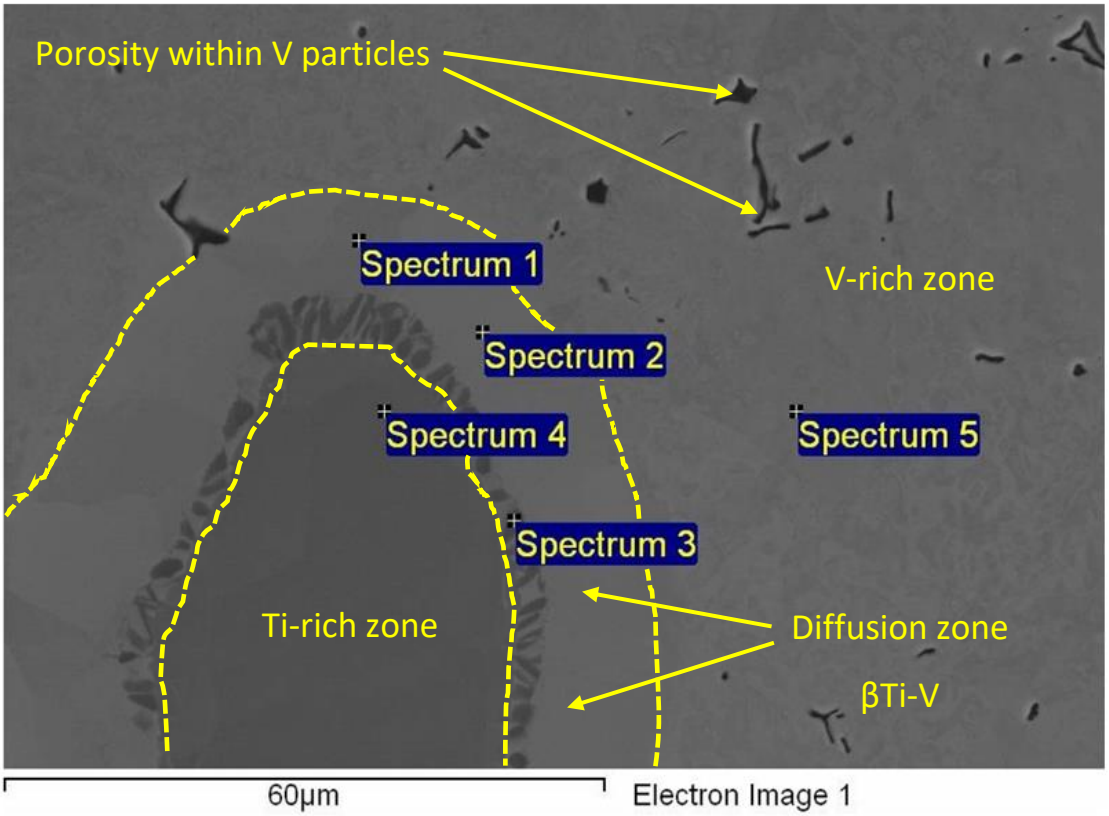

Spectrum	In stats.	C	Al	Ti	V	Total
Spectrum 1	Yes	3.23	2.43	35.04	59.30	100.00
Spectrum 2	Yes	3.49	3.19	41.74	51.58	100.00
Spectrum 3	Yes	8.59	0.86	77.83	12.18	100.00
Spectrum 4	Yes	-	5.75	88.71	5.07	100.00
Spectrum 5	Yes	0.23	-	-	99.77	100.00

Figure 4.16 Show the EDS analysis of the sintered sample type Ti/V4and how the diffusion zone enclosed the Ti-rich zone, porosity was identified within the vanadium particle. The table below the image indicates an approximate wt.%.of the chemical composition.

4.4 Mechanical properties

4.4.1 Hardness results

The results from Vickers hardness, HV, are shown in figure 4.17. A set of five readings of hardness for each sintered sample was obtained to determine the average hardness for each sintering condition. The measurements were made from the centre to the edge, at the middle of the 5 mm thickness of each sample. The variation in hardness among the sintered samples type Ti-6Al-4V was relatively small, in the range of 305±6HV_1, under different sintering times. Although, as the growth in α′ laths thickness was a function of time, the microstructure of Ti-6Al-4V samples showed a typical α/β structure, consisting of needles-like α delineated by β phases, see figure 4.5. A trend was identified of increase of sintering holding time promoting the hardness values. A study conducted by Falodun et al.[189] discussed the effect of increasing sintering temperature and sintering holding time on the density and hardness values of TiN sintered alloys. They confirmed that hardness values increases as the sintering holding time increases from 10 min to 30 min at sintering temperature of 1100 ˚C. The Vickers hardness versus sintering holding time shown in figure 4.17 reflects a trend similar to that reported by Falodun et al. [201], who found that increasing the sintering holding time resulted in increase in the hardness of the sintered samples types Ti/V1, Ti/V2, Ti/V3 and Ti/V4. Meanwhile, sintered sample type Ti/V1 showed an increment of hardness as a function of time, with an increment of 65±10HV_1 observed from 299±5HV_1 to a 367±10HV_1 when the sintering time was increased from 5 min to 20 min. The same behaviour was also observed for the sintered samples type Ti/V2. Upon increasing the sintering holding time to 20 min, despite having a 40wt. % of ductile vanadium alloy, the hardness values advanced by about 25%, recording a value of 347±13HV_1, compared to 289±6HV_1 at 5 min.

In relation to this work, Park et al. [182] reported great potential for increasing hardness values as the content of V reaches to 15 wt. % in CP-Ti alloy: however, a reduction will be evident as the amounts of the ductile vanadium become higher than 15 wt. %. Micro examination of the Ti/V alloys, as shown previously in figures 4.6, 4.7, 4.8, 4.9 and 4.12, indicates the formation of three phases, the α/β phases, the βTi-V phases and undiffused ductile particles of vanadium. A published work by Chu et al.[183] suggested that the phases of βTi-V usually exhibit a microhardness value of 364±7HV_1 when vanadium content is in the range of 14-15 wt. %. As suggested previously by Parl et al.[182] the alloys Ti/V1and Ti/V2 showed the highest hardness value of 367±10 HV_1 and 347±13HV_1, containing 20 wt.

% and 40 wt. % of vanadium, respectively, when they sintered for 20 min. The obtained hardness values of sintered samples type Ti/V1 and Ti/V2 in this work are more akin to those hardness values given by Chu et al.[183]. However, as highlighted in figure 4.17, a reduction in hardness was observed, contrary to the Park et al.[182] suggestion, for the sintered samples with higher amounts of V wt. %: Ti/V3 and Ti/V4. A drop in hardness measurements was identified of about ~100HV_1 for the hardness values of Ti/V3 sintered samples as compared to the hardness of Ti/V1 and Ti/V2, due to higher V amounts. While the difference in hardness value was higher in the case of sample type Ti/V4, about ~180HV_1 as compared with the obtained hardness values from the sintered sample types Ti/V1 and Ti/V2, the maximum hardness values for Ti/V3 and Ti/V4 obtained at maximum holding time were 257±4HV_1 and 170±7HV_1, respectively. Therefore, from the above, it can be concluded that increasing the sintering holding time is necessary to advance the hardness values and to promote the fully dense condition with minimal porosity.

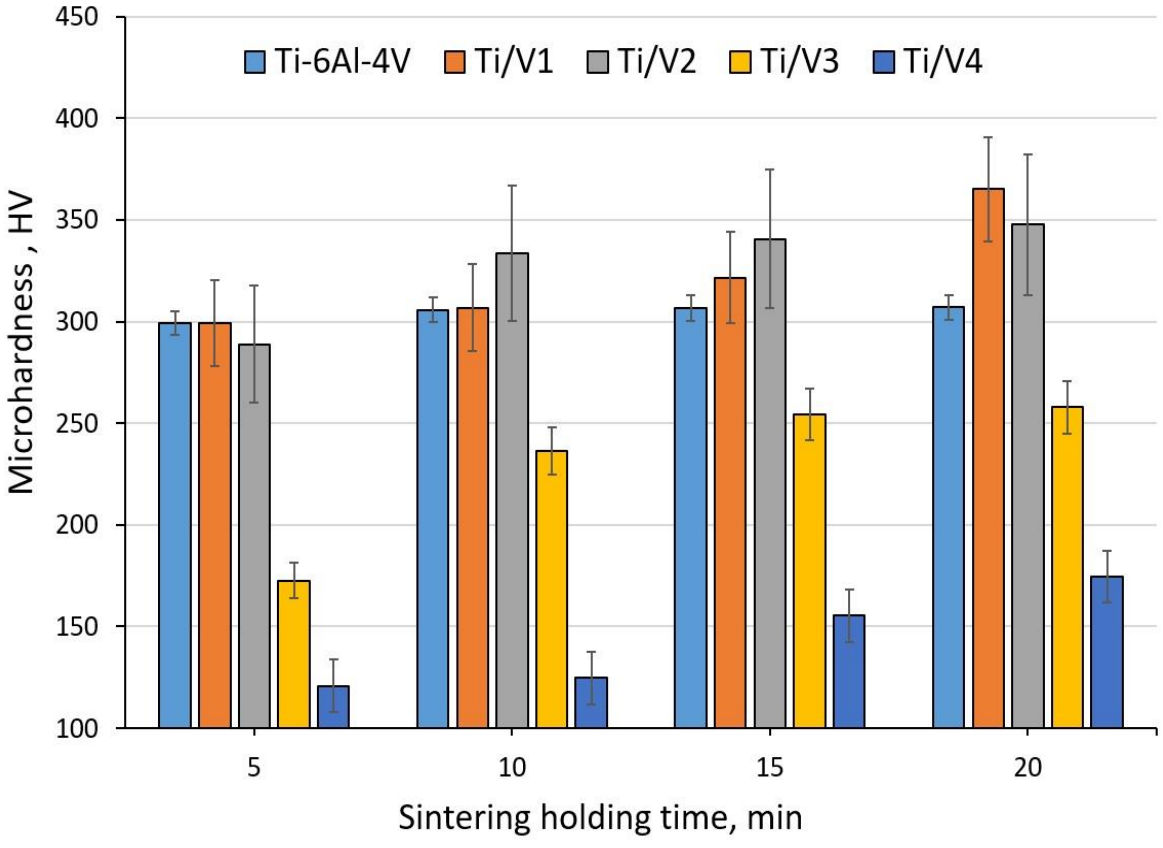

Figure 4.17 Show the effect of sintering time and V content on the hardness measurements. An increase in hardness was observed as the sintering time increased from 5 min to 20min, however, adding V to the mixture improve the hardness for Ti/V1 and Ti/V2, but a decline in the HV was evident when V content became 60 wt.% and 80% wt.

4.4.2 Tensile tests results

As mention previously in the methodology part, the sintered samples with different Ti wt.% and V wt.% amounts, were characterised mechanically according to E8/E8M-13a ASTM standard. Because there is no fully melting involves the sintering process only a small diffusion on the powder particle surfaces, the extracted tension samples from the sintered parts will require a low strain rate when they subjected to a tensile test to prevent rapid fracture. Therefore, a crosshead speed of 1mm/min was selected [181]. As the strain rate decreases, there is a great potential for enhancing the uniformity of elongation and improving the ductility behaviour during the tension test [202]. The tensile test was only carried out for the samples that sintered at a dwell time of 20 min. Figure 4.18 shows a set of tensile test samples prepared by EDM, each sintered sample having a gauge length of 12.5mm and thickness of 5mm. The tensile sample dimensions and the cross-head speed of 1mm/min were selected based on previous work conducted by Zarda et al. [146]. A sintered sample of Ti-6Al-4V powder alloy was processed by SPS without the addition of CP-V powder, at 1200˚C sintering temperature and 20 min dwell time, to be considered as a reference sample for comparison with the rest of the results of the blended sample.

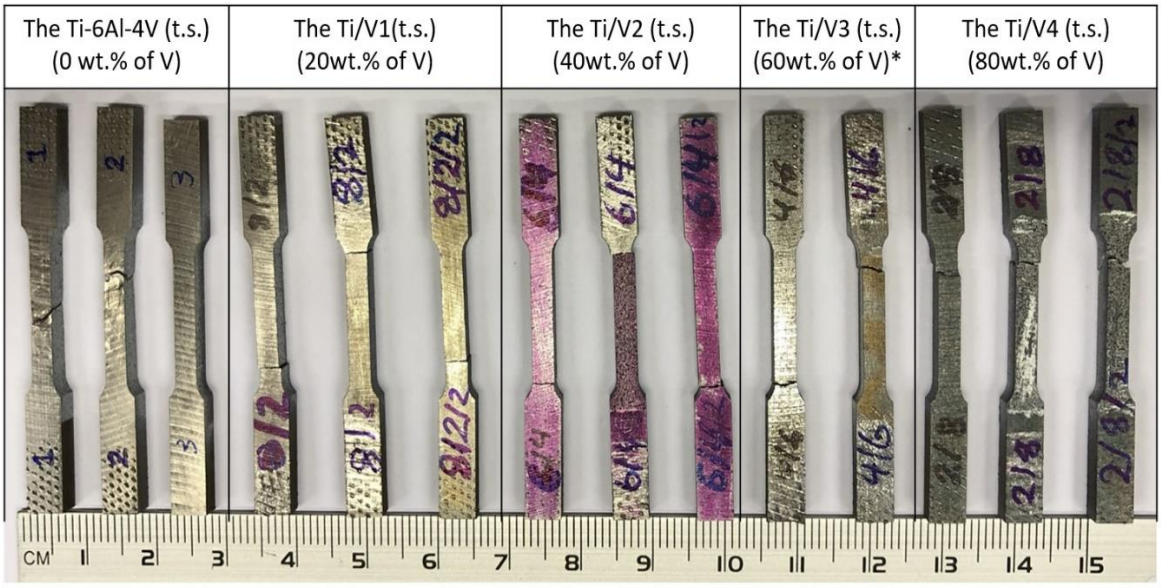

Figure 4.18 Show the tensile samples extracted from each sintered samples; three samples were prepared by EDM for each sintered alloy. * the third sample for the type Ti/V3 was not included in this image as it was broken into pieces.

Figure 4.19 shows the obtained tensile test curves which represent the tensile behaviour of the sintered samples containing different amounts of V wt.% and Ti wt.% upon applying the tensile test. The highest UTS was recorded for the reference sintered sample Ti-6Al-4V alloy, ~ 888 MPa with elongation reaching to 0.27%. A fully dense sample was achieved for the Ti powder alloy in all the selected dwell times. Figure 4.19a and c show a typical α′ phase structure of the Ti-6Al-4V alloy formed upon rapid cooling rate with the promotion of the tensile stress. Meanwhile, the other tested specimens with the addition of V wt.% showed different behaviour upon carrying out the tensile test. With the addition of 20 wt.% of vanadium, the sintered sample type Ti/V1 achieved a UTS of ~854 MPa with elongation of 0.13%. Sintering the alloy type Ti/V1 for 20 min was found preferable as a complete diffusion of vanadium particles in the Ti matrix was evident, as seen in figure 4.7, with no presence of pores or voids in the structure.microstructure.

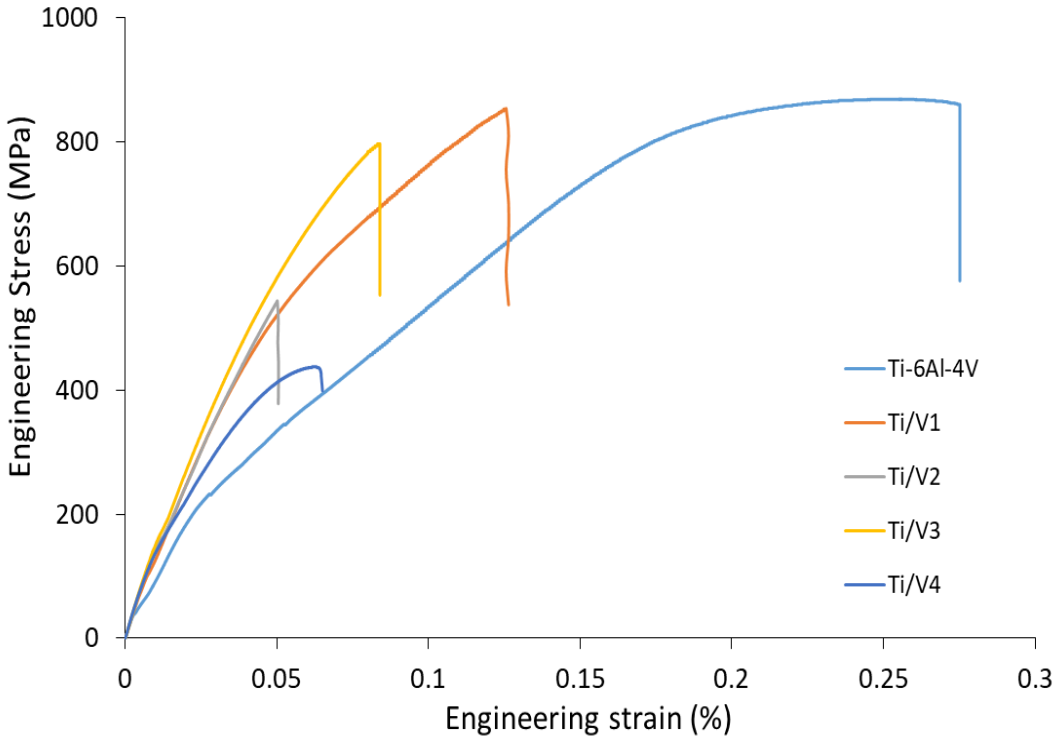

Figure 4.19 Show the effect of adding V wt.% to the on the tensile behaviour, all the samples sintered at 1200˚C sintering temperature for 20 min dwell time.

Meanwhile, the addition of 40 wt.% of vanadium produced a different impact on both hardness and tensile behaviours. The Ti/V2 sintered samples, despite having a higher amount of ductile vanadium alloy, recorded a higher hardness value, ~347±13. The trace of C in the mixed powder, suggesting the formation of IMCs Ti0.8V0.2C0.62 and Ti0.6V0.4C detected

by XRD analysis, may be another reason for the promotion of hardness values. The presence of porosity within the non-diffused V regions in the Ti/V2 sample was observed, as shown in figure 4.7, therefore, a ~544MPa was the maximum UTS obtained with a lower elongation of about 0.05% upon carrying out the tensile test. The sintered samples Ti/V3, which contained 60 wt.% of V and 40 wt.% of Ti, when subjected to the tensile test showed a high UTS of about 797 MPa but only 0.08% elongation. Despite the Ti/V3 alloy showing a lower hardness value of 255±7HV due to the high wt.% of ductile V, this alloy underwent a brittle fracture with no necking taking place upon commencing the tensile test. Due to the low diffusivity of V particles even at sintering temperature of 1200˚C and 20min sintering holding time, the presence of pores within the V-rich regions was identified, as shown in figure 4.8. Therefore, upon carrying out the tensile stress, a brittle fracture resulted, as these pores act as sites for crack initiation. Sintered sample type Ti/V4 showed the lowest UTS ~ 437MPa, with elongation of only 0.06%, which was attributed to the high amount of V wt.%, of about 80, and the 1200˚C and 20 min sintering conditions were not able to provide sufficiently dense materials. Therefore, large colonies of pores were located at the V-rich regions, with porosity apparent even at high sintering temperature and longer holding time, see images 4.9 and 4.20b, for example. Reduction in hardness was observed in the sintered samples with high V content of ~170±7HV1.

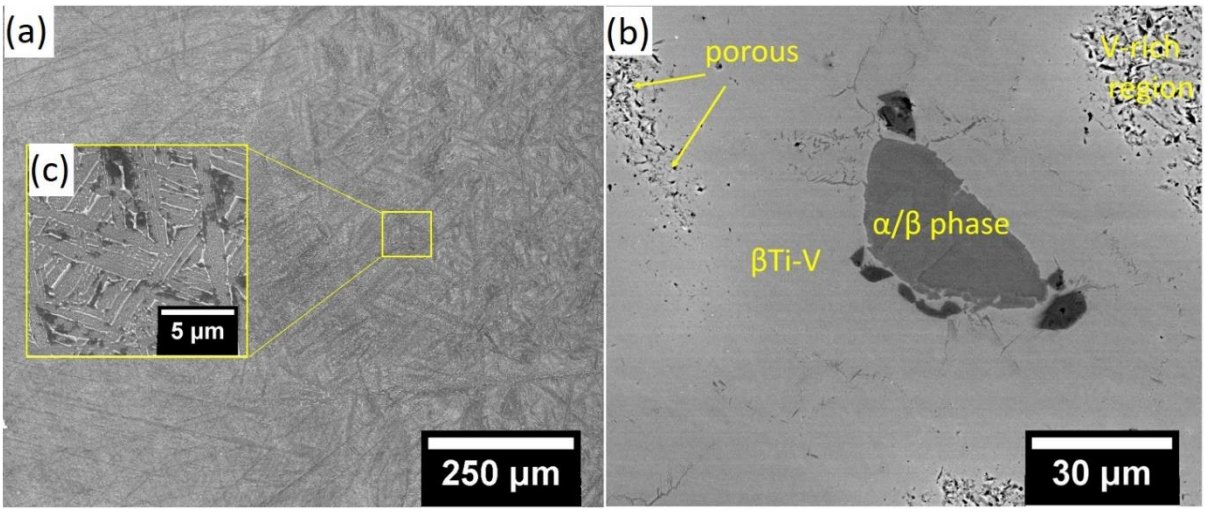

Figure 4.20 Show the different in microstructure of sintered samples for 20 min at 1200˚C for (a) a typical fine ά structures forms due to rapid cooling rate for Ti alloy and (b) the microstructure of the designed alloy type Ti/V4 showing three different regions which is; α/β structure represents the Ti-rich regions(dark colour), the βTi-V represent the diffusion regions (grey colour) and finally the V-rich regions which showing massive amount of pores between undiffused V particles .

It worth mentioning that due to the size limitation, the tensile samples were made by using a 60 mm diameter graphite mould, which help to provide a sintered disk with 5 mm thickness. Upon commencing the tensile test for Ti-6Al-4V alloy a slipping incident happen at the very beginning of the test when applying the load, therefore it can be seen from figure 4.20 abnormal behaviour in the tension curve of the Ti-6Al-4V tension sample and how it behaves under the applied load as compared with other tension samples of the designed alloys.

In summary, the selected sintering conditions were applied successfully to design new sintered alloys by mixing Ti and V powders in a specific wt.%. The micro-examination of the designed alloys reveals three regions. (1) an oval or circular zones with a dark colour which represent the α/β phase or the Ti-rich regions. (2) The lighter colour regions surrounded the α/β structure which shown previously in figures 4.6, 4.7, 4.8, 4.9, 4.12, 4.16 and 4.21, this represents the diffusion of V into the Ti matrix, and these regions are mainly of βTi-V. Finally (3), the two previous regions are surrounded by V particles; this was also observed at an earlier work [173]. As shown in figures 4.8 and 4.9, increasing the V amount shows excellent potential to improve ductility; however, a large amount of non-diffused V particles were observed, even with longer sintering time. Also, the presence of pores was evident, which confirms the necessity to increase the sintering temperature or sintering holding time to produce fully dense alloys with minimal porosity.

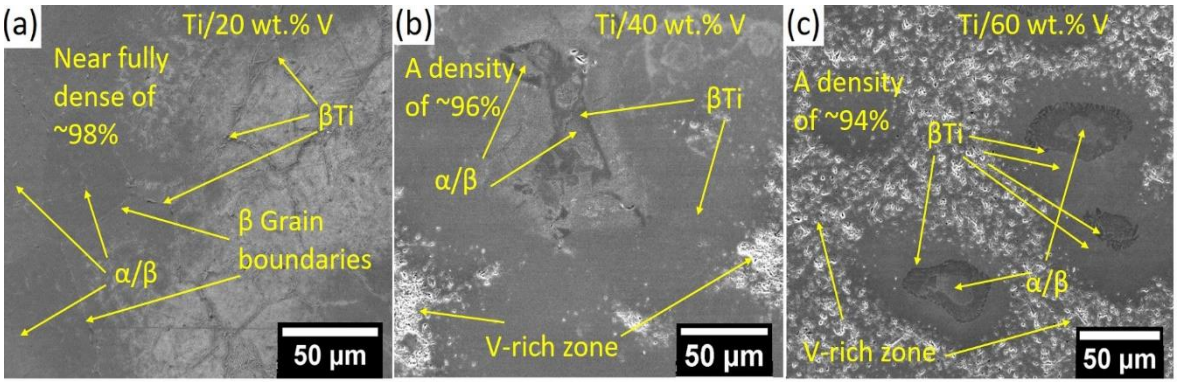

Figure 4.20 Show the SEM images of the microstructure of sintered samples (a) Ti/V1, (b) Ti/V2 and (c) Ti/V3. All the designed alloy were sintered under 1200 ˚C for 20 min.

4.5 Summary and conclusions

1. A Ti/V alloys were obtained successfully using Spark Plasma Sintering method.
2. The mixed powders of Ti and V were successfully processed by SPS at 1200˚C sintering temperature, 99kN applied force, 100˚C/min heating rate and 50˚C/min cooling rate.
3. The selected sintering parameters were suitable to achieve a fully dense sintered sample of Ti-6Al-4V under 5 min dwell time.
4. The increasing of the V wt. % powder in the Ti-V mixed powders, resulting in an increase in the holding time to 20 min as a necessity to advance the diffusivity of V particles in the Ti matrix and to produce fully dense alloy.
5. SEM and EDS confirmed elemental compositions and optical methods, showed three distinct regions, dark, grey, and bright, which are titanium-rich, Ti-V solid-state regions and vanadium regions, respectively.
6. XRD and EDS detected no secondary phases; however, a traced of C in the mixed powder suggesting the formation of IMCs $Ti_{0.8}V_{0.2}C_{0.62}$ and $Ti_{0.6}V_{0.4}C$ detected by XRD analysis, which may be another reason to promotes hardness value.
7. The maximum hardness values were recorded for designed sintered alloys type Ti/V1 and Ti/V2, about ~367±10HV and ~347±13HV1, respectively, at a maximum period of sintering holding time.
8. Both relative density and hardness of the designed alloys were a function of diffusion time at a fixed temperature of 1200˚C.
9. The presence of pores was evident, which confirms the necessity to increase the sintering holding time to produce fully dense alloys with minimal porosity.
10. The maximum UTS and elongation obtained for sintering Ti-6Al-4V powder alloy were ~888MPa and 0.27%, respectively.
11. The designed alloys type Ti/V1 and Ti/V3 showed UTS properties close to Ti-6Al-4V UTS of ~845MPa and ~797MPa, respectively.
12. The Ti/V3 alloy only achieved 0.08% elongation as compares to 0.17% from Ti/V1, due to the presence of porosity within V regions.
13. The presence of non-diffused particles in alloys Ti/V2 and Ti/V4 reduced the UTS to ~544 MPa and 437MPa with elongations of 0.6% and 0.05%, respectively.

CHAPTER 5: Effect of electron beam melting (EBM) parameters on the keyhole characteristics of titanium alloys weld tracks

Abstract

This chapter will highlight the steps employed to determine the best parameters to establish a keyhole weld gap in a titanium plate. The Arcam S12 EBM machine was adopted in this work. A design of experiments (DoE) based on normalised energy calculations was carried out, and weld beads-on-plate were employed to explore the best beam parameters that can achieve a full depth penetration with acceptable weldline features.

5.1 Introduction

Ti-6Al-4V is considered one of the most common titanium alloys for use in different applications. Its properties of low density, high elevated strength, high fatigue performance, good corrosion resistance and excellent weldability [4] make it a desirable option in the aerospace, thermochemical, automotive, medical and marine industries.

These excellent characteristics have led to the usage of this dual-phase alloy to cover half of the tonnage around the world as compared with other titanium alloys[203]. Joining titanium alloy Ti-6Al-4V is therefore considered one of the essential fabrication operations in these industries. When the titanium alloy is subjected to a welding thermal cycle involving heating, melting and then solidification, several changes take place in the microstructures and the mechanical properties. Each welding process impacts differently on the joint properties. Fusion welding processes such as EBW, LBW, PLW and GMAW have been used widely to join titanium alloys.

Moreover, the amount of the applied current controls the structure of the WZ and eventually affects the joint properties; for instance, where the welding method uses a high applied current, as in GMAW processes, the joint will be considered brittle, as it offers slow cooling rate. While in the case of EBW and LBW, the beam provides low heat input, which causes rapid cooling rate and the formation of α prime at the WZ provides a joint with high strength [56]. Mohandas et al. reported that if the WZ of the Ti-6Al-4V is subjected to a beam with low travel rate, there is a potential in avoiding the presence of porosity in the WZ; however, as the speed rate becomes lower, the plate-like α′ grains become of bigger size[58]. The Laser beam process was used by Cao et al. to study the effect of welding parameters on the microstructures and mechanical properties of Ti-6Al-4V weldments[8]. It has been found

that each welding process will have different variables, and those variables can cause dramatic changes to the welding profiles, joint microstructures and joint mechanical properties. Saresh et al. [30] studied the effect of welding process type on the formation of the keyhole in thick Ti-6Al-4V plates. The work included creating a joint with full penetration using LBW to accomplish a double-sided joint, which was suggested to overcome the lack of penetration that occurs when using EBW process to join thick sections of the same alloy [30].

In the present work, the Electron Beam melting process by Arcam S12 machine was used as the welding equipment to perform welds of 6 mm on Ti-6Al-4V plates using the bead-on-plate method. Further analysis on the effect of beam parameters, morphology and keyhole profile, is commented upon in order to offer acceptable welding settings. The methodology included the use of normalised (design of experiments) and discrete (linear) approaches. Further evaluation of the microstructure and mechanical properties is reported.

5.2 Materials and Methods

In this work, a Ti-6Al-4V plate with dimensions of 250mm x 150mm x 6mm was used. Table 5.1 shows the chemical composition of the selected plate. The weldtrack lines were obtained using an Arcam S12 machine located at the MAPP Centre, the University of Sheffield. Two approaches were employed to determine the required melting parameters. The melting tests were performed using Bead-on-Plate method. The Set I variables from the normalise approach was used to run the first order for obtaining the weldtracks. Then a second Set II of weldtracks was obtained with the Arcam S12 machine using variables suggested in a discrete way. After the melting process was completed, a macro-examination of the obtained weldtrack profiles was carried out to select the variables that offered an acceptable weld line with minimal defects and exclude the variables that produced defected weldtracks. The macro- examination was conducted according to BS 4677-001, BS EN ISO 6201-1 and the AWS 2001. After the macro examination, the weldtracks were sectioned across the weld line. Then a micro preparation procedure was carried out which involved mounting, grinding and polishing steps. The etching procedure was performed using Kroll's solution. A Nikon optical microscope was used to perform the microstructure analysis, and a Durascan instrument was used to carry out the microhardness measurements. The applied hardness load was set to 1HV, and the duration of the applied load was 20 seconds. A series of 22 indentations were made to measure the distribution of the hardness from the centre of the WZ toward the BM.

Table 5.1 The chemical composition of Ti-6Al-4V titanium alloy (wt%).

Elements	Ti	Al	Fe	C	V	N	O
Ti-6Al-4V (plate)	Balance	6.29	0.19	0.012	4.04	-	0.214

5.3 Design of experiments

Design of experiments (DoE) was followed in order to determine the critical parameters of the working zone and the optimal settings for the process. During the welding operation, the formation of the keyhole gap can be affected by several variables, such as the type of the welding process, welding current, welding speed, physical properties of the alloy, etc. Therefore, the DoE can help to create an interaction with several factors and the resulting design will reduce the number of experimental runs and, moreover, provide a reduction in the process parameters.

A normalising model by Thomas et al. [166] was employed. Set I of welds suggested parameters of beam speed and beam current based calculations for normalised beam power q^* and normalised traverse rate v^*[165] following previous attempts in the keyhole regime for 10 mm thick plates[167], see figure 5.1. Beam current was calculated from the constant voltage (60kV) used in the Arcam system to be further obtained from normalised beam power for $q^* = {Aq}/{[r_b \lambda (T_m - T_0)]}$ where A is the surface absorptivity (0.47), rb is the spot diameter (0.5 mm for an Arcam system [204]), λ is the thermal conductivity (15.75 W/m.K), T_m and T_0 are melting and initial temperature respectively [33][205][206]. Normalised beam power is in turn defined as; $q* = l^* v^* L_v^* + \frac{l^{*2} v^* L_m^*}{4} + \frac{2\pi l^*}{\ln(8)}$, where l* is the normalised depth of treatment (isopleth of 20 for this work considering a depth penetration of 10 mm and a spot size r_b = 0.5 mm), v^* is the normalised beam traverse rate (a value of 0.35 was determined following welding attempts reported previously [167]), L_m^* and L_v^* are volumetric latent heats of melting and vaporisation with values of 0.39 J/m^3 and 3.9J/m^3 for metals and alloys. Depending on the thermophysical properties of the dedicated alloy, such as density, melting temperature, thermal diffusivity and thermal conductivity, the model can determine the required energy and heat to melt the alloy. The model uses a Response Surface approach to draw an estimation for the required number of runs and the required variables of the process to create a keyhole in a plate. Table 5.2 shows the outcome summary of the normalising model.

Table 5.2 Show the Set I parameters proposed by the normalised model for creating the bead-on-plate weldtracks using Arcam S12 machine

Weldtrack (1-12)	Beam Current (mA)	Beam Travel (mm/s)	Theoretical Avg. Bead width (mm)	Experimental Avg. Bead width (mm)
(M1) a	29.57	2.93	4.15	5.48
(M2) b	26.59	3.22	2.20	5.2
(M3) c	33.16	3.22	2.20	3.75
(M4) d	26.72	3.22	4.10	4.24
(M5) e	30.00	4.06	2.56	3.75
(M6) f	35.03	4.06	2.98	6.25
(M7) g	30.00	4.06	2.67	3.94
(M8) h	30.00	4.06	2.98	3.05
(M9) i	30.00	4.06	2.98	4.81
(M10) j	27.30	5.11	3.33	2.88
(M11) k	33.87	5.11	2.95	4.33
(M12) l	30.59	5.62	3.50	5.10

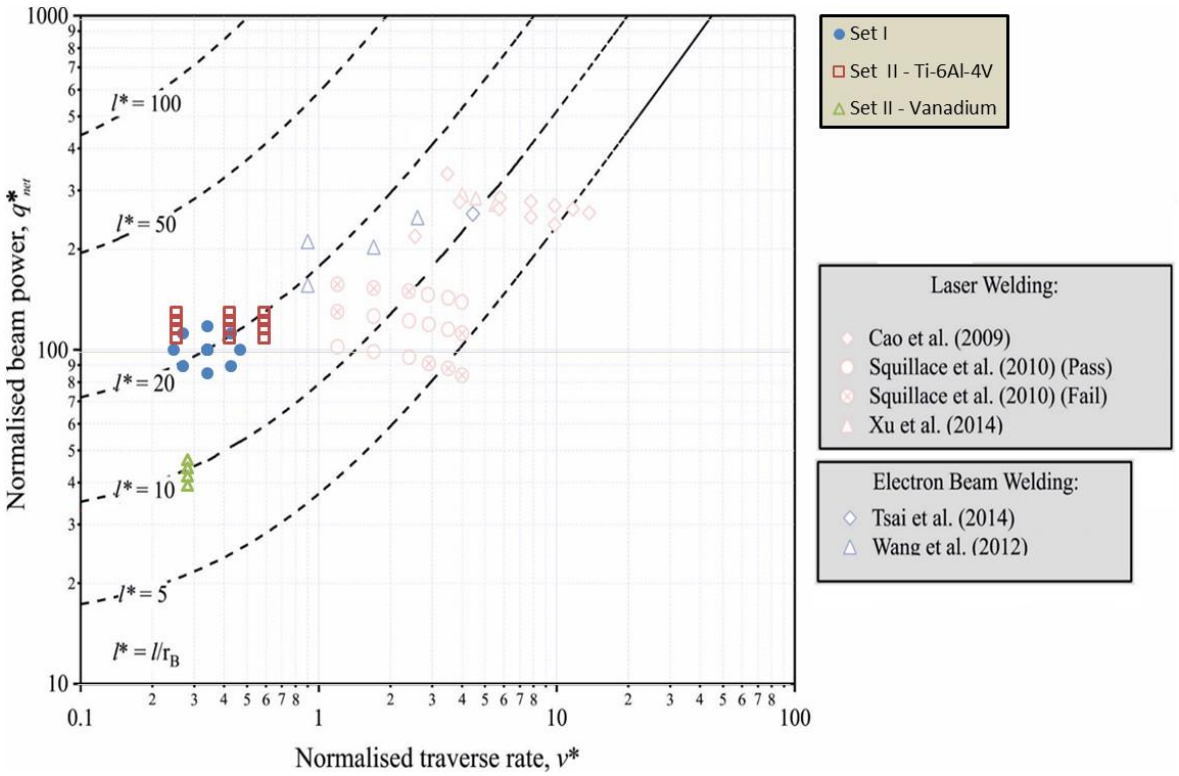

Figure 5.1Parameters of beam speed and beam current used for the set I and II in Ti-6Al-4V and vanadium plates. Additional literatures are shown for further reference.

Set II, on the other hand, was composed assigning beam current and beam speed at discretion based on set I result. This was in order to achieve the best weld features at full penetration. For the purposes of comparison, normalised values are plotted in figure 5.1, where the traverse rate was obtained from the expression for $v^* = {}^{vr_b}/_{a}$ where; *v* is the beam speed, and a is the thermal diffusivity, 5.79 x 10-6 m^2/s and 1.21 x 10-5 m^2/s for Ti-6Al-4V and CP-V [207]. Adopted values for absorptivity coefficient for vanadium was the same as Ti-6Al-4V due to minimum differences reported for flat surfaces [208].

5.4 Experimental procedures

The acquired variables from the normalising model were used as guide values for application to the Arcam computer. The operation mode of the Arcam machine was set to manual, to enable easy control of the location of the step-in and step-out of the welding line. The designated 6mm Ti-6Al-4V plate for the bead-on-plate trails was placed in the centre of the machine chamber and a series of measurements implemented to determine the exact location of the plate. Then these measurements were fed into the Arcam computer so that during the welding process, the beam would run over the required line. Throughout performing the experiments, the beam voltage was kept constant at 60kV, and the beam offset was maintained at -2mA, while the beam current (mA) and the beam travel speed (mm/sec.) were the parameters selected as variables in this study. In electron beam welding, the mechanisms of metal welding are well known as reported in the literature. Weglowski et al.[209]. In a similar way in this study, the electron beam starts moving, providing potential energy transformed kinetic energy and thermal energy impacting the surface of the plate. Soon the metal reaches a melting point, forming a pool of molten alloy in the beam spot. As the beam moves forward, a gap of a liquid alloy is formed along the travel direction of the beam. The variables from table 5.2 were the primary inputs used to perform weld beads on plate experiments. Twelve weldtracks were obtained, each of 50mm in length. Most of the weld lines showed abnormal features and imperfections such as undercut, underfill, excessive welding root, cavities and overlap. Figure 5.2 shows the weld beads-on-plate for further examination.

5.4.1 Weldtrack morphology and keyhole

In general, all the obtained weldtracks shown in figure 5.2 achieved a full penetration single-pass process depending on the Set I inputs; however, there was an apparent irregularity in the weld line profiles. As the beam moved forward, a narrow weld line was formed until 50% of its total length was completed. At this point, a dramatic change appeared in the weld linewidth due to the effect of the overlap caused by the travel of the beam pushing the molten metal, with most of the melted alloy accumulating at the end of the line in a hump-like formation. The total length of each line was in the range of 55-60 mm; however, the weld line was set to 50mm, and the extra length was due to the effect of step-in and step-out action. After the welding was complete, a visual inspection was performed using the BS EN 4677-001 and BS EN ISO 6520-1:2012 [210], [211] to determine and assess the quality of the weldtracks. The evaluation involved studying characteristics such as the weld line profile, the weld face width, the weld root width, additionally, examining the presence of weld defects such as face undercut, excessive face weld metal, excessive penetration and incomplete filled groove, porosity and cracks, if applicable.

According to the figure 5.2, despite most of the test variables in table 5.1 achieving weldtracks with full penetration, they failed to achieve a continuous smooth welding line and the appearance of most lines was predominantly intermittent, showing a wide weld seam with a deformed profile. Some of the weldtracks showed interruption of the position that produced a discontinuous weld line, especially when the beam was run at a slow rate, see weldtracks (a, b, f,h and l) in Set I figure 5.2, which might have been due to imbalance between the intensity of the beam current and the rate of travel speed. Meanwhile, the rest of the weldtracks shows a narrow gap at the beginning, and most of the molten metal had dropped out through the weld root, forming a saggy root defect see figure 5.3a, 5.3 d, 5.3e, 5.3e, 5.3f, 5.3j and 5.3k. The underfill condition was critical in most of the weld trucks, see figure 5.3. When a high beam current is applied, an excessive heat input occurs, leading to the melting of a high amount of the alloy at the weld face line; therefore, under the beam spot, the fusion metals will exhibit two conditions: gas and liquid. This was reported previously as due to the high heat input caused by high beam current, the alloy melts and evaporate from the WZ, leaving an insufficient amount of molten metal within the WZ [68]. In figure 5.3, which shows the keyhole cross-section profiles of the weldtracks, the collected data shown in figure 5.4 are very scattered and fluctuating due to the unbalance between the applied heat input and the travel rate, causing inhomogeneity in the production of the

weldtracks. Because the molten metal is denser in the liquid condition, it tends to settle at the keyhole bottom (root) due to gravity, while under the gas condition, a light vaporised metal attempts to make its way up towards the top of the keyhole, forming a convex shape along the weld and causing a deficiency of molten metal in the WZ. Examples for the underfill condition can be seen in figures 5.3a, 5.3d, 5.3e, 5.3f, 5.3g, 5.3i, 5.3k and 5.3l, most of which show a cross-section of a keyhole region with large cavities at the weld face and excessive size of solidified molten metal at the root.

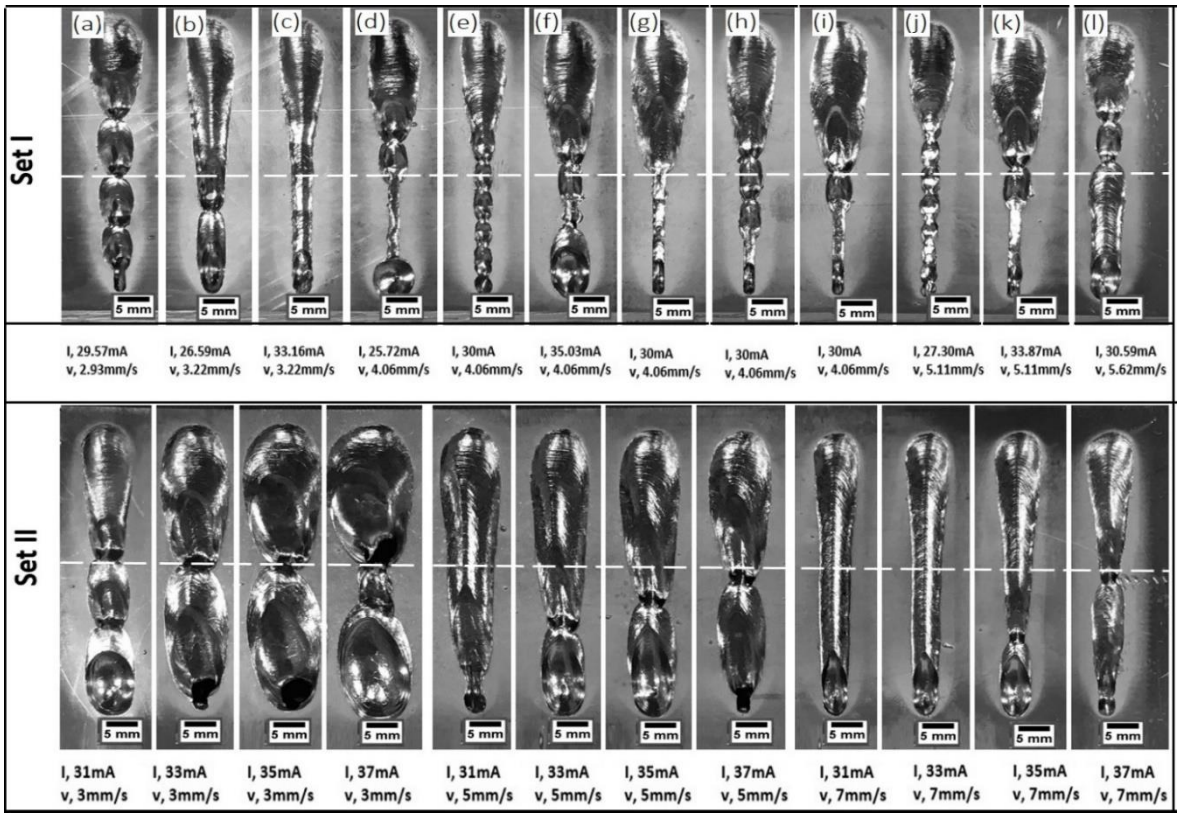

Figure 5.2Show the weldtracks achieved by Arcam S12 machine using Set I (the normalise approach) and Set II (the linear approach) inputs.

Most of the weldtracks had a hump along 50% of their length, see weldtracks (a-l) of Set I in figure 5.2, which was due to the overlap of the molten metal. This hump occurred when the titanium alloy melted and when the specific volume increased to about 16% of the original specific volume, meaning that the excessive molten metal was unable to fit in the original welding groove, which caused it to spill over the joint edges and created a hump-like formation [9]. This humping, according to Fotovvati et al.[212], is due to turbulence in the molten pool caused by vapour escaping from the WZ; additionally, the presence of the humping condition will affect the penetration depth of the keyhole, possibly because of the

rapid welding speed or an excessive heat input using high beam current affecting the fluidity of the melted alloy in the WZ [213].

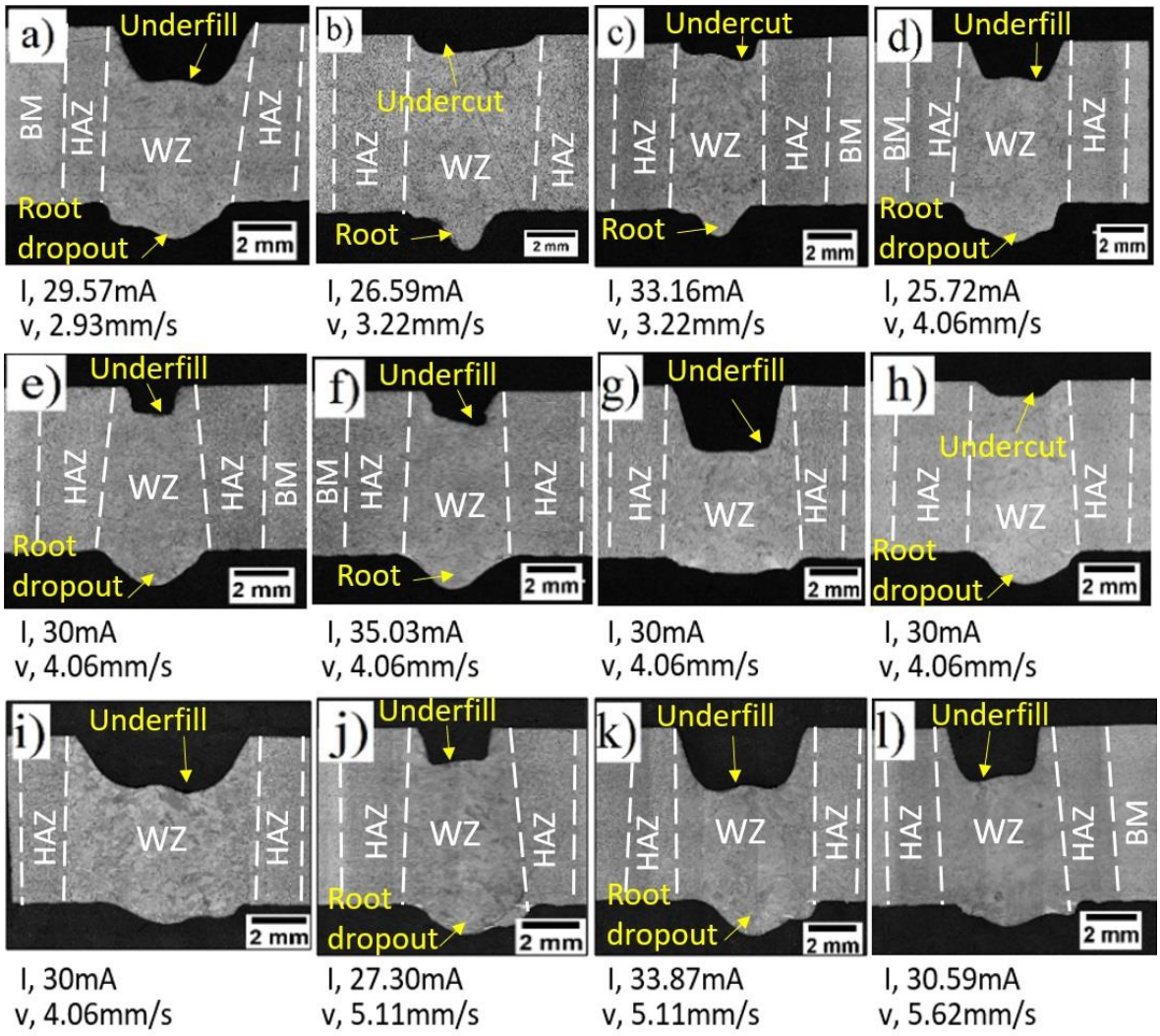

Figure 5.3 Optical micrograph of the cross-section images of the weldtracks obtained by adapting the (normalise approach) Set I inputs. Defects such as undercut, underfill and root drop-out were common issues in all the achieved weldtracks.

From figure 5.4, there is no clear trend in the formation of the keyhole shape; however, the speed rate and the intensity of the heat input from the beam current have a significant impact on the size, depth, width of the keyhole as seen in figure 5.3. The width of the keyholes varies widely with the level of the heat input, and the welding travel rates, as seen in figure 5.4. However, the intensity of the heat input showed a significant effect on the width of the keyhole resulting in a wide WZ when heat input increased either by increasing the beam current or lowering the beam travel speed. When the beam hits the alloy surface, it melts and changes from a solid-state into liquid. The beam then is surrounded with a thin layer of liquid

molten metal. As the beam moves forward, it pushes away the liquid to the sides and back due to the high pressures generated inside the keyhole by the melting process. When the beam shifts forward, the melting pool will no longer under the heat source, so it changes back to the solid-state.

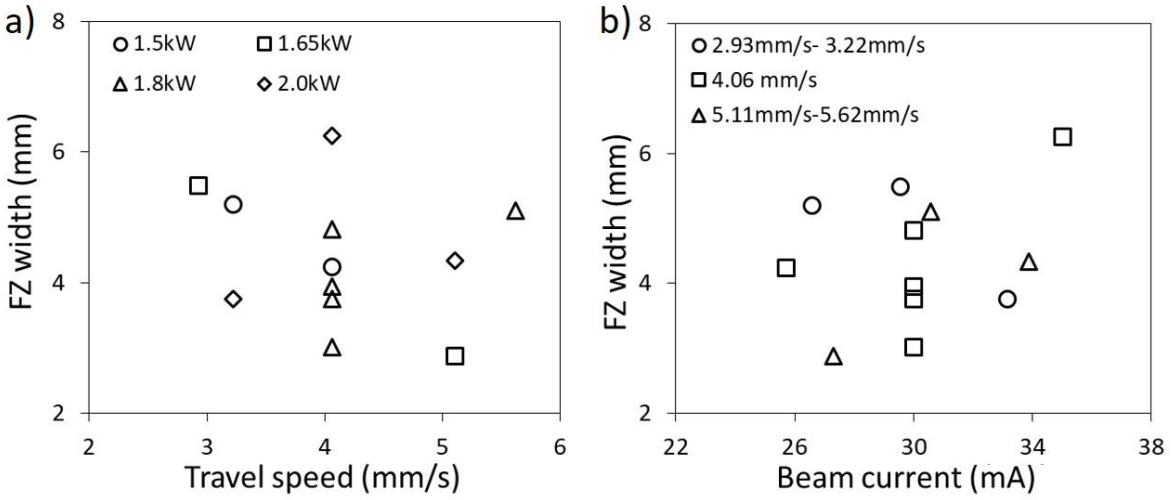

Figure 5.4 Shows (a) the relationship between travel speed and width of the WZ under different heat inputs, (b) the effect of beam currents on the width of the WZ.

The edges of the keyhole which are in direct contact with liquid metal are exposed to a high amount of heat input, see figure 5.3c, therefore upon cooling a complex structure will be formed in these adjacent areas which are known as heat-affected zones (HAZ) [214]. As shown in figure 5.2 and 5.3, the level of heat input represented by the beam current (I) and the rate of beam travel speed (v) have a unique influence on the width of the keyhole profile. On the other hand, the DoE method provides a set of weld speed rates to be used in order to determine the suitable rate of travel speed for maintaining a constant depth along the weldtracks. Figure 5.5 highlights the relationship between the speed and the heat input with respect to the keyhole depth of the weldtracks. Under relatively low travel speeds, the amount of heat input at the surface becomes excessive, leading to melting of the metal across a wide area and formation of a wide pool of molten metal at the surface. The low-speed rate also prolongs the solidification rate, allowing the metal to stay in the liquid phase for a long time, thereby causing large amounts of metal to melt and escape as molten metal and to hang beneath the base, forming what is known as excessive welding penetration at the root of the keyhole. Also, due to extended exposure to high heat input, the area adjacent to the melting zone, which is known as the HAZ increases eventually. The nature of the experiments meant

that several weldtracks were produced next to each other at the same time, and therefore, a measurement of adjacent heat affected zones was difficult due to their overlapping.

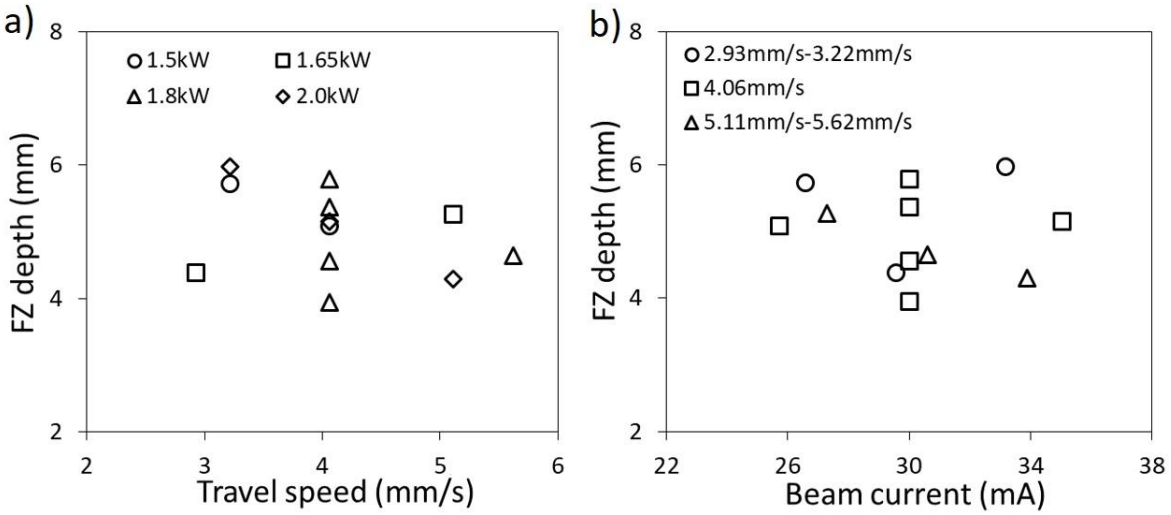

Figure 5.5 Shows (a) The effect of the travel speed on the depth of the keyhole weldtracks, (b) The impact of Beam currents on the keyhole depth

Additionally, from figure 5.3, it can be seen that in most of the cross-section area of the keyhole profiles, the weld face width is almost equal to the root width. The thin thickness of the titanium plate allows the heat from the beam to transfer in full from the top surface down to the base at the same level. This differs in the case of the thick sections, where the keyhole profile generally exhibits greater width of the fusion area on the top at the weld face, while the root exhibits the narrowest width in the WZ due to the high intensity of the beam at the surface resulting in melting of broad areas. Then, as the beam travels through the thickness, the intensity is reduced because the heat diffuses through the thickness and less melted area is formed, leaving a WZ of keyhole-like shape in the prior melted alloy. According to figures 5.3, the aspect ratio of the root width to weld face width of the fusion keyhole area, as seen in figure 5.6a, where most of the values close to (1) — indicating an equal in width for the face and the root of the WZ, which is evident in the case of the weldtracks carried out with high heat input. While the lower values, imply a narrow root and wide weld face, especially at fast rate travel speed and low heat input. Figure 5.6b indicates the impact of the heat input intensity according to the beam travel rate on the root dropout ratio; in general, this ratio directly proportional with welding speed rate. The high heat input using high beam current or low travel rate caused a saggy shape at the weldtracks' roots. These saggy roots represent the drop-out of metal or the collapse of metal from the weld root due to the keyhole melting

pool being subjected to prolonged heat exposure. The root dropout ratio in figure 5.6b represents the width of the root over the length of the root.

The only trail that produced a promising acceptable weld track profile was (c), see figure 5.2c in set I. The weld line was a result of using a beam current of 33.16mA and travel speed of 3.22mm/s; however, the undercut was still present in the WZ area at the bead surface, as is very clearly shown in figure 5.3c.

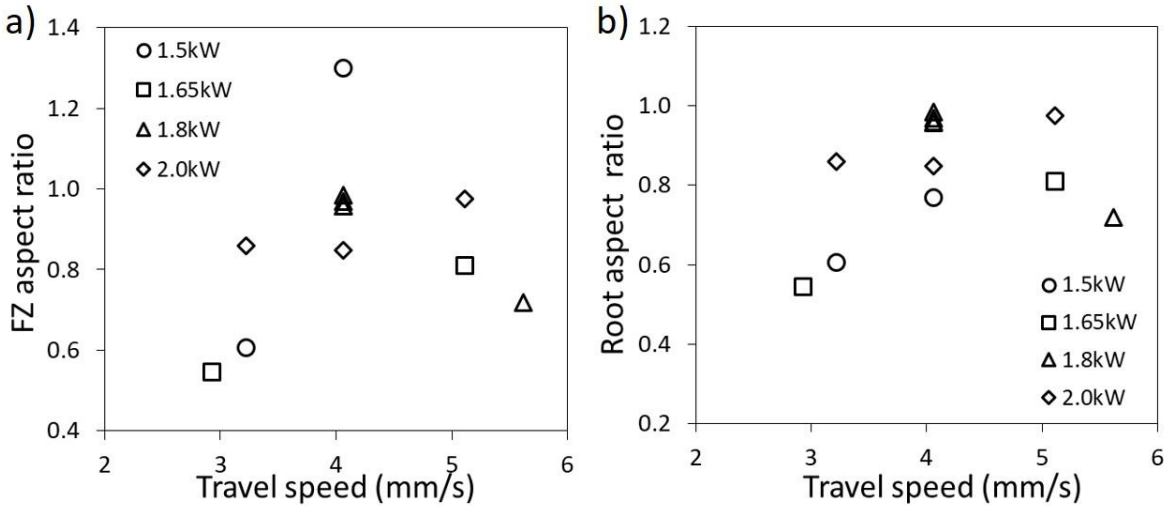

Figure 5.6 Showing experimental travel speed effect on the weldtrack keyhole dimensions,(a) FZ aspect ratio ($Root_W/Face_W$), and (b) Root aspect ratio (Root drop-out ratio).

5.4.2 Optimising the electron beam melting parameters

Despite the usefulness of the normalising approach for determining the highest and lowest values for required welding parameters such as welding current and travel speed, a set of variables was suggested the linear approach to refine welding parameters and to compare the results of the two methods. Table 5.3 shows the welding variables suggested by the linear method.

The linear method was proposed in order to make further adjustments to the electron beam melting parameters. Localising the levels of the variables offers an excellent chance to examine the effect of the interaction of the amount of the beam current and the beam travel on melting, solidification and the formed keyhole in the WZ.

Table 5.3 Illustrate the proposed parameters by the linear method for weldtracks obtained by Arcam S12 and the measurements of the width and depth of the obtained keyholes.

Weldtracks (1-12)	Travel speed (mm/s)	Beam current (mA)	Bead width, W (mm)	Bead depth, D (mm)
a	3	31	6.825	5.250
b	3	33	9.81	4.574
c	3	35	11.155	6.924
d	3	37	12.21	3.864
e	5	31	6.42	6.528
f	5	33	8.175	6.624
g	5	35	8.365	5.664
h	5	37	7.79	4.500
i	7	31	5.675	6.408
j	7	33	5.58	6.336
k	7	35	5.385	6.360
l	7	37	5.575	5.532

From figure 5.7, it can be seen that all the weldtracks achieved full penetration; however, each weldtrack produced during the fusion and solidification of the melting process has a unique profile. All the weldtracks carried out under low travel rate produced weld lines with a wide fusion weld face and excessive melt-through. This can be related to an increase in the level of the heat input when the beam travels in a slow rate, resulting in high amount of melted alloy and irregular weld face with a high chance of excessive root dropout or excessive root size. The distorted profile of the weldtracks was a common issue when the travel rate of the beam was set to 3mm/sec for the different weld beam currents. Figures 5.7a, 5.7b, 5.7c and 5.7d show the shallow weldtrack profiles produced using a beam with travel rate of 3 mm/sec and beam currents of 31mA, 33mA, 35mA and 37mA, respectively.

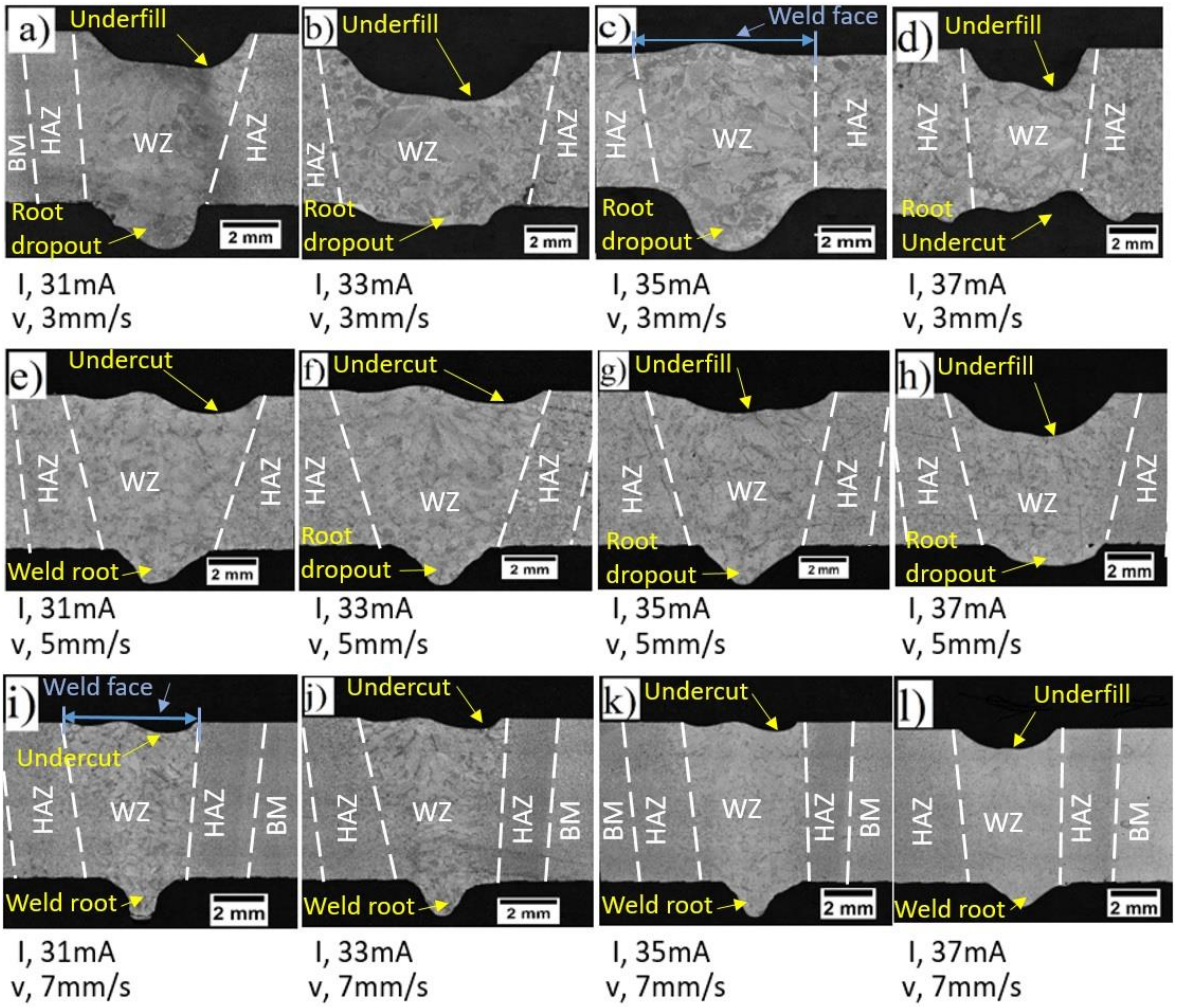

Figure 5.7 The cross-section profile of the weldtracks obtained by employing the (linear approach) Set II data. Defects such as undercut and underfill were common issue with high heat input and low welding speed.

When the travel rate was increased to 5mm/sec, the produced weldtracks started to become narrower when compared to those produced with a travel rate of 3 mm/sec. Figures 5.7e, 5.7f, 5.7g and 5.7h, represent the weldtracks produced using travel rate of 5mm/sec and beam currents of 31mA, 33mA, 35mA and 37mA, respectively. From the weldtrack profiles as the travel rate increased the effect of the heat input reduced, which leads to producing narrow weldtracks with straight lines. Unfortunately, these weldtracks contain defects represented by intermittents spots in the weld line profile, which are considered as defects and a major failure in welding inspection tests [215]. As the travel rate of the welding beam increased to 7mm per second, a clear improvement was observed in all weldtrack profiles, see figure 5.7i, 5.7j, 5.7k. This rate of beam speed provided smooth welding with an acceptable weldline profile represented by a straight, narrow weld face and acceptable undercut percentage[216]. However, the weldtracks started to become inconsistent in shape

as the heat input increased when the current of the beam was set to 35 mA and 37 mA, see figures 5.7k and 5.7l, and intermittent undercut started to form at the welding line and the undercut depth increased from 0.35mm to 0.69 mm when the beam current increases from 31mA to 37mA. From figure 5.8a, it has seen that the bead width size of the weldtracks is proportion inversely with the beam travel rates. However, the width of the WZ was a function of the heat input, as seen in figure 5.8b. Squillace et al. [9] and Karimzadeh et al. [56] reported that as the heat inputs increases, in term of increasing the beam current, the width of the WZ becomes wider due to the high heat input amount which advanced the size of the melting pool, especially when the beam travels at a low rate; 3mm/sec.

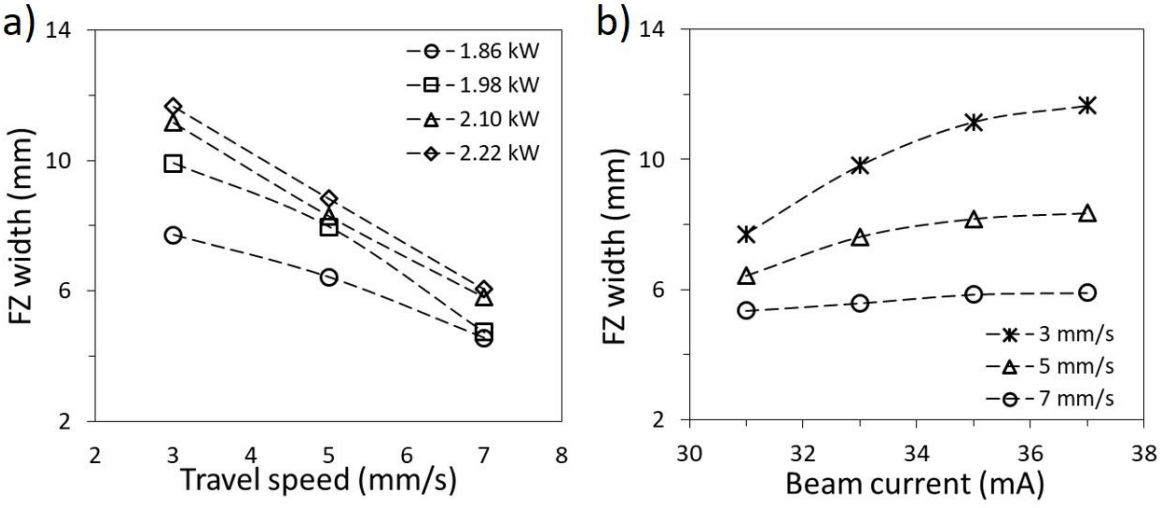

Figure 5.8 The effect of travel speed, specific beam current on the width of the weld keyhole for the weldtracks obtained using the linear method data.

It was reported that reduction or an undercut in the weldtracks takes place during the melting process of the alloy. The high heat input causes a certain amount of molten alloy to vaporise, shown as spatters alongside the weldtrack line [9]. Based on strict advice from the American Welding Society (AWS 2001) [217], welded joints with undercut depth exceeding 7% of the total thickness of the welded plate or lower than 0.1t (where t is the plate thickness) according to the BS EN 4677-001-2012 [211] are not acceptable, due to stress concentration this causes at the HAZ area of the welding joint. Therefore, this project adopts a maximum undercut depth of 0.45mm of the weldtracks for a plate of 6mm thickness. The undercut defect condition can be severe as shown in the cross-section weldtracks keyholes in figures 5.7a, 5.7b, 5.7d, 5.7e, 5.7g, 5.7h and 5.7l, (1.4, 2.14, 1.36, 0.64, 1.1, 1.4 and 0.69 respectively, or minor to acceptable (0.64, 0.35, 0.46 and 0.3) as in the weldtracks shown in

figures 5.7f, 5.7i, 5.7j, and 5.7k, respectively. The cross-section images of weldtracks achieved with the lowest rate of beam travel, 3mm/sec, are shown in figures 5.7a, 5.7b, 5.7c and 5.7d, respectively. Figure 5.9 draw a conclusion on the depth of the WZ affected by the amount of the applied heat input and how this depth can be affected as well with the rate of beam speed. There was clear underfill at the centre of the weldtrack face, caused by evaporation of the molten metal at low speed which resulted in extreme melting temperature that led to a phase transition from liquid to the gas phase. Also, the high heat input due to slow beam travel rate, the alloy will stay longer in the liquid condition, even when the heating source (the electron beam) removed. As a result, the adherent forces between the liquid molten metal and the solid metal decrease due to the reduction in the surface tension so these forces will not be able to hold and support the molten metal in the welding gap. Therefore, the melting pool will collapse and a large amount of molten alloy escape from the welding root, in the form of a big droplet, see figures 5.7a, 5.7b, 5.7c, and 5.7h, for an instant wich showing excessive root size.

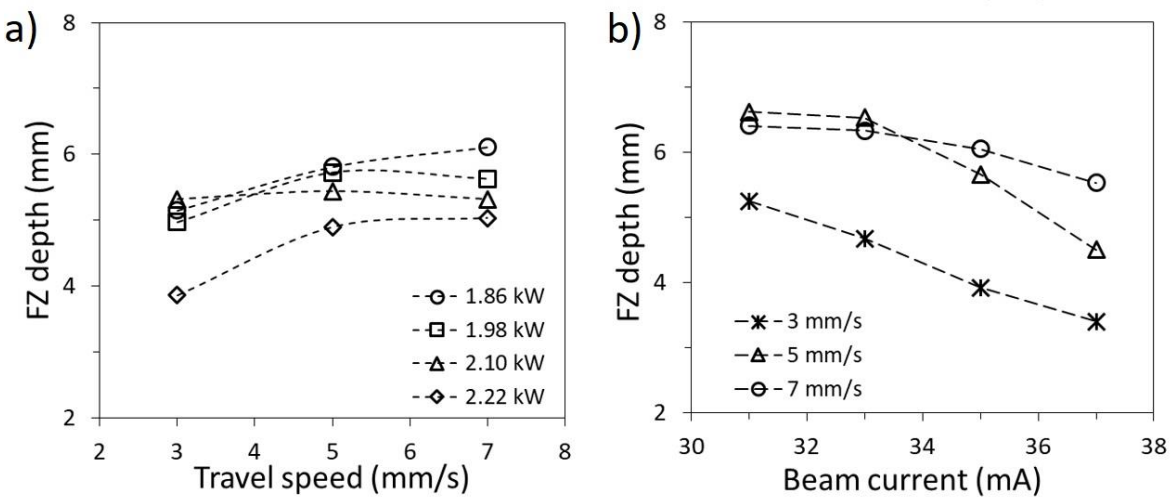

Figure 5.9 The effect of (a) travel speed and (b) beam current on the WZ depth.

Figure 5.10 (left) shows the effect of beam travel rate on the root drop-out ratio (d_{root}/w_{root}). With increasing the beam travel rate the drop-out ratio of the root increased and was situated in the range of (0.3-0.5), while with the low-speed rate the ratio fluctuated and the drop-out size varied with different beam current. The negative value indicates that the weldtrack has an undercut at the root area due to contraction of the molten metal after the solidification condition. Moreover, as the speed rate increased the keyhole profile take the shape of the cone were the wide base is the weld face, and the tip of the triangle is the root see figure 5.6k and 5.8l. Also, it was observed in figure 5.10 (Right) the aspect ratio of the root/face width

increased with increasing the heat input due to low travel rate. With high heat input travel through the alloy, the molten pool size at the root and the face will have the same width as shown figure 5.7a and 5.7b.

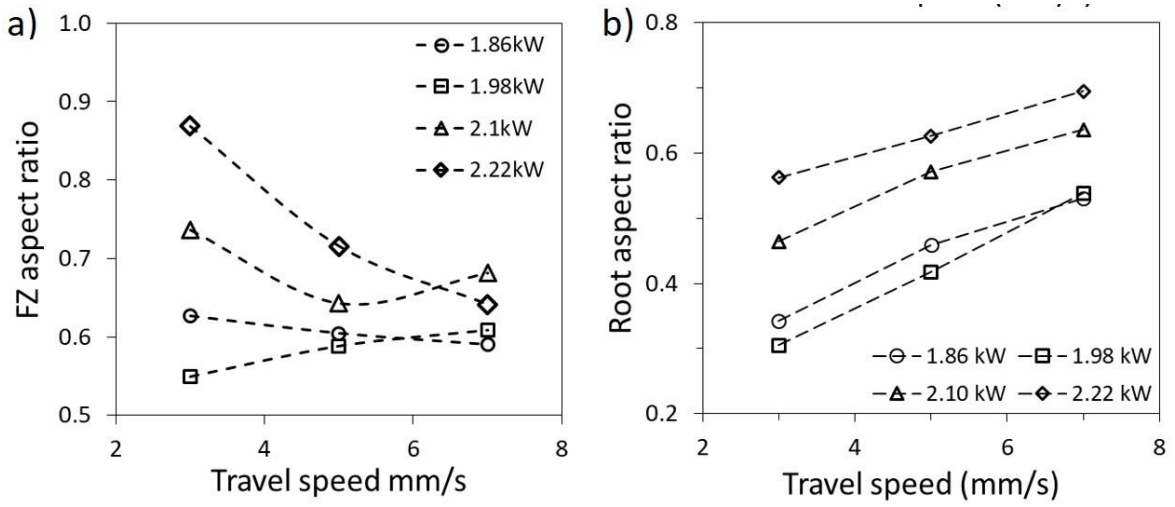

Figure 5.10 The effect of travel rate of the electron beam on (a) The FZ aspect ratio (root/face width) (b) the Root aspect ratio (root drop-out ratio).

5.5 Results and discussion

5.5.1 Microstructure analysis

The microstructure examination shows that the initial structure of the Ti-6Al-4V, as seen in fig 5.11, consists of equiaxed α grains and lamellar α/β grains, with a grain size of around ~36μm. When a beam of high-speed electrons hits the surface of an alloy, their kinetic energy will be transformed into thermal energy, which heats the metal to its melting point. Conditions for microstructural transformation are therefore given to create three areas. The welding zone, WZ, which represents the area that is subjected to the applied heat. The heat-affected zone (HAZ), an area affected by heat conduction and third, the unexposed area, the base metal (BM), with no change in microstructure. Figure 5.11 illustrates the three different regions in the cross-section of the weldtrack keyhole. During the heating process, the dual α/β structure changes to single β-phase when the alloy reaches the melting point. However, when the source of the applied heat is removed due to the beam travel, the solidification process begins as the melting pool gradually starts to cool down from the peak temperature. When the temperature reaches the β-transus, the single β-phase changes to acicular α´ structure upon rapid cooling rate. Figure 5.11c shows, as reported, the dendritic structure of the WZ, which consists of prior β- grain boundaries and a needle-like α´ structure [70].

Despite the thin section of the welded plates, the low travel rate of the welding beam prolongs the exposure of the alloy under high heat temperature, causing a slower cooling rate leads to a growth of the fine α′ to become thicker, and dendritic columnar structure[218] to form upon cooling from the fusion edges toward the welding centre line [13].

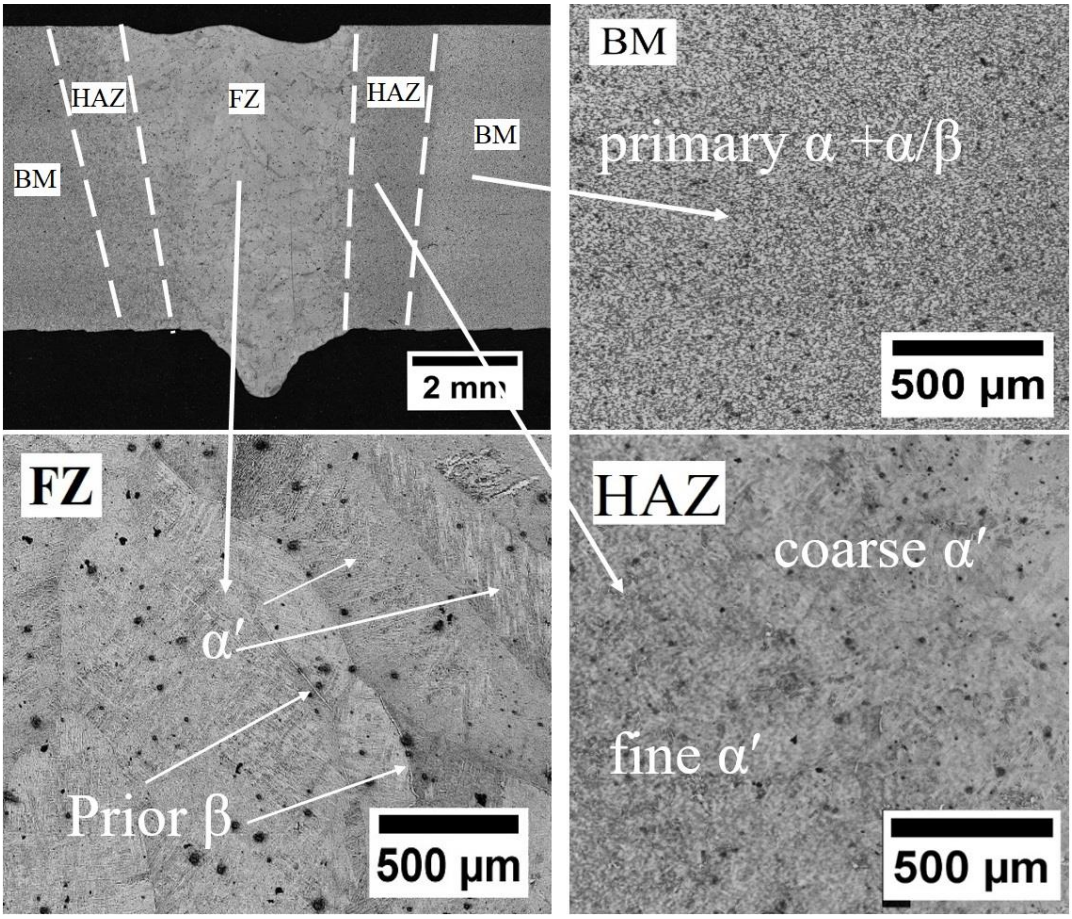

Figure 5.11 The cross-sectional microstructure of the weldtrack keyhole showing the three different regions: BM, HAZ and WZ. The BM is consist of primary α and α/ β phases. The WZ has a fine needle-like α′ prime (martensitic α) within the prior β boundaries, while the HAZ divided into fine α′ prime near the WZ and thick α′ prime lathes near the BM.

The average grain size at the WZ was about ~460µm. The micro-examination revealed that the transformation in the grain affected its size when moving from the WZ toward the HAZ and finally the BM, relocating grains in the WZ, due to the grain growth mechanisms. As shown in figure 5.11, the HAZ area has a complex structure with an average grain size of about ~248µm, caused by the HAZ's subjection to high beam current, which led to the primary α structure changing into β phase; then, upon rapid cooling the return of the β phase to its original structure was interrupted by the cooling process; instead, coarse grains of needles-like α´ structure were formed in the HAZ near the WZ. [43].

5.5.2 Microhardness measurements

Hardness measurement was carried out on the keyhole cross-section for each weldtrack for both normalised and linear approach. A series of 22 indentations were made from the centre of the WZ through the HAZ toward the BM. A Durascan instrument was used to apply a 1HV load for a period of time of 20 seconds to each indentation. The total measurement length from the centre of the WZ to the BM was about 5.7+/- 0.5mm. The measurement length varied due to the differences in the width of the WZ and the HAZ area for some of the weldtrack keyholes, influenced by the amount of the heat input (beam current) and the rate of the beam travel speed. Moreover, to avoid the distortion of the hardness measurements, the distance according to ISO 6507 was fixed at (3d), where (d) represents the width of the Vickers indentation at the alloy surface. Therefore, from the test, the (d) was about ~ 0.07615mm, and the distance between the two indentations was about 0.23mm.

Table 5.4 shows the obtained hardness values for the weldtracks achieved by the normalising DoE method. The results show variations which reflect changes in microstructure from the WZ to the HAZ and then to the BM. The lowest hardness, recorded at the BM, was about 325±5HV_1. The WZ recorded the highest hardness, reaching up to 387±4HV_1, which was caused by the fine needles-like α´ structure within the prior β grains. The high hardness of WZ due to the acicular α´ structure was also reported by Xinge et al. [203], Jing et al. [219], Yunlian et al. [52] and Balasubramanian et al. [4]. Meanwhile, the microhardness values of the HAZ were lower than for the WZ and were in the range of 340HV_1 to 355HV_1. A reduction in the hardness values can be seen in the HAZ area as moving in the direction of the BM. This reduction in the hardness was due to the increase in the thickness of the α´ laths structure.

Table 5.4 Show the average hardness measurement values for the WZ and the HAZ of the weldtrack keyholes of the Set I. The average HV_1 for the base metal (Ti-BM) was 325±5.

	M1	M2	M3	M4	M5	M6	M7	M8	M9	M10	M11	M12
HAZ HV	356 ±4	350 ±3	352 ±4	350 ±3	350 ±5	340 ±6	340 ±5	335 ±5	336 ±6	348 ±5	338 ±6	350 ±5
WZ HV	375 ±6	383 ±5	387 ±4	360 ±5	373 ±5	367 ±4	365 ±6	372 ±6	361 ±4	362 ±5	357 ±6	363 ±5

The welds from the linear approach showed similar hardness values to the welds obtained from the normalised approach. The microhardness measurements at the cross-section of the weldtrack keyholes show a typical gradient distribution of hardness values from the WZ centre toward the BM. As reported, the highest values were at the WZ, and the lowest hardness values were recorded at the BM; meanwhile, the HAZ areas showed hardness values between those of the WZ and the BM[43], [56][203][4]. The base metal, which consists of equiaxed α (primary α) grains and lamellar α/β grains, showed the lowest hardness values of 320±5HV_1, whereas the WZ areas recorded the highest hardness values, reaching up to 375HV_1. The WZ hardness measurements show uniform hardness values with minimal variation and ranging between 365±6HV_1 and 375±5HV_1. These high hardness values were due to the needle-like structure of α´ grains at the WZ. Despite the slight reduction in the ductility and the toughness of the joint, it provides a weld joint with high tensile strength [9].

Meanwhile, the hardness values of the HAZ were lower than the WZ measurements and fluctuated in a wide range, between 335±4HV_1 and 353±5HV_1, which was due to the slow cooling rate in the HAZ area allowing the forming of thick α´ grains. Therefore the HAZ will consist of a complex structure of α colonies containing fine and coarse α′ grains. This changing in grain size results in a reduction in the HAZ hardness values [220].

The hardness measurements also show that as the travel rate increased the hardness value increased as well. The behaviour is related to the amount of the heat input to the WZ, which correlates with cooling rate level. A reduction in the heat input takes place as the travel rate increased, causing an increase in the cooling rate, so rapid formation of hard fine plate-like α′ grains took place at the WZ. This behaviour was reported by Short et al. [7] and Squillace et al. [9]. Moreover, the increase of the heat input (beam current), as shown in figure 5.12, led to a reduction in the microhardness values of the WZ and the HAZ. The high heat input provides a longer time for the WZ to stay at elevated temperatures so that the cooling rate will be relatively slow; therefore, α´plates will start to develop from the grain boundary to form α- colonies. The slower the cooling rate, the bigger the size of these colonies, in which the grains are less hard than the fine platelet α´ grains. Figure 5.12 shows the gradient in the hardness values of the HAZ and the WZ as the beam current increased.

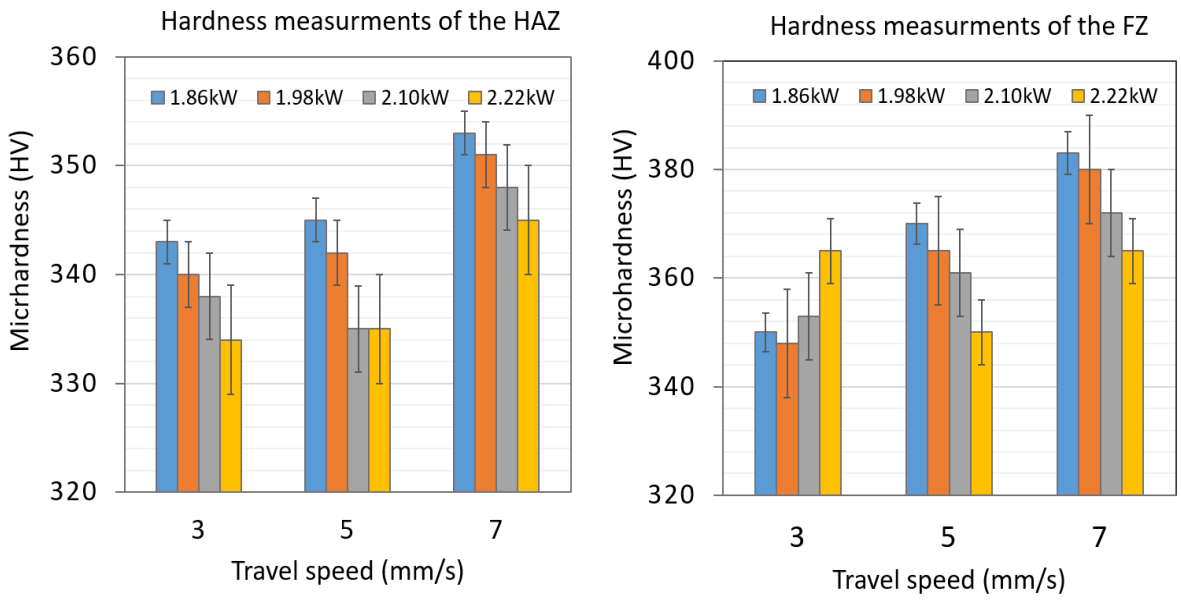

Figure 5.12 shows the effect of beam travel speed on the microhardness values for (left) the HAZ and (right) the WZ. A general trend was observed as the welding speed increase an increment in the HV value took place, due to the fast cooling rate. However, increasing the heat input tends to reduce the hardness value cause the WZ, or the HAZ will absorb a high amount of heat which keeps the WZ upon solidification at an elevated temperature so a reduction in cooling rate will happen and α´ grains become thicker.

5.6 Summary and conclusions

1. Weldtracks were obtained successfully by adopting the Arcam S12 system as a welding machine for this work.
2. The design of experiments (DoE) was an effective approach to identify promising welding parameters, and the optimised values obtained were useful in identifying a trend in beam speed and currents.
3. The Macro-examination carried out for the weld bead-on-plates show that both the amount of heat input and the beam travel rate has a direct impact on the weldtrack profiles.
4. The keyhole measurements for the weldtracks show that the width of the WZ is proportion directly with the amount of the heat input (beam current) and inversely with travel rate of the welding speed.
5. A trend was observed in the measurements of the keyhole depth, reveals that as the travel rate increased, the amount of the heat inputs decreased, which leads to a reduction in the fusion zone and the keyhole profile become narrower.
6. The keyhole measurements for the weldtracks obtained using the suggested parameters by the normalise approach showed a scattered behaviour in terms of the

effect of beam current and the beam travel rate on the WZ geometry. However, the effect of high heat input and the slower travel rate was resulting in a wide fusion zone, and the presence of defects such as underfill, undercut and excessive root size (saggy roots).

7. Meanwhile, the variables suggested by the linear approach to obtain upon keyhole measurements it shows more systematised behaviour in terms of the effect of the heat input and travel rate on the dimensions of the fusion zone.
8. The only variables that produced a promising acceptable weld track profile when adapting the normalise approaches were a beam current of 33.16mA at a travel rate of 3.22mm/s. Meanwhile, the discrete approach provides more accurate variables in terms of producing weldtracks with more acceptable weldline profile and minimal welding defects.
9. The maximum hardness values, $387\pm4HV_1$, recorded at the WZ, whereas the lowest hardness values, $325\pm5HV_1$, were shown in the BM. Meanwhile, the HAZ, recorded hardness values lower than the WZ values but higher than the BM values, ranging between $335\pm4HV_1$ and $353\pm5HV_1$ due to the presence of coarse α´ structure.
10. The discrete approach revealed a trend in terms of the effect of the beam heat input and beam travel rates on the microhardness values. The obtained hardness values were directly proportioned with the rate of the welding speed and inversely proportioned with applied heat input.
11. A reduction in the hardness values for the WZ and the HAZ was observed when the amount of the heat inputs increased as observed with low beam travel rate, i.e. 3mm/sec., which causes a reduction in the cooling rate allowing the fine α´ grains to grow and become thicker and less hard.

This chapter has presented the experimental techniques used to predict and evaluates the obtained welding parameters of the electron beam welding of Ti-6Al-4V. The following chapters will employ the techniques and the results obtained in Chapter 5 to be used in conducting an electron beam dissimilar welding between Ti-6Al-4V and CP-V alloys using the fillers metals designed previously in Chapter 4.

CHAPTER 6: Dissimilar-Metal welding of Ti-6Al-4V alloy to commercially pure vanadium alloy by Electron Beam welding

Abstract

The effect of welding parameter and the type of the filler alloy on the hardness distribution and microstructure across the dissimilar welding joints between Ti-6Al-4V and pure vanadium alloy were investigated. An optimisation was carried out to determine the best parameters to use with the Arcam S12 system EBM machine to perform the dissimilar welding process. The micro examination reveals four zones in the welding joint: the Ti-6Al-4V base metal (Ti-BM) zone, the (Ti-HAZ) zone, which is located between the welding zone (WZ) and the (Ti-BM) zone, and the commercially pure vanadium base metal alloy (V-BM) zone. The (V-HAZ) zone, which is located between the welding zones (WZ) and the (V-BM) zone. WZ and the Ti-HAZ showed the highest hardness values; The (Vi-HAZ) zone should the lowest HV value. The Ti-BM and V-BM values were around typical values. SEM and EDS were performed to identify the effect of the fabricated filler metal on the microstructure and mechanical properties of the welding zone (WZ).

6.1 Introduction

Over the last decade, the demand for joining dissimilar alloys has increased rapidly. By fabricating a composite structure, there is a great potential of combining different efficient properties in one place. However, in most applications that require structures made from titanium alloys, welding and joining will be the primary methods used to achieve such a structure. Welding and joining titanium alloys to different alloys is quite challenging due to the high possibility of the presence of undesirable brittle intermetallic components in the welding zone. The presence of these undesirable phases will lead to premature failure in the WZor the area adjacent to the weld zone. Therefore, since it is essential to overcome this problem, a ductile alloy was prefixed in the weld joint before conducting the welding operation. Improvement was observed in the welding joint, as a result of the changing in the WZ microstructure, and in the mechanical properties [28].

Titanium alloys have been used extensively in the industry, such as aerospace and chemical applications due to their high specific strength to weight ratio and high corrosion resistance [79]. An intermediate alloy was prefixed in the weld joint before conducting the welding operation. Several studies were conducted to explore the use of different types of interlayers to join titanium alloys to other alloys. Despite the reduction of embrittlement at the WZ, and the residual stresses, due to the presence of the solid solution phases in the structure, the risk of formation of IMCs is still present; even with optimising the welding parameters [107] the joint area is still considered the weakest part in the WZ and few methods have been developed to overcome this problem [115]. Different types of alloys were employed as filler metal prefixed in the welding joint, including vanadium, molybdenum, magnesium, tantalum, zirconium and niobium; however, while they reduce the formation of the brittle phases, they are very costly to use. An investigation was conducted by Chung et al. [14] on V alloys weldment to study the impact of the welding process and PWHT on the properties of the WZ.

Using EBW and LBW, beads-on-plate welds were created over a V-4Cr-4Ti alloy, then the microstructures and mechanical properties of the WZ were examined. The samples in the as-weld condition showed the highest hardness value; however, the ductility of these samples promotes when they subjected to an annealing process. The as-weld samples showed the lowest impact results, while an improvement was observed when the samples annealed at 1000˚C for 1hr. The microstructure of the WZ for EBW and LBW was mainly of a long grain with large size; however, when the annealing was applied, the long grains formed into smaller sized grains. Heo et al.[139] reported the effect of welding parameters on the morphology of the WZ for the bead on plate weld tracks made by LBW. Both the parent metal of the V-4Cr-4Ti and the WZ showed similar values for the Charpy impact test, contrary to the finding of Chung et al.[14]. Despite the improvement in impact resistance of the welded samples achieved by the annealing process, the hardness value was increased due to the presence of hard phases.

An interesting study of dissimilar joining was conducted by Nogami et al. [15] using the EBW method. Autogenous welding was achieved between pure vanadium alloy and stainless steel type 316L. The investigation studied the effect of beam location and PWHT on the microstructure and mechanical properties of the dissimilar welding. A reduction was observed in the hardness of the WZ, due to the minimal formation of hard σ phase, as the beam shifted away from the welding centre line toward the V side by 0.2mm and 0.4mm. The hardness value resulted of the PWHT for V-BM and 316L-BM showed almost an equal

value to the as-weld samples; however, the hardness value of the HAZ and the WZ, doubled as compared to the as-weld samples. It was confirmed as the samples annealed to 600C for 1hr; a precipitation hardening takes place, forming brittle phases such as NiV_3 and Ni_2V_3 in the WZ. Also, the formation of an interlayer between the V-BM and the WZ was growing to a thickness in the range of 20 μm -30 μm. Another study of dissimilar welding was made by Nogami et al. [16] to join pure vanadium alloy to 316L alloy by EBW, following their previous work in [15]. The effect of EBW parameters and the long periods of PWHT of 1, 10, 500 and 1000hr, on the WZ properties were investigated. The shifting effect of 0.2 and 0.4 mm of the beam position from the welding centre line to inside the vanadium alloy was also investigated. The study showed that the WZ and HAZ have the maximum hardness, while the BM showed less hardness in the case of the as-weld samples. Despite the beam position, the 600˚C annealing condition doubled the hardness value comparing to the as-weld samples. Annealing the WZ at 1000˚C for 1hr increased the hardness value of ~900HV. While ~1000HV was the hardness of the HAZ when it annealed at 600˚C for 1hr. As a result of the post-weld heat treatment, a formation of brittle phase such as the σ-phase V_3Ni was the suggested reason for increasing hardness.

In this work three novels ideas were suggested; firstly, optimisation will be carried out using Rosenthal equation and weld bead-on-plate to determine promising welding parameters to establish a keyhole gap utilising the electron beam melting Arcam S12 system as welding machine. Then to carried out dissimilar welding between Ti-6Al-4V alloy and commercially pure vanadium alloy using EBM Arcam S12 system autogenously. Secondly, a new approach was suggested to produce a filler metal, by mixing the powder of the selected alloys to be welds in a specific weight percentage and processed the mixed powder by the SPS machine, in order to create a filler metal with specific microstructure and mechanical properties that can help to achieve a reliable dissimilar welding between the selected alloys. Third and finally, applying the designed filler in the dissimilar joint using the promising parameters that utilised previously to conduct the dissimilar autogenous welding between Ti alloy and V alloy to study the effect of the selected welding parameters and the designed fillers metal on the microstructure and the mechanical properties of the welded joints.

6.2 Materials and methods for welding Ti-6Al-4V and CP-V

6.2.1 The electron beam welding machine

An electron beam melting (EBM) machine type Arcam S12 system, located at the Mapp research centre, University of Sheffield, was selected to carry out the welding process. The welding process was carried out under vacuum condition. The linear DoE method was adapted to determine the best welding parameters perform welding on 5mm titanium plate and a macro post-weld inspection was performed to evaluate the weldtracks and select the welding parameters that would provide weldtracks with a good quality profile. A bead-on-plate welds method was used to perform the optimisation of the welding parameters using the data in Table 6.1.

Table 6.1 The parameters obtained according to the linear approach to be used by Arcam S12 to perform the bead-on-plate weldtracks on 5mm Ti-6Al-4V plate.

Weldtracks (1-9)	Travel speed (mm/s)	Beam current (mA)	Bead width (mm)	Bead depth (mm)
a	7	31	4.2	4.51
b	7	30	4.07	4.71
c	7	29	3.7	4.51
d	9	31	3.58	4.65
e	9	30	3.33	4.88
f	9	29	3.21	4.53
g	11	31	2.72	4.98
h	11	30	2.59	4.89
i	11	29	1.85	4.97

6.2.2 Materials and Samples

As mentioned before, the selected alloys were titanium alloy type Ti-6Al-4V and commercially pure vanadium alloy; table 6.2 shows the chemical composition of the selected alloys. CP-V and Ti-6Al-4V have entirely different chemical and physical properties from each other. Table 6.3 gives a summary of the differences in physical properties between these two alloys. The selected alloys have a 5mm thickness and were prepared with dimensions of 50mm x 30mm using the electrical discharge machine (EDM).

Table 6.2 The chemical composition of Ti-6Al-4V and commercially pure vanadium alloys [wt. %].

Elements	Ti	Al	Fe	C	V	N	O
Ti-6Al-4V (plate)	Balance	6.29	0.19	0.012	4.04	-	0.214
Vanadium (CP-V) (plate)	<0.001	0.0065	0.0019	0.02	99.9	0.0085	0.025

Table 6.3 The physical properties of Ti-6Al-4V and commercially pure vanadium alloys [110], [121].

Alloy	Melting point/ ˚C	Density g/cc	Thermal conductivity (W/mK)	Thermal expansion (μm/mK)	Tensile strength, min, MPa	Hardness (HV)
Ti-6Al-4V	1649	4.43	6.7	9	900-1200	300-400
Vanadium (V)	1910	6.11	35	8.3	800	170

Due to the big difference in melting point between the Ti-6Al-4V (1649 ˚C) and the CP-V alloy (1910˚C), and before the dissimilar welding was performed, the best parameters obtained from the Ti weldtracks could not achieve full penetration, and no keyhole gap was created for the CP-V alloy. Therefore, another optimisation was required for the V alloy to find the best current that could be used to maintain the beam travel at 7mm/s as this rate of travel showed appropriate welding features. So, 31mA, 33mA, 35mA and 37mA were used to obtain weldtracks on the 5mm thickness of CP-V alloy by performing the bead weld-on-plate method as a technique with the aid of physical inspection, as explained previously in chapter five, to determine the required current to create a keyhole in the vanadium alloy.

6.2.3 Weldtracks and Welding Parameters.

A set of parameters controls the melting operation when using the Arcam S12, such as beam current (mA), beam accelerating voltage (kV), beam focuses offset (mA), beam travel rate (mm/s). Some of these parameters were kept consistent, namely, the accelerating voltage at 60kV and beam offset at -2mA, while both the beam current (mA) and the beam travel rate (mm/s) were variables. Table 6.1 lists the selected variables used to perform the weld bead-on-plate on 5mm Ti-6Al-4V plate to determine the best welding parameters that would

provide weldtracks with a good profile. Regarding the welding parameters, from the linear weldtracks outcome, and the weld bead-on-plate trails performed on the CP-V alloy plate, beam current 41mA, 39mA, 37mA, and 7mm/s travel rates were selected as variables for performing the dissimilar welding. The dissimilar welding was performed with butt position.

6.2.4 The designed filler Metals

Three filler types were selected to perform the dissimilar welding between titanium alloy type Ti-6Al-4V and commercially pure vanadium alloy: Ti/V1, Ti/V2 and Ti/V2; table 6.4 shows the chemical composition of each filler. The manufacturing of these fillers was explained thoroughly in chapter four. These new dissimilar welds were named as W1, W2 and W3.

Table 6.4 Show the chemical composition of the designed filler metals and processed by SPS.

	Filler metal	Ti-6Al-4V alloy (wt.%)	CP-V alloy (wt.%)
W1	Ti/V1 (80/20)	80	20
W2	Ti/V2 (60/40)	60	40
W3	Ti/V3 (40/60)	40	60

6.3 Microstructure analysis

The cross-sections of the keyhole area, see figure 6.1, of both the weldtracks and the dissimilar welded joint, were subjected to optical microscopy examination. The preparation procedures for the micro-examination were explained in the methodology, chapter three. Scanning electron microscopy (SEM) using the (FEI Inspect F) machine was employed to examine the WZ and the elemental composition quantifying was carried out by energy-dispersive x-ray spectroscopy (EDS) using the Philips XL30S FEG. Machine.

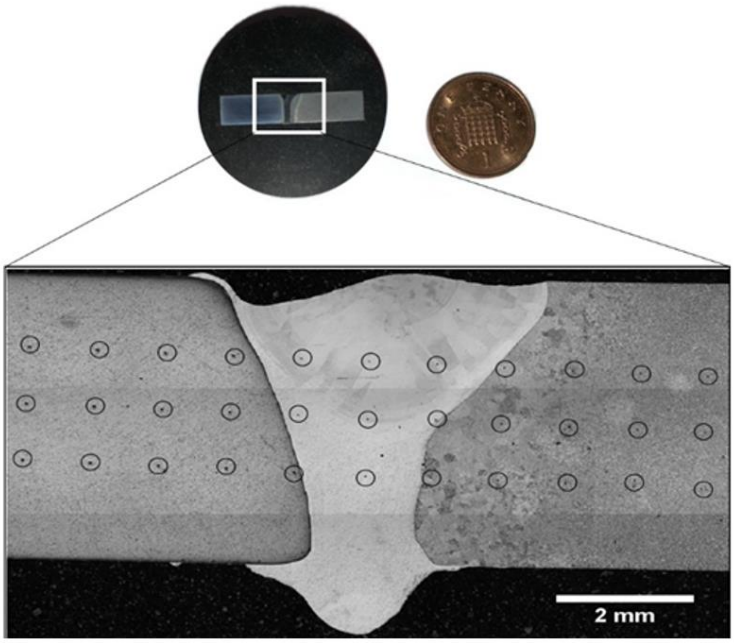

Figure 6.1 Shows the cross-section area of dissimilar welds prepared for the microstructural examination and the map line indentation performed to evaluate the microhardness value.

6.4 Mechanical Tests

The microhardness examination was carried out using the Durascan machine. The measurements were applied to cover the cross-section of the welding keyhole. Three lines of indentations were made at the upper, middle and lower sections of the keyhole cross-section to draw a map that could show the hardness values' distribution at the welding joint. The hardness parameter was a 1HV load for 20 sec. Dwell time, and the distance was 1mm between each indent. Figure 6.1 shows a dissimilar joint with indentation mesh on it.

The tensile test was carried out for the dissimilar welded samples to determine their mechanical properties. The cross-head speed was 1mm/min, and the universal testing machine type was Tinius Olsen H25I S, figure 6.2a. From each dissimilar welded plate, figure 5.2b, three tensile specimens, figure 6.2c, were extracted to determine the mechanical properties of the welded samples.

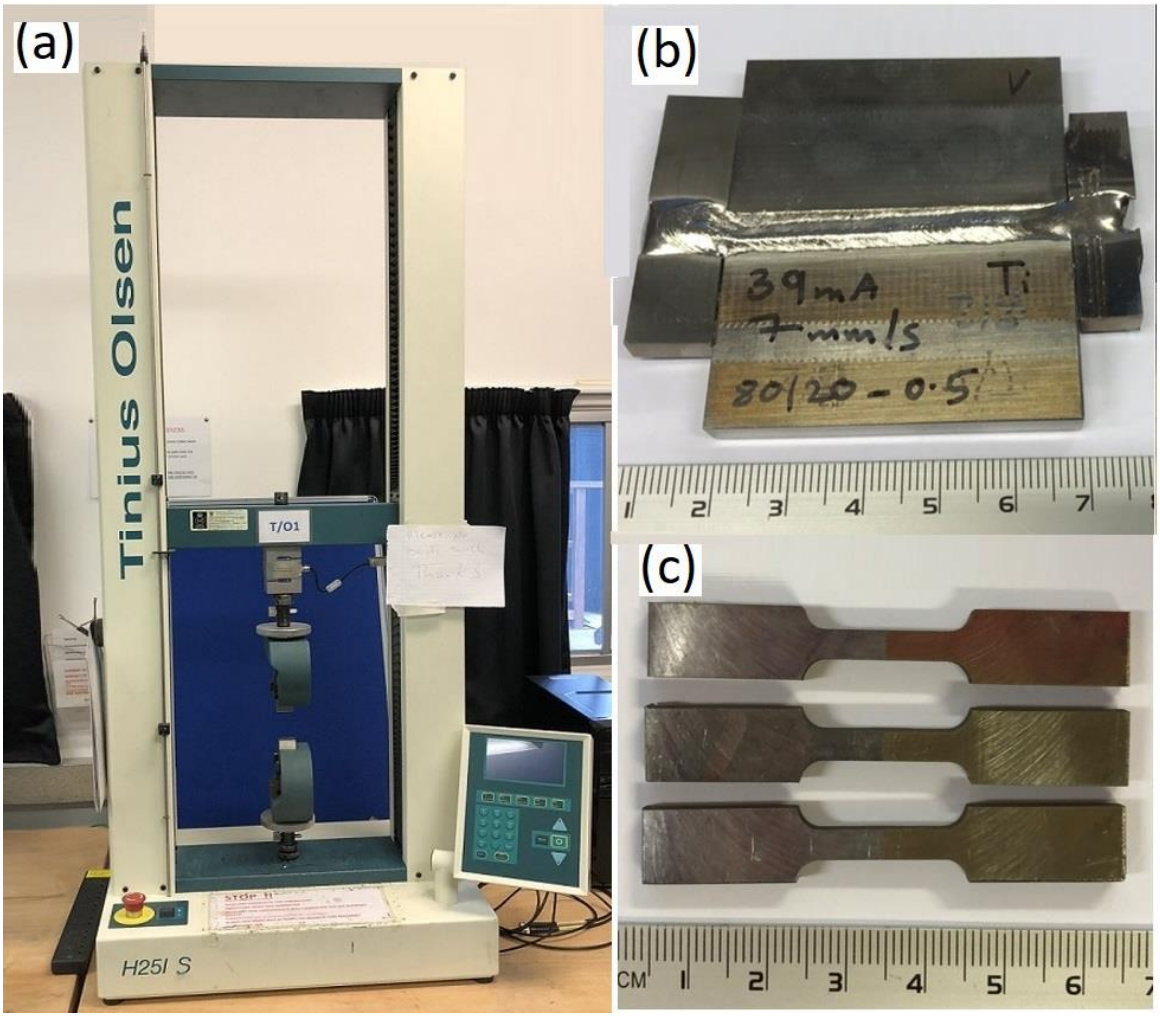

Figure 6.2 Shows (a) the tensile test machine used to carry out the tension test, (b) a dissimilar welded sample and (c) the extracted tensile specimen.

6.5 Results and Discussion

6.5.1 Weldtracks optimisation for Ti-6Al-4V alloy

The weld bead-on-plate was performed on a 5mm thickness of titanium plate type Ti-6Al-4V alloy. The new set of parameters was selected according to the outcome of the weldtracks of the set II (the linear method variables in chapter five). A second attempt was carried out using discrete approaches to determine the welding parameters. Table 6.1 lists the inputs used to perform the bead-on-plate using the ArcamS12 machine. Figure 6.3 shows the weldtracks obtained by ArcamS12. All the weld tracks achieved full penetration when the variables were selected considering the plate thickness, so the selection was in two directions, firstly, the current chosen was lower than that used for the 6mm titanium plate, at (31, 30 and 29) mA; secondly, the speed was increased. The discrete method was effective

in limiting the variables and localising the working range. Figure 6.3 shows that all the selected parameters achieved full penetration; however, the effect of the beam speed rate on the weldtrack profile was clear. It was clear that increasing the beam speed to 11mm/s provided an appropriate weldtrack profile, while the outcome of using the other two speeds, 7mm/s and 9mm/s, was a turbulence behaviour during the melting operation and discontinuities in the weldtrack profile. This is suggested to be due to an imbalance between the amount of the heat input and the beam speed as these discontinuities in weld track profile appeared to be higher at relatively slow speeds for a given current as seen in figures 6.3a, b and c. The effect of low beam speed on the size of the undercut was also reported by Cao et al. [8], who observed that as the speed increases the presence of undercut decreases. With low speed the chance of the melted alloy melting and evaporating is high, leaving the welding pool with a shortage of molten metal; also, there is a higher chance of the molten metal escaping from the welding root, see figures 6.4a, b, c, d for examples. Therefore, high speed is preferable to minimise the undercut formation at the weld face at the same given current, see figures 6.4 g, h and i for examples. Based on the analysis, the weld that showed the most promising weld line profile was 6.3a.

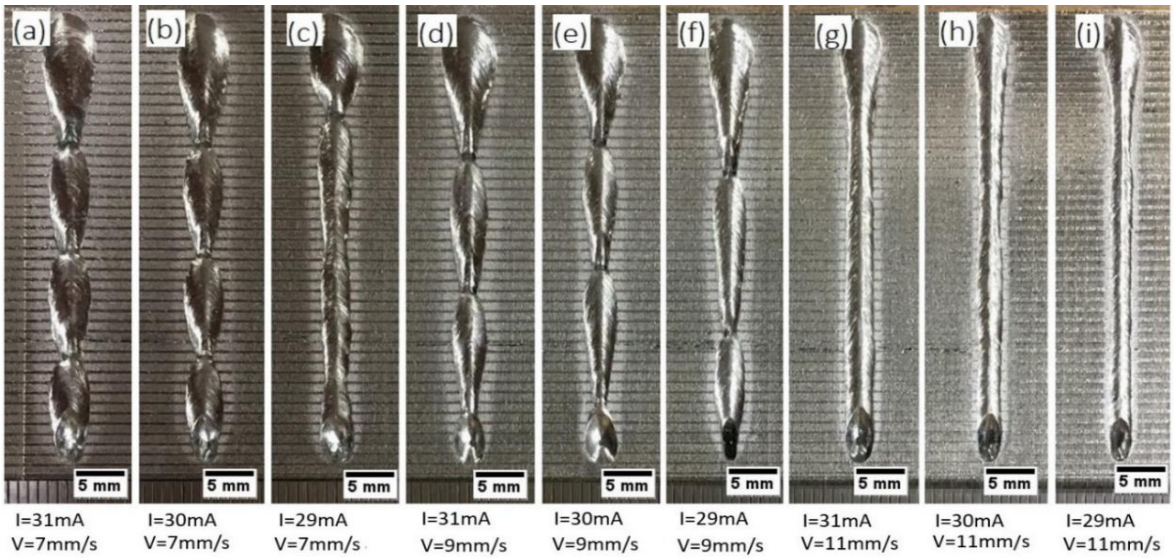

Figure 6.3 Shows the weldtrack achieved by the Arcam machine using the inputs proposed by the discrete DoE method.

6.5.2 Numerical modelling and Weld size

In order to predict the effect of the alloy physical properties on the geometry of the WZ, a modelling approach was conducted. The Rosenthal equation (equation 6.1) was adapted to determine approximated WZ depth to compare with experimental results. Energy from the applied beam is absorbed and distributed through the metal differently depending on the alloy physical properties[167]. The thermal modelling was performed to predict the depth of the keyhole formed by the EBM process. Rosenthal's equation depends on three assumptions; The physical properties of the material are constant and they affected by process temperature, (2) Both, travel rates and heat input are constant, and (3)the absence of convection and radiation condition in the alloy. Therefore, there is a great potential for error in this assumption. The four material properties required as an input for Rosenthal equation are the density, ρ, thermal conductivity, k, specific heat capacity, Cρ, and thermal diffusivity, α, where α = k / Cρ, and each one of these properties vary with temperature. The Mat lab software was used to run thermal modelling. However, the results from Rosenthal equation are based upon a beam efficiency of 100% assuming zero power loss.

Meanwhile, during the electron beam melting losses in energy is inevitable. Therefore, the fitting parameter, η, is necessary to account for both the energy loss and beam size, as required addition to validate the modelled results. A set of values of heat efficiency were selected to be 0.7, 0.8 and 0.9 to work as fitting parameters to predict more realistic results[167], [221].

$$T - T^{\circ} = \frac{\eta q}{2\pi k R} exp\left(\frac{-v(x - R}{2\alpha}\right) \dots\dots\dots\dots\dots\dots\dots\dots\dots\dots\dots\dots\dots\dots\dots\dots\dots. (6.1)$$

$$R = \sqrt{(x^2 + y^2 + z^2)} \dots\dots\dots\dots\dots\dots\dots\dots\dots\dots\dots\dots\dots\dots\dots\dots\dots\dots\dots\dots\dots\dots\dots (6.2)$$

The T_o is the initial temperature, q, is the amount heat input from the beam, k represents the thermal conductivity W/m.k, v, is the beam speed rate in the direction of x, α is the thermal diffusivity m^2/s, and R is shown in equation (6.2). Rosenthal equation, from typical physical properties, was able to determine a close range of WZ depth measurements of Ti-6Al-4V alloy and CP-V alloy, separately, with fitting parameters of 0.9, as shown in figure 6.4. The overall outcome suggests an increment in WZ depth as a function of applied beam power, q, for the selected BM alloys, i.e. Ti-6Al-4V and CP-V. However, a reduction in the WZ depth was evident in case of the Ti alloys with increasing the beam power, due to the excessive

melting and vaporising of the molten metal which causes a reduction in the welding zone size, sees figure 6.4a for an instant. The theoretical modelling for titanium and vanadium alloys gave a window to calculate the required heat input and travel rate to combine a high thermal conductive and high melting point vanadium alloy to the lower melting point and lower thermal conductive titanium alloy.

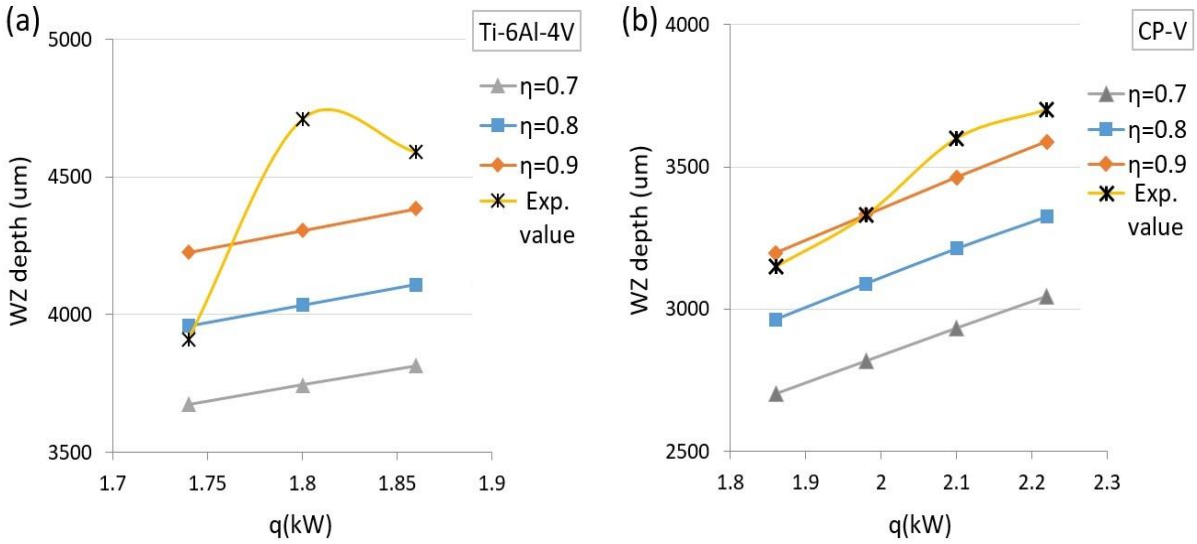

Figure 6.4 A comparison between the suggested depth obtained by Rosenthal equation with η values of 0.7, 0.8 and 0.9 and the obtained depths from the experimental work for (left) Ti-6Al-4V and (right) CP-V alloy, both BM, an increase in the depth was recorded as the applied heat increased.

The theoretical modelling was carried out for the dissimilar weldments with the filler metals types (Ti/V1, Ti/V2 and Ti/V3) and for the dissimilar welds without filler (Ti/V). The physical properties for filler alloys, such as density and thermal conductivity, were approximated based on the wt. % of the Ti and V in the designed filler by the rule of the mixture and then modelled by Rosenthal equation. The rule of mixture, shown in equation (6.3), is employed to calculate the properties of mixtures only, taking account of the volume fraction and a parameter (here physical properties) of each alloy, and is written as:

$$K = V_f(Ti) * (Ti)\, E_p + V_f(CP\text{-}V) * (CP\text{-}V)\, E_p \quad \ldots\ldots\ldots\ldots\ldots\ldots (6.3)$$

V_f and E_p are the volume fraction and physical properties of an alloy, and K is composed properties. A set of theoretical physical properties of the designed alloys were assumed, and table 6.5 illustrates those properties.

Table 6.5 Show the standard physical properties of Ti-6Al-4V and CP-V alloys and the theoretical properties of the designed alloys obtained from the Rule of Mixture.

	The standard physical properties of alloys		The physical properties obtained by the Rule of mixture approach			
Alloy type	Ti-6Al-4V	CP-V	Ti-V (autogenous welds)	Ti/V1 (alloy)	Ti/V2 (alloy)	Ti/V3 (alloy)
Relative density (g/cc)	4.43	6.1	5.265	4.764	5.098	5.432
Thermal conductivity (W/m.K)	6.7	35	13.65	12.36	18.02	23.68

Besides the several factors that can affect the beam efficiency and reduce the melting pool depth, such as physical properties, joint boundary conditions, and welding process parameters, adding the filler alloys into the joint can also affect the depth of the WZ. The differences in density, thermal conductivities, and melting points are physical properties which have significant potential for complicating and slowing down the melting process during the welding process, causing a reduction in welding efficiency.

The thermal modelling results provide a range of theoretical depths for the DW between Ti-6Al-4V and CP-V alloys with and without the presence of the designed fillers in the welding zone, as seen in figure 6.5. The experimental depths measurements of the dissimilar welds were close in value to the theoretical depths predicted by Rosenthal equation, with fitting parameters of 0.7, see figure 6.5 for example. A recent investigation by Wang et al. [222] confirms the effectiveness of high-efficiency values in the prediction of more realistic results. However, the reduction in fitting parameters from 0.9 to 0.7 suggested the requirement to increase the power of the beam to achieve the desired full depth. As the wt. % amount of the high melting point alloy, i.e. vanadium, increases in the welding zone, the intensity of the beam should be increased as well to the limit that could establish a WZ with full penetration. Figure 6.6 shows a comparison between the WZ depths measurements of the experimental dissimilar welds and the theoretical depth of the WZ predicted by the modelling approach. A general trend was evident of increase in welding depth as the power of the electron beam increased at constant travel speed of 7mm per second. Figure 6.4 and

6.6 are good examples to show that as the heat efficiency increased there was good potential for the suggested and experimental results to be close. This assumption was confirmed previously by Wang et al. [222] when studying the effectiveness of high-efficiency values in the prediction of more realistic results. The modelling approach in figures 6.4, 6.5 and 6.6 emphasises the effect of high heat input on the depth of the WZ; however, the experimental work showed that as the beam power increases, the dimensions of the WZ will deteriorate due to the high heat input causing metal vaporisation and excessive melting conditions.

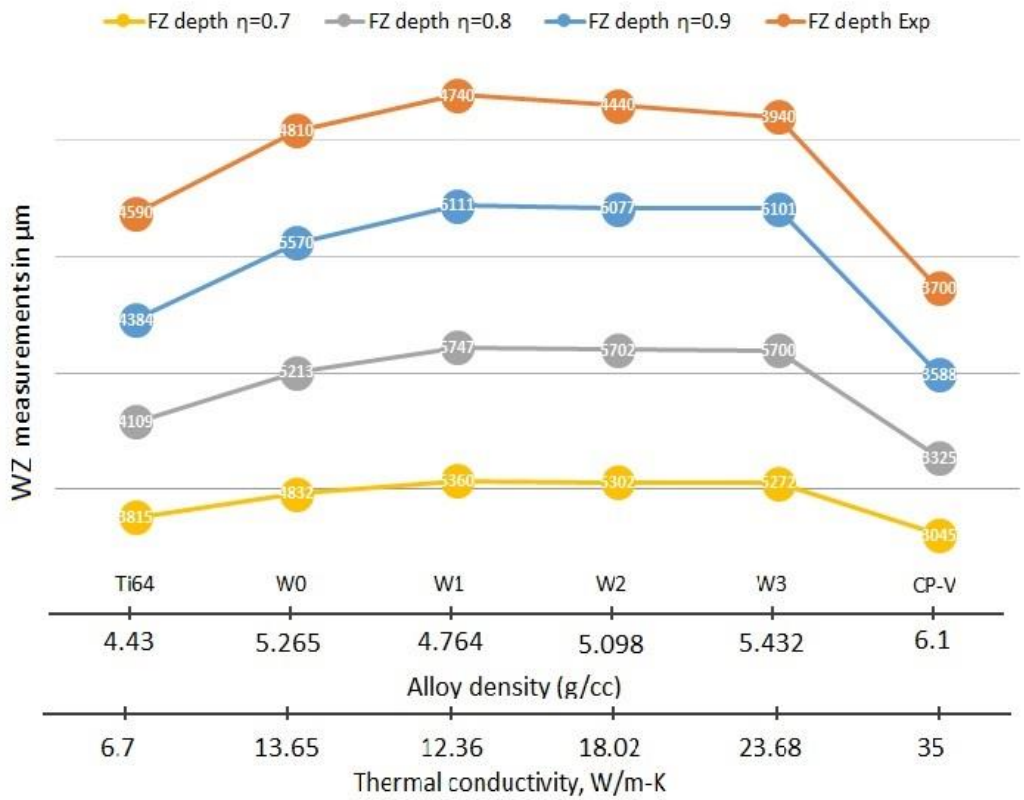

Figure 6.5 Show the effect of alloy suggested physical properties on the WZ depth at different η heat efficiency values as compared with depths obtained from the experimental work.

It is worth mentioning that the graphs in figures 6.6 were plotted using two data points only, which were obtained from two experimental attempts using beam currents of 37mA and 39mA at a constant beam travel rate of 7mm/second. Unfortunately, no further experiments were conducted due to alloys limitations; however, it was evident that the depth was a function of beam power at constant travel rate, and this depth will start to decline as the electron beam current becomes higher than 41mA, as confirmed from the autogenous dissimilar welds between Ti-6Al-4V and CP-V alloys carried out using 41mA beam current

and 7mm/sec. travel rate. The macro examination of the DW shows an increase in the formation of defects such as underfill and undercut as the beam current reached 41mA, indicating great potential for an intermittent weldline profile.

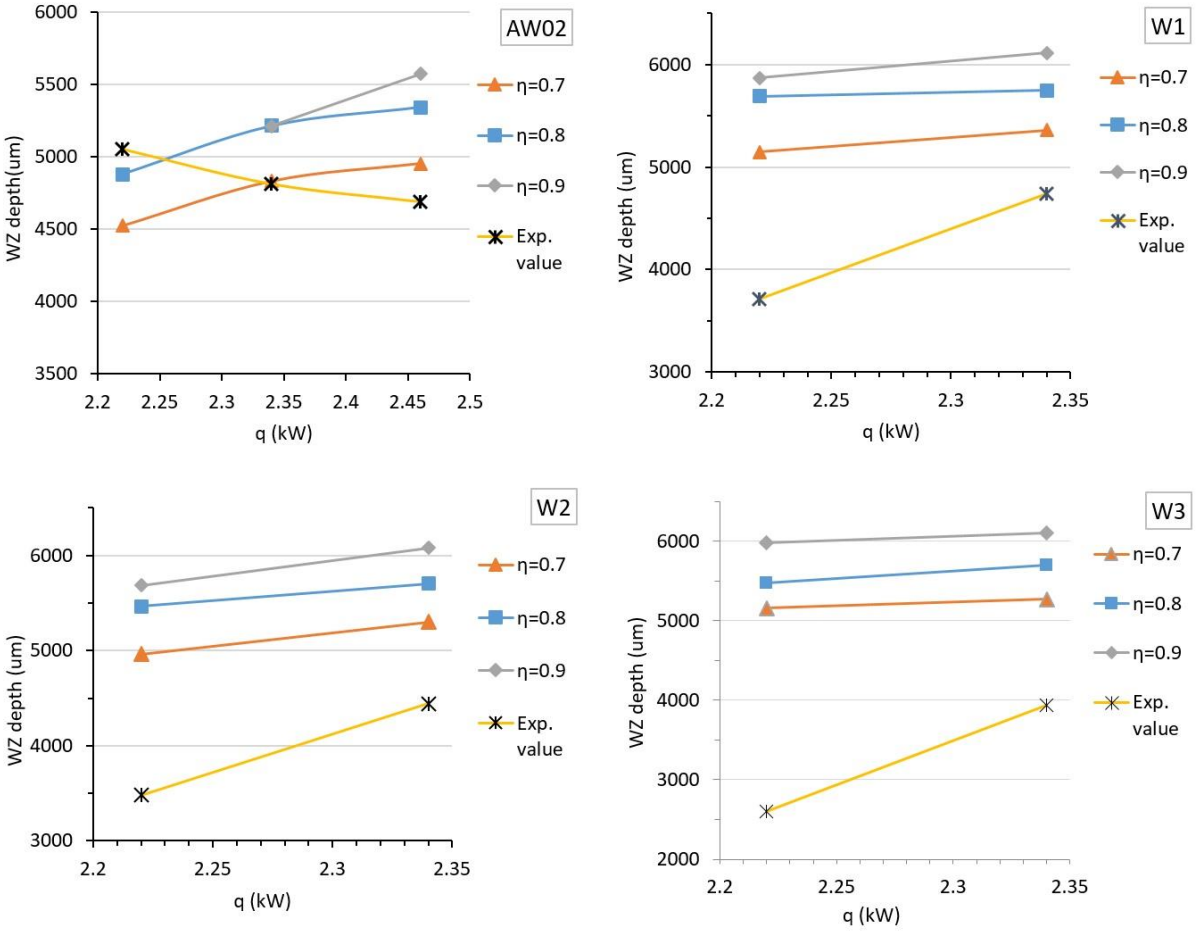

Figure 6.6 The experimental WZ depths of dissimilar welds as compared with theoretical depth predicted by Rosenthal equation with different fitting values (η) of 0.7, 0.8 and 0.9.

Furthermore, the boundary condition in the welding joint is another factor that can affect the joining process. The contact surfaces between the BM and the filler metals, the surface finishing of the joint area and the applied pressure on the joint area can have all effect in one and another on the efficiency of the fusion process during the welding.

The cross-section of the keyhole can be better appreciated after applying the micro preparation by metallographic means, see examples in figure 6.7. The undercut in the keyhole regions was well characterised as a deep hole in the centre of the WZ with a convex profile. At low travel rate the WZ becomes wider, as a large part of the area is melted down; also, the excess of heat input causes the molten metal to vaporise, causing a big gap on the top of the weldline, or it leads to what is known as excessive welding penetration at the root, see figure 6.7a,b,e. Measurements were carried out for the WZ regions of the Ti-6Al-4V in order to apply a further understanding of the relation of both the beam current and beam speed to keyhole formation. Figure 6.8 reflects the behaviour of the WZ profile against the applied welding parameters. Measurement of the width of the keyhole showed variation from wide at a low-speed rate to narrow at a faster rate. The width of the weld face (top) at low speed was equal to the width of the root, which indicates that the high heat input travels through the thickness at the same level, see figure 6.7a, b, c, f for examples. However, increasing the speed creates a favourable keyhole-like shape, characterised as wide at the top and narrower at the weld root, as shown in figure 6.7 g, h, i. It was identified that the speed of 11mm/s was enough to create a wide melt pool at the top of the weld line and this speed maintained enough heat from the beam to reach to the very end of the plate and to melt the full thickness during its travel without causing any over melting at the top or excessive melting at the bottom of the weld, i.e. the root. Figure 6.8 shows the measurements of the width and the depth of the weld. As the speed increased, the width of the WZ decreased due to the lower effect of the applied heat input as the beam travelled, see figure 6.8a. On one side the width was in inverse proportion with the beam speed rate, while on the other side it was in direct proportion with the beam current and this was confirmed by figures 6.8 a and b respectively. Regarding the depth of the WZ, the slow speed rate provides a keyhole of low depth due to the vaporising effect of the high melting temperature leading to creation of a deep underfill at the top of the weld face, see figure 6.7 a, c,d and f, or some of the molten alloy at the fusion state finds a way to escape from the rear side of the WZ, i.e. the roots, causing an excessive penetration and a large drop-out shape of solidified metal to accumulate at the root, see figure 6.7a,b,e.

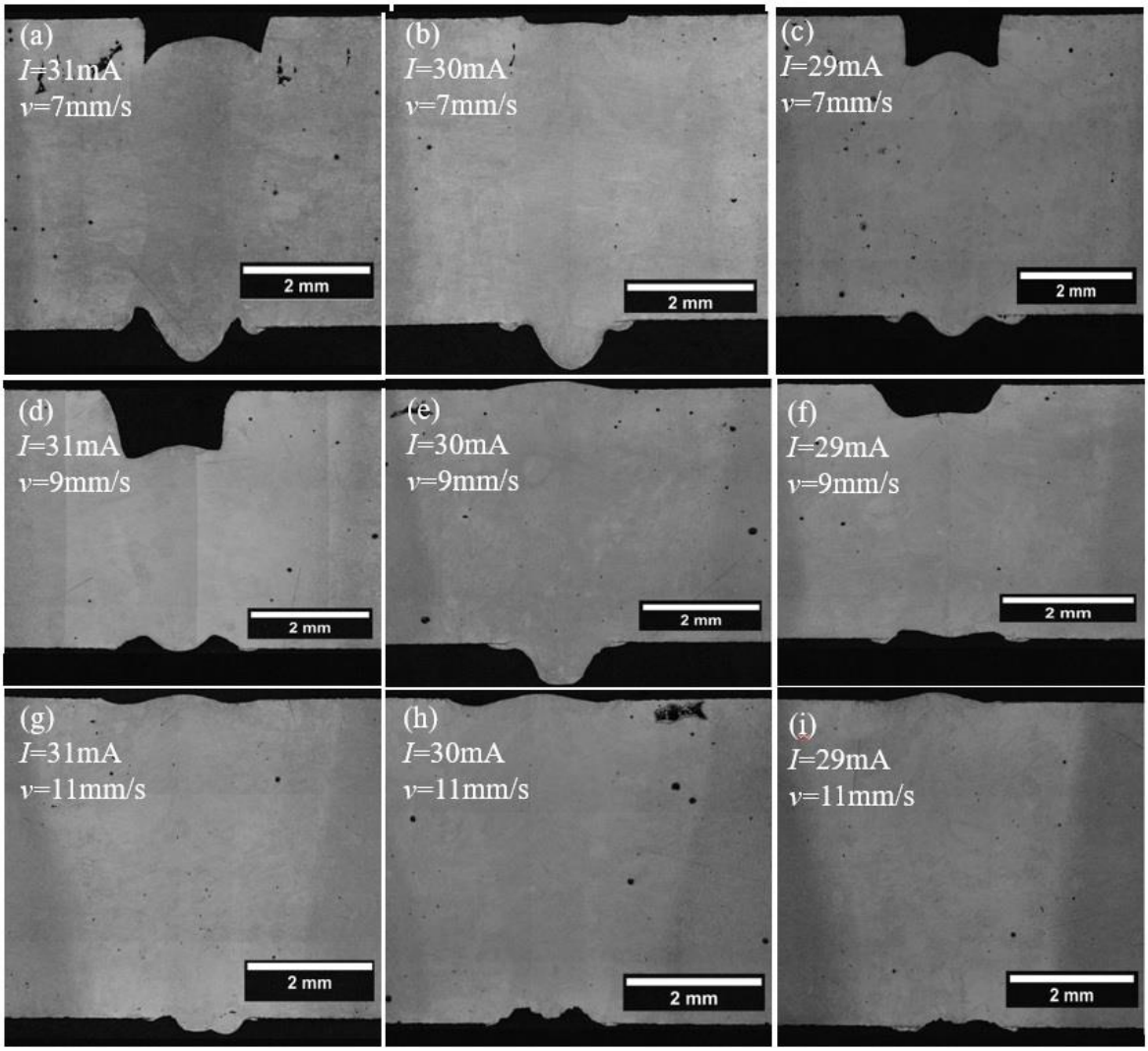

Figure 6.7 Cross-section images of the weldtracks obtained by inputs from the discrete DoE approach for the Ti-6Al-4V alloy.

However, if the WZ temperature is high enough, the molten metal which forms the drop-out at the root, detaches away from the root and once the molten pool starts to solidify, the remaining metal at the back of the joint shrinks toward the root as shown in figure 6.7 d,h,I, causing what is known as root concavity[210], [211]. Figure 6.8 shows the keyhole depth behaviour when using 7mm/s and 9mm/s beam speed. While the intermittent and the undercut and underfill were clear when applying these two speeds, see figure 6.3 for example, and a reduction in depth measurements observed as current from 29mA to 31mA in case of 7mm/sec beam speed see figure 6.8d. Meanwhile, when using a beam speed of 11mm/s the keyhole depth was almost equal at different selected beam currents of 29mA, 30mA and 31mA.

The discrete method and the keyhole measurements help to standardise the criteria to evaluate and select the best variables to be used in the next step, which involves the dissimilar welding between Ti-6Al-4V and pure vanadium alloy.

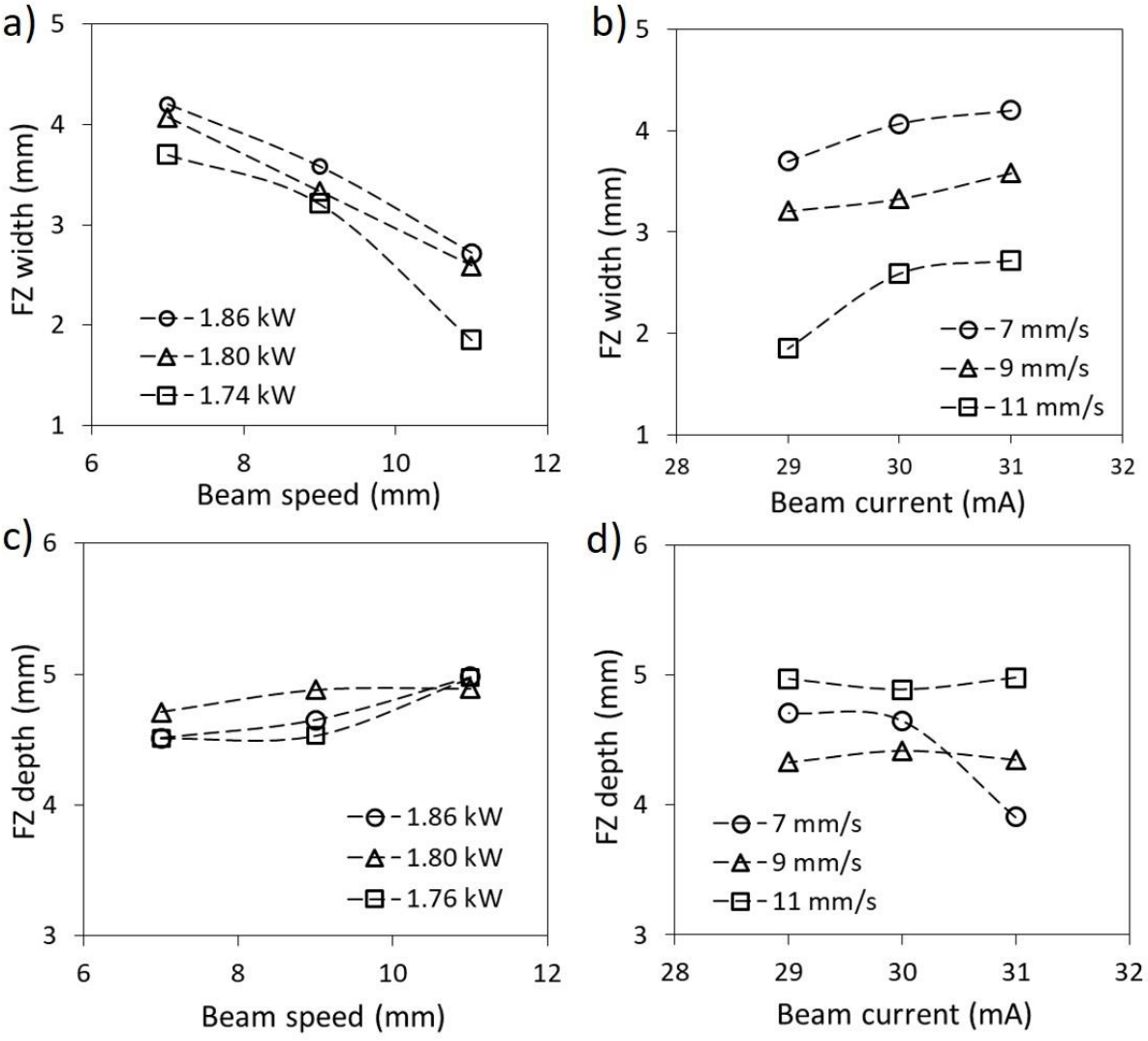

Figure 6.8 Plots showing the effect of beam speed and current for a linear method of the 5mm on: (a) the WZ width, and (c) the weld depth. Beam power is mentioned for further reference.

However, when applying those parameters over the vanadium plate, and taking into consideration the differences in melting point between Ti-6Al-4V and CP-V alloys, additional time will be required for V to reach the liquid phase using the same amount of heat inputs as used previously on Ti-6Al-4V. Therefore, the decision was made to lower the beam speed rate, from 11mm/s to 7mm/s, as it has a significant effect on the keyhole profile as was confirmed in previous trails in chapter five. It was suggested to carry out a weld bead-on-plates trails on the CP-V 5 mm plate using a 7mm/s beam speed and 31mA beam current,

see figure 6.9. The results showed a smooth line of weldtracks, but no penetration of the keyhole was observed, see figure 6.10a for an example. A new set of parameters was introduced to perform additional beads-on-plates for the vanadium alloy. After using the 31mA current, the new beam currents suggested were 33mA, 35mA and 37mA, keeping the beam speed constant at 7mm/s, see figures 6.9 and 6.10. From the cross-section of the CP-V keyhole profile, the depth of the keyhole increased from 63% of the total plate thickness at 31mA to reach ~75 % at 37mA current, this trend was predicted by Rosenthal equation as seen in figure 6.4b.

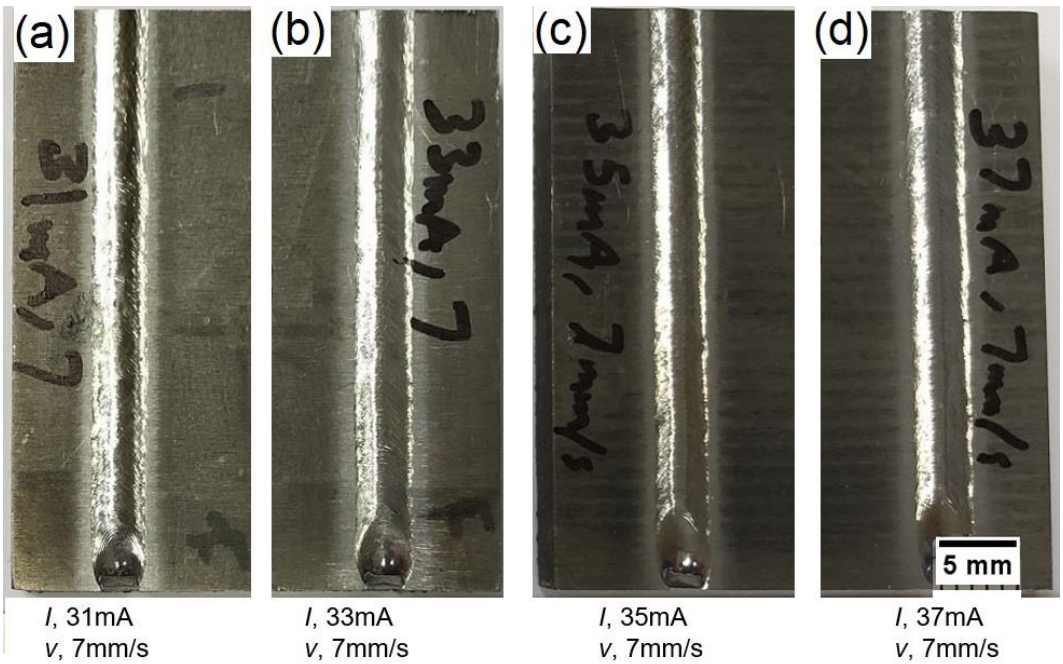

Figure 6.9 Optical image showing the bead-on-plate on CP-V alloy.

Figure 6.10 shows a summary of the inputs used to perform the weld beads-on-plate over the CP-V alloy and the images of the weldtrack keyholes, showing the variation with increasing depth. The measurements of the keyhole size were performed from the top of the keyhole to the lowest point affected by the electron beam. A steady increment in V keyhole was observed with energy. Depending on the outcome of measuring the cross-section of the keyhole sizes formed in the vanadium weldtracks by beam penetration in the CP-V alloy, a further adjustment was suggested latter for the welding variables, i.e. the beam current, to be used to perform the dissimilar welding between the Ti-6Al-4V and vanadium alloy.

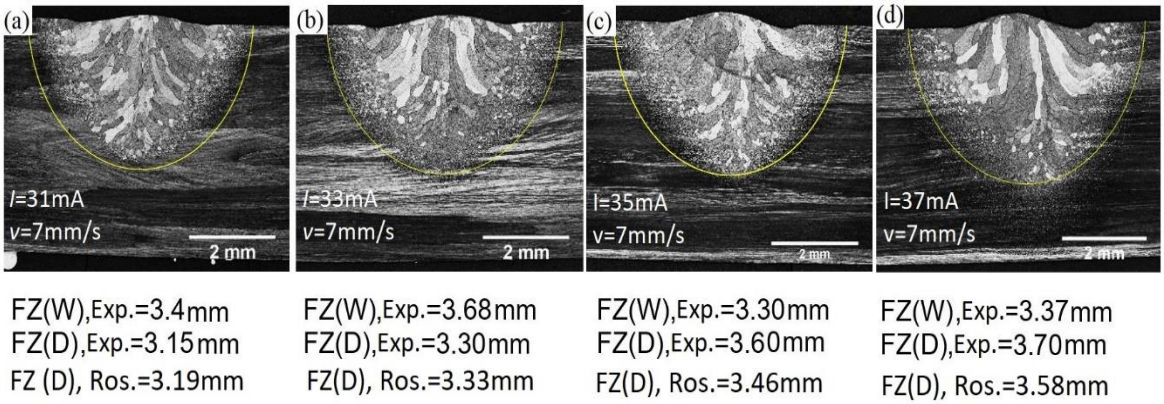

Figure 6.10 Optical images showing the WZ cross-section of vanadium weldtracks for (a) 31mA, (b) 33mA, (c) 35mA and (d) 37mA, all at 7mm/s and the same scale bar. The yellow line represents the numerical modelling of the WZ depth at η value of 0.9. Elongated grains towards the middle of the WZ can be observed.

6.6 Dissimilar welding

Based on the optimisations carried out, explained in chapter five, in sets I and II for 6mm Ti-6Al-4V plates, and the follow-up preliminary results from the discrete trails on 5mm Ti-6Al-4V plate and 5mm pure vanadium alloy plate, promising beam parameters were determined. The best welding parameters were selected by carrying out an inspection of each weldtrack using the appropriate welding inspection standards [210], [211]. From the above outcome, beam current of 37mA and travel at a speed of 7mm/s were identified as appropriate candidate parameters for performing autogenous dissimilar welding (AW01) as they would achieve a joint with full penetration. However, two addition joints (AW02 and AW03), using currents of 39mA and 41mA, respectively, were also applied in order to ensure the keyhole formed between Ti alloy and V alloy would achieve full penetration. A particular fixture was made to hold the two plates in butt position. Each plate has dimensions of 50 mm x 30 mm x 5 mm, and when they are fixed to each other, the total dimensions are 50mm x 60 mm x 5 mm. Figure 6.11 shows the fixture used to hold the two plates pre-welding operation.

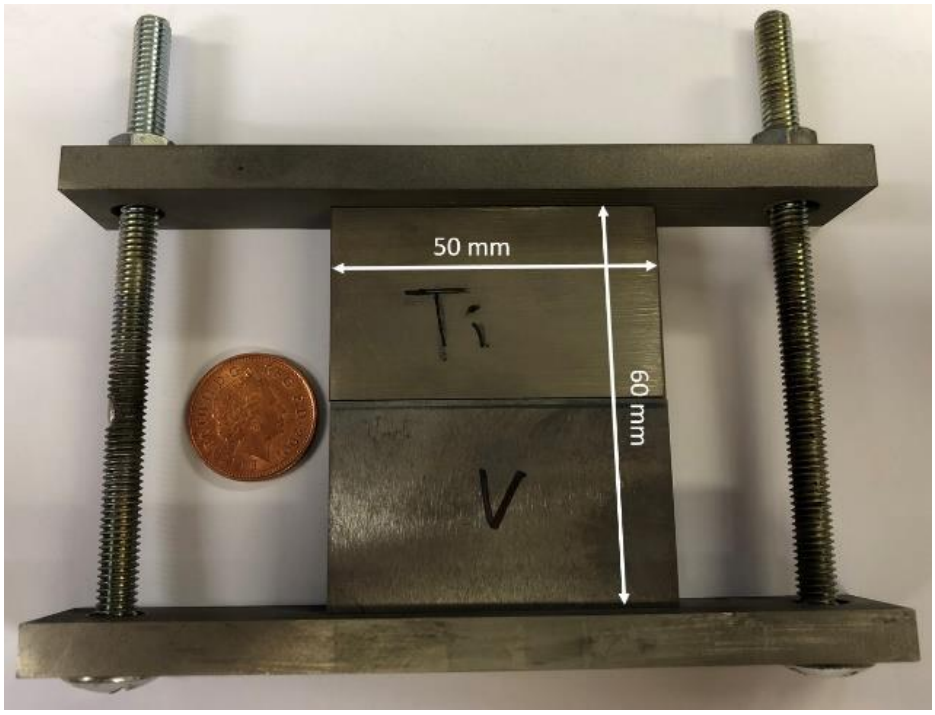

Figure 6.11 Shows the fixture used to hold the dissimilar plates into butt position pre-welding operation.

The prepared plates were placed inside the machine chamber, and the welding beam was applied at the middle of the joint under vacuum condition. The first dissimilar welding attempts were autogenous welding, achieved directly without adding interlayer, and a full penetration joint was successfully created between Ti-6Al-4V and CP-V, with no pores or post-weld cracks in the WZ. Three dissimilar joints, AW01, AW02 and AW03, were made using a beam travel speed of 7mm/s and beam currents of 37mA, 39mA, 41mA, respectively, see figure 6.12. All three currents showed a successful penetration; however when welding using 41mA current, defects, such as undercut, in the weldline started to show up and a non-continuous trail formed, due to instability in the keyhole melting pool caused by entrapped gas and metal vapour[223]. Figure 6.12c shows optical images which confirm that the disturbance increases with beam current.

Depending on the outcome of the autogenous dissimilar welding (without filler metal), the second phase of dissimilar welding between Ti-6Al-4V and vanadium alloy involved use of the designed alloy in table 6.4 as a filler metal. Three welding assemblies were prepared using a thin layer with a thickness of 5 mm of the designed fillers, Ti/V1, Ti/V2 and Ti/V3, prefixed at the welding joint. 37mA and 7mm/s were selected as the best variables for performing the welding.

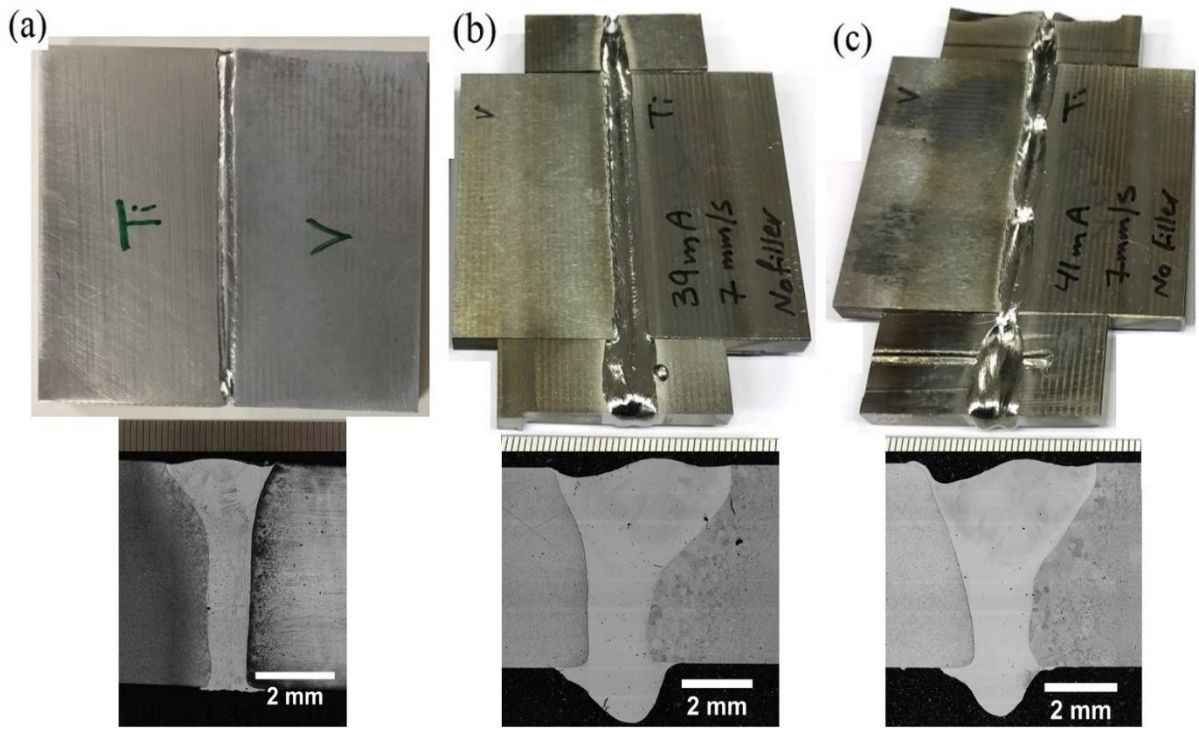

Figure 6.12 Optical images showing full penetration welding zones for three autogenous dissimilar welding joints of Ti-6Al-4V and CP-V at (a) AW01@37mA, (b) AW02@39mA and (c) AW03@41mA, all using 7mm/s beam speed

Despite using the same welding parameters that were used in dissimilar autogenous welding, upon applying the fusion welding process, a lack of penetration was observed in the WZ, see figure 6.13a, b and c. It was clear, from the microstructure of the cross-section images, that the amount of the heat input of 37mA current was not enough to achieve full penetration, as this beam current could not provide enough heat intensity to melt the full thickness of the joint upon applying the designed filler. Which resulting in observation as V wt.% in the filler metal increased, the depth of the WZ decreased, due to the high melting point of vanadium alloy[133]. The maximum WZ depth was about 3.71mm with a WZ width of 5.36mm for the dissimilar joint with filler type Ti/V1. The second filler type, Ti/V2, achieved a WZ depth of 3.48mm and a WZ width of about 6.17mm. The third filler, Ti/V3, showed a shallow depth reaching 2.60mm and WZ width of about 5.90mm. Both dissimilar joints, with Ti/V1 and Ti/V2, achieved a depth of ~ 75%, but the third filler was subjected to focus further as it only achieved a keyhole with 50% depth of the total thickness. Hence, an additional trail involving the reduction of the beam speed to 4mm/s was proposed, to give the beam the required time to melt its way through the plate thickness.

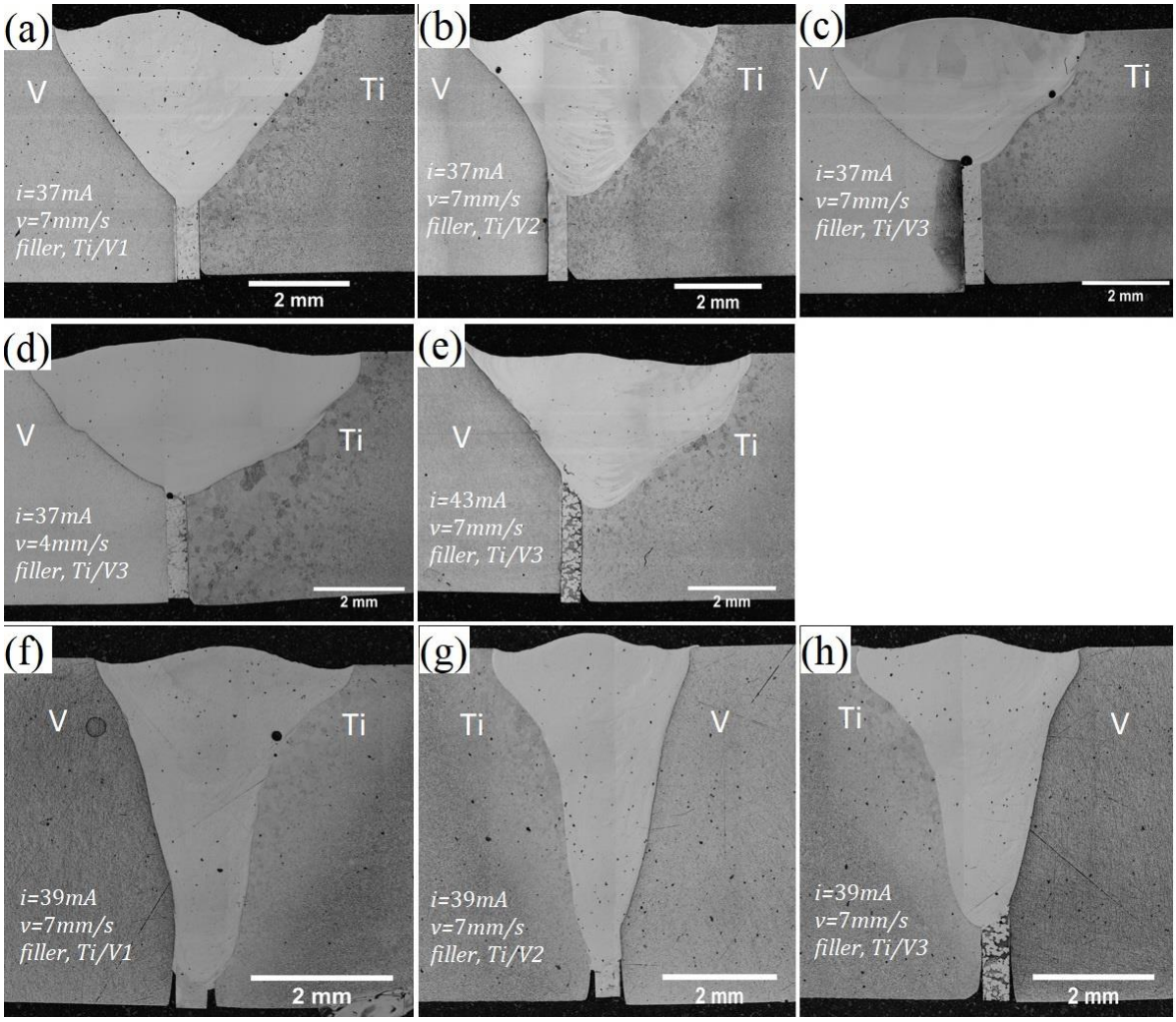

Figure 6.13 An optical images showing the effect of different welding parameters and different types of designed filler on the keyhole depth and width of the welding zone.

However, the WZ width increased to about 7.26mm [75], but with an increase in the depth of about 0.27mm as compared to the depth at 7mm/s, see figure 6.13d which shows the lack of penetration in the welding zone. It is unfavourable to use a low-speed rate as the amount of the heat input becomes higher, leading to a slow cooling rate, so both, the WZ and HAZ become wider, and grain growth will take place, and massive coarse grains of α′ will form[4].

The thermal modelling confirms a theoretical trend showing an increase in the depth will be achieved upon increasing the heat input when applying the designed fillers to the welding joints. A similar trend, experimentally, was also observed for the DW samples W1 and W2 as they achieved more depth as the beam power increased, see figure 6.6 for the DW W1, W2 and W3 samples.

Further adjustment was carried out to the welding parameters by increasing the beam current to 39mA and maintaining 7mm/sec beam speed to perform the dissimilar welding joint process with designed fillers. From the figures, 6.13 f, g and h improvement in the WZ dimensions could be observed along with a reduction in the WZ width and increase in the depth. The WZ widths measurements of Ti/V1, Ti/V2 and Ti/V3 joints were 3.64 mm, 3.46 mm and 3.66 mm, respectively. Improvements in the depth were observed, and the joints with fillers Ti/V1, Ti/V2 and Ti/V3 achieved depths of 4.74 mm, 4.44 mm and 3.94 mm, respectively. Those variables achieved a stable welding region with good welding profile and favourable welding keyhole-shape. Also, the penetration depth of the keyhole with narrow WZ was improved and achieved ~95% depth of the total joint thickness in the case of using Ti/V1 filler metal, see figure 6.13g, for example. This is suggested to be due to the heat source reached temperatures for Ti-rich compositions, allowing a liquid-solid transformation, at concentrations for binary mixings, into βTi-V with no intermediate transformations. This suggesting that the designed filler metal demonstrate an appropriate combination of physical properties which helped to establish a balance with the selected welding process variables during the joining of Ti-6Al-4V and CP-V alloy by creating a WZ with full depth, see figure 6.13f and g, and acceptable overall weldline features.

However, the dissimilar joint with Ti/V3 achieved 79% of the total joint thickness, but this was higher than the previous attempts. It is worthy of mention that when filler type Ti/V3 was subjected to a beam current of 43mA and beam speed of 7mm/s, the WZ became bigger, 6.59mm in width, and a shallow depth of 3.20mm was obtained. Also, a reduction in the welding metal was observed at this level of high heat input and, due to the vaporising effect, the concave shape was evident at the welding face as shown in figure 6.13e.

6.7 The microstructure analysis of the Ti-V dissimilar welding zones.

6.7.1 Optical analysis

All the welding joints, with or without filler metal, showed three regions: BM, HAZ and WZ. Figure 6.12 and 6.13 show the optical images of the transverse section from the welded joints. The favourable keyhole-shape of the WZ can be observed for the non-filler joints in figure 6.12 and figures 6.13 f, g and h, in the case of welded joints with designed fillers. In Figure 6.12a, full penetration dissimilar welding joints with asymmetrical WZ features can be observed. However, the lack of penetration was detected in all the dissimilar joints shown in figure 6.13. The optimised parameters (beam currents and Beam speed) were sufficient to create a full penetration in the case of direct joining without filler metal, figures 6.12 and 6.14a. However, as with the beam currents and the beam speed [224], adding the designed filler metals had a significant effect on the dimensions of the welding zone. The effect of high heat input was identified by wide WZ and shallow welding depth, see figure 6.13d, in the case of low-speed rate and 6.13e high beam current. Figure 6.14e presents the WZ structure, which, due to the rapid cooling rates, consists of fine needles-like α´ phase within large, about ~460μm, longitudinal prior β boundaries, which was confirmed previously in [67], [70], [125]. While, with a grain size of approximately ~248μm, the HAZ structure at the Ti side, consisted of acicular α structure and α colony [67], [120], [121], see figure 6.11c. Further toward the Ti-BM, the structure was mainly equiaxed α/β and the grain size was ~36μm, see figure 6.14a. Meanwhile, at the V-side, the HAZ region near the WZ was recognised by large grains with an approximate size of ~80μm, see figure 6.11d. Due to the full solid-solution in Ti-V systems, i.e. βTi-V solid-solution upon solidification [113], only intermediate transformations are expected to occur during liquid-solid transformations. This can also be suggested for Ti-6Al-4V and CP-V, favouring welding with no gas pores from mushy zones, cracking and shrinkage[225]. However, in the case of the V-HAZ, it showed less diverse microstructure, and only coarsening in the grains with a size of~80μm was observed, see images in figures 6.14d and 6.15a. The BM structure of both Ti-6Al-4V and CP-V is shown in figure 6.15. The equiaxed α/β structure of the titanium alloy can be seen in image 6.15b, while the image 6.15a shows the base metal of the cold-rolled as-received vanadium alloy.

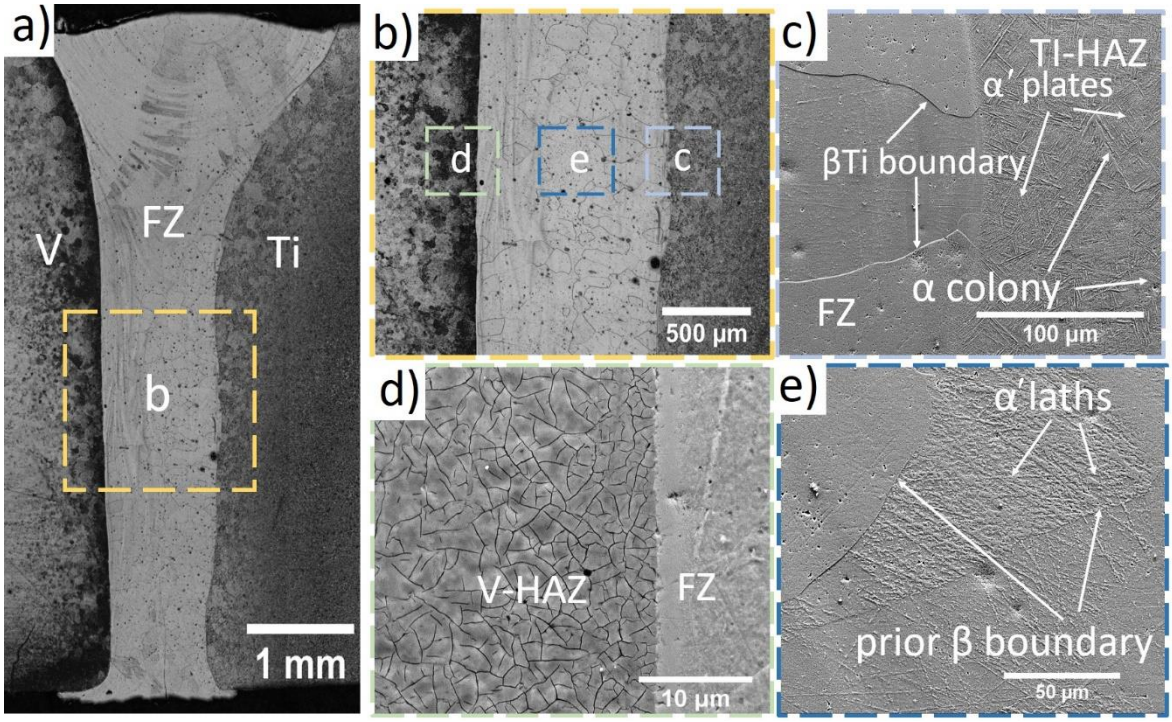

Figure 6.14 Optical microstructure of the autogenous dissimilar welding of Ti-6Al-4V alloy to CP-V alloy (without filler metal): (a) The microstructure of the WZ, (b) a close-up image of the joint zone, (c) α colony and acicular α structures at the Ti-HAZ, (d) the single-phase V-rich side near WZ, (e) the middle of the WZ showing fine α′ laths structures within prior β boundaries.

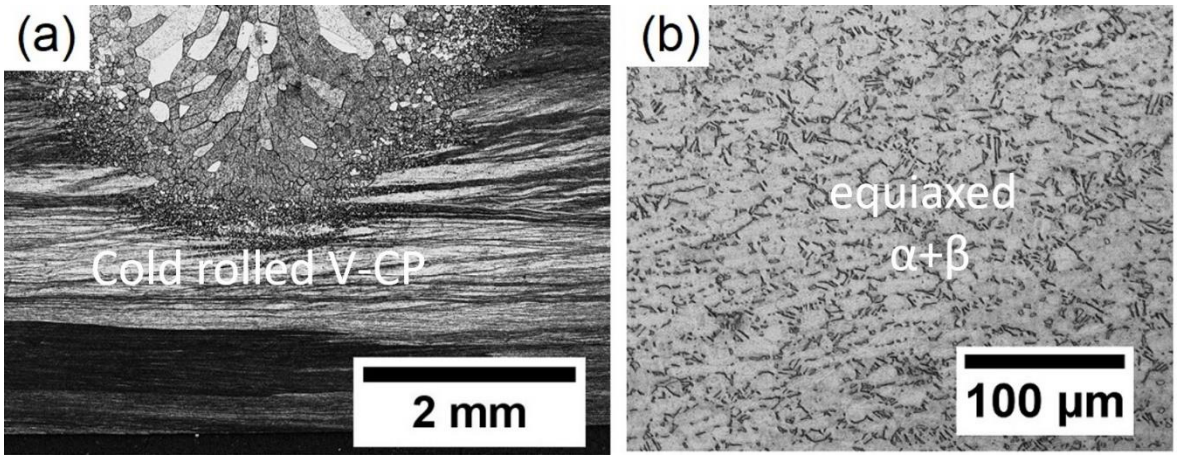

Figure 6.15 Optical images showing (a) the base metal of the cold-rolled CP-V alloy and (b) the base metal structure of T-6Al-4V

6.7.2 SEM/EDS analysis

Melting of the base metal, dilution of the filler metal, solidification of the weld bead, microstructural development in the weld bead and HAZ, and thermomechanical distortion and residual stresses all follow from the heat inputs of the welding process [226]. EDS analysis was performed on the welded joints achieved, with both the HAZ and WZ analysed to identify any changes which had taken place in the chemical composition or any developed phases. As vanadium does not display an allotropic transformation in the solid-state, it was expected that, upon cooling, any effect on the microstructure caused by heat sources would mainly be in the form of grain growth with no formation of second phase particles. However, the EDS analysis of the dissimilar WZ carried out by EBM system, revealed variation in the concentration of Ti and V due to the dilution between these two alloys during the melting phase. The elemental maps with EDS for the dissimilar autogenous welds, 37mA at 7mm/s, showed evidence of dilution of Ti and V alloys, see figure 6.16. It can be observed that vanadium distributes in a more spread out way across the weld than titanium for the given amount of EDS scanning time. Titanium and aluminium, on the other hand, can easily be identified on the WZ and titanium rich-side mainly.

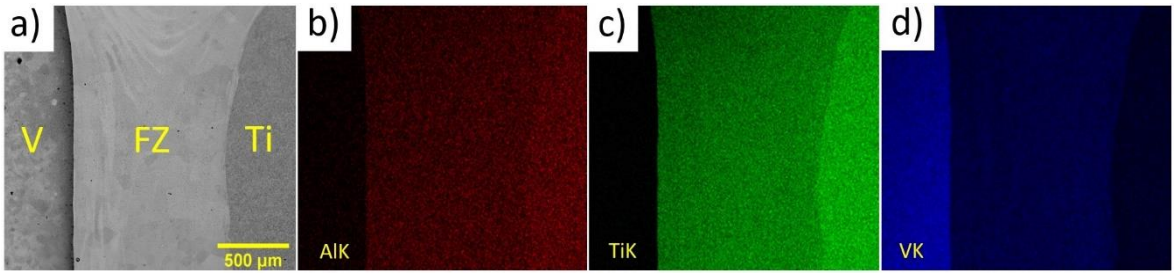

Figure 6.16 SEM images of the dilution between Ti and V alloys in the welding zone of the AW01 welded sample, including a) image by secondary electrons showing b) aluminium c) titanium and d) vanadium counts.

According to DuPont et al. [227] dilution can be defined as the proportion of base material in the resultant weld metal of a single bead deposit, which is the ratio of the cross-sectional area of molten base material to the total cross-sectional area of the fusion zone. The direct consequence of dilution is the difference in chemical composition of the final weld metal from both the base and filler materials, producing a new deposit alloy intermediate between the two. The melting of base metal and the subsequent mixing with filler metal causes the final chemistry of the weld deposit to be between that of the base and filler metals. When a filler metal has the same chemistry as the base metal, the final weld-metal chemistry remains

the same, theoretically[226]. Depending on the amount of base metal that is melted and the amount of filler metal that is added, the final chemistry of the weld deposit can be approximated using the dilution equation (6.4) proposed by DuPont et al. [227] and Francis et al. [228] based on welding parameters and the geometry of the WZ.

$$Dilution\ \% = \frac{\text{Weight of the melted base metal}}{\text{Weight of the total WZ}} * 100 \ldots\ldots\ldots\ldots\ldots\ldots\ldots\ldots (6.4)$$

The macroscopic analysis was conducted to evaluate the chemical composition of the weld metals by calculating the percentage dilution (D%) of the base metals as shown in figure 6.17, for which purpose the cross-section of the WZ was divided into different sections to estimate the total area of the welding zone. Using ImageJ software the melted BM and the welding zone areas were then measured. The WZ was divided into several sections, namely the Ti-BM area (A_{Ti}), V-BM area (A_v), the filler alloy area (A_f) and the total WZ area (A_{wz}) which is ($A_{Ti} + A_V + A_f$). This enabled the dilution (D) to be estimated using the equation (6.5):

$$D = \frac{A_{Ti} + A_V}{A_{WZ}} * 100 \ldots\ldots\ldots\ldots\ldots\ldots\ldots\ldots\ldots\ldots\ldots\ldots\ldots\ldots\ldots\ldots\ldots\ldots\ldots\ldots (6.5)$$

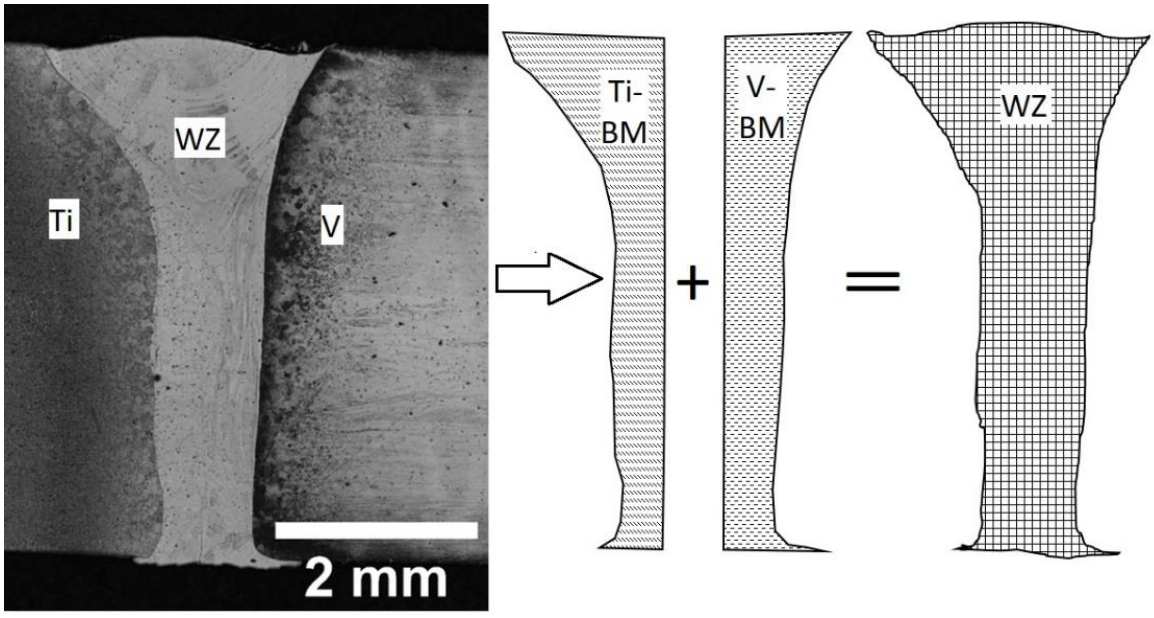

Figure 6.17 The cross-section and a schematic view of areas of base metals and WZ of a welded joint considered in graphical measurement for dilution calculation.

Table 6.6 illustrates the dilution percentage values calculated for different weld metals using equation (6.5). Despite using welding processes such as EBW, LBW and spot laser welding, these were considered low-dilution welds due to the small amount of melted base metal and most of the welds being conducted without filler alloy [229]. According to the dilution measurements of the autogenous welded sample type AW01, despite the narrow area of the WZ, a high percentage of dilution was observed. This indicates that the beam current of 37Ma at travel speed of 7mm/sec. was able to establish a welding beam with sufficient heat input to form a narrow keyhole with full penetration and with melting of only small areas of the two base metals, i.e. (Ti and V). Meanwhile, when the heat input increased as the beam currents increased from 39mA to 41mA, the molten pool became larger as the welding beam melted extra areas of the base metals, as seen in the autogenous dissimilar welded samples (AW02 and AW03), and the dilution % calculated from the fusion areas increased respectively from 85.10% to 89.39%.

Table 6.6 Show the dilution percentage (D%) calculations for different dissimilar weld metals. All the welds were conducted under constant welding travel rate of 7mm/sec.

	Autogenous weld (AW)			Dissimilar weld with filler alloy (DW)					
Beam current	37mA	39mA	41mA	37mA	37mA	37mA	39mA	39mA	39mA
Filler type	AW	AW	AW	Ti/V1	Ti/V2	Ti/V3	Ti/V1	Ti/V2	Ti/V3
Welded sample	AW01	AW02	AW03	W01	W02	W03	W1	W2	W3
$A_{TI}+A_V$ (mm^2)	6.52	14.74	13.62	10.28	10.56	11.29	5.02	5.27	5.81
A_{WZ} (mm^2)	6.71	17.32	15.24	11.75	11.54	11.45	8.09	8.08	7.74
D%	97.08	85.10	89.39	87.47	91.54	98.67	62.08	65.25	75.05

When the filler alloys were applied to the welding zone, a reduction in the dilution % was observed as the V wt. % increased in the filler metals. The dissimilar welds were carried out using welding variables of 37mA beam current and 7mm/sec welding speed. Upon applying the filler alloys, those variables produced an increase in the width of the welding zone without any progress in the depth of the welding zone, given that the heat intensity was only

able to melt the top face of the joint. The typical profile of these welds was a shallow WZ with lack of penetration and a reduction in the depth when the V wt. % increased from 20 to 60. Therefore, the heat intensity of the 37mA beam current was only able to fuse half of the depth length, and hence more heat input would be required to achieve a WZ with higher depth. The measurements of the WZ showed that dilution % is directly proportional to the area of the WZ. As the beam current was set to 39mA, the cross-sections of the DW samples type W1 and W2 showed a more favourable keyhole profile comprising a narrow welding zone with near full penetration. In addition, as the beam hits the surface joint, the filler alloy with the higher amount of high melting point alloy, i.e. vanadium, will require a longer time to melt the filler, so most of the heat will be trapped at the joint surface, thus leading to increased melting of the base metals at the surface of the weld. Therefore, the WZ becomes wider, and the joint shows a lack of penetration. Results showing large areas of the base metals melting into the welding pool will reflect advancement of the dilution %.

The EDS analysis of the dissimilar WZ in figure 6.18 showing different locations at the WZ was tested to identify the concentration percentages of Ti, V and Al in the welding zone. At the Ti-rich side, see figure 6.18b, the maximum V wt. % is ~26.64, while the Ti wt. % is about ~68.68. However, the Ti wt. % near the V-rich side becomes equal to V wt. %, see figure 6.18a, for example. Meanwhile, at the very edge of the fusion line at the V-rich side, the consecration of V wt. % was in the range of (~58 - ~80). Those readings give us some perception of how the concentration of titanium ranges from high to low as approaching the V-rich side, and vice versa, see figure 6.19. The EDS analysis was carried out for the WZ of the dissimilar welds with the designed filler. The results showed traces of C wt. % in the WZ due to the manufacturing process of the filler metals, which involves using graphite in the sintering process. Three locations of the WZ were selected for examination: near Ti side, the WZ centre and near V side. Figure 6.20 shows that the chemical composition in the WZ consists mainly of Ti, V, Al and in some cases C. The WZ analysis results show variation in the concentration of Ti and V with the type of filler used. Figure 6.21 shows the concentration of Ti, V and Al in the WZ. The W1 welds recorded the highest percentage of Ti across the WZ. When the filler was changed to Ti/V2 in welds W2 the Ti wt. % reduced, and on the other side, the V wt. % started to show improvement. The WZ of W3 showed even distribution wt. % of the elements in all three selected regions see figure 6.21 for examples.

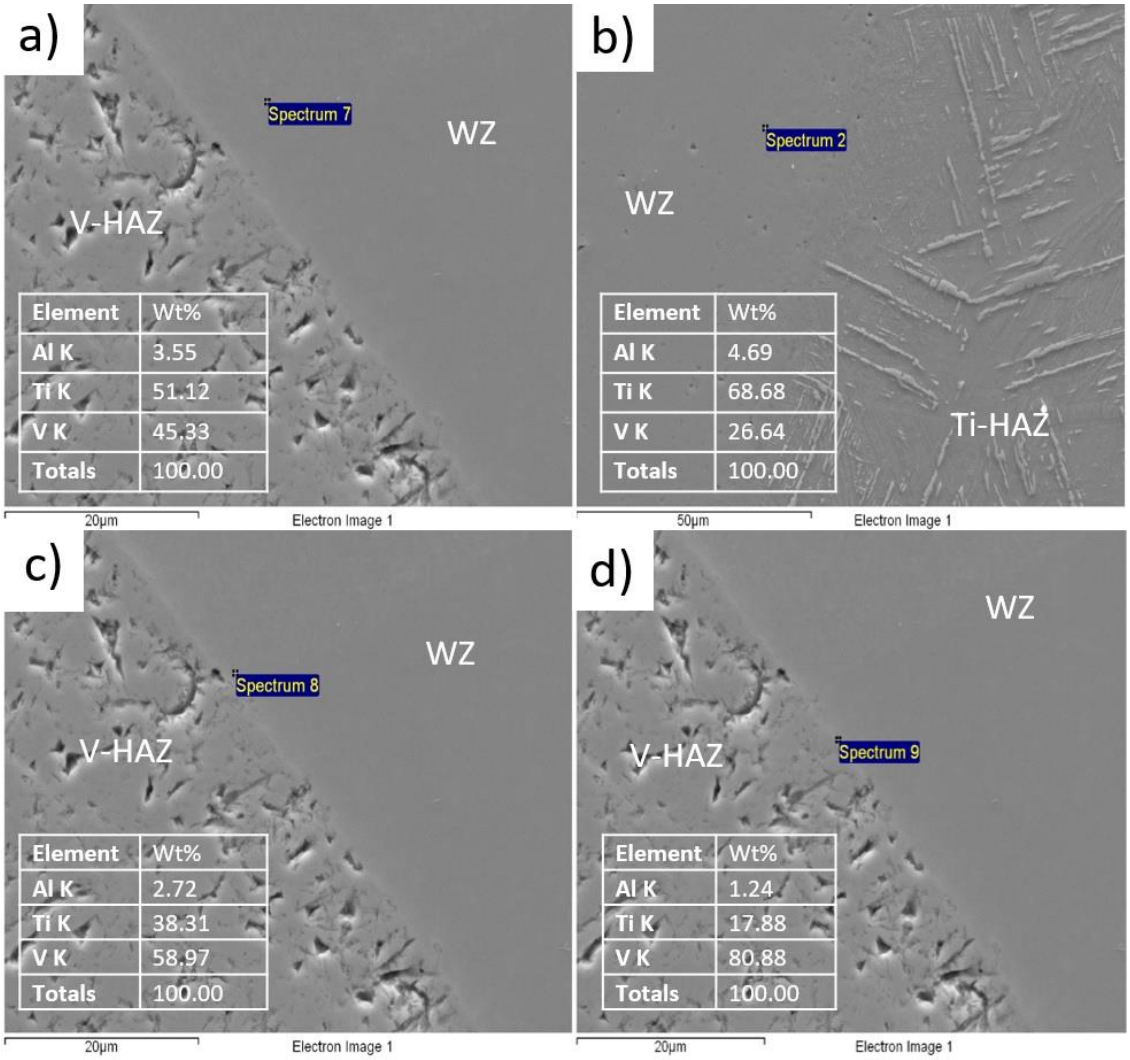

Figure 6.18 Show the concentration wt.% of Ti and V at different locations across the WZ of AW02 welded sample: (a), (c) and (d) near the V-rich side, and (b) near the Ti-rich side.

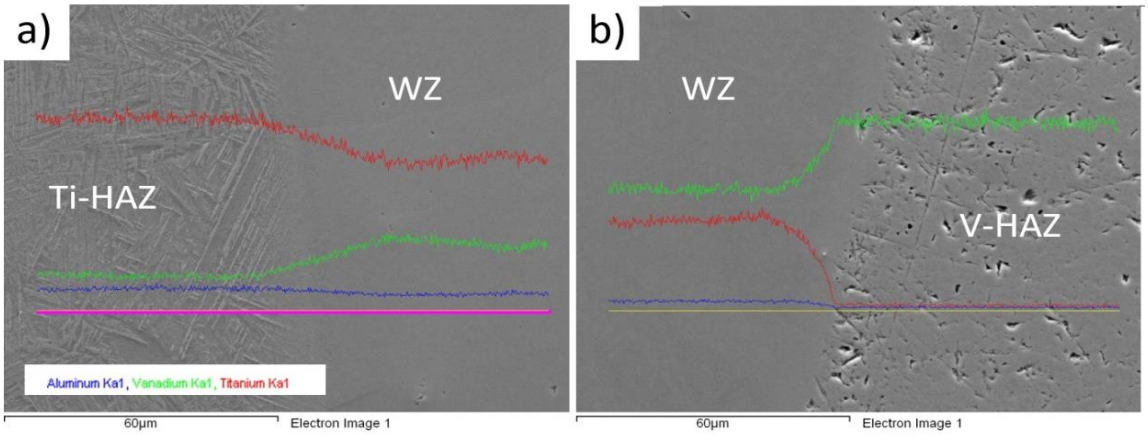

Figure 6.19 Show the concentration wt.% distribution of Ti, V and Al across the WZ: (a) near the Ti-rich side and (b) near the V-rich side. The mapping showing a close intensity rate near the V side as this zone contains 38 Ti wt.% and 55 V wt.%, while near the Ti side contains 62 Ti wt.% and 31 V wt.%.

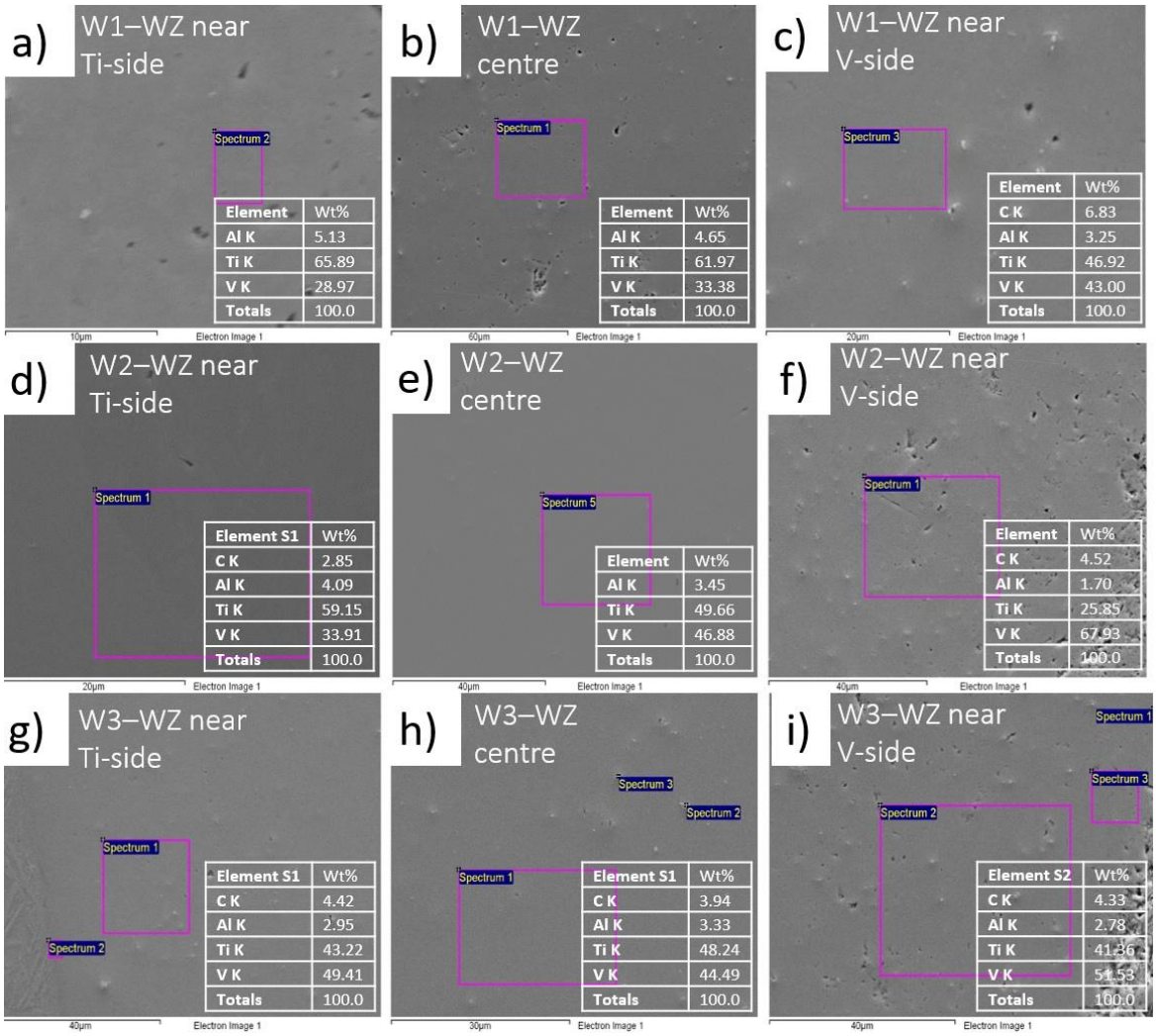

Figure 6.20 EDS analysis for the WZ of W1, W2 and W3 welded samples showing the concentrations wt.% distribution of Ti, V across the WZ at near the Ti-rich side, WZ centre and near the V-rich side

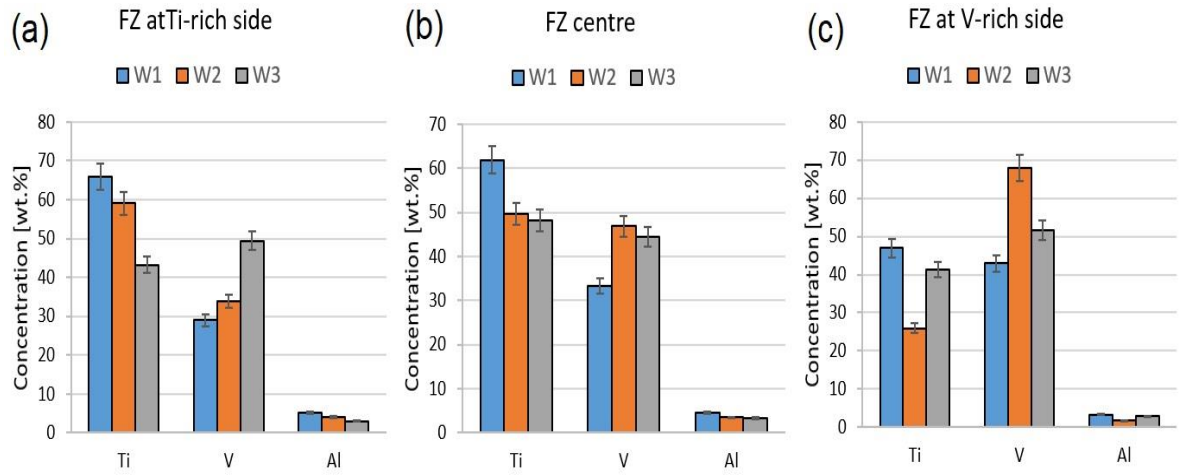

Figure 6.21 Showing approximate concentrations of Ti wt.%, V wt.% and Al wt.% across the WZ of welded samples type W1, W2 and W3.

6.8 Mechanical properties evaluation.

6.8.1 Hardness analysis

The microhardness measurements were carried out for all the weldtracks of Ti-6Al-4V and CP-V alloys. A typical hardness distribution was observed at the cross-section of the titanium bead-on-plates keyholes. The WZ shows the highest hardness values, reaching about 395±10 HV_1, due to the high cooling rate providing a fine α structure at the WZ, which was reported in [4], [13]. Meanwhile, the BM of Ti-6Al-4V showed the lowest hardness values, at about ~323±10 HV_1. The adjacent region to the WZ, represented by the HAZ, has been reported by [4], [42], [43], [68] to show a lower hardness than the WZ; due to the mixture in structure between the WZ and the BM, the hardness was intermediate between the WZ and the BM. As the HAZ structure showed a reduction in acicular α, a decline in hardness value was observed of about 376±8 HV_1. In contrast to the titanium alloy, the CP-V weldtracks showed a different distribution in terms of the hardness measurements. The BM of the CP-V with a banded-structure which was reported by Muroga et al.[230], see figure 6.15a, showed the highest hardness values, due to the cold-rolled effect, the maximum hardness at the V-BM reached about ~160±10 HV_1. Meanwhile, the WZ exhibited grain growth due to the thermal welding cycle, and the hardness value was the lowest compared to both BM and HAZ. The large grains of the WZ recorded a hardness value of about 93±5 HV_1. Even at different beam currents, the hardness value was low, and no further impact was observed when increasing the beam current from 31mA to 37mA at 7mm/s beam speed. The HAZ showed an intermediate hardness value in the range of 110±5 HV_1. Impagnatillo et al. [231] reported that subjecting the V-4Ti alloy to a higher temperature above 600 ˚C will reduce the hardness value.

Figure 6.22a, b and c shows the distribution of Vickers hardness measurements of non-filler (autogenous) dissimilar welds AW01, AW02 and AW03, respectively. The measurements were conducted to cover five regions: V-BM, V-HAZ, WZ, Ti-HAZ and Ti-BM. The measurement was set to begin at V-BM and end at Ti-BM. As the microstructure changed in these five regions, the measurements revealed variation in the hardness as the reading progressed from the V-BM, through the centre of the WZ, ending in the BM of the Ti. The hardness values for V-BM and Ti-BM were approximately 164±10 HV_1 and 334±10 HV_1, respectively. The highest hardness, of about ~383±5 HV_1, was shown in the Ti-HAZ region due to the presence of fine plate-like α structure which increments the hardness number, as confirmed in [9], [120], [121]. The lowest hardness values, of about 95±5 HV_1, were

recorded in the V-HAZ. In contrast to the high hardness values of the WZ found in the Ti weldtracks, reaching ~395 HV_1, this value was 100HV lower in the measurement carried out for the WZ of the dissimilar welding between Ti-6Al-4V and V alloys. The maximum hardness values of the autogenous WZ were in the range of 285±15 HV_1. According to the solid-solution of Ti-V systems, the WZ upon solidification will consist of βTi-V structure, with no intermediate transformations; the main structure will consist of Ti-V solid-solution with a cellular structure and different percentages of V about ~26±10%, as was confirmed by Tomashchuk et al.[113]. Aleksander et al. [32] report that the impact toughness improved significantly upon adding the vanadium alloy; however, a reduction in the hardness was observed as ductility improved.

However, figure 6.22 d, 6.22 e, and 6.22 f are showing the hardness distribution across the WZ of the dissimilar welds with the designed filler W1 (Ti/V), W2 (Ti/V2) and W3 (Ti/V3), respectively. Adding the filler metal to the melting zone causes a significant increase in the hardness values. According to the EDS analysis, in the middle of the W1 WZ, an increase in hardness measurements occurred from ~285±15 HV_1 to ~323±10 HV_1 when the concentrations of Ti and V changed from ~69 wt.% and 26 wt.% to ~61 wt.% and ~33 wt.%, respectively. While in WZs of W2 and W3, the hardness kept on rising with the increase in the V% over the Ti % in the filler metal. The maximum hardness of the WZ in the W2 welds was 24% higher when compared with the hardness values of the WZ of the non-filler welds AW01, AW02 and AW03. Increasing the concentrations of Ti wt.% and V wt.% to ~49 and 46, respectively, produced a hardness of ~350±5 HV_1. However, in W3 WZ, the hardness started to reduce as the V wt.% became higher in the designed filler over the Ti wt.% and the hardness value was only ~331 HV_1.

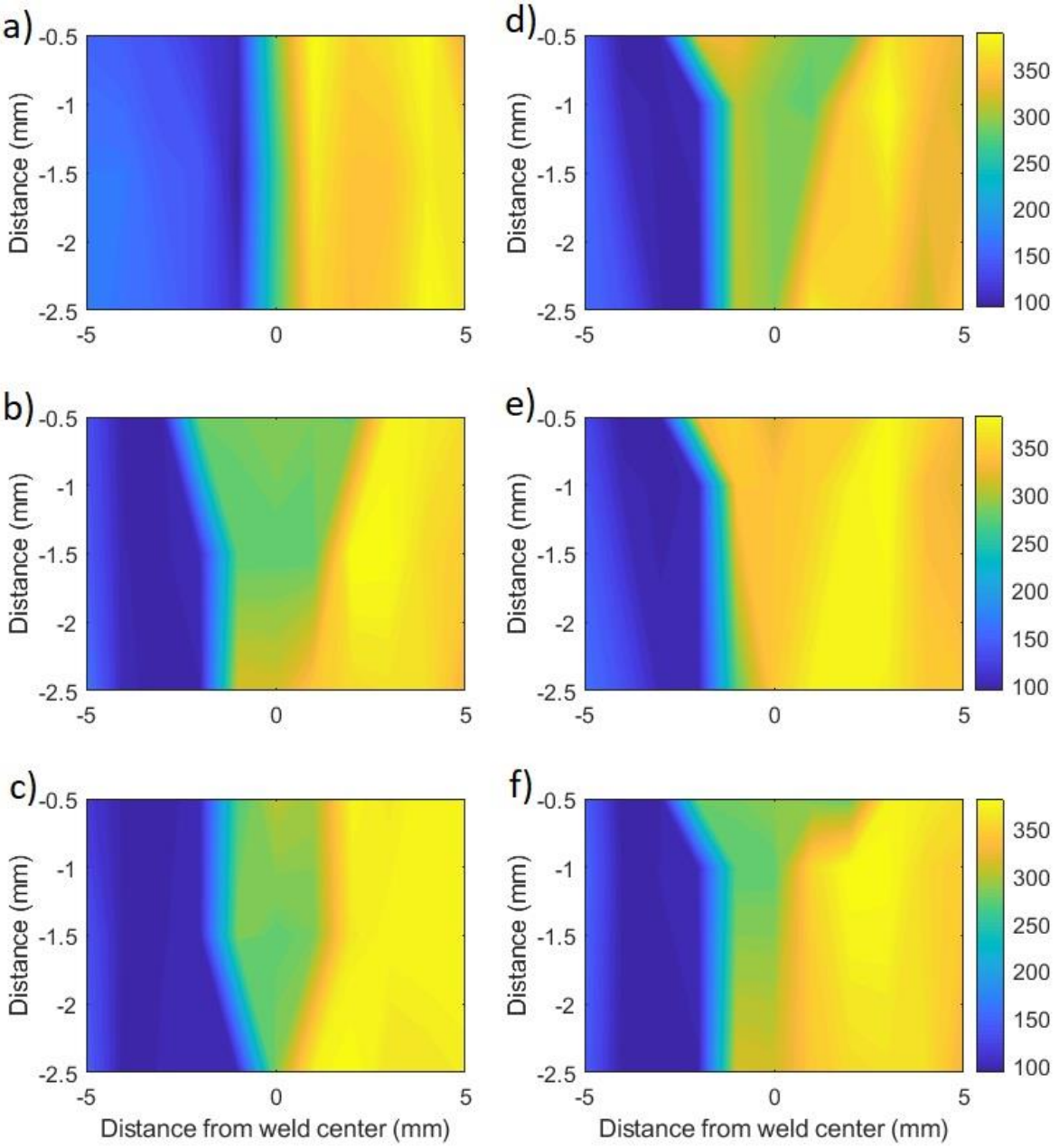

Figure 6.22 Microhardness distribution in the cross-section WZ of the autogenous welded samples (a) AW01, (b) AW02 and (c) AW03. The highest HV value and the lowest HV were at Ti-HAZ and V-HAZ about 395±5 HV_1 and 93±5 HV_1, respectively. While images (d), (e) and (f) represent the microhardness distribution across the WZ of the welds (W1, W2 and W3, respectively) carried out using the designed fillers metals. All the welds were performed at a welding speed of 7mm/s.

Despite the reduction in hardness of W3, its hardness was still about 12.5 wt.% higher than that at the non-filler (autogenous) AW0 welded samples. Figure 6.23 summarises the variation in hardness values with respect to the filler type used in the dissimilar welding between Ti-6Al-4V and CP-V alloys.

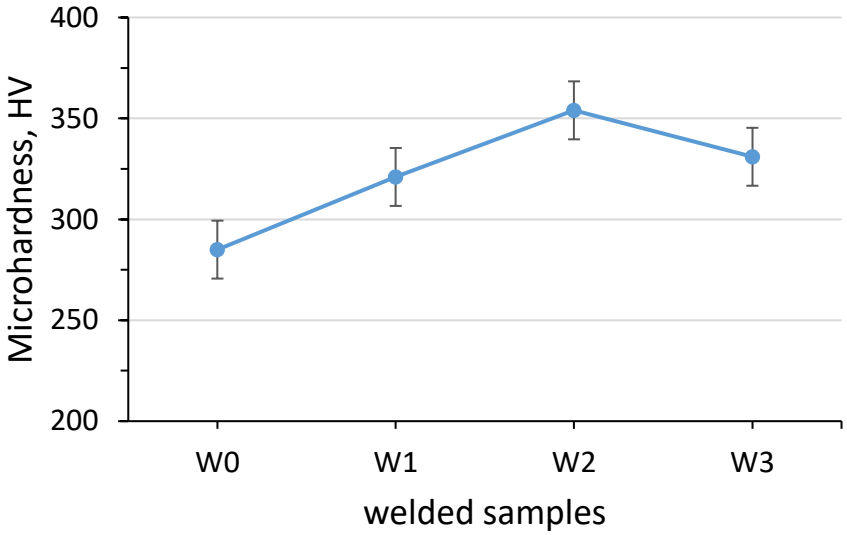

Figure 6.23 Show the effect of filler type used on the hardness values of the welded samples.

6.8.2 Tensile strength

It is well established that yield strength can be related to the hardness of metals[232]; in the case of titanium, its mechanical strength is well known to be highly influenced by the features of its microstructure, i.e. transformed α plate, plate colony and prior β grains [26]. Owing mainly but not entirely to these features, also to its rate of cooling from solidification and β-transus temperatures, the coarse grains in Ti-6Al-4V show low mechanical properties due to following analogous Hall-Petch relationships[233]. In the current investigation, lower mechanical properties were observed in the WZ compared to the titanium-rich weld side, HAZ and base metal. The vanadium-rich side, on the other hand, did not show a significant influence on the strengthening of the material upon welding.

Given that the strengthening mechanisms for metals mainly relate to grain size, material phase transformation, precipitation and work hardening, it was expected that vanadium, coarsening its microstructure upon local heating, as observed in figure 6.10, might contribute to a much lower extent than titanium. Additional tensile testing results in the form of stress-strain curves are shown in figure 6.24. It can be seen that a linear elastic region develops

briefly following a peak in strength to a plateau of close to 282 MPa. Material testing showed ductile failures near 23% of elongation approximately for all samples tested. Good consistency of results can be appreciated overall in terms of mechanical properties. In-situ observations in figure 6.25 showed neck formation during deformation, suggesting a ductile failure in the vicinity of the weld line, dashed inserted line. The stress-strain curves showed similar shape and values across the samples tested, suggesting that the failure was consistent, occurring at similar strength levels and appearing in the side of the metal with lower yield strength, i.e. vanadium. None of the samples fractured in the weld joint, suggesting the proposed method is effective for dissimilar welding.

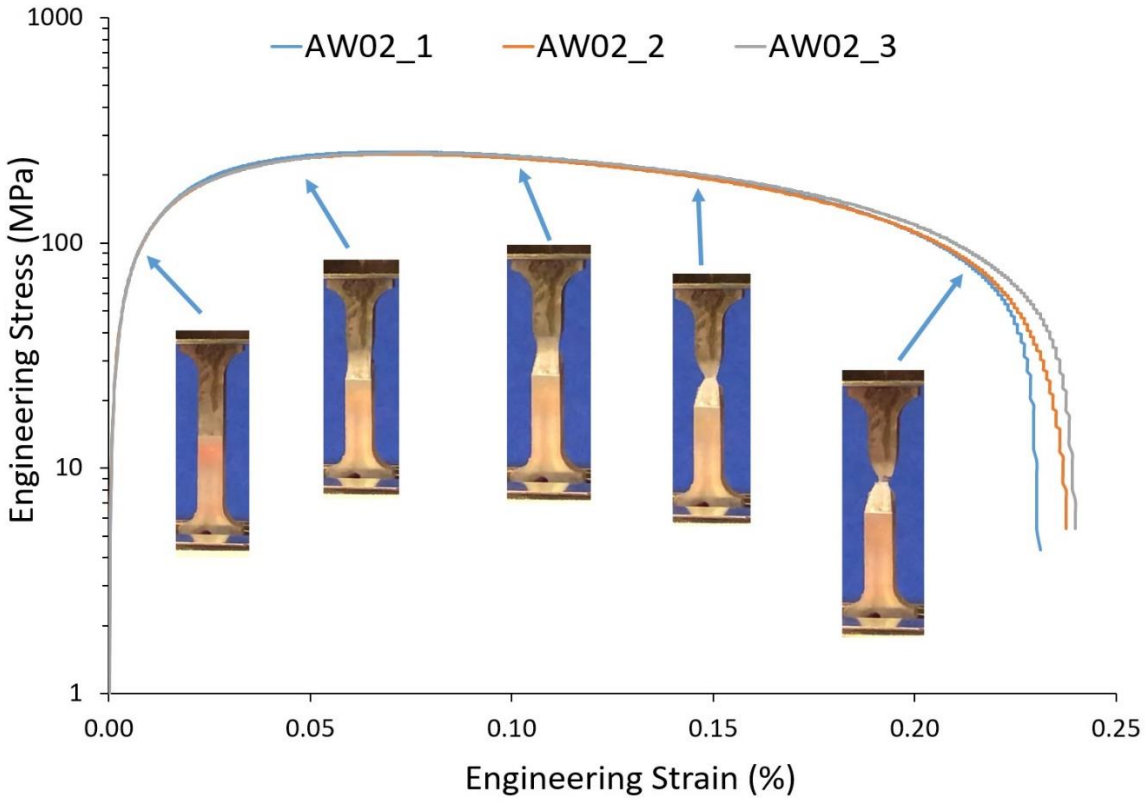

Figure 6.24 Stress-strain curves are showing linear elastic sections, plateau strength and failure to elongation of 23%.

Figure 6.26 shows the tensile behaviour of the welds sample with different types of filler metals. All the tensile samples show the same trend of the tension behaviour of the non-filler welds of ductile failure. In all the sample, the weakest zone in the welding joint was the HAZ [234], upon applying the tension load, the necking starts at the V-side precisely at the V-

HAZ. The UTS was recorded as 282 MPa, 250 MPa, 270 MPa and 248 MPa for the welds of W0, W1, W2 and W3, respectively. All the welded joint with designed fillers showed a joint efficiency of ~ 88.6%, 95% and 88%, for the fillers types Ti/V, Ti/V2 and Ti/V3, respectively, of the tensile strength obtained of the non-filler (autogenous) dissimilar welds, giving an indication of a successful welded joint as the fracture was out of the WZ. The effect of the welding thermal cycle was apparent on the V alloy, as the HAZ showed the lowest hardness values as compared with other regions in the welded samples. The micro-examination showed a grain growth due to the high heat input increased the ductility of the V-HAZ, and the growth was incremented as moving from the V-BM toward the centre of the WZ. In all the tension specimens of the DW samples, the ductile fracture was observed. During the test, a nominal drop of the stress happen as the necking start to form. A consideres constriction approach was employed to determine the maximum stress at the nocking point. By drawing a tangent line to the true stress-strain curves, and this line started from (-1) of the negative strain axis, the contact point will indicate the maximum σu applied that causes the alloy to be deformed at specific strain rate, where u is express the necking condition. Table (6-5) list the obtained ultimate stress of the tensile tests at the necking points of the welded samples.

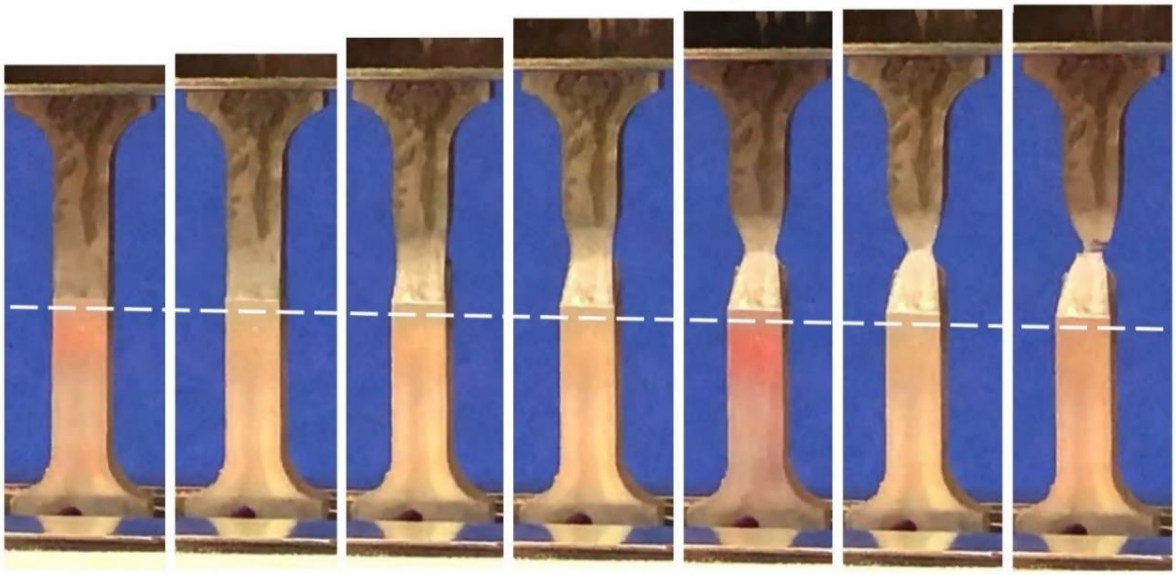

Figure 6.25 Images taken during testing in sample AW02 at 0.027, 0.053, 0.107, 0.160, 0.18 and 0.21 of engineering strain.

Table 6.7 The maximum stress at the point of necking obtained by applying consederais consetrcation approach.

Tension sample	σ_u (MPa)	Extension ratio, ε
Ti64 BM alloy	1138	1.16
AW02 -(no filler)	304	0.07
W1 -filler(Ti/V1)	270	0.08
W2 -filler(Ti/V2)	293	0.08
W3 -filler(Ti/V3)	273	0.095

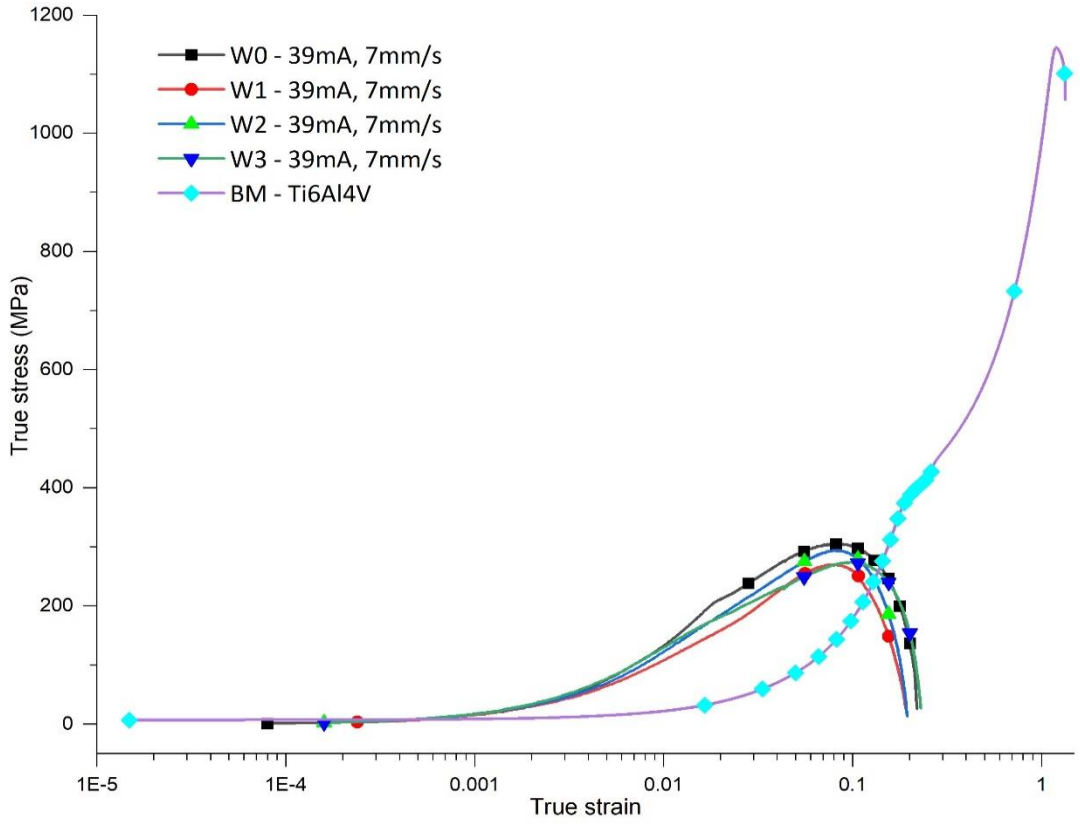

Figure 6.26 True stress-strain curves show the tension behaviour of the dissimilar welds with and without the filler metal.

6.9 Conclusions

1. It is possible to produce dissimilar welded joints between Ti-6Al-4V and commercially pure vanadium with graded microstructures using Electron Beam Melting (EBM) Arcam S12 system.
2. Design of experiments and linear approaches were essential to introduce promising welding parameters to be used to optimise the required welding variables to achieve an acceptable keyhole profile with full penetration for both Ti-6Al-4V and CP-V alloys.
3. Numerical modelling provides suggestions on how the obtained welding parameters from the DoE and the physical properties of the welded alloys can effect on the formation of the keyhole during the welding process and the geometry of the WZ, eventually.
4. Welding beam current and travel rate have a significant impact on the WZ geometry.
5. The welding process parameters of 37mA and 7mm/s beam travel offered the best welding parameters to achieve a full depth keyhole in term of high depth to narrow welding zone in case of non-filler (autogenous) dissimilar joints.
6. A full penetration was obtained when applying welding parameters of 39mA and 41mA at 7mm/s welding speed. However, an increase was recorded in the WZ width as a function of the beam current.
7. Although the full penetration obtained for the dissimilar welding between Ti and V using 37mA and 7mm/s, a Lack of penetration was identified upon using the designed filler metals in the joining process. Only ~75% depth was achieved for the DW samples W1 and W2, due to the increase in wt.% of V in the filler alloy which required further heat input to obtain a molten pool along with the total thickness of the plate.
8. Setting the welding beam current to 39mA at a constant welding speed of 7mm/s, has a great potential on increasing the depth of the keyhole, and a ~95% depth of the total thickness in the case of W1 and W2 welds with filler type Ti/V1 and Ti/V2, respectively was achieved.
9. Hardness testing reveals graded structures across both base metals, HAZ and WZ regions. On one end, the V rich-side seemed to retain base metal properties, contrary to titanium that developed a wider range of hardness suggesting a wide diversity in the microstructure.

10. Optical microscopy distinguished the Ti-HAZ structure with coarser microstructural features, i.e. α colony and α plate.
11. In vanadium, the variation in mechanical properties between the WZ and the far end of vanadium base metal seems to be low, suggesting a not significant effect on the microstructure [113].
12. EDS analysis showed how the vanadium has diluted across the FZ material due to elemental composition present in all materials to join, while titanium, could be observed to be well-delimited at the vanadium – WZ boundary.
13. Mechanical properties of microhardness showed low values in the WZ and the lowest hardness values in CP-V with higher values in the Ti-rich side. Increasing the wt.% of V in the WZ showed an increase in the hardness value compared to the non-filler welds.
14. Additionally, tensile tests from dissimilar welded plates showed values of yield strength close to 282 MPa, with elongation to failure close to 23% for the non-filler welds, while the using the designed filler provides a joints efficiency with strength reaches about 95% of the non-filler joint strength. Failure fracture was found to be off the weld line and on the side of vanadium, suggesting favourable dissimilar welding with fairly high elongation values for titanium with reduced strength to failure.

CHAPTER 7: Conclusion and recommendations

7.1 Conclusion of the work

The efforts of this work were focused on the ability to carry out dissimilar welding (DW) between titanium alloys Ti-6Al-4V and commercially pure vanadium alloy. The investigations carried out in this work are best summarised into three sections. Firstly, the microstructure and mechanical properties of Ti-V alloys produced by spark plasma sintering, discussed in Chapter 4, gave an insight into approaches used to design these alloys and the influence of the powder mixture percentage and the SPS parameters on the properties of the sintered alloys. As a result, those designed alloys were introduced as filler materials in the dissimilar-metal welding between Ti and V alloys described in Chapter 6. The effects of electron beam melting (EBM) parameters on the keyhole characteristics of titanium alloys weld tracks were discussed in Chapter 5 prior to determining the potential welding parameters to be employed in the dissimilar welding in Chapter 6. The conclusions from these chapters are summarised here.

7.1.1 Microstructure and mechanical properties of Ti-V alloys produced by spark plasma sintering

- A near fully dense alloy of Ti/V1 containing 80 wt. % of Ti-6Al-4V and 20 wt. % of CP-V was processed successfully by the SPS method using a 1200˚C sintering temperature, 100˚C/min heating rate and 5 min holding time.
- Increasing the wt. % addition of the high melting point alloy, i.e. vanadium, from 20 to 80 promotes the necessity to increase the holding time to 20 min to advance the diffusivity of the vanadium particles within the Ti matrix and to produce a fully dense sintered alloy.
- The microstructure examination of the sintered alloys reveals three regions: dark, grey and light-coloured, which represent Ti-rich, βTi-V and V-rich regions, respectively. Although no secondary phases were detected by XRD or EDS, a trace of C particles was observed that promoted the formation of IMCs in the sintered alloys such as $Ti_{0.8}V_{0.2}C_{0.62}$ and $Ti_{0.6}V_{0.4}C$, which caused increase in hardness, especially in alloy Ti/V2.

- The study showed that both relative density and hardness of the designed alloys were functions of diffusion time at a fixed sintering temperature of 1200˚C; however, the presence of pores was evident, which indicates the importance of increasing the holding time during the sintering process to produce fully dense alloys with minimal porosity.
- The hardness value showed an increment as the V wt. % increased to 20 and 40 as compared with hardness value 305±6 HV_1 of the sintered alloy Ti-6Al-4V. The designed alloys Ti/V1 and Ti/V2 recorded the maximum hardness values, of about ~367±10 HV_1 and ~347±13 HV_1, respectively when sintered for 20 min.
- The sintered alloy Ti-6Al-4V provided the maximum σu and elongation of ~888MPa and 0.27%, respectively, while similarly the designed alloys Ti/V1 and Ti/V3 showed a tensile strength value close to Ti-6Al-4V, recording high strength of ~845MPa and ~797MPa, but poor elongations of only 0.08% and 0.17%, respectively, due to the presence of porosity within the V regions. The presence of non-diffused particles in alloys Ti/V2 and Ti/V4 reduced the UTS to ~544 MPa and 437MPa with elongations of 0.6% and 0.05%, respectively.

7.1.2 The effect of electron beam melting (EBM) parameters on the keyhole characteristics of titanium alloys weld tracks

- The design of experiments (DoE) was an effective approach to identify promising welding parameters. Using an empirical equation developed by Thomas et al. [166], the welding variables were determined promptly. A solid substrate of Ti-6Al-4V was used to obtain weldtracks by adopting the Arcam S12 system as a welding machine and the suggested welding variables by the normalising approaches for this work.
- The macro-examination of the bead-on-plate and the keyhole measurements of the WZ show that both heat input and the beam travel rate have a direct impact on the weldtrack profiles. As a result, the width of the WZ is directly proportional to the amount of the heat input (beam current) and inversely with the travel rate of the welding speed.
- The keyhole measurements for the weldtracks, obtained using the suggested parameters by the normalised approach, showed a scattered behaviour; however, the

suggested variables of the linear approach showed more systematised behaviour in terms of the effect of the heat input and travel rate on the WZ geometry.

- From the calculations of the keyhole depths, a trend was observed showing that as the travel rate increased, the amount of the heat inputs decreased, which led to a reduction in the fusion zone and a keyhole with a narrower profile.
- The WZ microstructure of Ti-6Al-4V typically consists of a transformed colony/Widmanstätten α+β microstructure with α´ delineating prior β grain boundaries. Meanwhile, the HAZ showed a complex structure consisting of fine ά laths near the WZ and becoming thicker with increasing proximity to the Ti-BM.
- The discrete approach revealed a trend in terms of the effect of the beam heat input and beam travel rates on the microhardness values. The obtained hardness values were directly proportional with the rate of the welding speed and inversely proportional with the applied heat input. The WZ showed the maximum hardness values of~ 387±4 HV_1, while the equiaxed BM recorded the lowest hardness values of ~325±5HV. Meanwhile, due to the presence of fine and coarse α´ structure, the HAZ showed hardness values higher than in the BM but below the WZ values, between 335±4 HV_1 and 353±5 HV_1.
- The hardness measurements for the WZ and the HAZ showed a reduction in the hardness values when the amount of the heat inputs increased as the beam travelled at a low rate, i.e. 3mm/sec. As a result, a reduction in the cooling rate took place, allowing the fine α´ grains to grow and become thicker and less hard.

7.1.3 Dissimilar welding of Ti-6Al-4V alloy to commercially pure vanadium alloy by Electron Beam method

- A dissimilar welded joint between Ti-6Al-4V and commercially pure vanadium with graded microstructures was successfully carried out using the electron beam melting additive manufacturing (EBM) Arcam S12 system.
- Numerical modelling developed by Thomas et al. provides suggestions on how the obtained welding parameters from the DoE and the physical properties of the welded alloys can affect the formation of the keyhole and the geometry of the WZ, eventually. The DoE was essential to introduce promising welding parameters, and the linear approach was essential to limit down those parameters by accepting only

the variables that would achieve an acceptable keyhole profile with full penetration for the Ti-V dissimilar welds.

- The full penetration autogenous dissimilar welds, AW01, AW02 and AW03, were obtained when applying welding parameters of 37mA, 39mA and 41mA at a constant welding speed of 7mm/s. However, an increase was recorded in the WZ width as a function of the beam current. The welding parameters of 37mA and 7mm/s beam travel offered the best welding variables in terms of minimal defects and high depth to narrow welding zone.
- Upon using the designed filler metals, Ti/V1, Ti/V2 and Ti/V3, a lack of penetration was identified in the WZ, and only ~75% depth was achieved for the DW samples W1 and W2, comparing to the AW01 samples, due to the presence of high amounts of high melting point V particles in those filler alloys which caused delay in the fusion process when using the same welding parameters for the autogenous welding.
- The cross-section examination showed an increase in the width of the WZ and a reduction in the keyhole depth as the wt. % of V increased in the filler alloy. This indicates that the heat input obtained from the welding variables of 37mA welding current and 7mm/sec. travel rate was insufficient to maintain a melting condition in the dissimilar joint, due to the high melting point and high thermal conductivity of the V alloy, which caused a deterioration in the fusion process to take over, and only the top half part of the joint melted.
- An improvement was achieved in terms of the WZ geometry when the welding beam current was set to 39mA with maintaining the welding speed at 7mm/s. The obtained heat input from those welding variables showed great potential for increasing the depth of the keyhole, and a ~95% depth of the total thickness was achieved in the cases of W1 and W2 welds with filler types Ti/V1 and Ti/V2, respectively.
- A wide diversity was observed in the microstructure of Ti-V welding zone, containing large βTi grains with a fine needles-like ά structured within. The optical microscopy distinguished the Ti-HAZ structure with fine and coarser microstructural features, i.e. α colony and α′ plate. Meanwhile, the V-HAZ showed less diversity, with the only observed change in the size of the grains being from fine near the WZ to large as the scan moved toward the V-BM.
- The EDS analysis showed how the vanadium was diluted across the FZ material and mixed with the Ti alloy. The WZ area measurements showed that the dilution

percentage was a function of the heat input. However, as the V wt. % increases in the filler alloy the dilution increases as well in terms of the WZ becoming broader and less in-depth.

- The hardness measurements of the dissimilar welding zone confirmed that graded structures spanned from the base metals to the WZ, passing through the HAZ across the Ti-V welded joint. On one end, the V rich-side seemed to retain base metal properties, with the variation in mechanical properties between the WZ and the far end of the vanadium base metal seeming to be low, suggesting a not significant effect on the microstructure [113]. However, upon being subjected to the welding thermal cycle, the titanium alloy developed a wider range of hardness, suggesting a wide diversity in the microstructure.
- The microhardness measurements showed that the highest hardness value was in the Ti-HAZ and the lowest at the V-HAZ. Meanwhile, as the WZ structure showed a mixture of ductile phase βTi-V and fine ά grains, the hardness value was situated between the low values of the V-HAZ and the highest recorded at Ti-HAZ. Besides, the WZ showed an increment in hardness value compared to the non-filler welds as the wt. % of V increased in the filler metal from 20 to 40 as reported by Chu et al. [183], suggesting that the phases of βTi-V usually exhibits a microhardness value of 364±7 HV_1 when the vanadium content is in the range of 14-15 wt. %. However, as the ductile V wt. % became higher in the filler metal used in the dissimilar welding, i.e. between 60 and 80, the hardness values of the WZ declined.
- The autogenous dissimilar welds type AW02 showed a higher value of tensile strength close to 282MPa, with elongation to failure close to 23%. Also, the dissimilar welded samples W1, W2 and W3, using the designed alloy as filler metal, showed a high joint efficiency with strengths of 88.6%, 95% and 88%, respectively, which are close to the strength obtained from the AW02 sample. Failure fracture was found to be off the weld line and on the side of the vanadium, suggesting favourable dissimilar welding with fairly high elongation values for titanium with reduced strength to failure.

7.2 Future work suggestions

Further investigations that could be carried out regarding this work include the following:

- Study the effect of milling time on the properties of the designed alloys when using high energy ball milling.
- Although the dissimilar welding was carried out successfully by Arcam S12 system, further aspects could be explored when performing the welding method, including the effect on the properties of the welded samples of shifting the beam position about 0.2mm or 0.4mm or 0.6mm from the centre of the welding line to the Ti- side or shifting the beam toward the V-side.
- Study the effect of preheating and post-weld heat treatments on the characterisation of the dissimilar joints.
- Explore the impact of welding method on the properties of the dissimilar welded joint when using such as LBW method to carry out the welding.
- Study the ability to weld dissimilar metals by using the SPS furnace as a joining method. It could be useful to study the diffusion process between Ti-6Al-4V and CP-V alloys. Also, selected powder mixtures could be applied between these two alloys, in the powder condition, to work as an interlayer in the WZ.
- Further investigation of the SPS method could be carried out to study the effect of SPS variables on the diffusion process between Ti-6Al-4V and CP-V alloys.

PUBLICATIONS AND CONFERENCE PRESENTATION

1. A. Moosa, B. Wynne, I. Todd Investigate the characterisation of Ti-6Al-4V/V composites consolidate by Spark Plasma Sintering. MAPP 1st International Conference - 30th-31st January 2018, Sheffield, UK.

2. A. Moosa, B. Wynne I. Todd, Joining Lightweight Dissimilar Alloys by Using Electron Beam Welding. The TMS 2018 annual meeting on March 11-15, 2018, Phoenix, Arizona, USA. (Winner of the young professional poster competition of the Materials Processing and Manufacturing Division (MPMD) TMS2018).

3. A. Moosa, E. Hernandez-Nava, N. Boone, J. R. Willmott, B. Wynne, I. Todd. Dissimilar welding of Ti-6Al-4V - vanadium by Electron Beam Melting-Additive Manufacturing system. (In-Preparation)

CHAPTER 8: REFERENCES.

[1] Z. Sun and R. Karppi, "The application of electron beam welding for the joining of dissimilar metals: An overview," *J. Mater. Process. Technol.*, vol. 59, pp. 257–267, 1996.

[2] N. Inagaki, I., Shirai, Y., Takechi, T., Ariyasu, "Application and Features of Titanium for the Aerospace Industry," *Nippon Steel Sumitomo Met. Tech. Rep.*, no. 106, pp. 22–27, 2014.

[3] J. Matthew J. Donachie, *Titanium - A Techinacal Guide*, Second. Ohio, 2000.

[4] T. S. Balasubramanian, M. Balakrishnan, V. Balasubramanian, and M. Muthu Manickam, "Effect of welding processes on joint characteristics of Ti–6Al–4V alloy," *Sci. Technol. Weld. Join.*, vol. 16, no. 8, pp. 702–708, Nov. 2011.

[5] Y. Li, S. Hu, J. Shen, and B. Hu, "Dissimilar welding of H62 brass-316L stainless steel using continuous-wave Nd:YAG laser," *Mater. Manuf. Process.*, vol. 29, no. 8, pp. 916–921, 2014.

[6] R. Pederson, F. Niklasson, F. Skystedt, and R. Warren, "Microstructure and mechanical properties of friction- and electron-beam welded Ti-6Al-4V and Ti-6Al-2Sn-4Zr-6Mo," *Mater. Sci. Eng. A*, vol. 552, pp. 555–565, 2012.

[7] A. B. Short, " Gas tungsten arc welding of α + β titanium alloys: a review ," *Mater. Sci. Technol.*, vol. 25, no. 3, pp. 309–324, 2009.

[8] X. Cao and M. Jahazi, "Effect of welding speed on butt joint quality of Ti-6Al-4V alloy welded using a high-power Nd:YAG laser," *Opt. Lasers Eng.*, vol. 47, no. 11, pp. 1231–1241, 2009.

[9] A. Squillace, U. Prisco, S. Ciliberto, and A. Astarita, "Effect of welding parameters on morphology and mechanical properties of Ti-6Al-4V laser beam welded butt joints," *J. Mater. Process. Technol.*, vol. 212, no. 2, pp. 427–436, 2012.

[10] P. Q. Xu, L. Li, and C. Zhang, "Microstructure characterization of laser welded Ti-6Al-4V fusion zones," *Mater. Charact.*, vol. 87, pp. 179–185, 2014.

[11] S. Wang and X. Wu, "Investigation on the microstructure and mechanical properties of Ti-6Al-4V alloy joints with electron beam welding," *Mater. Des.*, vol. 36, pp. 663–670, 2012.

[12] lng H. Schultz, *Electron beam welding*. Cambridge, England, 1993.

[13] C. J. Tsai and L. M. Wang, "Improved mechanical properties of Ti-6Al-4V alloy by

electron beam welding process plus annealing treatments and its microstructural evolution," *Mater. Des.*, vol. 60, pp. 587–598, 2014.

[14] H. M. Chung, J. H. Park, R. V. Strain, K. H. Leong, and D. L. Smith, "Mechanical properties and microstructural characteristics of laser and electron-beam welds in V-4Cr-4Ti," *J. Nucl. Mater.*, vol. 258–263, no. PART 2 B, pp. 1451–1457, 1998.

[15] S. Nogami, J. Miyazaki, A. Hasegawa, T. Nagasaka, and T. Muroga, "Study on electron beam weld joints between pure vanadium and SUS316L stainless steel," *J. Nucl. Mater.*, vol. 442, no. 1-3 SUPPL.1, pp. S562–S566, 2013.

[16] S. Nogami, J. Miyazaki, T. Nagasaka, A. Hasegawa, and T. Muroga, "Study on Dissimilar-Material Welding with Vanadium and Austenitic Stainless Steel," *Fusion Sci. Technol.*, vol. 60, no. 1, pp. 417–421, 2017.

[17] M. Peters and C. Leyens, *Titanium and Titanium Alloys: Fundamentals and Applications*, vol. 1. WILEY-VCH Verlag GmbH & Co. KGaA, 2003.

[18] H. M. Flower, "Light alloys: metallurgy of the light metals," *Int. Mater. Rev.*, vol. 37, no. 1, pp. 196–196, 2012.

[19] R. R. Boyer and R. D. Briggs, "The use of β titanium alloys in the aerospace industry," in *Journal of Materials Engineering and Performance*, 2013, vol. 22, no. 10, pp. 2916–2920.

[20] J. Matthew J. Donachie, *Titanium A Technical guide*, 2nd Editio., vol. 99, no. 5. ASM International, 2003.

[21] W. Sha and S. Malinov, "Modelling of microstructure, properties and applications," in *Titanium Alloys*, Woodhead Publishing Ltd., 2009, pp. 203–236.

[22] I. Weiss and S. . Semiatin, "Thermomechanical processing of alpha titanium alloys—an overview," *Mater. Sci. Eng. A*, vol. 263, no. 2, pp. 243–256, 2002.

[23] R. R. Boyer, "An overview on the use of titanium in the aerospace industry," *Mater. Sci. Eng. A*, vol. 213, no. 1–2, pp. 103–114, 1996.

[24] T. Ahmed and H. J. Rack, "Phase transformations during cooling in α+β titanium alloys," *Mater. Sci. Eng. A*, vol. 243, no. 1–2, pp. 206–211, 2002.

[25] R. Ding and Z. X. Guo, "Microstructural evolution of a Ti-6Al-4V alloy during β-phase processing: Experimental and simulative investigations," *Mater. Sci. Eng. A*, vol. 365, no. 1–2, pp. 172–179, 2004.

[26] H. J. Green, J. R. Sutton, E. E. Wolfel, J. T. Reeves, G. E. Butterfield, and G. A. Brooks, "Altitude acclimatization and energy metabolic adaptations in skeletal muscle during exercise.," *J. Appl. Physiol.*, vol. 73, no. 6, pp. 2701–8, Dec. 1992.

[27] A. L. Pilchak and T. F. Broderick, “Evidence of a massive transformation in a Ti-6Al-4V solid-state weld?,” *Jom*, vol. 65, no. 5, pp. 636–642, 2013.

[28] J. L. Barreda, F. Santamaría, X. Azpiroz, A. M. Irisarri, and J. M. Varona, “Electron beam welded high thickness Ti6Al4V plates using filler metal of similar and different composition to the base plate,” *Vacuum*, vol. 62, no. 2–3, pp. 143–150, 2001.

[29] M. Gao, Z. M. Wang, X. Y. Li, and X. Y. Zeng, “Laser keyhole welding of dissimilar Ti-6Al-4V titanium alloy to AZ31B magnesium alloy,” *Metall. Mater. Trans. A Phys. Metall. Mater. Sci.*, vol. 43, no. 1, pp. 163–172, 2012.

[30] N. Saresh, M. G. Pillai, and J. Mathew, “Investigations into the effects of electron beam welding on thick Ti-6Al-4V titanium alloy,” *J. Mater. Process. Technol.*, vol. 192–193, pp. 83–88, 2007.

[31] S. D. Meshram and T. Mohandas, “A comparative evaluation of friction and electron beam welds of near-α titanium alloy,” *Mater. Des.*, vol. 31, no. 4, pp. 2245–2252, 2010.

[32] C. Zheng *et al.*, “Effect of microstructures on ballistic impact property of Ti-6Al-4V targets,” *Mater. Sci. Eng. A*, vol. 608, pp. 53–62, 2014.

[33] G. Welsch, R. Boyer, and E. W. Collings, *Materials properties handbook: Titanium alloys, 2nd ed*. 1998.

[34] M. Alali, “Through-thickness microstructure and mechanical properties of electron beam similar welded AISI 316L stainless steel and dissimilar welded AISI 316L/ Ti6Al4V,” University of Sheffield, Ph.D thesis, 2017.

[35] E. Hernández-Nava, “A study on the mechanical properties of micro-truss Ti-6Al-4V materials fabricated by Electron Beam Melting", Ph.D thesis, 2016.

[36] J. Huang, “The Characterisation and Modelling of Porosity Formation in Electron Beam Welded Titanium Alloys,” Ph.D thesis, The University of Birmingham, 2011.

[37] B. Ralph, *Titanium alloys: An atlas of structures and fracture features*, vol. 59, no. 3. CRC Press, 2008.

[38] W. B. L. and R. F. K.C. Winco Yung, Ralph, “An investigation into welding parameters affecting the tensile properties oftitanium welds,” *J. ofMaterials Process. Technol.*, vol. 63, no. 96, pp. 759–764, 1997.

[39] J. M. Oh, B. G. Lee, S. W. Cho, S. W. Lee, G. S. Choi, and J. W. Lim, “Oxygen effects on the mechanical properties and lattice strain of Ti and Ti-6Al-4V,” *Met. Mater. Int.*, vol. 17, no. 5, pp. 733–736, 2011.

[40] M. Lamirand, J. L. Bonnentien, G. Ferrière, S. Guérin, and J. P. Chevalier, “Effects

of interstitial oxygen on microstructure and mechanical properties of Ti-48AI-2Cr-2Nb with fully lamellar and duplex microstructures," *Metall. Mater. Trans. A Phys. Metall. Mater. Sci.*, vol. 37, no. 8, pp. 2369–2378, 2006.

[41] L. Griffing, "Metals and Their Weldability," in *Welding Handbook*, vol. 4, L. Griffing, Ed. American Welding Society, 1972.

[42] F. Caiazzo, V. Alfieri, G. Corrado, F. Cardaropoli, and V. Sergi, "Investigation and Optimization of Laser Welding of Ti-6Al-4V Titanium Alloy Plates," *J. Manuf. Sci. Eng.*, vol. 135, 2013.

[43] E. Akman, A. Demir, T. Canel, and T. Sinmazçelik, "Laser welding of Ti6Al4V titanium alloys," *J. Mater. Process. Technol.*, vol. 209, no. 8, pp. 3705–3713, 2009.

[44] T. Otani, "Titanium Welding Technology," *Nippon STEEL Tech. Rep. No.*, no. 95, pp. 88–92, 2007.

[45] W. Bochnowski, "Microstructure and Microhardness of Ti6Al4V Alloy Treated by GTAW SiC Alloying," *Arch. Foundry Eng.*, vol. 12, no. 2, pp. 261–266, 2012.

[46] J. C. Chen and C. X. Pan, "Welding of Ti-6Al-4V alloy using dynamically controlled plasma arc welding process," *Trans. Nonferrous Met. Soc. China (English Ed.*, vol. 21, no. 7, pp. 1506–1512, 2011.

[47] M. Yang, H. Zheng, B. Qi, and Z. Yang, "Effect of arc behavior on Ti-6Al-4V welds during high frequency pulsed arc welding," *J. Mater. Process. Technol.*, vol. 243, pp. 9–15, 2017.

[48] T. Mohandas, D. Banerjee, and V. Kutumbarao, "Elevated temperature properties of electron beam welds of an α+β titanium alloy," *Mater. Sci. Eng. A*, vol. 269, no. 1–2, pp. 217–224, 2002.

[49] A. M. Irisarri, J. L. Barreda, and X. Azpiroz, "Influence of the filler metal on the properties of Ti-6Al-4V electron beam weldments. Part I: Welding procedures and microstructural characterization," *Vacuum*, vol. 84, no. 3, pp. 393–399, 2009.

[50] X. Yang, S. Li, and H. Qi, "Ti-6Al-4V welded joints via electron beam welding: Microstructure, fatigue properties, and fracture behavior," *Mater. Sci. Eng. A*, vol. 597, pp. 225–231, 2014.

[51] A. Gursel, "Crack risk in Nd: YAG laser welding of Ti-6Al-4V alloy," *Mater. Lett.*, vol. 197, pp. 233–235, 2017.

[52] Q. Yunlian, D. Ju, H. Quan, and Z. Liying, "Electron beam welding, laser beam welding and gas tungsten arc welding of titanium sheet," *Mater. Sci. Eng. A*, vol. 280, no. 1, pp. 177–181, 2000.

[53] P. Q. Xu, “Microstructure characterization of Ti-6Al-4V titanium laser weld and its deformation,” *Trans. Nonferrous Met. Soc. China (English Ed.*, vol. 22, no. 9, pp. 2118–2123, 2012.

[54] X. Y. Wang, W. Y. Li, T. J. Ma, and A. Vairis, “Characterisation studies of linear friction welded titanium joints,” *Mater. Des.*, vol. 116, pp. 115–126, 2017.

[55] D. G. Sanders, P. Edwards, A. M. Cantrell, K. Gangwar, and M. Ramulu, “Friction stir-welded titanium alloy Ti-6Al-4V: Microstructure, mechanical and fracture properties,” *Jom*, vol. 67, no. 5, pp. 1054–1063, 2015.

[56] F. Karimzadeh, M. Salehi, A. Saatchi, and M. Meratian, “Effect of microplasma arc welding process parameters on grain growth and porosity distribution of thin sheet Ti6Al4V alloy weldment,” *Mater. Manuf. Process.*, vol. 20, no. 2, pp. 205–219, 2005.

[57] M. Akbari, S. Saedodin, D. Toghraie, R. Shoja-Razavi, and F. Kowsari, “Experimental and numerical investigation of temperature distribution and melt pool geometry during pulsed laser welding of Ti6Al4V alloy,” *Opt. Laser Technol.*, vol. 59, pp. 52–59, 2014.

[58] T. Mohandas, D. Banerjee, and V. . Kutumba Rao, “Observations on impact toughness of electron beam welds of an α+β titanium alloy,” *Mater. Sci. Eng. A*, vol. 254, no. 1–2, pp. 147–154, 2002.

[59] S. H. Wang, M. D. Wei, and L. W. Tsay, “Tensile properties of LBW welds in Ti-6Al-4V alloy at evaluated temperatures below 450 °C,” *Mater. Lett.*, vol. 57, no. 12, pp. 1815–1823, 2003.

[60] K. P. Rao, K. Angamuthu, and P. B. Srinivasan, “Fracture toughness of electron beam welded Ti6Al4V,” *J. Mater. Process. Technol.*, vol. 199, no. 1, pp. 185–192, 2008.

[61] Wayne M. Thomas, E. D. Nicholas, J. C. Needham, M. G. Murch, P. Temple-Smith, and C. J. Dawes, *Friction welding*. Cambridge, 1995.

[62] X. Jiang, B. P. Wynne, and J. Martin, “Variant selection in stationary shoulder friction stir welded Ti-6Al-4V alloy,” *J. Mater. Sci. Technol.*, vol. 34, no. 1, pp. 198–208, 2018.

[63] D. G. Sanders, M. Rarnulu, and P. O. Edwards, “Superplastic forming of friction stir welds in titanium alloy 6AI-4V: Preliminary results,” *Materwiss. Werksttech.*, vol. 39, no. 4–5, pp. 353–357, 2008.

[64] G. Buffa, A. Ducato, and L. Fratini, “FEM based prediction of phase transformations during Friction Stir Welding of Ti6Al4V titanium alloy,” *Mater. Sci. Eng. A*, vol. 581, pp. 56–65, 2013.

[65] K. Gangwar and M. Ramulu, “Friction stir welding of titanium alloys: A review,” *Mater. Des.*, vol. 141, pp. 230–255, 2018.

[66] S. Mironov, Y. S. Sato, and H. Kokawa, “Friction-stir welding and processing of Ti-6Al-4V titanium alloy: A review,” *J. Mater. Sci. Technol.*, vol. 34, no. 1, pp. 58–72, 2018.

[67] Z. L. Lei, R. C. Zhu, L. Huang, Z. J. Dong, and Y. B. Chen, “Microstructure and mechanical properties of laser welded Ti–22Al–27Nb/TC4 dissimilar alloys,” *Mater. Sci. Eng. A*, vol. 559, pp. 909–916, 2012.

[68] A. S. H. Kabir, X. Cao, M. Medraj, P. Wanjara, J. Cuddy, and A. Birur, “Effect of Welding Speed and Defocusing Distance on the Quality of Laser Welded Ti-6Al-4V,” *Proc. Mater. Sci. Technol. 2010 Conf.*, pp. 2787–2797, 2010.

[69] X. L. Gao, L. J. Zhang, J. Liu, and J. X. Zhang, “A comparative study of pulsed Nd: YAG laser welding and TIG welding of thin Ti6Al4V titanium alloy plate,” *Mater. Sci. Eng. A*, vol. 559, pp. 14–21, 2013.

[70] H. Yu, F. Li, J. Yang, J. Shao, Z. Wang, and X. Zeng, “Investigation on laser welding of selective laser melted Ti-6Al-4V parts: Weldability, microstructure and mechanical properties,” *Mater. Sci. Eng. A*, vol. 712, no. October 2017, pp. 20–27, 2018.

[71] X. L. Gao, L. J. Zhang, J. Liu, and J. X. Zhang, “Porosity and microstructure in pulsed Nd:YAG laser welded Ti6Al4V sheet,” *J. Mater. Process. Technol.*, vol. 214, no. 7, pp. 1316–1325, 2014.

[72] J. Xu, Y. Rong, Y. Huang, P. Wang, and C. Wang, “Keyhole-induced porosity formation during laser welding,” *J. Mater. Process. Technol.*, vol. 252, no. July 2017, pp. 720–727, 2018.

[73] R. Blondeau, *Metallurgy and Mechanics of Welding: Processes and Industrial Applications*. New Jersey, USA: ISTE, 2008.

[74] P. F. Mendez and T. W. Eagar, “New Trends in Welding in the Aeronautic Industry,” in *New Trends for the Manufacturing in the Aeronautic Industry*, 2002.

[75] S. Kou, *Welding Metallurgy, Second Edition*, Second edi. Hoboken, New Jersey.: John Wiley & Sons, Inc., 2002.

[76] P. Fu, Z. Mao, C. Zuo, Y. Wang, and C. Wang, “Microstructures and fatigue properties of electron beam welds with beam oscillation for heavy section TC4-DT alloy,” *Chinese J. Aeronaut.*, vol. 27, no. 4, pp. 1015–1021, 2014.

[77] X. Li, S. Hu, J. Xiao, and L. Ji, “Effects of the heterogeneity in the electron beam welded joint on fatigue crack growth in Ti-6Al-4V alloy,” *Mater. Sci. Eng. A*, vol.

529, no. 1, pp. 170–176, 2011.

[78] Z. Bing *et al.*, “Pilula Anticoncepcional,” *Trans. Nonferrous Met. Soc. China*, vol. 6326, no. 51075089, pp. 1–5, 2011.

[79] G. A. O. Yefei, T. Takuya, and N. Kazuhiro, “Dissimilar Welding of Titanium Alloys to Steels,” *Join. Weld. Res. Inst.*, vol. 41, no. 2, 2012.

[80] M. Ghosh and S. Chatterjee, “Effect of interface microstructure on the bond strength of the diffusion welded joints between titanium and stainless steel,” *Mater. Charact.*, vol. 54, no. 4–5, pp. 327–337, 2005.

[81] M. Ghosh, S. Das, P. S. Banarjee, and S. Chatterjee, “Variation in the reaction zone and its effects on the strength of diffusion bonded titanium-stainless steel couple,” *Mater. Sci. Eng. A*, vol. 390, no. 1–2, pp. 217–226, 2005.

[82] S. Kundu, S. Sam, and S. Chatterjee, “Evaluation of interface microstructure and mechanical properties of the diffusion bonded joints of Ti-6Al-4V alloy to micro-duplex stainless steel,” *Mater. Sci. Eng. A*, vol. 528, no. 15, pp. 4910–4916, 2011.

[83] B. Alemán, L. Gutiérrez, and J. J. Urcola, “Interface microstructures in diffusion bonding of titanium alloys to stainless and low alloy steels,” *Mater. Sci. Technol.*, vol. 9, no. 8, pp. 633–641, Aug. 1993.

[84] R. Soltani Tashi, S. A. A. Akbari Mousavi, and M. Mazar Atabaki, “Diffusion brazing of Ti-6Al-4V and austenitic stainless steel using silver-based interlayer,” *Mater. Des.*, vol. 54, pp. 161–167, 2014.

[85] S. Zakipour, A. Amadeh, M. Samavatian, A. Khodabandeh, and A. Halvaee, “The effect of interlayer thickness on liquid state diffusion bonding behavior of dissimilar stainless steel 316/Ti-6Al-4V system,” *Mater. Lett.*, vol. 142, pp. 168–171, 2014.

[86] P. Li, J. Li, J. Xiong, F. Zhang, and S. H. Raza, “Diffusion bonding titanium to stainless steel using Nb/Cu/Ni multi-interlayer,” *Mater. Charact.*, vol. 68, pp. 82–87, 2012.

[87] H. C. Dey, M. Ashfaq, A. K. Bhaduri, and K. P. Rao, “Joining of titanium to 304L stainless steel by friction welding,” *J. Mater. Process. Technol.*, vol. 209, no. 18–19, pp. 5862–5870, 2009.

[88] P. Li, J. Li, M. Salman, L. Liang, J. Xiong, and F. Zhang, “Effect of friction time on mechanical and metallurgical properties of continuous drive friction welded Ti6Al4V/SUS321 joints,” *Mater. Des.*, vol. 56, pp. 649–656, 2014.

[89] X. Li, J. Li, Z. Liao, F. Jin, F. Zhang, and J. Xiong, “Microstructure evolution and mechanical properties of rotary friction welded TC4/SUS321 joints at various rotation

speeds," *Mater. Des.*, vol. 99, pp. 26–36, 2016.

[90] I. Tomashchuk and P. Sallamand, "Metallurgical Strategies for the Joining of Titanium Alloys with Steels," *Adv. Eng. Mater.*, vol. 20, no. 6, pp. 1–17, 2018.

[91] S. Celik and R. Cakir, "Effect of Friction Stir Welding Parameters on the Mechanical and Microstructure Properties of the Al-Cu Butt Joint," *Metals (Basel).*, vol. 6, no. 6, p. 133, 2016.

[92] M. W. B. Santos, A. Farias, M. S. Filho, and G. F. Batalha, "Microstructural Development of a Friction Stir Welded Ti-6Al-4V Sheet," *Manuf. Sci. Technol.*, vol. 3, no. 5, pp. 210–217, 2015.

[93] P. M. Mashinini, I. Dinaharan, J. David Raja Selvam, and D. G. Hattingh, "Microstructure evolution and mechanical characterization of friction stir welded titanium alloy Ti–6Al–4V using lanthanated tungsten tool," *Mater. Charact.*, vol. 139, no. March, pp. 328–336, 2018.

[94] A. Fuji, K. Ameyama, and T. H. North, "Influence of silicon in aluminium on the mechanical properties of titanium/aluminium friction joints," *J. Mater. Sci.*, vol. 30, no. 20, pp. 5185–5191, 1995.

[95] S. Ji, Y. Jin, Y. Yue, L. Zhang, and Z. Lv, "The effect of tool geometry on material flow behavior of friction stir welding of titanium alloy," *Eng. Rev.*, vol. 33, no. 2, pp. 107–13, 2013.

[96] A. R. Nasresfahani, A. R. Soltanipur, K. Farmanesh, and A. Ghasemi, "Effects of tool wear on friction stir welded joints of Ti–6Al–4V alloy," *Mater. Sci. Technol. (United Kingdom)*, vol. 33, no. 5, pp. 583–591, 2017.

[97] Y. J. Ko, K. J. Lee, and K. H. Baik, "Effect of tool rotational speed on mechanical properties and microstructure of friction stir welding joints within Ti-6Al-4V alloy sheets," *Adv. Mech. Eng.*, vol. 9, no. 8, pp. 1–7, 2017.

[98] M. Cheepu, M. Ashfaq, and V. Muthupandi, "A New Approach for Using Interlayer and Analysis of the Friction Welding of Titanium to Stainless Steel," *Trans. Indian Inst. Met.*, vol. 70, no. 10, pp. 2591–2600, 2017.

[99] R. Kumar and M. Balasubramanian, "Comparative Study of Ti Alloy and Stainless Steel 304L Friction Welded Joint with Different Interlayer Process Methods," *Appl. Mech. Mater.*, vol. 766–767, pp. 739–744, 2015.

[100] K. N. Campo, L. C. Campanelli, L. Bergmann, J. F. dos Santos, and C. Bolfarini, "Microstructure and interface characterization of dissimilar friction stir welded lap joints between Ti-6Al-4V and AISI 304," *Mater. Des.*, vol. 56, pp. 139–145, 2014.

[101] K. Gangwar, M. Ramulu, A. Cantrell, and D. Sanders, “Microstructure and Mechanical Properties of Friction Stir Welded Dissimilar Titanium Alloys: TIMET-54M and ATI-425,” *Metals (Basel).*, vol. 6, no. 10, p. 252, 2016.

[102] M. Fazel-Najafabadi, S. F. Kashani-Bozorg, and A. Zarei-Hanzaki, “Joining of CP-Ti to 304 stainless steel using friction stir welding technique,” *Mater. Des.*, vol. 31, no. 10, pp. 4800–4807, 2010.

[103] A. Wu, Z. Song, K. Nakata, J. Liao, and L. Zhou, “Interface and properties of the friction stir welded joints of titanium alloy Ti6Al4V with aluminum alloy 6061,” *Mater. Des.*, vol. 71, pp. 85–92, 2015.

[104] Y. Chen, “Study on the Joining of Titanium and Aluminum Dissimilar Alloys by Friction Stir Welding,” *Open Mater. Sci. J.*, vol. 5, no. 1, pp. 256–261, 2012.

[105] S. Chen, L. Li, Y. Chen, J. Dai, and J. Huang, “Improving interfacial reaction nonhomogeneity during laser welding-brazing aluminum to titanium,” *Mater. Des.*, vol. 32, no. 8–9, pp. 4408–4416, 2011.

[106] B. Majumdar, R. Galun, A. Weisheit, and B. L. Mordike, “Formation of a crack-free joint between Ti alloy and Al alloy by using a high-power CO2 laser,” *J. Mater. Sci.*, vol. 32, no. 23, pp. 6191–6200, 1997.

[107] S. J. Lee, H. Nakamura, Y. Kawahito, and S. Katayama, “Weldability of Ti and Al dissimilar metals using single-mode fiber laser,” *J. Laser Micro Nanoeng.*, vol. 8, no. 2, pp. 149–154, 2013.

[108] G. Casalino, M. Mortello, and P. Peyre, “Yb-YAG laser offset welding of AA5754 and T40 butt joint,” *J. Mater. Process. Technol.*, vol. 223, pp. 139–149, 2015.

[109] H. Li, D. Sun, X. Gu, P. Dong, and Z. Lv, “Effects of the thickness of Cu filler metal on the microstructure and properties of laser-welded TiNi alloy and stainless steel joint,” *Mater. Des.*, vol. 50, pp. 342–350, 2013.

[110] I. Tomashchuk, P. Sallamand, H. Andrzejewski, and D. Grevey, “The formation of intermetallics in dissimilar Ti6Al4V/copper/AISI 316 L electron beam and Nd:YAG laser joints,” *Intermetallics*, vol. 19, no. 10, pp. 1466–1473, 2011.

[111] I. Mitelea, C. Groza, and C. Craciunescu, “Copper interlayer contribution on Nd:YAG laser welding of dissimilar Ti-6Al-4V alloy with X5CrNi18-10 steel,” *J. Mater. Eng. Perform.*, vol. 22, no. 8, pp. 2219–2223, 2013.

[112] M. Gao, C. Chen, L. Wang, Z. Wang, and X. Zeng, “Laser-Arc Hybrid Welding of Dissimilar Titanium Alloy and Stainless Steel Using Copper Wire,” *Metall. Mater. Trans. A Phys. Metall. Mater. Sci.*, vol. 46, no. 5, pp. 2007–2020, 2015.

[113] I. Tomashchuk, D. Grevey, and P. Sallamand, “Dissimilar laser welding of AISI 316L stainless steel to Ti6-Al4-6V alloy via pure vanadium interlayer,” *Mater. Sci. Eng. A*, vol. 622, no. November, pp. 37–45, 2015.

[114] H. Li, D. Sun, X. Cai, P. Dong, and X. Gu, “Laser welding of TiNi shape memory alloy and stainless steel using Co filler metal,” *Opt. Laser Technol.*, vol. 45, no. 1, pp. 453–460, 2013.

[115] S. T. Auwal, S. Ramesh, F. Yusof, and S. M. Manladan, “A review on laser beam welding of titanium alloys,” *Int. J. Adv. Manuf. Technol.*, vol. 97, no. 1–4, pp. 1071–1098, 2018.

[116] S. Chen, L. Li, Y. Chen, and J. Huang, “Joining mechanism of Ti/Al dissimilar alloys during laser welding-brazing process,” *J. Alloys Compd.*, vol. 509, no. 3, pp. 891–898, 2011.

[117] P. Peyre, L. Berthe, M. Dal, S. Pouzet, P. Sallamand, and I. Tomashchuk, “Generation and characterization of T40/A5754 interfaces with lasers,” *J. Mater. Process. Technol.*, vol. 214, no. 9, pp. 1946–1953, 2014.

[118] John Norrish, *Advanced welding processes: Technologies and process control*. Cambridge, England, UK: Woodhead Publishing Limited, 2006.

[119] S. Q. Wang, W. Y. Li, K. Jing, X. Y. Zhang, and D. L. Chen, “Microstructural evolution and mechanical properties of electron beam welded dissimilar titanium alloy joints,” *Mater. Sci. Eng. A*, vol. 697, no. May, pp. 224–232, 2017.

[120] V. Esfahani Yeganeh and P. Li, “Effect of beam offset on microstructure and mechanical properties of dissimilar electron beam welded high temperature titanium alloys,” *Mater. Des.*, vol. 124, pp. 78–86, 2017.

[121] H. Zhang, P. He, J. Feng, and H. Wu, “Interfacial microstructure and strength of the dissimilar joint Ti3Al/TC4 welded by the electron beam process,” *Mater. Sci. Eng. A*, vol. 425, no. 1–2, pp. 255–259, 2006.

[122] H. T. Zhang, H. Y. Zhao, and W. X. He, “Microstructure and fracture behaviour of Ti3Al/TC4 dissimilar materials joints welded by electron beam,” *Bull. Mater. Sci.*, vol. 33, no. 6, pp. 707–711, 2010.

[123] S. Q. Wang, J. H. Liu, and D. L. Chen, “Tensile and fatigue properties of electron beam welded dissimilar joints between Ti-6Al-4V and BT9 titanium alloys,” *Mater. Sci. Eng. A*, vol. 584, pp. 47–56, 2013.

[124] S. Q. Wang, W. Y. Li, Y. Zhou, X. Li, and D. L. Chen, “Tensile and fatigue behavior of electron beam welded dissimilar joints of Ti-6Al-4V and IMI834 titanium alloys,”

Mater. Sci. Eng. A, vol. 649, pp. 146–152, 2016.

[125] S. Q. Wang, J. H. Liu, and D. L. Chen, "Effect of strain rate and temperature on strain hardening behavior of a dissimilar joint between Ti-6Al-4V and Ti17 alloys," *Mater. Des.*, vol. 56, pp. 174–184, 2014.

[126] T. Wang, B. G. Zhang, G. Q. Chen, J. C. Feng, and Q. Tang, "Electron beam welding of Ti-15-3 titanium alloy to 304 stainless steel with copper interlayer sheet," *Trans. Nonferrous Met. Soc. China (English Ed.*, vol. 20, no. 10, pp. 1829–1834, 2010.

[127] Z. Zeng *et al.*, "Laser joining of NiTi to Ti6Al4V using a Niobium interlayer," *Acta Mater.*, vol. 105, pp. 9–15, 2015.

[128] A. Kar, S. K. Choudhury, S. Suwas, and S. V. Kailas, "Effect of niobium interlayer in dissimilar friction stir welding of aluminum to titanium," *Mater. Charact.*, vol. 145, no. August, pp. 402–412, 2018.

[129] H. M. Zhang, Y. J. Chao, and Z. Luo, "Effect of interlayer on microstructure and mechanical properties of Al–Ti ultrasonic welds," *Sci. Technol. Weld. Join.*, vol. 22, no. 1, pp. 79–86, 2017.

[130] C. H. Muralimohan, M. Ashfaq, R. Ashiri, V. Muthupandi, and K. Sivaprasad, "Analysis and Characterization of the Role of Ni Interlayer in the Friction Welding of Titanium and 304 Austenitic Stainless Steel," *Metall. Mater. Trans. A Phys. Metall. Mater. Sci.*, vol. 47, no. 1, pp. 347–359, 2016.

[131] M. Ghosh, S. Kundu, S. Chatterjee, and B. Mishra, "Influence of interface microstructure on the strength of the transition joint between Ti-6Al-4V and stainless steel," *Metall. Mater. Trans. A Phys. Metall. Mater. Sci.*, vol. 36, no. 7, pp. 1891–1899, 2005.

[132] H. Y. Chan and R. K. Shiue, "Study of brazing Ti-6Al-4V and TZM alloy using pure silver," *J. Mater. Sci. Lett.*, vol. 22, no. 23, pp. 1659–1663, 2003.

[133] T. Wang, B. Zhang, H. Wang, and J. Feng, "Microstructures and mechanical properties of electron beam-welded titanium-steel joints with vanadium, nickel, copper and silver filler metals," *J. Mater. Eng. Perform.*, vol. 23, no. 4, pp. 1498–1504, 2014.

[134] T. Wang, B. Zhang, G. Chen, and J. Feng, "High strength electron beam welded titanium-stainless steel joint with V/Cu based composite filler metals," *Vacuum*, vol. 94, pp. 41–47, 2013.

[135] S. Nemat-Nasser and W. Guo, "High strain-rate response of commercially pure vanadium," *Mech. Mater.*, vol. 32, no. 4, pp. 243–260, 2000.

[136] R. F. Mattas, B. A. Loomis, and D. L. Smith, “Vanadium alloys for fusion reactor applications,” *JOM*, vol. 44, no. 8, pp. 26–29, 1992.

[137] S. Mukherjee and N. I. Jamnapara, “Materials research and development opportunities in fusion reactors,” *Proceedings of the Indian National Science Academy*, vol. 81, no. 4. pp. 827–839, 2015.

[138] H. Watanabe, A. Higashijima, N. Yoshida, T. Nagasaka, and T. Muroga, “The microstructure of laser welded Y doped V-4Cr-4Ti alloys after ion irradiation,” *J. Nucl. Mater.*, vol. 386–388, no. C, pp. 598–601, 2009.

[139] J. M. Chen, V. M. Chernov, R. J. Kurtz, and T. Muroga, “Overview of the vanadium alloy researches for fusion reactors,” in *Journal of Nuclear Materials*, 2011, vol. 417, no. 1–3, pp. 289–294.

[140] N. J. Heo, T. Nagasaka, T. Muroga, A. Nishimura, K. Shinozaki, and N. Takeshita, “Metallurgical and mechanical properties of laser weldment for low activation V-4Cr-4Ti alloy,” *Fusion Eng. Des.*, vol. 62, pp. 749–755, 2002.

[141] D. He, Z. Fu, W. Wang, J. Zhang, Z. A. Munir, and P. Liu, “Temperature-gradient joining of Ti-6Al-4V alloys by pulsed electric current sintering,” *Mater. Sci. Eng. A*, vol. 535, pp. 182–188, 2012.

[142] N. Sharma, S. N. Alam, and B. C. Ray, “Fundamentals of spark plasma sintering (SPS): An ideal processing technique for fabrication of metal matrix nanocomposites,” in *Spark Plasma Sintering of Materials: Advances in Processing and Applications*, P. Cavaliere, Ed. Cham: Springer International Publishing, 2019, pp. 21–59.

[143] P. Cavaliere, B. Sadeghi, and A. Shabani, “Spark plasma sintering: Process fundamentals,” in *Spark Plasma Sintering of Materials: Advances in Processing and Applications*, P. Cavaliere, Ed. Cham: Springer International Publishing, 2019, pp. 3–20.

[144] W. Brian James, “Powder Metallurgy Methods and Applications,” in *ASM Handbook, Powder Metallurgy*, vol. 7, 2015, pp. 1172–1176.

[145] I. C. and Y. Zhao, *Advances in Powder Metallurgy Properties, processing and applications*. Cambridge, UK: Woodhead Publishing Limited, 2013.

[146] M. Zadra, F. Casari, L. Girardini, and A. Molinari, “Microstructure and mechanical properties of cp-titanium produced by spark plasma sintering,” *Powder Metall.*, vol. 51, no. 1, pp. 59–65, 2008.

[147] R. Orrù, R. Licheri, A. M. Locci, A. Cincotti, and G. Cao, “Consolidation/synthesis

of materials by electric current activated/assisted sintering," *Mater. Sci. Eng. R Reports*, vol. 63, no. 4–6, pp. 127–287, 2009.

[148] C. Musa *et al.*, "Energy efficiency during conventional and novel sintering processes: the case of Ti-Al_2O_3-TiC composites," *J. Clean. Prod.*, vol. 17, no. 9, pp. 877–882, 2009.

[149] N. S. Weston, F. Derguti, A. Tudball, and M. Jackson, "Spark plasma sintering of commercial and development titanium alloy powders," *J. Mater. Sci.*, vol. 50, no. 14, pp. 4860–4878, 2015.

[150] R. Nicula, F. Lüthen, M. Stir, B. Nebe, and E. Burkel, "Spark plasma sintering synthesis of porous nanocrystalline titanium alloys for biomedical applications," *Biomol. Eng.*, vol. 24, no. 5, pp. 564–567, 2007.

[151] M. Kon, L. M. Hirakata, and K. Asaoka, "Porous Ti-6Al-4V Alloy Fabricated by Spark Plasma Sintering for Biomimetic Surface Modification," *J. Biomed. Mater. Res. - Part B Appl. Biomater.*, vol. 68, no. 1, pp. 88–93, 2004.

[152] F. Zhang, E. Otterstein, and E. Burkel, "Spark plasma sintering, microstructures, and mechanical properties of macroporous titanium foams," *Adv. Eng. Mater.*, vol. 12, no. 9, pp. 863–872, 2010.

[153] S. Muñoz and U. Anselmi-Tamburini, "Temperature and stress fields evolution during spark plasma sintering processes," *J. Mater. Sci.*, vol. 45, no. 23, pp. 6528–6539, 2010.

[154] D. Garbiec, P. Siwak, and A. Mróz, "Effect of compaction pressure and heating rate on microstructure and mechanical properties of spark plasma sintered Ti6Al4V alloy," *Arch. Civ. Mech. Eng.*, vol. 16, no. 4, pp. 702–707, 2016.

[155] L. Bolzoni, P. G. Esteban, E. M. Ruiz-Navas, and E. Gordo, "Mechanical behaviour of pressed and sintered titanium alloys obtained from prealloyed and blended elemental powders," *J. Mech. Behav. Biomed. Mater.*, vol. 14, pp. 29–38, 2012.

[156] I. M. Robertson and G. B. Schaffer, "Design of titanium alloy for efficient sintering to low porosity," *Powder Metall.*, vol. 52, no. 4, pp. 311–315, 2009.

[157] R. Chaudhari and R. Bauri, "Microstructure and Mechanical Properties of Titanium Processed by Spark Plasma Sintering (SPS)," *Metallogr. Microstruct. Anal.*, vol. 3, no. 1, pp. 30–35, 2014.

[158] A. W. Fliflet, G. Chevallier, K. Crosby, M. A. Imam, C. Estournes, and L. L. Shaw, "Enhancement in Ti–6Al–4V sintering via nanostructured powder and spark plasma sintering," *Powder Metall.*, vol. 57, no. 2, pp. 147–154, 2014.

[159] Montgomery, “Design and Analysis of Experiments,” in *Design and Analysis of Experiments*, North Carolina, USA: SAS Institute Inc., 2013.

[160] V. Dey, D. K. Pratihar, G. L. Datta, M. N. Jha, T. K. Saha, and A. V. Bapat, “Optimization and prediction of weldment profile in bead-on-plate welding of Al-1100 plates using electron beam,” *Int. J. Adv. Manuf. Technol.*, vol. 48, no. 5–8, pp. 513–528, 2010.

[161] E. M. Anawa, A. G. Olabi, and F. A. Elshukri, “Modeling and optimization of tensile shear strength of Titanium/Aluminum dissimilar welded component,” *J. Phys. Conf. Ser.*, vol. 181, no. 1, 2009.

[162] S. M. Bayazid, H. Farhangi, and A. Ghahramani, “Investigation of Friction Stir Welding Parameters of 6063-7075 Aluminum Alloys by Taguchi Method,” *Procedia Mater. Sci.*, vol. 11, no. 2010, pp. 6–11, 2015.

[163] B. Liao, Y. Shi, Y. Cui, S. Cui, Z. Jiang, and Y. Yi, “Mathematical Model for Prediction and Optimization of Weld Bead Geometry in All-Position Automatic Welding of Pipes,” *Metals (Basel).*, vol. 8, no. 10, p. 756, 2018.

[164] V. Gunaraj and N. Murugan, “Application of response surface methodology for predicting weld bead quality in submerged arc welding of pipes,” *J. Mater. Process. Technol.*, vol. 88, no. 1, pp. 266–275, 1999.

[165] J. C. Ion, H. R. Shercliff, and M. F. Ashby, “Diagrams for laser materials processing,” *Acta Metall. Mater.*, vol. 40, no. 7, pp. 1539–1551, 1992.

[166] M. Thomas, G. J. Baxter, and I. Todd, “Normalised model-based processing diagrams for additive layer manufacture of engineering alloys,” *Acta Mater.*, vol. 108, pp. 26–35, 2016.

[167] S. S. Al-bermani, “An Investigation into Microstructure and Microstructural Control of Additive Layer Manufactured Ti-6AI-4V by Electron Beam Melting, Ph.D thesis,” University of Sheffield, 2011.

[168] S. K. Vajpai *et al.*, “The Development of High Performance Ti-6Al-4V Alloy via a Unique Microstructural Design with Bimodal Grain Size Distribution,” *Metall. Mater. Trans. A Phys. Metall. Mater. Sci.*, vol. 46, no. 2, pp. 903–914, 2015.

[169] D. C. Hofmann *et al.*, “Developing gradient metal alloys through radial deposition additive manufacturing,” *Sci. Rep.*, vol. 4, 2014.

[170] J. Li *et al.*, “The effects of spark-plasma sintering (SPS) on the microstructure and mechanical properties of BaTiO3/3Y-TZP composites,” *Materials (Basel).*, vol. 9, no. 5, p. 320, 2016.

[171] R. Maeda *et al.*, “High performance Ti-6Al-4V alloy by creation of harmonic structure design,” *IOP Conf. Ser. Mater. Sci. Eng.*, vol. 63, p. 012030, 2014.

[172] K. Sim, G. Wang, J. Ju, J. Yang, and X. Li, “Microstructure and mechanical properties of a Ti−22Al−25Nb alloy fabricated from elemental powders by mechanical alloying and spark plasma sintering,” *J. Alloys Compd.*, vol. 704, no. February, pp. 425–433, 2017.

[173] A. Mróz, D. Garbiec, A. Wielowiejska-Giertuga, T. Wiśniewski, M. Gierzyńska-Dolna, and A. Martyła, “Structural, mechanical and tribological properties of spark plasma sintered Ti6Al4V alloy,” *Arch. Metall. Mater.*, vol. 61, no. 2A, pp. 665–670, 2016.

[174] X. Lu, B. Sun, T. Zhao, L. Wang, C. Liu, and X. Qu, “Microstructure and mechanical properties of spark plasma sintered Ti-Mo alloys for dental applications,” *Int. J. Miner. Metall. Mater.*, vol. 21, no. 5, pp. 479–486, May 2014.

[175] J.-M. Oh *et al.*, “Sintering Properties of Ti–6Al–4V Alloys Prepared Using Ti/TiH_2 Powders,” *Mater. Trans.*, vol. 54, no. 1, pp. 119–121, 2013.

[176] M. Galati and L. Iuliano, “A literature review of powder-based electron beam melting focusing on numerical simulations,” *Additive Manufacturing*, vol. 19. Elsevier B.V., pp. 1–20, 2018.

[177] A. Genga *et al.*, “SEM-EDS investigation on PM10 data collected in Central Italy: Principal Component Analysis and Hierarchical Cluster Analysis,” *Chem. Cent. J.*, vol. 6, no. SUPPL.2, p. S3, 2012.

[178] P. D. Ngo, “Energy Dispersive Spectroscopy,” in *Failure Analysis of Integrated Circuits*, L. C. Wagner, Ed. Boston, MA: The Springer International Series in Engineering and Computer Science, 2012, pp. 205–215.

[179] D. E. Newbury and N. W. M. Ritchie, “Performing elemental microanalysis with high accuracy and high precision by scanning electron microscopy/silicon drift detector energy-dispersive X-ray spectrometry (SEM/SDD-EDS),” *J. Mater. Sci.*, vol. 50, no. 2, pp. 493–518, 2014.

[180] ASTM Standard, “E384 -17: Standard Test Method for Microindentation Hardness of Materials,” *ASTM Int.*, pp. 1–40, 2017.

[181] K. Kumar *et al.*, “Use of miniature tensile specimen for measurement of mechanical properties,” *Procedia Eng.*, vol. 86, pp. 899–909, 2014.

[182] M. Anandajothi, S. Ramanathan, V. Ananthi, and P. Narayanasamy, “Fabrication and characterization of Ti6Al4V/TiB2–TiC composites by powder metallurgy method,”

Rare Met., vol. 36, no. 10, pp. 806–811, 2017.

[183] Z. H. Zhang, X. B. Shen, F. C. Wang, S. Wei, S. K. Li, and H. N. Cai, "Microstructure characteristics and mechanical properties of TiB/Ti-1.5Fe-2.25Mo composites synthesized in situ using SPS process," *Trans. Nonferrous Met. Soc. China (English Ed.*, vol. 23, no. 9, pp. 2598–2604, 2013.

[184] S. Decker, J. Lindemann, and L. Krüger, "Synthesis and mechanical properties of TiAl particle reinforced Ti-6Al-4V," *Mater. Sci. Eng. A*, vol. 674, pp. 361–365, 2016.

[185] J. Schmidt, T. Weissgaerber, T. Schubert, and B. Kieback, "Spark Plasma Sintering of Intermetallics and Metal Matrix Composites," *Eur. Congr. Exhib. Powder Metall. Eur. PM Conf. Proc.*, vol. 1, p. 93, 2005.

[186] B. Liu, S. Huang, L. Chen, J. Van Humbeeck, and J. Vleugels, "Rapid synthesis of dense NiTi alloy through spark plasma sintering of a TiH2/Ni powder mixture," *Mater. Lett.*, vol. 191, pp. 89–92, 2017.

[187] S. Ghesmati Tabrizi, A. Babakhani, S. A. Sajjadi, and W. J. Lü, "Microstructural aspects of in-situ TiB reinforced Ti-6Al-4V composite processed by spark plasma sintering," *Trans. Nonferrous Met. Soc. China (English Ed.*, vol. 25, no. 5, pp. 1460–1467, 2015.

[188] L. M. Kang *et al.*, "Designing ultrafine lamellar eutectic structure in bimodal titanium alloys by semi-solid sintering," *J. Alloys Compd.*, vol. 702, pp. 51–59, 2017.

[189] C. Yu, P. Cao, and M. Jones, "Microstructural Evolution during Pressureless Sintering of Blended Elemental Ti-Al-V-Fe Titanium Alloys from Fine Hydrogenated-Dehydrogenated Titanium Powder," *Metals (Basel).*, vol. 7, no. 8, p. 285, 2017.

[190] H. L. Shao, J. J. Song, D. Q. Sun, and Z. K. Zhao, "Micro-structure and properties of Ti6Al4V/nHA composite material prepared by spark plasma sintering," *Mater. Res. Innov.*, vol. 19, no. sup4, pp. S157–S162, 2015.

[191] K. Arshad *et al.*, "Influence of vanadium precursor powder size on microstructures and properties of W-V alloy," *Int. J. Refract. Met. Hard Mater.*, vol. 50, pp. 59–64, 2015.

[192] Y. Q. Zhao, S. W. Xin, and W. D. Zeng, "Effect of major alloying elements on microstructure and mechanical properties of a highly β stabilized titanium alloy," *J. Alloys Compd.*, vol. 481, no. 1–2, pp. 190–194, 2009.

[193] Y. F. Yang, H. Imai, K. Kondoh, and M. Qian, "Enhanced Homogenization of Vanadium in Spark Plasma Sintering of Ti-10V-2Fe-3Al Alloy from Titanium and

V-Fe-Al Master Alloy Powder Blends," *Jom*, vol. 69, no. 4, pp. 663–668, 2017.

[194] Y. F. Yang and M. Qian, "Spark plasma sintering and hot pressing of titanium and titanium alloys," *Titan. Powder Metall. Sci. Technol. Appl.*, no. December, pp. 219–235, 2015.

[195] N. S. Weston, "A novel solid-state processing route to generate cost-effective titanium alloy components," Ph.D thesis, The University of Sheffield, 2017.

[196] R. Chaudhari and R. Bauri, "Reaction mechanism, microstructure and properties of Ti-TiB insitu composite processed by spark plasma sintering," *Mater. Sci. Eng. A*, vol. 587, pp. 161–167, 2013.

[197] L. de M. Amorim, N. Vicente Jr., M. A. C. Berton, and C. E. B. Marino, "Harmonic Structured Ti6Al4V by Spark Plasma Sintering," *Mater. Sci. Forum*, vol. 899, no. July, pp. 452–457, 2017.

[198] X. P. Wang *et al.*, "Effect of milling time on microstructure of Ti35Nb2.5Sn/10HA biocomposite fabricated by powder metallurgy and sintering," *Trans. Nonferrous Met. Soc. China (English Ed.*, vol. 22, no. 3, pp. 608–612, 2012.

[199] T. Borkar, S. Nag, Y. Ren, J. Tiley, and R. Banerjee, "Reactive spark plasma sintering (SPS) of nitride reinforced titanium alloy composites," *J. Alloys Compd.*, vol. 617, pp. 933–945, 2014.

[200] ASM Handbook, "Alloy Phase Diagrams," *ASM Int. Mater. Park. OH*, vol. 3, no. 2, pp. 222–276, 1982.

[201] S. R. Oke, O. O. Ige, O. E. Falodun, B. A. Obadele, M. B. Shongwe, and P. A. Olubambi, "Optimization of process parameters for spark plasma sintering of nano structured SAF 2205 composite," *J. Mater. Res. Technol.*, vol. 7, no. 2, pp. 126–134, 2018.

[202] K. V. Ivanov and E. V. Naydenkin, "The effect of strain rate on tensile behavior and deformation mechanisms of ultrafine-grained aluminum," *IOP Conf. Ser. Mater. Sci. Eng.*, vol. 63, no. 1, 2014.

[203] X. Zhang, J. Zhang, F. Chen, Z. Yang, and J. He, "Characteristics of Resistance Spot Welded Ti6Al4V Titanium Alloy Sheets," *Metals (Basel).*, vol. 7, no. 10, p. 424, 2017.

[204] S. S. Al-Bermani, M. L. Blackmore, W. Zhang, and I. Todd, "The origin of microstructural diversity, texture, and mechanical properties in electron beam melted Ti-6Al-4V," *Metall. Mater. Trans. A Phys. Metall. Mater. Sci.*, vol. 41, no. 13, pp. 3422–3434, 2010.

[205] ASM Handbook, “Properties and Selection: Nonferrous Alloys and Special-Purpose Materials,” *ASM Int. Mater. Park. OH*, vol. 2, 1998.

[206] “www.matweb.com.” .

[207] J. W. Arblaster, “Thermodynamic Properties of Vanadium,” *J. Phase Equilibria Diffus.*, vol. 38, no. 1, pp. 51–64, 2017.

[208] C. D. Boley, S. C. Mitchell, A. M. Rubenchik, and S. S. Q. Wu, “Metal powder absorptivity: modeling and experiment,” *Appl. Opt.*, vol. 55, no. 23, p. 6496, 2016.

[209] M. S. Węglowski, S. Błacha, and A. Phillips, “Electron beam welding - Techniques and trends - Review,” *Vacuum*, vol. 130, no. May, pp. 72–92, 2016.

[210] BSI, “BS EN ISO 6520-1: Welding and allied processes — Classification of geometric imperfections in metallic materials — Part 1: Fusion welding,” *Br. Stand.*, vol. 3, 2007.

[211] BSI, “BS EN 4677-001: Welded and brazed assemblies for aerospace construction — Joints of metallic materials by electron beam welding Part 001 : Quality of welded assemblies,” *BSI Standards Publication*. 2012.

[212] B. Fotovvati, S. F. Wayne, G. Lewis, and E. Asadi, “A Review on Melt-Pool Characteristics in Laser Welding of Metals,” *Adv. Mater. Sci. Eng.*, vol. 2018, 2018.

[213] T. C. Nguyen, D. C. Weckman, D. A. Johnson, and H. W. Kerr, “High speed fusion weld bead defects,” *Sci. Technol. Weld. Join.*, vol. 11, no. 6, pp. 618–633, 2006.

[214] J. H. Liu, C. H. Du, C. T. Li, H. Bin Xu, and Y. Luo, “The Evaporation Effect of Front Keyhole Wall in Penetration Welding with an Electron Beam,” *Mater. Sci. Forum*, vol. 686, pp. 355–360, 2011.

[215] A. Ribolla, G. L. Damoulis, and G. F. Batalha, “The use of Nd:YAG laser weld for large scale volume assembly of automotive body in white,” *J. Mater. Process. Technol.*, vol. 164–165, pp. 1120–1127, 2005.

[216] European Standard, “EN ISO 5817 Welding - Fusion-welded joints in steel, nickel, titanium and their alloys (beam welding excluded) - Quality levels for imperfections,” *Eur. Comm. Standarization*, 2014.

[217] American Welding Society, “AWS D17.1, Specification for Fusion Welding for Aerospace Applications,” in *American National Standard*, Miami, Florida: American Welding Society, 2001.

[218] J. Sánchez-Amaya *et al.*, “Microstructure and Mechanical Properties of Ti5553 Butt Welds Performed by LBW under Conduction Regime,” *Metals (Basel).*, vol. 7, no. 7, p. 269, 2017.

[219] J. Liu, X. L. Gao, L. J. Zhang, and J. X. Zhang, “Effects of the Heterogeneity in the Electron Beam Welded Joint on Mechanical Properties of Ti6Al4V Alloy,” *J. Mater. Eng. Perform.*, vol. 24, no. 1, pp. 319–328, 2015.

[220] B. G. Zhang, M. X. Shi, G. Q. Chen, and J. C. Feng, “Microstructure and defect of titanium alloy electron beam deep penetration welded joint,” *Trans. Nonferrous Met. Soc. China (English Ed.*, vol. 22, no. 11, pp. 2633–2637, 2012.

[221] E. Hernández-Nava, “A study on the mechanical properties of micro-truss Ti-6Al-4V materials fabricated by Electron Beam Melting,” Ph.D thesis, University of Sheffield, 2016.

[222] Y. Wang, P. Fu, Y. Guan, Z. Lu, and Y. Wei, “Research on modeling of heat source for electron beam welding fusion-solidification zone,” *Chinese J. Aeronaut.*, vol. 26, no. 1, pp. 217–223, 2013.

[223] T. a Palmer, J. W. Elmer, R. Pong, and M. D. Gauthier, “Welding of Vanadium , Tantalum , 304L and 21-6-9 Stainless Steels , and Titanium Alloys at Lawrence Livermore National Laboratory using a Fiber Delivered 2 . 2 kW Diode Pumped CW Nd : YAG Laser,” 2006.

[224] T. Song, D. Mo, Y. Fang, X. Jiang, and Y. Wang, “Influence of Welding Speed on the Microstructure and Mechanical Properties of Electron Beam-Welded Joints of TC4 and 4J29 Sheets using Cu/Nb Multi-Interlayers,” *Metals (Basel).*, vol. 8, no. 10, p. 810, 2018.

[225] BSI, “BS EN ISO 5817:2007 Welding — Fusion-welded joints in steel , nickel , titanium and their alloys (beam welding excluded) — Quality levels for imperfections,” *BSI Stand. Publ.*, vol. 3, p. 38, 2007.

[226] ASM Handbook, *Welding, Brazing and Soldering*, vol. 6. ASM International: Materials Park, OH, 1993.

[227] J. N. DuPont and A. R. Marder, “Dilution in single pass arc welds,” *Metall. Mater. Trans. B Process Metall. Mater. Process. Sci.*, vol. 27, no. 3, pp. 481–489, 1996.

[228] J. A. Francis, B. Bednarz, and J. V. Bee, “Prediction of steady state dilution in multipass hardfacing overlays deposited by self shielded flux cored arc welding,” *Sci. Technol. Weld. Join.*, vol. 7, no. 2, pp. 95–101, 2002.

[229] R. E. Avery, “Guidelines for welding dissimilar metals,” *Chem. Eng. Prog.*, no. May, 1991.

[230] T. Muroga *et al.*, “Vanadium alloys - Overview and recent results,” *J. Nucl. Mater.*, vol. 307–311, no. 1 SUPPL., pp. 547–554, 2002.

[231] A. Impagnatiello, T. Toyama, and E. Jimenez-Melero, “Ti-rich precipitate evolution in vanadium-based alloys during annealing above 400 °C,” *J. Nucl. Mater.*, vol. 485, no. March, pp. 122–128, 2017.

[232] A. G. Quarrell, “The Hardness of Metals,” *Nature*, vol. 170, no. 4333, p. 818, 1952.

[233] S. L. Semiatin and T. R. Bieler, “The effect of alpha platelet thickness on plastic flow during hot working of Ti-6Al-4V with a transformed microstructure,” *Acta Mater.*, vol. 49, no. 17, pp. 3565–3573, 2001.

[234] A. Fall, M. Jahazia, A. R. Khodabandehb, and M. H. Fesharakib, “Effect of process parameters on microstructure and mechanical properties of friction stir-welded Ti–6Al–4V joints,” *Int. J. Adv. Manuf. Technol.*, pp. 1–13, 2016.